

**IMPROVED MODELING OF EVAPOTRANSPIRATION USING SATELLITE
REMOTE SENSING AT VARYING SPATIAL AND TEMPORAL SCALES**

A Dissertation

by

DI LONG

Submitted to the Office of Graduate Studies of
Texas A&M University
in partial fulfillment of the requirements for the degree of

DOCTOR OF PHILOSOPHY

August 2011

Major Subject: Biological and Agricultural Engineering

**IMPROVED MODELING OF EVAPOTRANSPIRATION USING SATELLITE
REMOTE SENSING AT VARYING SPATIAL AND TEMPORAL SCALES**

A Dissertation

by

DI LONG

Submitted to the Office of Graduate Studies of
Texas A&M University
in partial fulfillment of the requirements for the degree of

DOCTOR OF PHILOSOPHY

Approved by:	Vijay P. Singh
Chair of Committee,	Clyde L. Munster
Committee Members,	Ralph A. Wurbs
	Steven M. Quiring
Head of Department,	Stephen W. Searcy

August 2011

Major Subject: Biological and Agricultural Engineering

ABSTRACT

Improved Modeling of Evapotranspiration using Satellite Remote Sensing at Varying
Spatial and Temporal Scales. (August 2011)

Di Long, B.S., Tsinghua University, China;

M.S., Institute of Geographic Sciences and Natural Resources Research, Chinese

Academy of Sciences

Chair of Advisory Committee: Dr. Vijay P. Singh

The overall objective of the dissertation was to improve the spatial and temporal representation and retrieval accuracy of evapotranspiration (ET) using satellite imagery. Specifically, (1) aiming at improving the spatial representation of daily net radiation ($R_{n,24}$) under rugged terrains, a new algorithm, which accounts for terrain effects on available shortwave radiation throughout a day and utilizes four observations of Moderate-resolution Imaging Spectroradiometer (MODIS)-based land surface temperature retrievals to simulate daily net longwave radiation, was developed. The algorithm appears to be capable of capturing heterogeneity in $R_{n,24}$ at watershed scales. (2) Most satellite-based ET models are constrained to work under cloud-free conditions. To address this deficiency, an approach of integrating a satellite-based model with a large-scale feedback model was proposed to generate ET time series for all days. Results show that the ET time series estimates can exhibit complementary features between the potential ET and the actual ET at watershed scales. (3) For improving the operability of

Two-source Energy Balance (TSEB) which requires computing resistance networks and tuning the Priestley-Taylor parameter involved, a new Two-source Trapezoid Model for ET (TTME) based on deriving theoretical boundaries of evaporative fraction (EF) and the concept of soil surface moisture availability isopleths was developed. It was applied to the Soil Moisture and Atmosphere Coupling Experiment (SMACEX) site in central Iowa, U.S., on three Landsat TM/ETM⁺ imagery acquisition dates in 2002. Results show the EF and latent heat flux (LE) estimates with a mean absolute percentage difference (MAPD) of 6.7% and 8.7%, respectively, relative to eddy covariance tower-based measurements after forcing closure by the Bowen ratio technique. (4) The domain and resolution dependencies of the Surface Energy Balance Algorithm for Land (SEBAL) and the triangle model were systematically investigated. Derivation of theoretical boundaries of EF for the two models could effectively constrain errors/uncertainties arising from these dependencies. (5) A Modified SEBAL (M-SEBAL) was consequently proposed, in which subjectivity involved in the selection of extreme pixels by the operator is eliminated. The performance of M-SEBAL at the SMACEX site is reasonably well, showing EF and LE estimates with an MAPD of 6.3% and 8.9%, respectively.

DEDICATION

To my father, Guohong Long, and my mother, Yimin Xiong

ACKNOWLEDGMENTS

To begin with, I would like to extend my gratitude to my academic advisor, Professor Vijay P. Singh, who provided me guidance, support, and encouragement in my research during years at Texas A&M University. He offered constructive and timely suggestions on my work, and also gave me ample space and freedom to conduct my research. Dr. Singh is so knowledgeable and a wise professor in the areas of hydrology, hydraulics, and environmental engineering. I only learned a small portion of his specialty during my Ph.D. study. However, his extreme diligence and devotion to the work, and great generousness and kindness to his students, colleagues, friends, and people he might not know all around the world will encourage me to continue the journey of research and service to others. Being a student of and working with Professor Singh at TAMU would be one of the greatest occurrences in my lifetime.

I would also like to thank Dr. Clyde M. Munster, Dr. Ralph A. Wurbs, and Dr. Steven M. Quiring for their insightful guidance and support during my research work. Special thanks go to Dr. Lei Meng, Dr. Bailang Yu, Li Kui, Zengchao Hao, Chao Li, Dr. Ashok K Mishra, Dr. Hemant Chowdhary, Huijuan Cui, and Prakash Chundun for their encouragement and support during my stay at TAMU. Thanks also go to the department faculty and staff for making my time at TAMU a great experience.

I also want to extend my gratitude to National Snow and Ice Data Center which provided Soil Moisture Atmosphere Coupling Experiment (SMACEX) data sets used in the dissertation research. All people involved in the field campaign are greatly

appreciated. This work was financially supported by the United States Geological Survey (USGS, project 2009TX334G) through the project “Hydrological Drought Characterization for Texas under Climate Change, with Implication for Water Resources Planning and Management.”

Finally, I would like to thank my aunt who passed away recently. She provided me tremendous support since I was young. Gratitude goes to my farther and mother, whose love, support, and kindness give me confidence, wisdom, strength, and endurance to pursue my dreams.

TABLE OF CONTENTS

	Page
ABSTRACT	iii
DEDICATION.....	v
ACKNOWLEDGMENTS.....	vi
TABLE OF CONTENTS	viii
LIST OF FIGURES.....	xi
LIST OF TABLES.....	xix
 CHAPTER	
I INTRODUCTION.....	1
1.1. Background	1
1.2. Objectives.....	7
1.3. Methodology.....	8
1.4. Significance of research	10
1.5. Organization of dissertation.....	11
 II ESTIMATION OF DAILY AVERAGE NET RADIATION FROM MODIS DATA AND DEM.....	 13
2.1. Introduction	13
2.2. Study site and data description.....	18
2.3. Methodology.....	23
2.4. Results and discussion.....	38
2.5. Conclusions	60
 III INTEGRATION OF THE GG MODEL WITH SEBAL TO PRODUCE ET TIME SERIES OF HIGH SPATIAL RESOLUTION AT WATERSHED SCALES	 63

CHAPTER		Page
	3.1. Introduction	63
	3.2. Critique of methods to generate ET time series	67
	3.3. Proposed integration method	70
	3.4. Application	77
	3.5. Results and discussion	85
	3.6. Summary and conclusion	103
IV	A TWO-SOURCE TRAPEZOID MODEL FOR ET (TTME) FROM SATELLITE IMAGERY	105
	4.1. Introduction	105
	4.2. Model formulation.....	109
	4.3. Study site and data processing.....	126
	4.4. Results	135
	4.5. Discussion.....	147
	4.6. Concluding remarks.....	156
V	SENSITIVITY OF SEBAL TO CHANGES IN INPUT VARIABLES, DOMAIN SIZE AND SATELLITE SENSOR.....	158
	5.1. Introduction	158
	5.2. Study site, data and variable derivation.....	163
	5.3. Sensitivity analysis of H	167
	5.4. Selection of extreme pixels	176
	5.5. Domain scale effect	180
	5.6. Resolution scale effect.....	187
	5.7. Concluding remarks.....	193
VI	A MODIFIED SURFACE ENERGY BALANCE ALGORITHM FOR LAND (M-SEBAL) BASED ON A TRAPEZOIDAL FRAMEWORK.....	195
	6.1. Introduction	195
	6.2. Model formulation.....	198
	6.3. Results and discussion.....	207
	6.4. Summary of model advantages and limitations.....	226
	6.5. Concluding remarks.....	228

CHAPTER		Page
VII	ADDRESSING THE SCALE DEPENDENCIES OF REMOTE SENSING-BASED TRIANGLE MODELS	230
	7.1. Introduction	230
	7.2. Model formulation.....	234
	7.3. Domain scale effects.....	241
	7.4. Resolution scale effects	253
	7.5. Conclusions	264
VIII	CONCLUSIONS, LIMITATIONS AND RECOMMENDATIONS FOR FUTURE RESEARCH.....	267
	8.1. Conclusions	267
	8.2. Limitation of research	271
	8.3. Recommendations of future research	273
	REFERENCES.....	275
	VITA.....	302

LIST OF FIGURES

	Page
Figure 1.1 A framework of ET time series modeling system	11
Figure 2.1 Location (a) and land use (b) of the Baiyangdian watershed in North China with relevant information	21
Figure 2.2 Sensitivity analysis of instantaneous direct solar radiation S_{in} to atmospheric attenuation variables	26
Figure 2.3 A sketch for illustrating determination of sunrise and sunset angles for sloping land surfaces in case b	31
Figure 2.4 Variations in direct and diffuse solar radiation ($W m^{-2}$) with solar zenith angle on the range of $[0, \pi/2]$ under different atmospheric transmissivity and elevation conditions	34
Figure 2.5 Distributions of sunrise and sunset angles (rad) of the Baiyangdian watershed on Feb 9, May 9, Aug 13 and Nov 11	39
Figure 2.6 Variations in simulated daily average direct solar radiation ($W m^{-2}$) with slopes for different azimuths across the Baiyangdian watershed on Apr 25, 2007	43
Figure 2.7 Variations in simulated daily average direct solar radiation ($W m^{-2}$) with slopes for different azimuths across the Baiyangdian watershed on Sep 19, 2007	44
Figure 2.8 Frequency distributions of the difference between simulated $S_{in,24}$ ($W m^{-2}$) from assuming the land surface to be horizontal across the study watershed and $S_{in,24}$ ($W m^{-2}$) from the adopted geometric model for sloping land surfaces with slopes larger than 25° and 45° on Apr 25 and Sep 19, respectively (A bin size of $5 W m^{-2}$ is specified).....	47
Figure 2.9 Simulated DANSR ($W m^{-2}$) over the Baiyangdian watershed for six clear sky days in the year 2007	50
Figure 2.10 Comparisons of estimates of DANLR ($W m^{-2}$) from the one observation-based method and the four observations-based method against the Penman equation across 18 weather stations over the Baiyangdian watershed for six clear sky days in the year 2007.....	52

Figure 2.11 Comparisons of estimates of DANLR (W m^{-2}) from the one observation-based method and the four observations-based method against the Penman equation across 18 sites over the Baiyangdian watershed for the whole study period	54
Figure 2.12 Simulated DANR (W m^{-2}) over the Baiyangdian watershed for six clear sky days in the year 2007	56
Figure 2.13 Relationships between DANR and elevation across the study watershed for six clear sky days in the year 2007	59
Figure 3.1 Sensitivity analysis of the FAO56 reference ET equation (a) and the GG model (b), with reference values: $R_{n,24}=17.28 \text{ MJ m}^{-2} \text{ d}^{-1}$, $e_s-e_a=1 \text{ kPa}$, $u_2=2 \text{ m s}^{-1}$, and $T_a=27 \text{ }^\circ\text{C}$	70
Figure 3.2 Flow diagram of the inputs and outputs of the GG model.....	76
Figure 3.3 Selection of hot and cold pixels from the contextual map of NDVI and LST for simulating daily ET by SEBAL under cloud-free days	81
Figure 3.4 Calibration of the functional relationship between D and G in the GG model using SEBAL-based ET estimates for the Baiyangdian watershed on 12 cloud-free days in year 2007, with showing GG 1989 and GG 1996	83
Figure 3.5 Evaporative fractions and crop coefficients from SEBAL of the Baiyangdian watershed on 28 cloud-free days in year 2007, with showing corresponding daily precipitation and mean values of these estimates.....	87
Figure 3.6 Variations in the FAO56-based reference ET, pan ET, and precipitation of the Baiyangdian watershed for the Anxin, Fuping, Yixian, and Anguo stations in year 2007.....	90
Figure 3.7 ET Time series from the evaporative fraction method, the crop coefficient method, and the proposed integration method of the Baiyangdian watershed in year 2007, with showing corresponding observations of daily precipitation and pan ET	92
Figure 3.8 Observations of the pan ET and actual ET estimates from the evaporative fraction method (a), the crop coefficient method (b), and the proposed integration method (c) of the Baiyangdian watershed	

	Page
for days with $R_{n,24} > 100 \text{ W m}^{-2}$	94
Figure 3.9 Comparison of predictions of daily ET from the modified GG and GG 1989 for the Baiyangdian watershed in year 2007 and SEBAL-based counterparts	98
Figure 3.10 Spatial distributions of ET estimates from SEBAL, the modified GG model, GG 1989 and 1996 of the Baiyangdian watershed on April 25, 2007	101
Figure 4.1 A sketch (a) of the trapezoid f_c - T_{rad} space involved in TTME and (b) illustrates the decomposition of T_{rad} into T_s and T_c	112
Figure 4.2 Flow chart of TTME	125
Figure 4.3 Location and the false color composite of Landsat TM imagery acquired on June 23, 2002, of the SMACEX study site at Ames, central Iowa, U.S.	127
Figure 4.4 Comparison of the observed energy availability ($R_n - G$) and the sum of observed sensible and latent heat fluxes ($LE + H$), showing the averaged closure ratio (CR) of 0.85	129
Figure 4.5 Comparison of surface albedo retrievals from Landsat TM/ETM ⁺ imageries using observed near-surface vapor pressure and MOD05_L2 precipitable water products, respectively	133
Figure 4.6 Comparison of R_n , G , H , and LE fluxes (W m^{-2}) from TTME with corresponding eddy covariance tower-based measurements (W m^{-2}) at the SMACEX site on DOY 174, 182 and 189 in 2002	136
Figure 4.7 Comparison of EF from TTME with corresponding eddy covariance tower-based EF at the SMACEX site on DOY 174, 182 and 189 in 2002	139
Figure 4.8 Spatial distribution of LE_c (W m^{-2}) and LE_s (W m^{-2}) from TTME at the SMACEX site on DOY 174, 182 and 189 in 2002	140
Figure 4.9 Sensitivity analysis of TTME to T_{rad} and T_a in (a), α_c , α_s , $\alpha_{c,\text{max}}$, and $\alpha_{s,\text{max}}$ in (b), and u^* , e_a , and h_c in (c).	143

- Figure 5.1 The Baiyangdian watershed (watershed I) with its sub-watersheds, the Zhulong River watershed (watershed II) and the Sha River watershed (watershed III) and relevant facilities, North China..... 164
- Figure 5.2 Sensitivity analysis of a , b , and H estimates to $T_{s,hot}$ and $T_{s,cold}$ for 28 initial value conditions, with the maximum, minimum, and mean variations for the 28 sets of reference values at each perturbation of $T_{s,hot}$ and $T_{s,cold}$ (0.5 K with the limits of $\pm 5K$). High-low lines on each plot represent the maximum and minimum variations. Dashed lines represent the mean variation. 170
- Figure 5.3 Sensitivity analysis of a , b , and H estimates to $R_{n,hot}$ and G_{hot} for 28 initial value conditions, with the maximum, minimum, and mean variations for the 28 sets of reference values at each perturbation of $R_{n,hot}$ and G_{hot} (5% with the limits of $\pm 50\%$). High-low lines on each plot represent the maximum and minimum variations. Dashed lines represent the mean variation..... 172
- Figure 5.4 Sensitivity analysis of a , b , and H estimates to $z_{om,hot}$ under the conditions of $z_{oh,hot}=0.1$ m and $z_{oh,hot}=0.1z_{om,hot}$ for 28 initial value conditions, respectively, with maximum, minimum, and mean variations for the 28 sets of reference values at each perturbation of $z_{om,hot}$ (5% with the limits of $\pm 50\%$). High-low lines on each plot represent the maximum and minimum variations. Dashed lines represent the mean variation. 174
- Figure 5.5 Sensitivity analysis of a , b , and H estimates to u_{200} for 28 initial value conditions, with maximum, minimum, and mean variations for the 28 sets of reference values at each perturbation (5% with the limits of $\pm 50\%$). High-low lines on each plot represent the maximum and minimum variations. Dashed lines represent the mean variation... 176
- Figure 5.6 Selection of extreme pixels for watersheds I, II, and III, respectively, on May 6, 14, 25, and 29, 2007 based on scatterplots of NDVI and LST. Black dots represent scatterplots for watershed I, red dots for watershed II, and blue dots for watershed III. Points of the intersection of black, red, and blue lines show the identified extreme pixels for watersheds I, II, and III, respectively. 180
- Figure 5.7 Shift of extreme pixels within watersheds I (1), II (2), and III (3) on 6, 14, 25, and 29 May 2007. Numbers along the symbols represent

extreme (s) for each watershed (s). Shift of extreme pixels within watersheds for the same day is represented with the same line style.	182
Figure 5.8 Comparison of H estimates between watersheds I, II, and III on May 6, 14, 25, and 29, 2007, MAPD, RMSD, slope, intercept, and R^2	185
Figure 5.9 Extreme pixels from Landsat TM-based and MODIS-based contextual maps of NDVI and LST for watershed I on May 19, 2007, points of the intersection of red lines represent the locations of the hot pixels and blue lines represent the locations of the cold pixels.	189
Figure 5.10 Comparison of H estimates from Landsat TM and MODIS images of watershed I on May 19, 2007. Landsat TM-based estimates of a 120 m resolution are aggregated to that of a 960 m resolution.....	190
Figure 5.11 Frequency distributions and relevant cumulative distributions of H estimates from Landsat TM and MODIS images of watershed I on May 19 2007. A bin size is set to 5 W m^{-2}	191
Figure 6.1 A schematic of the scatterplot of remotely sensed f_c and T_{rad} , colored circles represent pixels with varying f_c and T_{rad} . Quadrangle AB'CD represents real physical limits of the f_c - T_{rad} space. Point A represents the bare surface with the largest water stress (i.e., EF=0), point B' represents the bare surface without water stress (i.e., EF=1), point C represents the fully vegetated surface without water stress (i.e., EF=1), and point D represents the fully vegetated surface with the largest stress (i.e., EF=0). Trapezoid ABCD represents the reasonably simplified framework of quadrangle AB'CD, in which point B represents the bare surface without water stress (EF=1). Side AD is the warm edge representing surfaces of EF=0 for a full range of f_c , and side BC is the horizontal cold edge representing surfaces of EF=1 for a full range of f_c . Red dashed lines (①-③) represent hot extremes, which could be selected, involved in SEBAL, corresponding to points E, A, and F. Blue dashed lines (④-⑥) represent cold extremes, which could be selected, involved in SEBAL, corresponding to points G, C, and H.....	200

- Figure 6.2 Variation in EF with T_{rad} in SEBAL for $f_c=0.2, 0.4$, and 0.6 , respectively, given a set of coefficients a ($=0.27$) and b ($=-80.35$ K) derived from $T_{\text{rad,hot}}=316.3$ K and $T_{\text{rad,cold}}=300.1$ K and other characteristic variables, and typical values involved in ΔE_i203
- Figure 6.3 Comparison of R_n , G , H , and LE fluxes (W m^{-2}) from M-SEBAL with corresponding eddy covariance tower-based measurements (W m^{-2}) for the SMACEX site on DOY 174, 182 and 189 in 2002.208
- Figure 6.4 Comparison of EF from M-SEBAL with corresponding eddy covariance tower-based EF for the SMACEX site on DOY 174, 182 and 189 in 2002210
- Figure 6.5 Scatterplots of f_c and T_{rad} for the SMACEX site for DOY 174 and 182 in 2002, numbered red circles represent hot extreme candidates, and numbered blue circles represent cold extreme candidates. Red and blue lines represent limiting edges of the trapezoidal framework, showing $T_{s,\text{max}}$, $T_{c,\text{max}}$, and $T_{s,\text{min}}(T_a)$ for both days.213
- Figure 6.6 Estimates of R_n (magenta cross), G (green asterisk), H (red cross), and LE (blue circle) from SEBAL for 9 cases of combinations of selected extremes at the SMACEX site for DOY 174.217
- Figure 6.7 Estimates of R_n (magenta cross), G (green asterisk), H (red cross), and LE (blue circle) from SEBAL for 9 cases of combinations of selected extremes at the SMACEX site for DOY 182.218
- Figure 6.8 Variation of relative errors of H retrievals from SEBAL (triangle) and M-SEBAL (circle) with f_c for DOY 174 and 182, respectively.221
- Figure 6.9 Spatial distributions of H estimates from SEBAL and M-SEBAL, frequency distributions (on the right of the H maps), and their cumulative curves for DOY 174 and 182224
- Figure 6.10 Spatial distributions of LE estimates from SEBAL and M-SEBAL, frequency distributions (on the right of the ET maps), and their cumulative curves for DOY 174 and 182.225
- Figure 7.1 A schematic of the scatterplot of remotely sensed NDVI and T_{rad} , colored circles represent pixels with varying NDVI and T_{rad} . Side AC is the warm edge (①) of triangle ABC, whose ϕ values are equal to $\phi_{\text{min},i}$ for each NDVI value or NDVI class i . Side AE is the

warm edge (②) of rectangle models (simplified from triangle models) whose ϕ value is equal to zero. Side AD is the warm edge (③) representing surfaces of EF=0 for a full range of NDVI in trapezoid model ABCD. Side BC is the horizontal cold edge representing surfaces of EF=1 for a full range of NDVI.	235
Figure 7.2 False color composite of Landsat TM imagery acquired on June 23, 2002, covering the SAMCEX site (domain 1), progressively enlarged domains 2 and 3, and the entire scene of the Landsat TM imagery (domain 4)	242
Figure 7.3 Scatterplots of NDVI and T_{rad} derived from Landsat TM imagery for four domains with relevant observed and theoretically derived limiting edges on DOY 174.....	245
Figure 7.4 Scatterplots of NDVI and T_{rad} derived from Landsat ETM ⁺ imagery for four domains with relevant observed and theoretically derived limiting edges on DOY 182.....	246
Figure 7.5 Comparison of EF estimates from triangle models and corresponding flux tower-based measurements for four domains on DOY 174 under three scenarios	248
Figure 7.6 Comparison of EF estimates from triangle models and corresponding flux tower-based measurements for four domains on DOY 182 under three scenarios	249
Figure 7.7 Variations in the mean absolute percentage difference (MAPD) and the root mean square deviation (RMSD) between the EF estimates from triangle models under three scenarios and the measurements with domain for DOY 174 and 182, respectively.....	250
Figure 7.8 Scatterplots of 16-day composite NDVI (MOD13A2 on DOY 177) and T_{rad} (MOD11_L2 on DOY 182) for four domains with relevant observed and theoretically derived limiting edge.....	255
Figure 7.9 MODIS-based EF estimates and corresponding EF measurements for four domains on DOY 182, red circles represent EF estimates from the theoretical warm edge and the cold edge of average air temperature of domain 1 (T_m), and black symbols represent EF estimates from the observed warm edge and the cold edge formed by T_m	258

Page

Figure 7.10 Variations in MAPD and RMSD between the MODIS-based EF estimates and the corresponding measurements with domain on DOY 182	259
Figure 7.11 MODIS-based scatterplot of NDVI- T_{rad} for domain 1 with observed and theoretically derived limiting edges on DOY 182	261
Figure 7.12 MODIS-based T_{rad} distribution (blue bars with a bin size of 0.5 °C) for domain 1 and remotely sensed T_{rad} values at flux towers (red bars) on DOY 182	263

LIST OF TABLES

	Page
Table 2.1 Day of year (DOY), Terra-MODIS overpass time and relevant weather conditions for six clear sky days in the year 2007	23
Table 2.2 Distributions of sunrise and sunset angles (rad) for two days in the summer half-year and two days in the winter half-year over the Baiyangdian watershed in the year 2007	40
Table 2.3 Statistics about DANSR (W m^{-2}) over Baiyangdian watershed for six clear sky days in the year 2007	49
Table 2.4 Bias, RMSE, and coefficient of determination (R^2) for DANLR from using one observation of MOD11_L2 LST acquired around 10:30 a.m. and using four observations of MOD11A1 and MYD11A1 LST acquired on 10:30 a.m. and 10:30 p.m., and 1:30 a.m. and 1:30 p.m., respectively, relative to the Penman equation using meteorological data across 18 weather stations for six clear sky days in the year 2007	53
Table 2.5 Estimated DANR (W m^{-2}) over the Baiyangdian watershed for six clear sky days in the year 2007	57
Table 3.1 MODIS data products used in this study and their associated properties .	79
Table 3.2 Regression coefficients of the exponential relationship between D and G and associated statistics (n is the number of samples, RSS is the residual sum of squares and R^2 is the coefficient of determination) ...	85
Table 3.3 Statistics of the estimates of ET from GG 1989 and the modified GG model versus SEBAL-based ET predictions	99
Table 4.1 Parameters of Landsat imageries covering the SMACEX site for three study days in 2002	131
Table 4.2 Statistics on discrepancies between the simulated energy balance components from TTME, and the eddy covariance energy and heat fluxes in the SMACEX site for three test dates. The observed fluxes are corrected by the Bowen ratio (BR) technique	137

Table 4.3 Relative sensitivity S_i (%) of LE estimates from TTME to each input variable at the SMACEX site on three study days, variations of T_a and T_{rad} are in K and variations of the other variables are in percentage (%).	144
Table 4.4 Statistics on discrepancies between flux estimates from SEBAL, SEBS, and TSEB, against eddy covariance-based measurements for the SMACEX site in the literature. Closure techniques involve residual (RE) and Bowen ratio (BR) methods. Hyphen (-) denotes null value. The unit of bias and RMSD is $W\ m^{-2}$ and MAPD is percentage (%).	148
Table 5.1 Sensitivity of SEBAL to all local and global variables for 28 sets of reference values for the Baiyangdian watershed in 2007. Variations of the variables and H estimates are in percentage and variations of land surface temperatures are in K. Min, Max, and Mean represent the minimum, maximum, and mean variations in H estimates, respectively.	169
Table 5.2 Characteristic variables of extreme pixels for watersheds I, II, and III on May 6, 14, 25, and 29, 2007 for investigating the domain dependence of SEBAL.	183
Table 6.1 Statistics on discrepancies between simulated energy balance components from M-SEBAL, and the eddy covariance energy and heat fluxes at the SMACEX site for three test dates in 2002. The observed fluxes are corrected by the Bowen ratio (BR) technique.	209
Table 6.2 Extreme pixels with their characteristic variables as inputs of SEBAL at the SMACEX site for DOY 174 and 182 in 2002, cases 1-9 represent all combinations of three hot pixels (numbering 1-3) and three cold pixels (numbering 4-6) selected from the satellite imagery.	215
Table 6.3 Statistics of discrepancies between the H and LE retrievals from SEBAL and tower-based measurements at the SMACEX site for DOY 174 and 182 in 2002 under 9 cases (1-9) representing different combinations of extreme hot pixels (numbering 1-3) and cold pixels (numbering 4-6) selected from Landsat TM imagery.	216
Table 7.1 Regression coefficients of observed limiting edges derived from Landsat TM/ETM ⁺ imageries for four domains around the SMACEX site on two study days in 2002.	246

	Page
Table 7.2 Differences between the Landsat TM/ETM ⁺ -based EF estimates and the measurements, e.g., Root Mean Square Difference (RMSD), Mean Absolute Percentage Difference (MAPD), and Bias within four study domains at the SMACEX site on DOY 174 and 182 under three scenarios of limiting edges.....	250
Table 7.3 Regression coefficients of observed limiting edges derived from Landsat ETM ⁺ imageries and MODIS-based T_{rad} and NDVI products for four domains around the SMACEX site on two study days in 2002.....	256
Table 7.4 Differences between the MODIS-based EF estimates and the measurements, e.g., RMSD, MAPD, and bias within four study domains at the SMACEX site on 182 under three scenarios of limiting edges	260

CHAPTER I

INTRODUCTION

1.1. Background

Evapotranspiration (ET) comprises evaporation from the soil surface and transpiration from vegetation. As the largest outgoing component in the water balance equation, i.e., 60-65% of the precipitation at the global scale (Brutsaert, 2005), ET is a key variable for understanding the hydrologic cycle, the energy balance on the Earth's surface, as well as the carbon flow to and from the terrestrial biosphere. Much research and many applications associated with hydrology, water resources, agriculture, meteorology, and forestry require detailed information of ET across a range of spatial and temporal scales, e.g., water resources allocation and management, crop yield forecasting, weather prediction, and vulnerability of forests to fire (Anderson et al., 2007a; Bastiaanssen et al., 2005; McCabe and Wood, 2006). A multitude of studies have shown that ET involves complex interactions between water and energy fluxes, and is primarily controlled by water and energy availability, surface resistance, and the ambient environment. These factors vary with terrain, land cover, and other surface characteristics (Baldocchi et al., 2001; Betts et al., 1997; Penman, 1948; Priestley and Taylor, 1972; Vorosmarty et al., 1998).

Traditionally, ET has been measured by lysimeter, Energy Balance Bowen Ratio (EBBR) systems, and eddy correlation techniques. Yet, such techniques are generally

This dissertation follows the style of Journal of Hydrology.

subject to point, field, or landscape scales (Baldocchi et al., 2001; Brotzge and Crawford, 2003; Gentine et al., 2007; Yunusa et al., 2004). For a river basin system with a few human activities, ET at annual or interannual scales can be approximately estimated by water budget calculations as the residual term of precipitation and streamflow observed at a handful of hydrometeorological stations. However, it seems far from satisfactory to understand ET at finer timescales and spatial scales.

On the other hand, a considerable amount of modeling effort has been made to address simulation of actual ET at field scales, in which the Penman-Monteith equation (Monteith, 1965; Penman, 1948) and its variant, FAO56 equation (Allen, 2000), have been widely used to estimate potential/reference ET. Along with crop coefficients obtained from field experiments, the actual ET can be estimated by reducing the reference ET proportionally in terms of crop coefficients. It is noted that the Penman-Monteith type equation tends to provide the potential/reference ET under wet environments and requires a large amount of micrometeorological data (e.g., air temperature, vapor pressure deficit, photosynthetic active radiation, and CO₂ concentration) and physiologic parameters (e.g., vegetation height and leaf area index) to characterize stomatal and soil surface resistances.

These measured and simulated ET values, however, cannot be directly extrapolated to a larger scale (e.g., watershed/regional and continental scales). Also, expensive facilities of these observations and measurements make it infeasible to detect ET over large areas, especially over mountainous areas and underdeveloped regions. In hydrological modeling, parameterization of ET in many physically based distributed

hydrologic models seems inadequate to capture the spatial patterns and magnitude of ET within a river basin system (Vorosmarty et al., 1998). The ET term is often taken as a dustbin to imbue uncertainties arising from the deficiencies in the model physics and inputs. The conventional measurement techniques and simulation approaches have been far from satisfactory to result in an enhanced understanding of ET over large heterogeneous areas with varying land cover types and surface characteristics.

The advent of satellite remote sensing represents a major technological breakthrough in improving our understanding of global dynamics and processes on the land surface, in the oceans, and in the lower atmospheres. It may be the only viable approach to handle the spatial variability of drainage basin properties and hydrologic processes (Engman, 1996). In particular, satellite remote sensing has provided the Earth science communities with an unprecedented opportunity to retrieve critical land and atmospheric variables at a range of coverage (e.g., swath width of 2,330 km for the Moderate-resolution Imaging Spectroradiometer (MODIS) sensor onboard Terra and Aqua satellites), spatial scales (e.g., $10^2 \sim 10^3$ m space scales) and temporal scales (e.g., real time, daily, and biweekly) from recorded reflected and/or emitted electromagnetic radiation (radiance) by sensors (e.g., multispectral scanners, cameras, and detectors) onboard satellite platforms.

Numerous remote sensing-based models built on the surface energy balance equation have been developed to reproduce surface fluxes across a variety of spatial scales. These models incorporate remotely sensed land surface temperature (LST)/radiative temperature (T_{rad}) which is able to capture turbulent fluxes at the

interface between the land surface and the atmosphere, surface albedo which depicts the reflectance characteristic of the land surface, and/or Vegetation Index (VI)/fractional vegetation cover (f_c) which reflects vegetation information of the surface (Bastiaanssen et al., 1998a; Jiang and Islam, 2001; Kustas and Norman, 1996; Nishida et al., 2003; Norman et al., 1995; Su, 2002). Estimates of ET from these models can be gainfully employed in determining water consumption by agricultural crops, water resources management (e.g., assist policy-makers in addressing the issue of consumptive water use, including beneficial and non-beneficial depletions), hydrologic modeling (e.g., forecasting river stage and flood potential and constraining recharge in groundwater simulations), forest management (e.g., monitoring forest health and vulnerability to fire), and numerical weather predictions and general circulation models by prescribing important boundary conditions (Anderson et al., 2007a; Bastiaanssen et al., 2005; Norman et al., 2003).

The beauty of new technology is, however, not always impeccable. The introduction of satellite remote sensing in ET modeling is beset with a series of significant issues associated with the reliability of ET retrievals, limitations in their temporal resolution, as well as scale issues involved in both model physics and satellite imagery:

(1) Parameterization of daily net radiation (DNR). DNR, the primary driving force of turbulent water and heat fluxes at the interface between the land surface and the lower atmosphere, has not been well parameterized under rugged terrain conditions. In most satellite-based ET models, DNR is a critical variable linking remotely sensed latent heat

flux (LE) to 24h-integrated ET. The daily net shortwave radiation (DNSR), a key component of DNR, is often parameterized by assuming extensively flat land surfaces across a study site. This may not hold true under rugged terrain conditions. In addition, another key component in DNR, the daily net longwave radiation (DNLR), is calculated by the FAO56 equation and a large amount of meteorological forcing or is reliant on field measurements. Inadequacies in parameterization of DNSR and DNLR would lead to uncertainties in the resulting ET estimates.

(2) Temporal extension. The merits of satellite remote sensing, especially the thermal band information in investigating the large-scale water cycle and surface fluxes which are highly variable over space and time are significantly shadowed due to cloud cover and infrequent image availability for high spatial resolution imagery (e.g., biweekly for Landsat TM/ETM⁺) as governed by the satellite overpass schedule. This constrains most of the satellite-driven ET modeling schemes to work under cloud-free days. The snapshot of LE on a few cloud-free days seems inadequate to provide continuous monitoring of water consumption by agricultural crops and evolution of droughts.

(3) Spatial scale and scaling issues. Numerous satellite-based algorithms have been developed to estimate ET over large heterogeneous areas. Such algorithms, e.g., Surface Energy Balance Algorithm for Land (SEBAL) (Bastiaanssen et al., 1998a; Bastiaanssen et al., 1998b) and triangle/trapezoid models (Jiang and Islam, 2001), are typically developed and tested at the resolution scale of a certain sensor based on the assumption of homogeneity within the pixel resolution. However, there is a tendency in

the scientific community to directly apply ET algorithms developed at fine-resolution data (e.g., Landsat TM/ETM⁺) to coarse MODIS data (Gebremichael et al., 2010). It is therefore important to quantitatively assess the transferability of existing ET algorithms across spatial scales. Furthermore, the performance of these algorithms may depend on the size of the modeling domain. This means that some critical boundary conditions/variables intrinsic in these models would vary with the domain size. The resolution dependence and domain dependence are considered a significant obstacle at the accurate derivation of ET by satellite approaches and to build an understanding of sub-pixel variation in ET for relatively coarse satellite images.

(4) Subjectivity involved in selecting extreme pixels in SEBAL. SEBAL has been used worldwide to estimate ET and facilitate water resources management over the past 15 years (Bastiaanssen et al., 2010; Bastiaanssen et al., 2005). Two extremes, termed hot pixel and cold pixel, are required to determine the boundary conditions of LE to deduce surface fluxes and ET for the remaining pixels across a scene. However, the two extremes are selected from satellite imagery by the operator; different operators may select different extremes and therefore derive ET estimates of varying magnitudes and distributions. To that end, the ET estimates from SEBAL are often misinterpreted and large uncertainties may be involved.

(5) Applicability of two-source models. Most satellite-based models pertain to the one-source scheme, which means that evaporation from the soil surface cannot be discriminated from vegetation transpiration. However, water consumption by crops and transpired by vegetation are more meaningful in many applications than soil surface

evaporation, e.g., as a metric for root zone moisture conditions in water balance models (Crow et al., 2008). The existing two-source models, e.g., Two-source Energy Balance (TSEB) (Norman et al., 1995) require parameterization of networks of surface and vegetation canopy resistances. The data requirement cannot be always satisfied. A new operational two-source model is therefore needed to allow separate evaluation of soil surface evaporation and vegetation transpiration in a simpler manner.

1.2. Objectives

The overall goal of the dissertation research is aimed at advancing the spatial representation and accuracy of ET retrievals at a range of spatial and temporal scales from satellite remote sensing and modeling. To achieve this, multiple objectives encircling the five issues expounded above are to:

- (1) Improve the spatial representation and reliability of DNR from satellite remote sensing under rugged terrains;
- (2) Improve the temporal resolution of satellite-based ET estimation models so as to generate ET time series on a daily basis;
- (3) Investigate the scale effects resulting from varying spatial resolutions of satellite sensors and modeling domain sizes in SEBAL;
- (4) Develop a new algorithm to determine the boundary conditions of SEBAL so as to reduce subjectivity and scale effects involved;
- (5) Investigate the resolution and domain dependencies of triangle models, and develop an algorithm to reduce these scale dependencies; and

- (6) Develop a new two-source model for ET, which is capable of generating reliable vegetation transpiration and soil surface evaporation by fewer inputs without computing the resistance networks.

1.3. Methodology

The problems that each objective aims to address will be first examined. A range of physically based models in combination with satellite imageries of high spatial resolution (i.e., Landsat ET/ETM⁺) and moderate spatial resolution (i.e., MODIS) will be developed or adopted to resolve these problems. Specifically, these approaches include:

(1) A mathematical model depicting the geometric relationship between the incident solar radiation and the sloping land surface will be adopted to simulate instantaneous incoming shortwave radiation. Specifically, sunrise and sunset angels for a generic surface (including the sloping surface and the flat surface) will be analytically derived so as to calculate DNSR. In addition, four observations of LST from Terra- and Aqua-MODIS will be tentatively used to simulate DNLR.

(2) Remote sensing-based ET models have been shown to be capable of producing reasonable ET distribution over large heterogeneous areas (Anderson et al., 2007a; Anderson et al., 2007b; Bastiaanssen et al., 2002; Batra et al., 2006; Gao and Long, 2008; Jiang and Islam, 2001; Krajewski et al., 2006; Kustas et al., 2007; Nishida et al., 2003; Zhang, 2009). The large-scale feedback model developed by Granger and Gray (1989) can essentially generate ET times series with routine weather data (Allen et al., 2007; Armstrong et al., 2008; Crago and Crowley, 2005; Liu et al., 2006; Xu and Singh, 2005).

There is a functional relationship between the relative drying power of air and the relative evaporation involved in the feedback model. Integration of remotely sensed ET retrievals on cloud-free days into the reconstruction of the functional relationship would allow producing an ET time series of high spatial resolution at watershed/regional scales.

(3) The domain dependence of SEBAL will be investigated by first performing sensitivity analysis of sensible heat flux (H) estimation to model inputs, in particular the model sensitivity to two extreme temperatures. Then, the model will be applied to varying domain sizes and satellite platforms. The H retrievals from SEBAL will subsequently be evaluated.

(4) Two theoretical boundary conditions of evaporative fraction (EF)/LE within a study site given certain time, meteorological conditions, and surface characteristics will be derived by examining the radiation budget and energy balance states for critical extreme surfaces in the f_c - T_{rad} space. The SEBAL-based ET estimates will be constrained by the derived theoretical boundary conditions rather than the selected extreme pixels directly from satellite imagery.

(5) The domain and resolution dependencies of triangle models will be investigated by applying to varying domain sizes and to varying satellite platforms. In particular, variations in the observed warm (upper) and cold (lower) edges with the domain size and satellite platform involved in the triangle models will be investigated. The theoretical boundary conditions of EF for the triangle models will be derived to reduce uncertainties in the derivation of the observed boundary conditions.

(6) By interpreting the contextual f_c - T_{rad} space and introducing the concept of soil

surface moisture availability isopleths superimposed in the space, T_{rad} will be decomposed into temperature components (T_c for vegetation and T_s for soil). Vegetation transpiration and soil surface evaporation will be separately simulated by the newly developed Two-source Trapezoid Model for ET (TTME) algorithm.

1.4. Significance of research

The significance of the dissertation research is twofold. First, a new ET time series modeling system will be synergistically developed. The modeling system consists of an improved daily net radiation algorithm, an integration technique to reproduce ET for cloudy days, and a new two-source trapezoid model for ET (Fig. 1). Second, the scale effects of SEBAL and triangle models will be elaborated to provide insights into correct interpretation of the model outputs. Model performance and mechanisms of error propagation will be unraveled. A framework to constrain errors due to the scale effects will be proposed. It is expected that the modeling system would be capable of generating reliable ET time series of high spatial resolution across large areas, which would greatly benefit a range of applications, like agricultural water use, water resources planning, watershed integrative management, forest management, and drought forecasting. In addition, the research would be helpful for correctly interpreting the model outputs from SEBAL and triangle models. A new framework could be incorporated into SEBAL and triangle models so as to produce scale-independent outputs. An elevated understating of turbulent energy fluxes on the Earth surface and the effect of land surface heterogeneity on the hydrologic cycle would be gained.

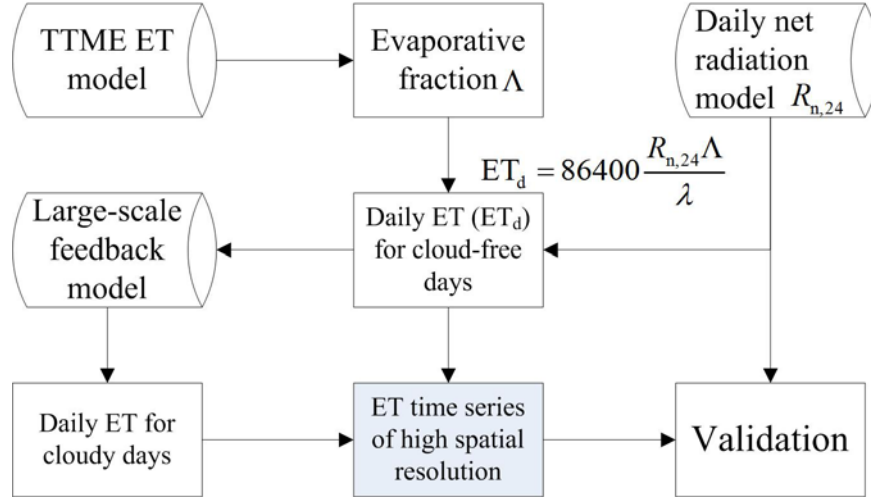


Figure 1.1 A framework of ET time series modeling system.

1.5. Organization of dissertation

Chapter II presents a new algorithm to simulate DNR over large heterogeneous areas from MODIS data products and Digital Elevation Models (DEMs). In Chapter III, an approach of integrating the SEBAL algorithm with the GG model will be developed to produce an ET time series of high spatial resolution at watershed/regional scales. Chapter IV focuses on developing a new two-source model based on the trapezoid framework of remotely sensed f_c - T_{rad} space. A systematic investigation into the model sensitivity and domain and resolution dependencies of the SEBAL algorithm is presented in Chapter V. Aiming at addressing the scale dependencies and subjectivity involved in SEBAL, Chapter VI concentrates on the modification of the SEBAL algorithm by deriving theoretical boundary conditions without directly selecting extreme pixels in an image. Chapter VII presents an investigation into the scale effects of triangle models and a framework to restrain uncertainties arising therefrom. The major conclusions, limitations in research, and recommendations for future work are given in

Chapter VIII.

This research is primarily motivated by improving the estimation of ET across a variety of spatial and temporal scales in the context of increasing access to satellite imageries, advancements in thermal infrared remote sensing, and relevant algorithms to modeling surface fluxes. The accuracy and reliability of ET retrievals and the applicability and operability of models are the core issues of modeling efforts. Our research would result in an improved estimation of ET time series and a framework to restrain uncertainties arising from scale effects and deficiencies in model physics, and even inspire new approaches to simulating surface fluxes and ET based on satellite techniques.

CHAPTER II

ESTIMATION OF DAILY AVERAGE NET RADIATION FROM MODIS DATA AND DEM

2.1. Introduction

Compared with instantaneous net radiation, 24-h integrated net radiation or daily average net radiation (DANR) consisting of daily average net shortwave radiation (DANSR) and daily average net longwave radiation (DANLR) has more applications for atmospheric and hydrologic modeling and water resources management, and especially for quantifying land surface evapotranspiration (ET) from satellite imagery (Allen et al., 2006; Bastiaanssen, 2000; Bisht et al., 2005; Fortin et al., 2008; Gao and Long, 2008; Gao et al., 2008; Samani et al., 2007). DANR is a critical variable linking estimates of instantaneous latent heat flux (typically at satellite overpass time) from energy balance-based models (Bastiaanssen et al., 1998a; Su, 2002) and daily estimates of ET (in units of mm d^{-1}) on the basis of an assumption that retrieved evaporative fraction (defined as the ratio between latent heat flux to available energy) remains fairly constant during cloudless days for which advection occurs occasionally (Brutsaert and Sugita, 1992; Crago, 1996; Kustas et al., 1994a; Shuttleworth et al., 1989). Daily ET can be subsequently obtained using the evaporative fraction to partition DANR (Ahmad et al., 2006; Bastiaanssen et al., 1998a; Jiang and Islam, 2001; Norman et al., 2003; Su, 2002). The evaporative fraction can significantly affect the spatial representation of estimates of ET across large heterogeneous areas, reflecting the combined effects of soil moisture, availability of radiative energy, vegetation type and its state, and meteorological

conditions on the latent heat flux (Batra et al., 2006; Nishida et al., 2003). DANR, to a large extent, determines the magnitude of estimates of ET for a given evaporative fraction from a pixel standpoint. It is thus believed that a considerable effort should be made to substantially improve the accuracy of both evaporative fraction and DANR, with the objective to make reliable predictions of ET. On the other hand, although comparisons of satellite-based latent heat flux with point-scale ground observations or more regionally with aircraft for several retrievals have been performed, it seems that to date there have not been universally acceptable approaches to effectively assessing the accuracy of the extrapolated daily ET from evaporative fraction. Discretization of ground-based measurements, the number of measurements, the difference between satellite-based pixel scales (e.g., 1000 m) and measurement scales (e.g., 100 m), and errors associated with such measurements should be taken into account (Bisht et al., 2005; Kempf and Tyler, 2006; McCabe and Wood, 2006). It appears that although evaluation of the accuracy of spatially distributed estimates of ET from remote sensing-based energy balance models cannot be readily performed, improvements in the daily estimates of ET could be potentially achieved by increasing the number and/or frequency of ground-based observations of each component of DANR or significantly enhancing the capability of the parameterization scheme of DANR to represent reality.

In some cases, DANR can be obtained directly from field measurements or weather stations (Bastiaanssen, 2000; Jegede, 1997; Kempf and Tyler, 2006; McCabe and Wood, 2006). Nevertheless, limited field measurements and weather stations that can provide ground-based measurements of DANR or the components of DANR (e.g., DANSR and

DANLR) often inhibit practical applications of remote sensing-based surface flux models to large heterogeneous areas (Irmak et al., 2003; Samani et al., 2007; Su et al., 2005), especially mountainous areas having exceedingly sparse measurements or stations. Furthermore, weather stations are generally located in flat areas so that the observations of DANR tend to represent limited surrounding areas, which may exclude sloping land surfaces or mountainous areas (Allen et al., 2006; Thornton et al., 2000). Then maps of DANR and associated components are derived through some type of parameterization scheme incorporating meteorological and/or remotely sensed data for practical ET estimation over large domains (Allen et al., 1998; Bisht et al., 2005; Bois et al., 2008; Choudhury, 1997; Fortin et al., 2008; Hurtado and Sobrino, 2001; Jacobs et al., 2000; Kim and Hogue, 2008; Lagouarde and Brunet, 1993; Mahmood and Hubbard, 2002; Samani et al., 2007; Thornton and Running, 1999).

Allen et al. (1998) proposed a framework, known as the FAO56 method which has been widely used to estimate DANR from routinely observed meteorological data, for calculating reference ET and quantifying crop water requirement. The parameterization scheme of DANSR seems to be applicable to flat areas because of the exclusion of the effects of terrain factors (e.g., slope and azimuth) on solar radiation. Regarding the parameterization scheme of DANLR, it should be noted that the FAO56 equation involving the terms for correcting the Stefan-Boltzmann Law using air humidity and cloudiness is a site-specific method, not applicable to large heterogeneous areas. Therefore, to calculate DANR the FAO56 method should be used with caution for satellite-based ET estimation across large heterogeneous areas.

Jacobs et al. (2000) utilized Geostationary Operational Environmental Satellite (GOES) data to detect cloud cover throughout a day and subsequently derived instantaneous direct solar radiation and net radiation on a 15-min basis and DANR for ET estimation over wetlands in the Paynes Prairie Preserve, North Central Florida. However, the relatively low spatial resolution of GOES data would not be adequate to estimate DANR and ET over mountainous areas. Bisht et al. (2005) developed a sinusoidal model similar to Lagouarde and Brunet's (1993) methodology to estimate DANR based on estimates of instantaneous net radiation from MODIS data products. One of the strengths of this model is direct simulation of DANR from retrieved instantaneous net radiation for clear sky days, without the requirement of parameterization schemes for each component of DANR.

In addition, the model accounts for the effects of differences in sunrise and sunset angles on DANR, with specification of varied values of sunrise and sunset angles for a different Day of Year (DOY) but same values for the entire study region for the same DOY due to the domination of flat areas over the Southern Great Plains, United States. It is, however, noted that the model would not be suitable for implementation in mountainous areas because of the existence of a wide range of sunrise and sunset angles for sloping land surfaces. Moreover, integrating all components of DANR into a simple sinusoidal model would introduce certain errors to estimates of DANR resulting from the difference in the temporal phase of shortwave radiation and longwave radiation throughout a day, showing that the longwave radiation is not negligible but the shortwave radiation is non-existent during nighttime.

This study focuses on two issues associated with DANR estimation. First, in application of DANR and ET estimation across large heterogeneous domains for clear sky days, the effect of terrain factors on solar radiation should be quantified instead of simplifying terrain through an assumption of uniform extensive slopes and azimuths. For instance, some specific sloping land surfaces with steep slopes facing north in middle or high latitude areas may receive solar radiation only during a very short period or even may not receive at all. Some sloping land surfaces, by contrast, may be illuminated by direct solar radiation twice a day, meaning that there exist two sets of sunrise and sunset angles. These extreme examples are rare but may be important in some applications to mountainous areas (Allen et al., 2006; Gao et al., 2008). Second, DANLR also serves as a critical component in DANR. In many applications, DANLR has been obtained using one observation of land surface temperature (LST) from satellite imagery acquired at near midday as a surrogate of daily average LST in combination with meteorological data to calculate daily upwelling and downwelling longwave radiation (Hurtado and Sobrino, 2001; Kustas et al., 1994b; Lagouarde and Brunet, 1993; Roerink et al., 1997). In addition, DANLR can also be estimated by making use of the FAO56 method and incorporating a wealth of meteorological data. However, for satellite observation-based ET estimation, the utility of existing methods to parameterize DANLR needs to be further examined in that the difference in the representativeness of daily average LST induced by the difference in the overpass time of varying satellite platforms may result in disparate DANLR retrievals. Furthermore, an associated problem has to be investigated if one observation of LST can appropriately represent daily average LST for

calculating upwelling longwave radiation.

Two MODIS (Moderate-resolution Imaging Spectroradiometer) sensors, onboard the Earth Observing System EOS-AM (Terra) and EOS-PM (Aqua), have remarkable advantages over other sensors for providing much more spatially distributed land and atmospheric data products, such as surface albedo, surface emissivity, and atmospheric profile temperatures at relatively higher spatial and temporal scales, in particular the critical variable LST at most four observations per day. This opens a new opportunity to more reliably parameterize DANR across large heterogeneous areas and to eliminate the need for a large amount of ground-based measurements to estimate DANSR, DANLR, and DANR, and related site-specific calibration for operational ET estimation.

The objectives of this chapter are to (1) analyze physical mechanisms for how each component of DANR varies with time during a day, and then improve the parameterization scheme of DANSR by quantifying the effects of terrain factors on solar radiation for sloping land surfaces; (2) improve DANLR estimation using four observations of LST from MODIS data products, DEM, and minimum meteorological data; and (3) examine the relationship between DANR and terrain factors.

2.2. Study site and data description

2.2.1. Study site

Located in North China, the study site is the Baiyangdian watershed, extending in latitude from around 37.8° to 40.4°N and in longitude from around 113.3° to 116.6°E (Fig. 2.1a). Hebei and Shanxi Provinces and Beijing City contribute to 80.4%, 12.3%

and 7.3% of its total area of 31,200 km², respectively. Elevations decrease from the northwest of the watershed, Taihang mountainous areas, to the southeast plain, ranging from around 2784 m to 0 m, showing that mountainous areas (elevation above 100 m) occupy approximately 53% of this watershed. Eight main streams of the Daqing River provide primary water sources for four irrigation districts, reservoirs, industrial and municipal use in this watershed, finally converging to Baiyangdian Lake, the largest lake on the North China Plain. In general, woodland and grassland dominate northwest mountainous areas, and cropland is distributed across plain areas, with statistics of a land use map (Fig. 2.1b) derived from Landsat TM images in the year 2000 showing that dry land, shrub and moderate grassland account for 33.6%, 12.1% and 12.0% of the watershed, the three largest land covers, respectively.

Mean annual temperature is between 6.8 °C and 12.7 °C (the daily maximum value is 43.3 °C and the daily minimum value is -30.6 °C), with a mean annual precipitation of 548 mm and a mean annual pan evaporation of 1500-2000 mm according to historical weather records of recent 50 years from Baoding, Shijiazhuang, Wutaishan, Weixian, and Huailai weather stations within or adjacent to the watershed. Over the recent two decades, drought frequency over Baiyangdian Lake has increased rapidly, in particular since year 2000, showing that the water level of this lake declines below the warning water level of 6.5 m during several months in a year and surface runoff into Baiyangdian Lake has reduced drastically. However, the precipitation of this watershed has not yet shown an evidently decreasing trend. Central and local administrations relevant to water resources management have thus conducted several inter-basin water transfer projects

from reservoirs and rivers within or adjacent to this watershed to address increasingly severe water shortage crises and to sustain drinking water requirement and ecological integrity over the Baiyangdian areas. Therefore, it is critical to explore the reasons for droughts over this area in the context of climate change and intensifying human activities through reliable estimation of ET and water budget. Reliably modeling DANR is the first step to determine ET amount and distribution over this watershed as indicated above.

2.2.2. Data description

Meteorological data on a daily basis relevant to the parameterization schemes of DANSR, DANLR and DANR, such as daily mean temperature, daily mean vapor pressure, were obtained by averaging *in-situ* measurements from 18 weather stations within the study watershed. Of the 18 weather stations, Baoding and Fuping stations can provide the observations of air temperature, vapor pressure and atmospheric pressure at a 1-h interval. The other stations can provide relevant observations at 6-h intervals. Daily

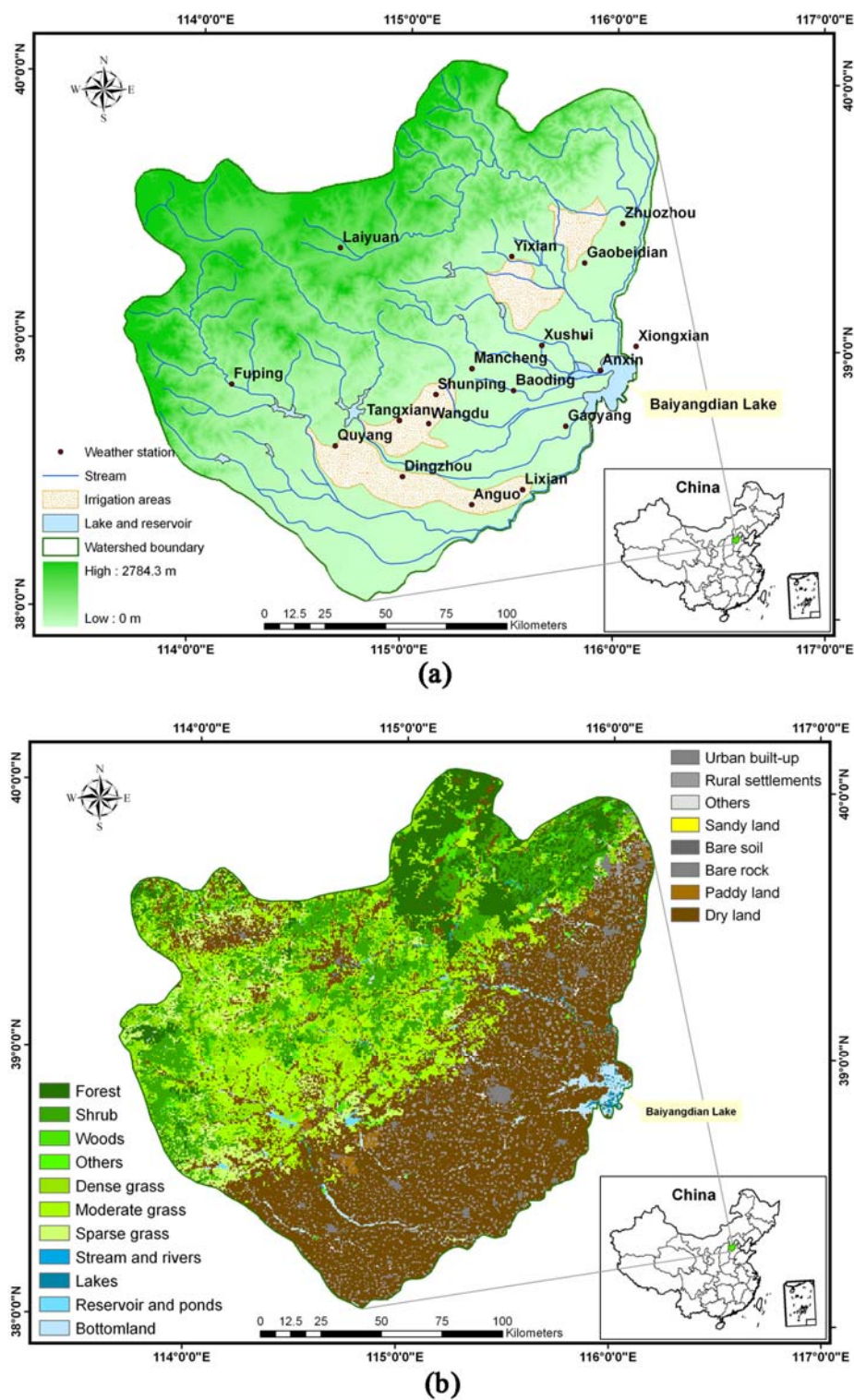


Figure 2.1 Location (a) and land use (b) of the Baiyangdian watershed in North China with relevant information.

actual sunshine duration is available by accumulating *in-situ* measurements at 1-h intervals during daytime. Terrain factors, like slope, azimuth and elevation, can be directly extracted from Shuttle Radar Topography Mission (SRTM) digital elevation models (resampled to 100 m).

MODIS data products, MOD11_L2 (the level 2 MODIS LST and emissivities for bands 31 and 32 daily data) are retrieved as 1 kilometer pixel by a generalized split-window LST algorithm (Wan and Dozier, 1996). MOD11A1 and MYD11A1 from Terra-MODIS and Aqua-MODIS (the level 3 MODIS LST and emissivities for bands 31 and 32 daily data), are generated in a sinusoidally projected tile by mapping the level 2 LST product on a 1 kilometer grid and are retrieved by the algorithm taking into account the dependence of retrieved LST on the viewing angle based on the physics-based day/night LST algorithm (Wan and Li, 1997). MOD11_L2, MOD11A1 and MYD11A1 were utilized to simulate daily surface upwelling longwave radiation and to examine the difference in retrievals between using one observation of LST from MOD11_L2 and using four observations of LST from MOD11A1 and MYD11A1.

MCD43A3, the 16-day composite level 3 gridded albedo products in the sinusoidal projection, provides both directional hemispherical reflectance (black-sky albedo in the extreme case of completely direct illumination) and bihemispherical reflectance (white-sky albedo in the extreme case of completely diffuse illumination) at a spatial resolution of 500 m. MOD04 provides daily level 2 aerosol depth at 0.550 μm wavelength product of spatial resolution of 10 km. MCD43A3 and MOD04 were jointly utilized to simulate land surface albedo in terms of the algorithm developed by Lucht et

al. (2000). Six clear sky days in the year 2007 were selected in terms of the MOD11_L2 LST product with less than 10% cloud cover relative to the entire scene. Table 2.1 contains DOY, Terra-MODIS overpass time and some variables with respect to weather conditions.

Table 2.1 Day of year (DOY), Terra-MODIS overpass time and relevant weather conditions for six clear sky days in the year 2007

Calendar day (DOY)	Terra daytime overpass time, UTC	Daily actual sunshine duration (h)	Daily potential duration (h)	Daily Cloudiness (%)
25th Apr(115)	03:15	11.9	13.4	1.1
9th May (129)	03:25 and 03:30	11.8	13.9	18.6
15th Jun (166)	03:45	10.7	14.7	20.9
19th July (200)	03:35	12.1	14.4	47.2
13rd Aug (225)	03:35 and 03:30	12.1	13.6	13.5
19th Sep (262)	03:45	10.3	12.1	8.9

2.3. Methodology

DANR can be expressed as follows:

$$R_{n,24} = (1-r)(S_{in,24} + S_{d,24}) + (L_{d,24} - L_{u,24}) \quad (2.1)$$

where $R_{n,24}$ is the DANR ($W m^{-2}$), r is the land surface albedo (dimensionless) which is assumed to be similar to the surface albedo during the morning overpass (Bastiaanssen, 2000), $S_{in,24}$ is the daily average direct solar radiation ($W m^{-2}$), $S_{d,24}$ is the daily average diffuse solar radiation ($W m^{-2}$), $(1-r)(S_{in,24} + S_{d,24})$ is also termed the daily average net shortwave radiation (DANSR), $L_{d,24}$ is the daily average downwelling longwave radiation ($W m^{-2}$), and $L_{u,24}$ is the daily average upwelling longwave radiation ($W m^{-2}$), $(L_{d,24} - L_{u,24})$ is also termed the daily average net longwave radiation (DANLR).

2.3.1. Parameterization scheme of DANSR

(1) From S_{in} to $S_{in,24}$ for sloping land surfaces

Instantaneous direct solar radiation S_{in} for a given sloping land surface at a given moment (typically satellite overpass) can be expressed as:

$$S_{in} = \frac{I_0}{d^2} \cos(i) \cdot \tau^m \quad (2.2)$$

$$m = \frac{P_a}{101.3 \cos(i)} \quad (2.3)$$

where I_0 is the solar constant (around 1367 W m^{-2}), d is the Earth-Sun distance in astronomical units, τ is the atmospheric transmissivity (dimensionless), m is the optical air mass number (dimensionless), P_a is the atmospheric pressure (kPa), which could be assumed to be a function of elevation in this watershed [$P_a = 101.3 \exp(-\text{elevation}/8200)$], i is the solar zenith angle (rad), and $\cos(i)$ is the cosine of solar zenith angle (dimensionless).

A sensitivity analysis of S_{in} to atmospheric attenuation variables has been performed in order to quantify the degree to which they influence the magnitude of S_{in} (Fig. 2.2). Results show that the atmospheric transmissivity and elevation are positively correlated with S_{in} , with a 10% increase in atmospheric transmissivity and elevation resulting in around 14.6% and 0.061% increase in the magnitude of S_{in} , respectively. On the contrary, a 10% increase in the solar zenith angle (SZA) will result in around 12.5% reduction in S_{in} . This is because of an increase in the distance of sunlight propagating in the atmosphere and thus an increase in atmospheric attenuation. It is concluded that the

atmospheric transmissivity is quite sensitive to the simulation of S_{in} . In many cases, instantaneous atmospheric transmissivity for clear sky days is determined merely by elevation (Melesse and Nangia, 2005; Wu et al., 2006). This approximation would lead certain errors to resulting S_{in} , especially for those days when cloud cover is significant. However, it should be pointed out that one of our purposes was to derive $S_{in,24}$ rather than S_{in} . We adopted another method to deal with daily average atmospheric transmissivity in the following text.

On the other hand, accurately simulating atmospheric transmissivity at satellite overpass virtually requires detailed information on atmospheric composition with its state from radiosounding data. It is, however, not readily available in most cases. Through measurement of atmospheric transmissivity for clear sky days, Liu and Jordan (1960) stated that τ is between 0.45 and 0.75. In addition, Gates (1980) stated that under typical clear sky days, τ is between 0.6 and 0.7. Under extreme clear sky condition, τ reaches around 0.75. Here, we take τ for 0.7 for clear sky days for which good quality MODIS data products were available.

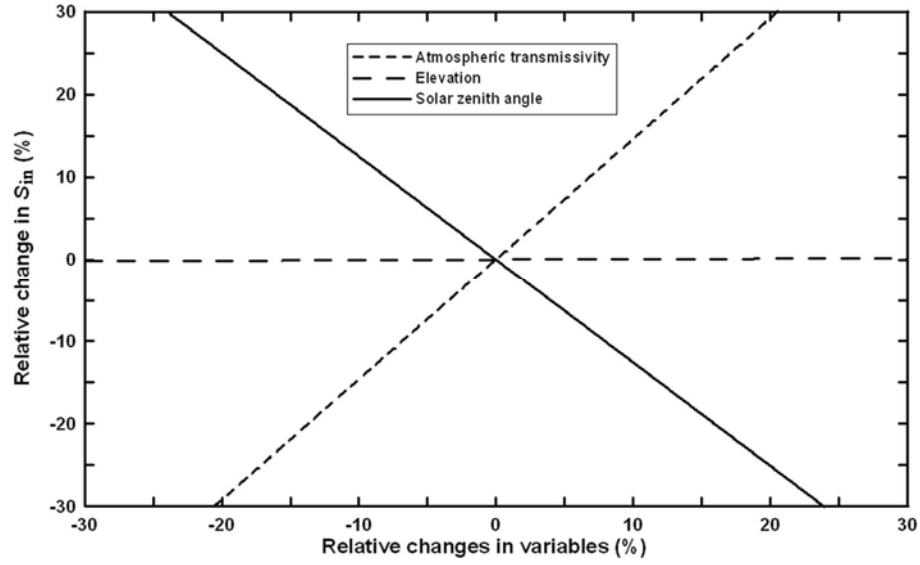


Figure 2.2 Sensitivity analysis of instantaneous direct solar radiation S_{in} to atmospheric attenuation variables.

It is worthwhile to note that for flat land surfaces, the solar zenith angle is simply a function of local standard time, latitude and solar declination; for sloping land surfaces, it additionally incorporates terrain effects, such as slope and azimuth (Fu, 1983; Morse et al., 2000):

$$\begin{aligned} \cos(i) = & \sin \delta (\sin \varphi \cos \alpha - \cos \varphi \sin \alpha \cos \beta) \\ & + \cos \delta \cos \omega (\cos \varphi \cos \alpha + \sin \varphi \sin \alpha \cos \beta) + \cos \delta \sin \alpha \sin \beta \sin \omega \end{aligned} \quad (2.4)$$

where δ is the solar declination, φ is the latitude (rad), α is the slope (rad), β is the azimuth (from due south, clockwise positive value, counterclockwise negative value, so the range of value is $[-\pi, \pi]$); ω is the solar angle ($=\pi(t-12)/12$, and t is the local standard time).

An expression of $S_{in,24}$ can be obtained through an integral of S_{in} from sunrise angle ω_1 to sunset angle ω_2 . The instantaneous atmospheric attenuation τ^m in S_{in} should be

replaced by the daily atmospheric transmissivity $(a+bn/N)$ and then the expression should be divided by the total length of one day 2π (in the unit of solar angle) for calculating the integral mean on the range of $[-\pi, \pi]$:

$$\begin{aligned}
 S_{\text{in},24} &= (a + b \frac{n}{N}) \frac{I_0}{2\pi d^2} \int_{\omega_1}^{\omega_2} (\sin \delta \cdot u + \cos \delta \cos \omega \cdot v + \cos \delta \sin \beta \sin \alpha \sin \omega) d\omega \\
 &= (a + b \frac{n}{N}) \frac{I_0}{2\pi d^2} [u \sin \delta (\omega_2 - \omega_1) + v \cos \delta (\sin \omega_2 - \sin \omega_1) \\
 &\quad - \sin \beta \sin \alpha \cos \delta (\cos \omega_2 - \cos \omega_1)]
 \end{aligned} \tag{2.5}$$

$$u = \sin \varphi \cos \alpha - \cos \varphi \sin \alpha \cos \beta \tag{2.6}$$

$$v = \cos \varphi \cos \alpha + \sin \varphi \sin \alpha \cos \beta \tag{2.7}$$

$$N = \frac{12(\omega_2 - \omega_1)}{\pi} \tag{2.8}$$

where n is the actual sunshine duration (h), which was obtained by interpolating 18 point-based observations of actual sunshine duration by an inverse distance square method, N is the potential sunshine duration (h), which can be expressed by the sunrise and sunset angles, ω_1 and ω_2 , a is a regression constant characterizing the fraction of extraterrestrial radiation reaching the Earth on overcast days ($n=0$), $a+b$ is the fraction of extraterrestrial radiation reaching the Earth on clear sky days ($n=N$).

Values of a and b may vary with geographical locations and climate zones. The FAO method (Allen et al., 1998) recommends that a be taken as 0.25 and b be taken as 0.50, if no actual solar radiation data are available and no calibration has been carried out for improved a and b estimates. Chen et al. (1995) made a regression analysis using observations of daily net radiation over the North China Plain and concluded that a and b could be specified as 0.17 and 0.54.

It is obvious that for theoretically solving Eq. (2.5), a parameterization scheme of sunrise and sunset angles, which incorporates the effects of terrain factors on the duration of sloping land surfaces being illuminated, the frequency of being illuminated during a day, and subsequently on the magnitude of the availability of direct solar radiation for sloping land surfaces, is virtually critical. The quantified ω_1 and ω_2 are thus input to Eq. (2.5) to compute $S_{in,24}$. Apparently the parameterization scheme of sunrise and sunset angles is only determined by the geometric relationship between the solar incidence and the sloping surface, being independent of Eq. (2.5).

(2) ω_1 and ω_2 for sloping land surfaces

The reasons why the critical solar angles (ω_1 and ω_2) should be quantified and the relationship between critical solar angles for sloping land surfaces and for flat land surfaces should be explored are as follows: As we know, critical solar angles for flat land surfaces are symmetrical (Gao et al., 2008), exhibiting the same absolute values but with inverse signs. However, the critical solar angles for sloping land surfaces probably show different absolute values, moreover, even the same sign. For instance, for certain sloping land surfaces facing north and located in middle or high latitudes in winter, they may receive solar irradiance merely in the morning or in the afternoon. For some particular cases, they may be illuminated twice during daytime, namely having two sets of ω_1 and ω_2 . Consequently, if those sloping land surfaces were assumed to be flat surfaces in the calculation of critical solar angles for estimating direct solar radiation, it would lead to gross errors in the estimates of $S_{in,24}$ and eventually DANR and ET.

The ‘computed critical solar angles’ for sloping land surfaces can be directly obtained by allowing S_{in} in Eq. (2.4) to be zero, obtaining at most two real roots with opposite or identical signs (Gao et al., 2008). Only after comparing the ‘computed critical solar angles’ for sloping land surfaces with that for flat land surfaces in terms of a set of physical and mathematical principles can we determine the absolute values with their signs of the ‘actual critical solar angles’ for sloping land surfaces.

Let ω_{s1} and ω_{s2} be the roots Eq. (29) in Gao et al. (2008), respectively, and $\omega_{s2} > \omega_{s1}$. Both ω_{s1} and ω_{s2} are a function of not only the latitude and solar declination determining the macroscopic distribution of direct solar radiation from the perspective of the scene, but also the slope and azimuth causing the microscopic variation in direct solar radiation for a specific sloping land surface. Additionally, let the sunrise and sunset angles for flat land surfaces be $-\omega_H$ and ω_H (ω_H is absolutely positive) which are simply a function of latitude and solar declination. All mathematical expressions of ω_{s1} , ω_{s2} , $-\omega_H$, and ω_H can also be found in Fu (1983) and Gao et al. (2008). Here, a comprehensive mathematical analysis of the relationship between $(\omega_{s1}, \omega_{s2})$ and $(-\omega_H, \omega_H)$ has been made in order to specify ω_1 and ω_2 for a given sloping surface. The solutions of critical solar angles should inherently satisfy a set of physical and mathematical principles simultaneously as follows:

A. Only when $\cos(i) \geq 0$ can the sloping land surface be illuminated, otherwise it would produce nonphysical solutions, such as the presence of receiving direct solar radiation when specific terrain actually deflates sunlight.

B. The sunrise angle for sloping land surfaces, ω_1 , should not be earlier than that for

flat land surfaces at the same latitude. Similarly, the sunset angle for sloping land surfaces, ω_2 , should not be later than that for flat land surfaces.

On the basis of the two basic principles stated above, the sunrise and sunset angles can be specified by exploring the relationship among ω_{s1} , ω_{s2} , $-\omega_H$ and ω_H .

a. If $\omega_{s1} \leq \omega \leq \omega_{s2}$, $\cos(i) \geq 0$ can be satisfied; thus the sunrise and sunset angles can be specified in terms of the principle B, namely,

$$\omega_1 = \max(\omega_{s1}, -\omega_H); \omega_2 = \min(\omega_{s2}, \omega_H).$$

b. If $\omega < \omega_{s1}$ or $\omega > \omega_{s2}$, $\cos(i) \geq 0$ can be satisfied; thus the sunrise and sunset angles can be specified in terms of principle B. There are four kinds of possibilities in case b.

(a) If computed $|\omega_{s1}| < \omega_H$ and $|\omega_{s2}| < \omega_H$, the specific sloping land surface has two sets of sunrise and sunset angles, which means that it can be illuminated twice a day. Hence the critical solar angles are $\omega_1 = -\omega_H$, $\omega_2 = \omega_{s1}$ and $\omega_1 = \omega_{s2}$, $\omega_2 = \omega_H$, respectively.

(b) If computed $|\omega_{s1}| < \omega_H$ and $|\omega_{s2}| > \omega_H$, $|\omega_{s2}| > \omega_H$ contradicting principle B, accordingly there is only one set of critical solar angle for this case, namely, $\omega_1 = -\omega_H$, $\omega_2 = \omega_{s1}$.

(c) If computed $|\omega_{s1}| > \omega_H$ and $|\omega_{s2}| < \omega_H$, $|\omega_{s1}| > \omega_H$ contradicting principle B, accordingly there is also one set of critical solar angle for this case, namely, $\omega_1 = \omega_{s2}$, $\omega_2 = \omega_H$.

(d) If computed $|\omega_{s1}| < \omega_H$ and $|\omega_{s2}| > \omega_H$, both contradicting principle B, therefore the specific sloping land surface cannot receive direct solar radiation during the whole day.

The four possibilities discussed in case b are illustrated in a sketch in Fig. 2.3.

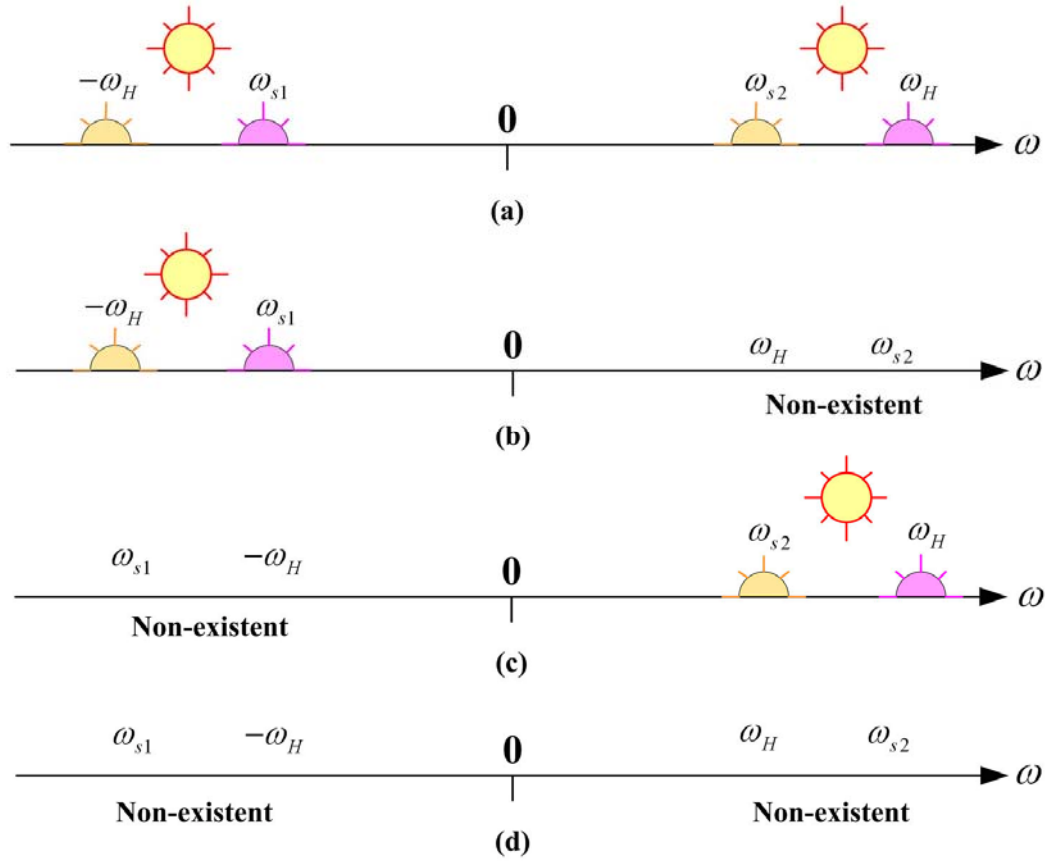


Figure 2.3 A sketch for illustrating determination of sunrise and sunset angles for sloping land surfaces in case b.

c. If real roots for ω_{s1} and ω_{s2} are non-existent, the sunrise and sunset angles can be specified directly in terms of principles A and B. Therefore, there are two possibilities in case c.

(a) If whatever value ω is within its domain of definition $[-\pi, \pi]$, $\cos(i) \geq 0$ can be satisfied, corresponding to the situation that terrain does not deflate the direct solar radiation for a specific sloping land surface during the whole day, thus $\omega_1 = -\omega_H$, $\omega_2 = \omega_H$.

(b) If whatever value ω is within its domain of definition $[-\pi, \pi]$, $\cos(i) \geq 0$ cannot be

satisfied, corresponding to the situation that terrain deflates the direct solar radiation during the whole day, thus the specific sloping land surface cannot receive direct solar radiation, namely $S_{in,24}$ is zero.

The seven kinds of possibilities involved in the three cases analyzed above entirely cover all the relationships between computed critical solar angles (ω_{s1} , ω_{s2}) for sloping land surfaces and intrinsic critical solar angles ($-\omega_H$, ω_H) for flat land surfaces at the same latitude. The sunrise and sunset angles, ω_1 and ω_2 , can be eventually determined for each grid of DEM of the study site. The $S_{in,24}$ value for sloping land surfaces can subsequently be retrieved by inputting the sunrise and sunset angles to Eq. (2.5). For flat land surfaces, it is evidently one particular case for Eq. (2.5) where $\alpha=0$.

(3) From S_d to $S_{d,24}$ for sloping land surfaces

When solar radiation propagates through the atmosphere, a major portion of it transmits through the atmosphere and ultimately interacts with the Earth's surface, namely the direct solar radiation, a small portion of it is absorbed or reflected back into space by the atmosphere, and the left portion of solar radiation is scattered by the atmosphere, finally also reaching the Earth's surface, namely the diffuse solar radiation. For accurately modeling the diffuse solar radiation, it would require specific information on atmospheric composition. Liu and Jordan (1960) have proposed an alternative and straightforward method to estimate instantaneous diffuse solar radiation S_d for clear sky days given by

$$S_d = 0.3(1 - \tau^m) \frac{I_0}{d^2} \cos(i) \quad (2.9)$$

It can be seen from Eq. (2.9) that S_d is 0.3 times the difference between S_{in} not being attenuated by the atmosphere and S_{in} being attenuated by the atmosphere, a relatively constant proportion. P_a involved in m and τ do not vary greatly for a particular location on a daily basis. Thereby, it seems that $S_{d,24}$ may rely on the solar zenith angle.

We examined the variation in S_d with the solar zenith angle within the range of $[0, \pi/2]$ in an attempt to determine some kind of approach to simulating $S_{d,24}$. The variations in S_{in} and S_d under the conditions of the atmospheric transmissivity of 0.7 and 0.6 and the elevations of 20 m and 1200 m have been modeled, respectively, based on Eq. (2.9) (Fig. 2.4). Results suggest that S_{in} varies dramatically with the solar zenith angle during a day, whereas S_d remains fairly constant during daytime except for short periods after sunrise and before sunset (solar zenith angle approaches 90°). Additionally, S_{in} at higher elevations is greater than that at lower elevations. On the contrary, S_d at higher elevations is smaller than that at lower elevations. As for the effect of atmospheric transmissivity on solar radiation, S_{in} increases with atmospheric transmissivity, while S_d decreases with an increase in atmospheric transmissivity.

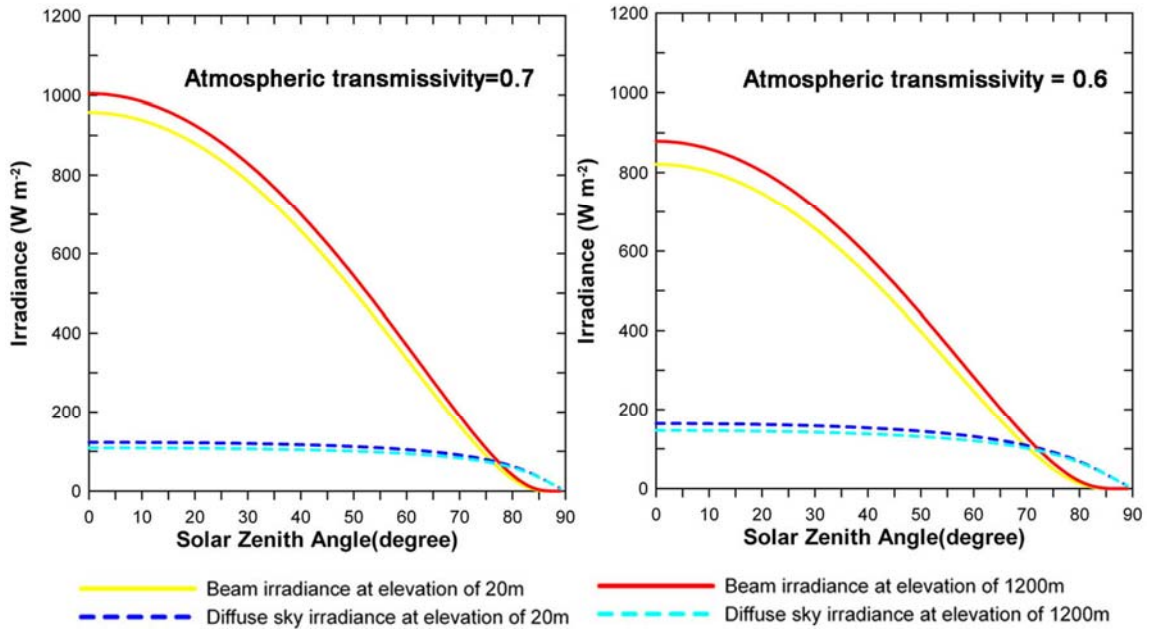


Figure 2. 4 Variations in direct and diffuse solar radiation (W m^{-2}) with solar zenith angle on the range of $[0, \pi/2]$ under different atmospheric transmissivity and elevation conditions.

It may be concluded that S_d remains fairly constant during daytime, which implies that $S_{d,24}$ may be estimated by multiplying the fraction of the daytime to the length of day (24 hours) to the magnitude of S_d .

$$S_{d,24} = \frac{S_d \times N}{24} \quad (2.10)$$

2.3.2. Parameterization scheme of DANLR

Numerous theories and practices have shown that although instantaneous net longwave radiation accounts for only a small portion of total instantaneous net radiation, daily average net longwave radiation DANLR is not negligible due to its domination in the nighttime. In general, DANLR contributes a negative quantity to DANR in that the Earth-Atmosphere system is able to balance the accumulated energy available from the

shortwave radiation in the daytime by constantly emitting longwave radiation during the whole day. Thereby, DANLR is also critical in the calculation of DANR.

DANLR is defined as the difference between the daily average downwelling longwave radiation $L_{d,24}$ from the atmosphere and the daily average upwelling longwave radiation $L_{u,24}$ from the Earth's surface as follows:

$$L_{24} = L_{d,24} - L_{u,24} = \varepsilon_a \sigma T_a^4 - \varepsilon \sigma T_s^4 \quad (2.11)$$

where ε_a is the daily average atmospheric emissivity (dimensionless) which was calculated by Brutsaert's (1975) formula shown in Eq. (2.12), σ is the Stefan-Boltzmann constant ($5.67 \times 10^{-8} \text{ W m}^{-2} \text{ K}^{-4}$), T_a is the daily average air temperature at screen level (K). Maps of daily average temperature can be made using multi-variate regression analysis based on the observations of air temperature from weather stations and their corresponding elevations, longitudes and latitudes. ε is the land surface emissivity which can be calculated using a nonlinear formula (Liang, 2004) shown in Eq. (2.13). T_s is the land surface temperature (K) which can be obtained from MOD11_L2, MOD11A1 and MYD11A1 data products.

$$\varepsilon_a = 1.24(e_a / T_a)^{1/7} \quad (2.12)$$

$$\varepsilon = 0.273 + 1.778\varepsilon_{31} - 1.807\varepsilon_{31}\varepsilon_{32} - 1.037\varepsilon_{32} + 1.774\varepsilon_{32}^2 \quad (2.13)$$

where e_a is the daily average vapor pressure at screen level (hPa), ε_{31} and ε_{32} are the emissivities in MODIS channels 31, 32, respectively, which can also be obtained from MOD11_L2 data product.

It should be pointed out that plenty of research and applications relative to the

estimation of DANLR have only taken advantage of one near midday observation of LST from some type of remotely sensed images. On the one hand, remotely sensed images with high spatial but low temporal resolution or fewer bands (e.g., Landsat TM and Advanced Spaceborne Thermal Emission and Reflection Radiometer, ASTER) are not capable of offering sufficient information on thermal infrared bands for retrieving LST. On the other hand, remotely sensed images with high temporal resolution (e.g., MODIS) have not yet been adequately exploited for estimating DANLR.

In many applications, estimation of $L_{u,24}$ is generally based on an assumption that if a satellite overpasses a study site at near midday, the instantaneous LST retrieved from some kind of remotely sensed data can be taken as the daily average LST for calculating $L_{u,24}$ (Hurtado and Sobrino, 2001; Kustas et al., 1994b; Lagouarde and Brunet, 1993; Roerink et al., 1997). However, the use of one observation of remotely sensed LST acquired at near midday perhaps needs to be further examined, given that the time of polar orbiting satellites overpass varies much with remote sensing systems, which would result in the difference in the magnitude of LST and thus the estimates of $L_{u,24}$.

Comparisons of estimates of DANLR from the use of one observation of Terra-MODIS LST and that from the weather data-based Penman equation (Penman, 1948) given as Eq. (2.14) were performed to investigate the usefulness of the one observation-based method:

$$L_{24} = -\sigma \left(\frac{T_{\max,d}^4 + T_{\min,d}^4}{2} \right) (0.56 - 0.25\sqrt{e_a}) \left(0.1 + 0.9 \frac{n}{N} \right) \quad (2.14)$$

where $T_{\max,d}$ and $T_{\min,d}$ are the daily maximum and minimum temperature (K),

respectively; and e_a is the daily average vapor pressure (kPa). Eq. (2.14) has been shown to be capable of reliably estimating DANLR across the study site (Yin et al., 2008). It should be noted that Eq. (2.14) is a site-specific empirical equation. It was developed and calibrated to estimate DANLR by circumventing the requirement of LST and land surface emissivity that had not been readily available for physically-based Eq. (2.11) through conventional methods, especially at watershed or regional scales.

The advent of remote sensing techniques provides an opportunity to capture spatially consistent and distributed variables (e.g., LST, and ϵ). In addition, it should be emphasized that one of our purposes is to develop a method to estimate DANLR directly based on Eq. (2.11) using remotely sensed data in conjunction with minimum of meteorological data. It is expected that the retrieved distributed DANLR has a higher spatial resolution in comparison with the predictions made from the Penman equation (Penman, 1948). The proposed method would eliminate the need for calibration required by the Penman equation when applied to other regions.

MODIS data has prominent advantages over other remotely sensed data that it can offer a wealth of thermal infrared information from both Terra and Aqua satellites. We may utilize at most four observations of remotely sensed LST for a given area to track the diurnal cycle of LST, greatly helpful in retrieving DANLR over large heterogeneous areas. The four observations of MODIS LST are acquired around 10:30 a.m. and 10:30 p.m. for Terra-MODIS, and 1:30 AM and 1:30 PM for Aqua-MODIS, respectively. Every two snapshots of each satellite are just in the processes of the rise and fall of LST during a day. This particularity is greatly beneficial in capturing the diurnal cycle of LST

and thus to estimating $L_{u,24}$.

Since meteorological variables (e.g., air temperature) and land surface fluxes (e.g., radiation) basically present similar periodic fluctuations with solar zenith angle for clear sky days, or just have certain lag phrase, LST which is greatly affected by the variation patterns of meteorological variables and land surface fluxes follows closely the diurnal variation in the air temperature as well. We first fitted a cubic polynomial function using four observations of Terra-MODIS and Aqua-MODIS temperatures, and then calculated the average value of this fitting function on $[0, 24]$. The fitting of a cubic polynomial function can be expressed as

$$T_s = \frac{\int_0^{24} (a_1 t^3 + a_2 t^2 + a_3 t + a_4) dt}{24} = 3456a_1 + 192a_2 + 12a_3 + a_4 \quad (2.15)$$

where a_i ($i=1, \dots, 4$) are regression coefficients which can be obtained by fitting a polynomial function using the four observations of MODIS LST. Ultimately, it seems logical that the average value could serve as the daily average LST in Eq. (2.11) to calculate DANLR.

2.4. Results and discussion

2.4.1. Sunrise and sunset angles

The distributions of sunrise and sunset angles across the study watershed for four days are presented in Fig. 2.5 and Table 2.2, in which two days are in the summer half-year (9 May and 13 August) and two days are in the winter half-year (9 February

and 1 November) for explicitly illustrating their essential spatial patterns.

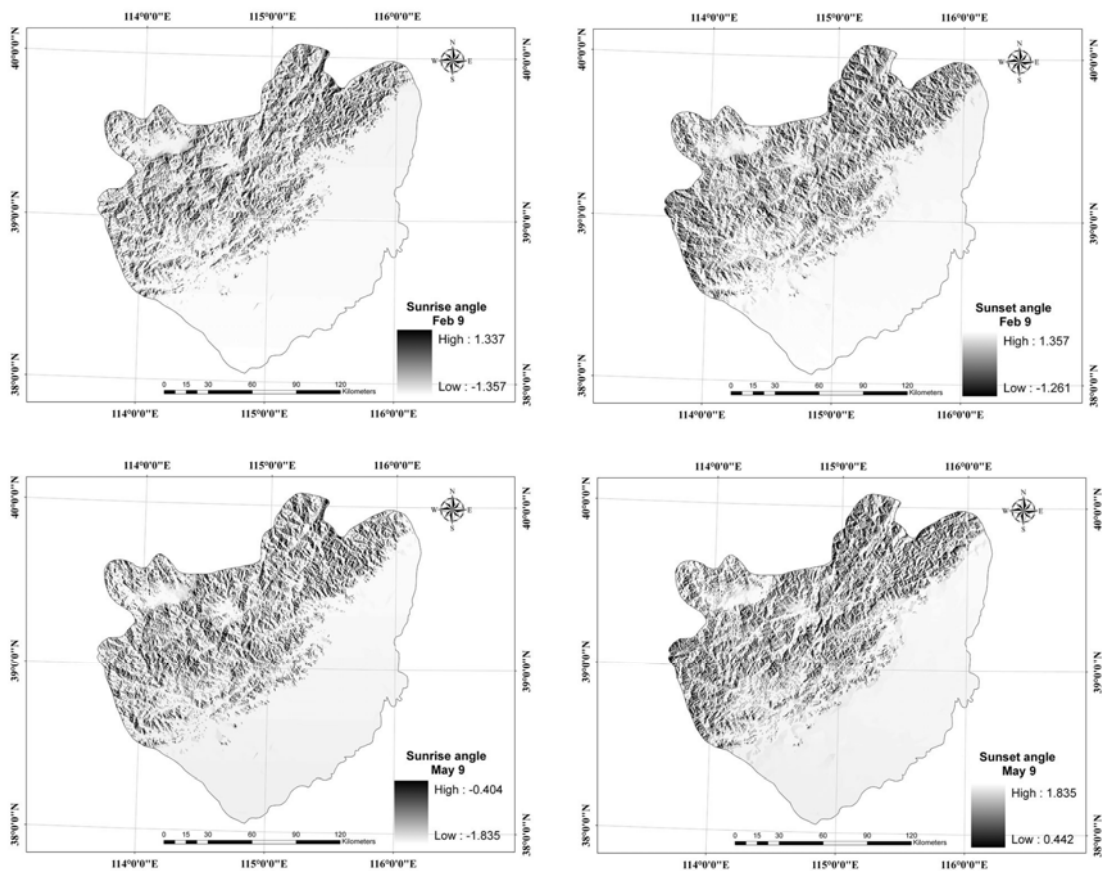


Figure 2.5 Distributions of sunrise and sunset angles (rad) of the Baiyangdian watershed on Feb 9, May 9, Aug 13 and Nov 11.

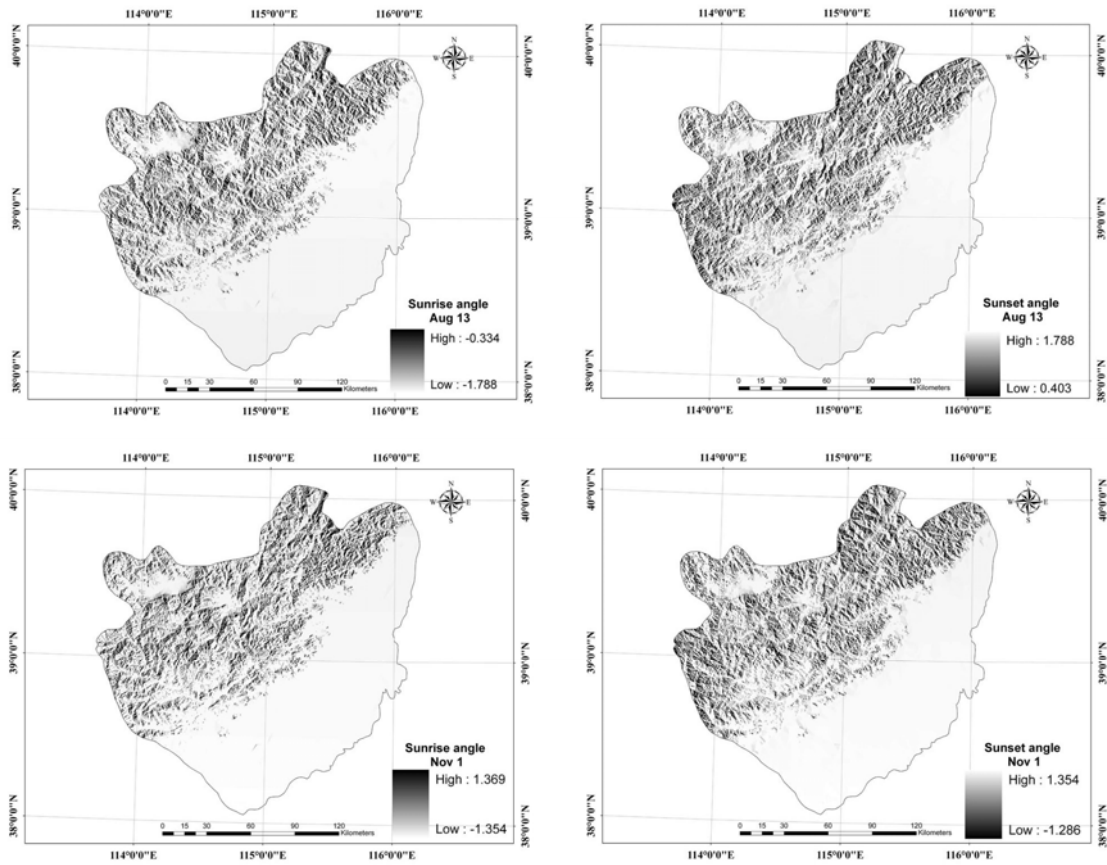


Figure 2.5 Continued.

Table 2.2 Distributions of sunrise and sunset angles (rad) for two days in the summer half-year and two days in the winter half-year over the Baiyangdian watershed in the year 2007

Calendar day (DOY)	Average ω_H	Rang of ω_1	Range of ω_2	The number of pixels not receiving direct solar radiation	The number of pixels having two sets of sunrise and sunset angles
May 9 (129)	± 1.826	$[-1.836, -0.405]$	$[0.442, 1.836]$	529	1
Aug 12 (224)	± 1.781	$[-1.789, -0.335]$	$[0.404, 1.789]$	215	1
Feb 9 (40)	± 1.349	$[-1.357, 1.337]$	$[-1.261, 1.357]$	522	0
Nov 1 (305)	± 1.351	$[-1.354, 1.369]$	$[-1.287, 1.354]$	571	0

From Fig. 2.5 and Table 2.2, it appears that the adopted geometric model is capable of capturing the spatial variability in sunrise and sunset angles under complex terrain conditions over the entire scenes. First, sunrise angles are earlier for the summer half-year than those for the winter half-year and sunset angles for the summer half-year are later compared with those for the winter half-year. In other words, the direct solar radiation availability for sloping surfaces in the summer half-year is larger than that in the winter-half year.

Second, there are marked differences between the sunrise angles for sloping surfaces and those for flat surfaces across this watershed for a specific day. For instance, the difference between the earliest sunrise angle and the latest sunrise angle on November 1 incredibly reaches the order of 10.4 hours ($1.369 + 1.354 = 2.723$ rad), and similarly, the difference between the earliest sunset angle and the latest sunset angle also spans a long period of 10.1 hours ($1.354 + 1.287 = 2.641$ rad). This highlights the heterogeneity in the terrain of the study watershed. For some specific sloping land surfaces in the study watershed, they can only be illuminated by direct sunlight late in the morning or early in the afternoon that are quite short compared with the flat surface at the same latitude.

Third, the number of pixels that could not receive direct sunlight or have two sets of sunrise and sunset angles is relevant to their specific slopes, azimuths and DOY. There was approximately an area of 5.71 km^2 not receiving direct solar radiation on November 1. In addition, there was only one pixel on May 9 and August 13 being illuminated twice a day. It is noted that the accuracy of solar critical angles depends largely on the

resolution and accuracy of DEM used. This means the finer DEM, the more accurate magnitudes of sunrise and sunset angles.

In summary, if the sunrise and sunset angles for the whole watershed were simulated irrespective of terrain factors, it would introduce gross errors to the simulation of sunshine duration and $S_{in,24}$ for sloping surfaces. What we have done is restoring realistic illumination conditions in simulation of $S_{in,24}$ by adequately taking into account the effects of terrain factors on deriving critical solar angles, which would greatly improve the spatial representation of estimates of DANR and ET.

2.4.2. Daily average direct solar radiation

Daily average direct solar radiation can be derived through inputting quantitatively determined sunrise and sunset angles to Eq. (2.5) and observations of actual solar duration and other terrain parameters. For examining the characteristics of the variation in direct solar radiation with terrain factors and evaluating the utility of the adopted geometric model to estimate $S_{in,24}$, the variation trends in $S_{in,24}$ with slopes for given azimuths on April 25 and September 19 have been, respectively, examined (Figs. 2.6 and 2.7).

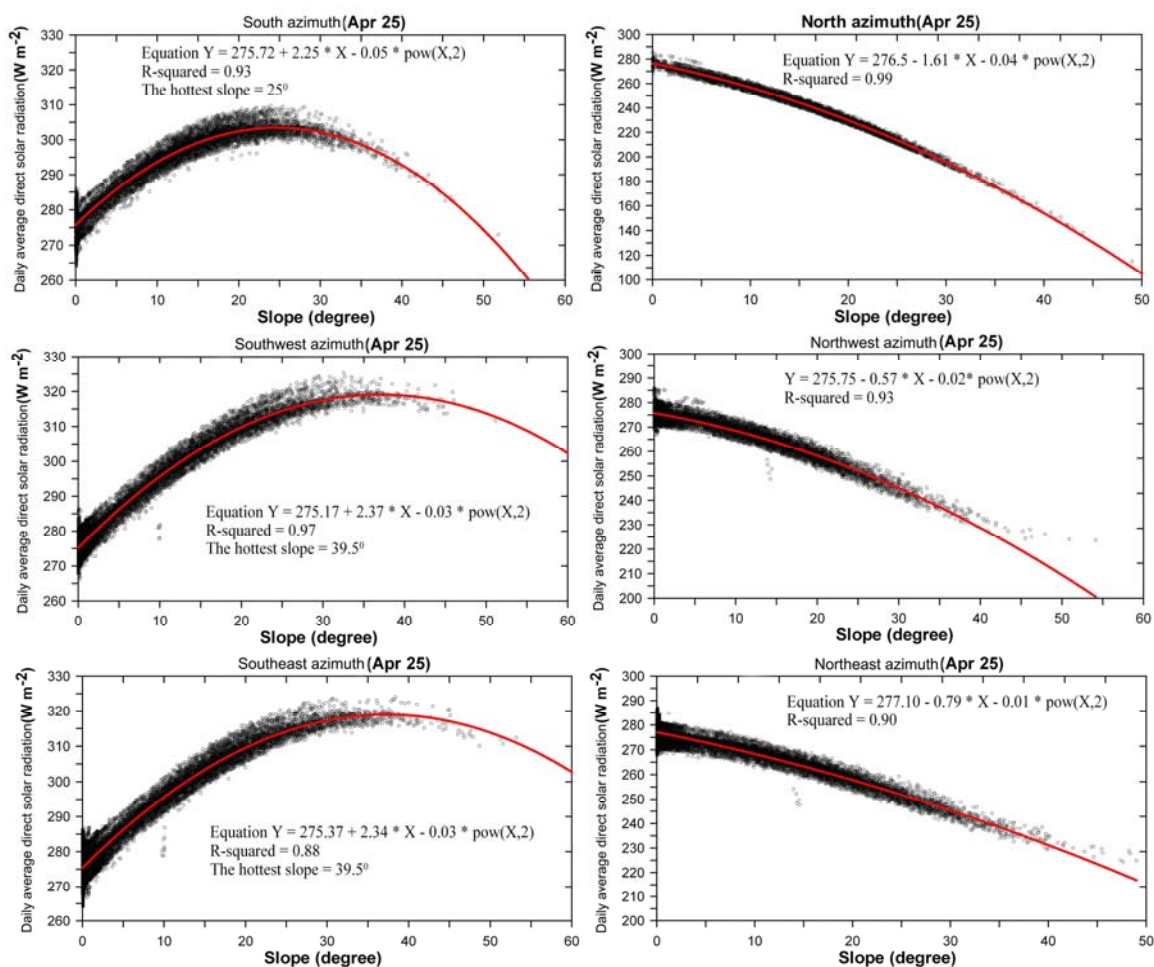


Figure 2.6 Variations in simulated daily average direct solar radiation (W m⁻²) with slopes for different azimuths across the Baiyangdian watershed on Apr 25, 2007.

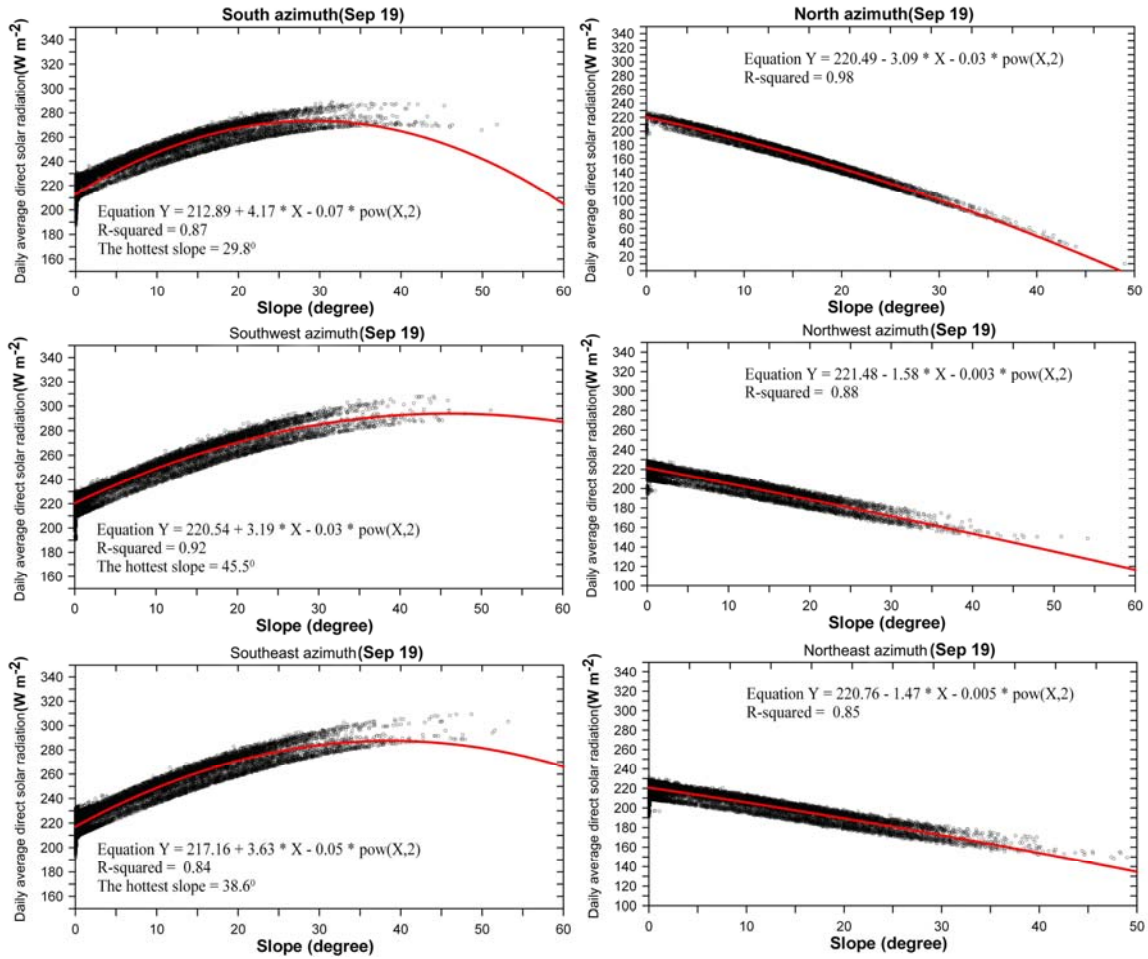


Figure 2.7 Variations in simulated daily average direct solar radiation (W m^{-2}) with slopes for different azimuths across the Baiyangdian watershed on Sep 19, 2007.

Both days explicitly show that there is a kind of ‘hottest slope’ for the sloping land surface facing south (due south, southwest, and southeast), presenting that from 0° to the hottest slope, $S_{\text{in},24}$ increases with slopes. However, if slopes exceed the turning point, $S_{\text{in},24}$ for sloping land surfaces will decrease with an increase in slopes up to lower than $S_{\text{in},24}$ for the flat land surface at certain large slopes. Namely, the sloping land surfaces facing south have the potential to receive more direct solar radiation than the flat land surfaces (slope= 0°).

In addition, the hottest slope and modeled $S_{in,24}$ for April 25 were generally smaller than that for September 19 (25° , 39.5° and 39.5° for the sloping surface facing south, southwest and southeast on 25 April; 29.8° , 45.5° and 38.6° on 19 September). This could be ascribed to different solar declination values, April 25 having a smaller solar declination value than September 19 ($12^\circ 59'$ for 25 April, $0^\circ 35'$ for 19 September that is quite close to the autumnal equinox in 2007). By contrast, the sloping land surface facing north (north, northwest, and northeast) could not present similar variation trends as the sloping land surface facing south, exhibiting that $S_{in,24}$ for the surface facing north declined rapidly with an increase in slopes from the flat surface (slope= 0°). The declining rate for September 19 was more rapid than that for April 25. As for the variation trends for different azimuths, $S_{in,24}$ for the land surface facing due south and due north vary with slopes more dramatically than that facing southwest or southeast and northwest or northeast. The southwest and southeast azimuths tend to receive much more direct solar radiation compared with other azimuths of this study watershed on the two tested days.

Frequency distributions of the difference between the simulated $S_{in,24}$ from assuming the entire land surface to be flat and that from the geometric model for sloping land surfaces larger than 25° and 45° on April 25 and September 19, respectively, are shown in Fig. 2.8. Results indicate that the largest differences between two methods

would incredibly reach the order of 199.4 W m^{-2} and 204.6 W m^{-2} on April 25 and September 19, respectively. In general, the simple way would underestimate $S_{\text{in},24}$ by 10.6 W m^{-2} and 17.0 W m^{-2} , when the slope is larger than 25° for the two tested day. Furthermore, with an increase in slope from larger than 25° to larger than 45° , the difference between the two methods would increase, showing that the standard deviation increased significantly from 39.6 W m^{-2} to 60.1 W m^{-2} on April 25 and from 57.9 W m^{-2} to 70.3 W m^{-2} on September 19, respectively.

To sum up, it was found that the proposed geometric model has the capability to capture the characteristics of the variation in direct solar radiation with not only the latitude and solar declination, but also terrain factors (slope, azimuth, elevation) across the entire watershed. Without accounting for terrain effects, the results would not present the detailed spatial heterogeneity and temporal variation trends in modeled $S_{\text{in},24}$, and would result in gross errors under some specific terrain conditions.

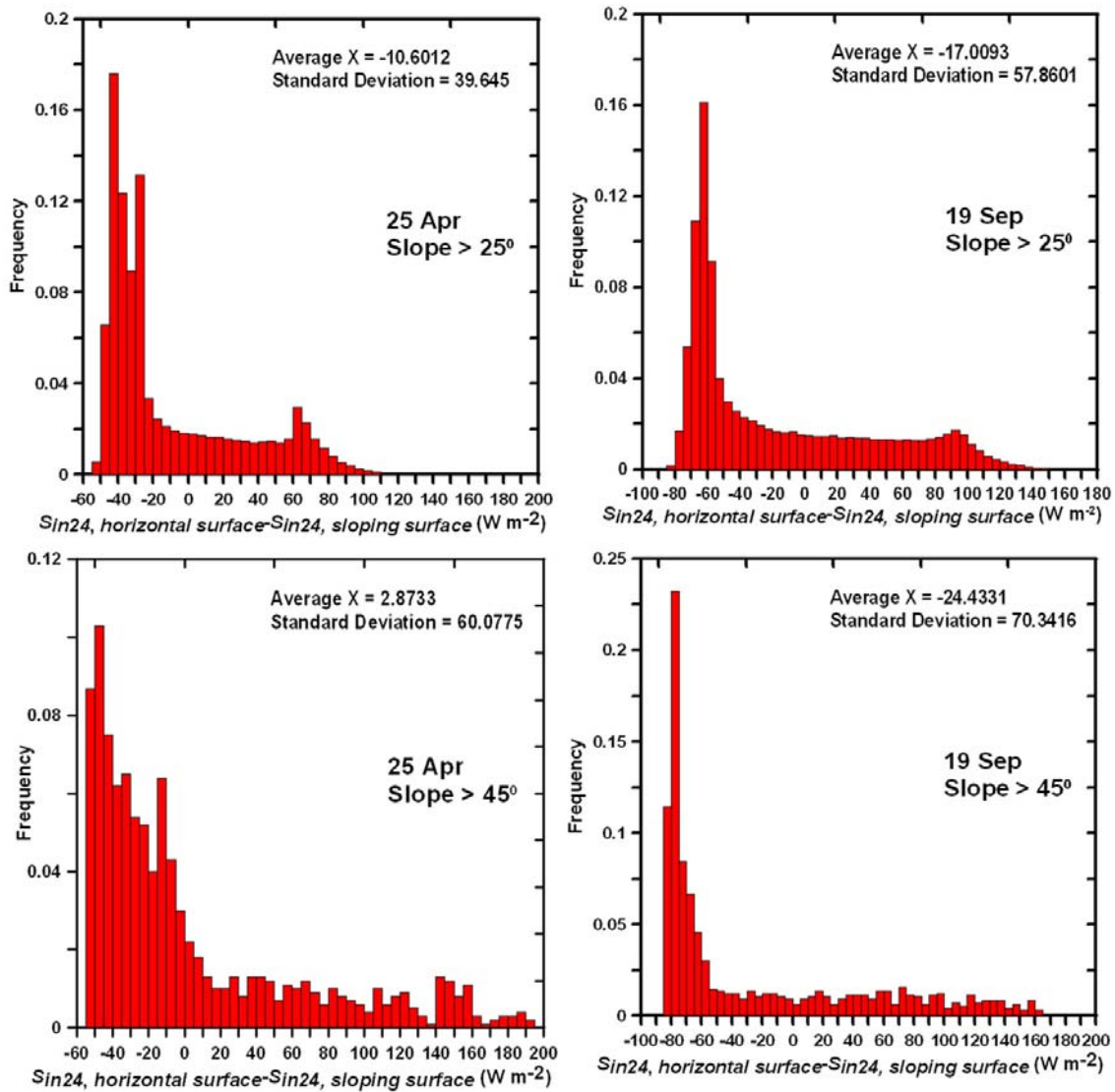


Figure 2.8 Frequency distributions of the difference between simulated $S_{in,24}$ (W m⁻²) from assuming the land surface to be horizontal across the study watershed and $S_{in,24}$ (W m⁻²) from the adopted geometric model for sloping land surfaces with slopes larger than 25° and 45° on Apr 25 and Sep 19, respectively (A bin size of 5 W m⁻² is specified).

2.4.3. Daily average net shortwave radiation

After $S_{in,24}$ and $S_{d,24}$ were simulated on the basis of the geometric model and the characteristic of diffuse solar radiation, DANSR can be ultimately calculated in

combination with the surface albedo from MODIS black-sky and white-sky albedo products (MCD43A3, 500 m) and MODIS aerosol optical depth product (MOD04, 1000 m). It is noted here that the resolution of $S_{in,24}$ and $S_{d,24}$ (100 m) differs from that of MODIS data products. $S_{in,24}$ and $S_{d,24}$ had to be thus resampled to 500 m by bilinear interpolation so as to be consistent with the resolution of MODIS albedo products.

Fig. 2.9 and Table 2.3 show the essential characteristics of the spatial distribution of DANSR from the proposed method over the Baiyangdian watershed. It can be inferred that terrain factors are primarily responsible for the spatial variability in DANSR under the condition of the uniform distribution of actual sunshine duration in Eq. (2.5). The retrieved DANSR on April 25, May 9, August 13, and September 19 distinctly show that DANSR over northwest mountainous areas is larger than that over southeast plain areas, resulting primarily from the difference in atmospheric attenuation between mountainous and plain areas. Higher elevation areas usually correspond to lower atmospheric attenuation and therefore larger shortwave radiation.

Furthermore, surface albedo is found to be an important factor affecting the spatial variation in DANSR. It is obvious that DANSR of Baiyangdian Lake is larger than that of surrounding dry land for six tested days. This is probably because of the surface albedo of water body and ambient humid environment being smaller than that of dry

land, therefore showing a relatively larger DADSR. DANSR on June 15 and July 19 did not show similar spatial distributions as the other four clear sky days, which could be attributed to heterogeneous distribution of observed sunshine duration across the entire study watershed for the two days. This tampered the spatial pattern of DANSR that should exhibit for clear sky days. With respect to the variation in DANSR with DOY, the mean of estimates of DANSR increased with dates, peaked on July 19 with a value of 335.6 W m^{-2} , and then decreased with dates. This trend could be closely related to the variation in solar declination.

Table 2.3 Statistics about DANSR (W m^{-2}) over Baiyangdian watershed for six clear sky days in the year 2007

Calendar day (DOY)	Maximum	Minimum	Mean	Standard deviation
Apr 25 (115)	347.1	94.8	292.8	18.5
May 9 (129)	349.4	132.5	301.4	15.4
Jun 15 (166)	366.1	171.0	304.4	15.0
July 19 (200)	382.0	184.1	335.6	11.1
Aug 13 (225)	354.8	104.4	300.0	17.7
Sep 19 (262)	342.1	21.9	249.8	27.9

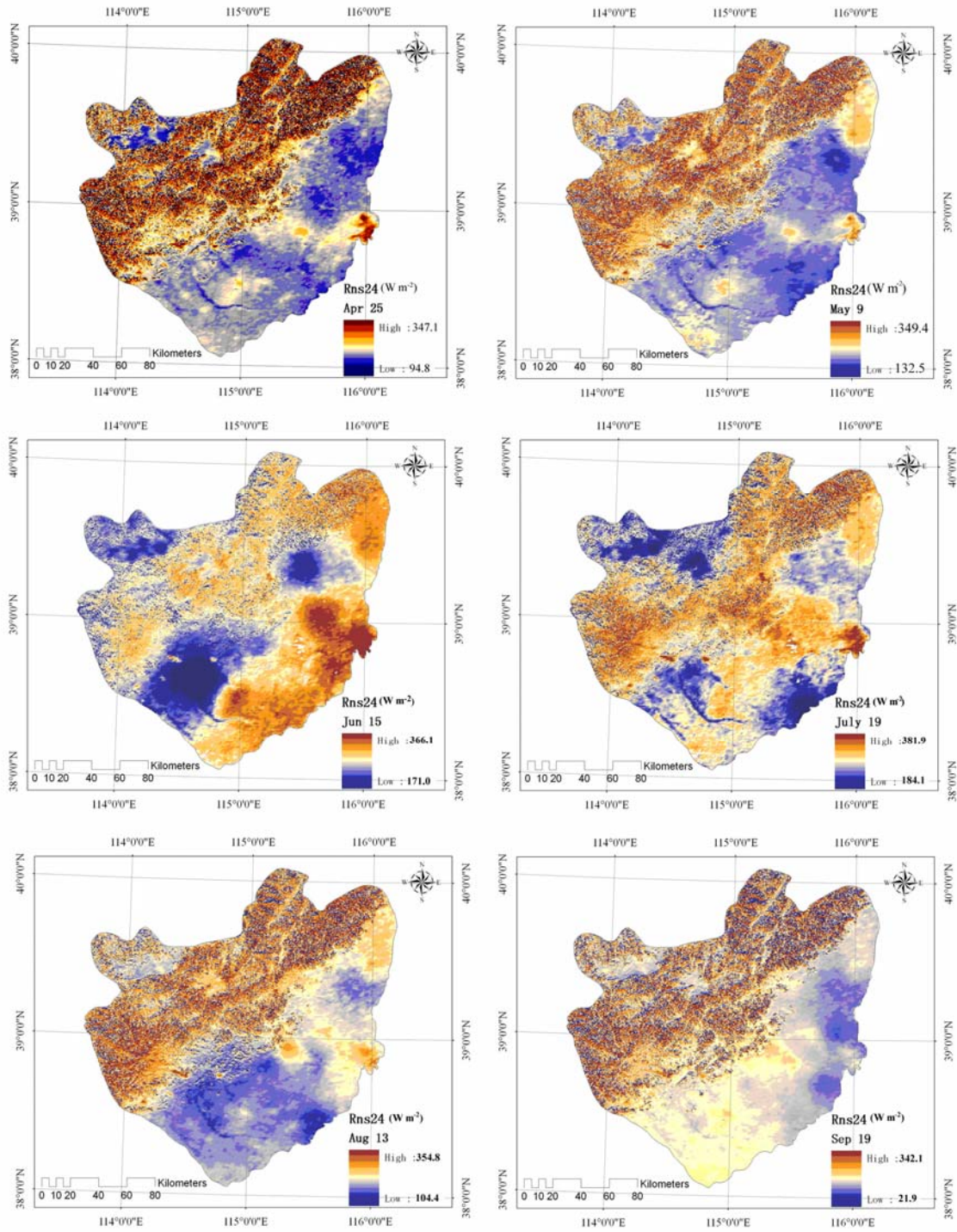


Figure 2.9 Simulated DANSR (W m⁻²) over the Baiyangdian watershed for six clear sky days in the year 2007.

2.4.4. Daily average net longwave radiation

DANLR from four observations of LST from MOD11A1 and MYD11A1 data products (termed four observations-based method hereafter), and one observation of LST from MODIS11_L2 (termed one observation-based method hereafter) were produced. Their utility and accuracy were examined in detail on the basis of the Penman equation over 18 sites for six tested clear sky days.

Results (Fig. 2.10 and Table 2.3) suggest that a noticeable discrepancy between the one observation-based method and the Penman equation exists, showing the maximum bias and root mean square error (RMSE) on the order of -48.7 W m^{-2} and 54.8 W m^{-2} on May 9, respectively, and the minimum bias and RMSE on the order of -12.6 W m^{-2} and 16.3 W m^{-2} on September 19, respectively. The four observations-based method could however dramatically improve the accuracy of estimates of DANLR, exhibiting good agreement with the Penman equation in terms of the maximum bias and RMSE of only 14.0 W m^{-2} and 16.7 W m^{-2} on April 25, respectively. In addition, results also clearly demonstrate a relatively strong correlation between the four observation-based method and the Penman equation in terms of a higher R^2 in comparison with the one observation-based method. Overall, the one observation-based method systematically underestimates DANLR due primarily to relatively higher LST values acquired around 10:30 a.m. compared with relatively lower daily LST from the four observations-based method.

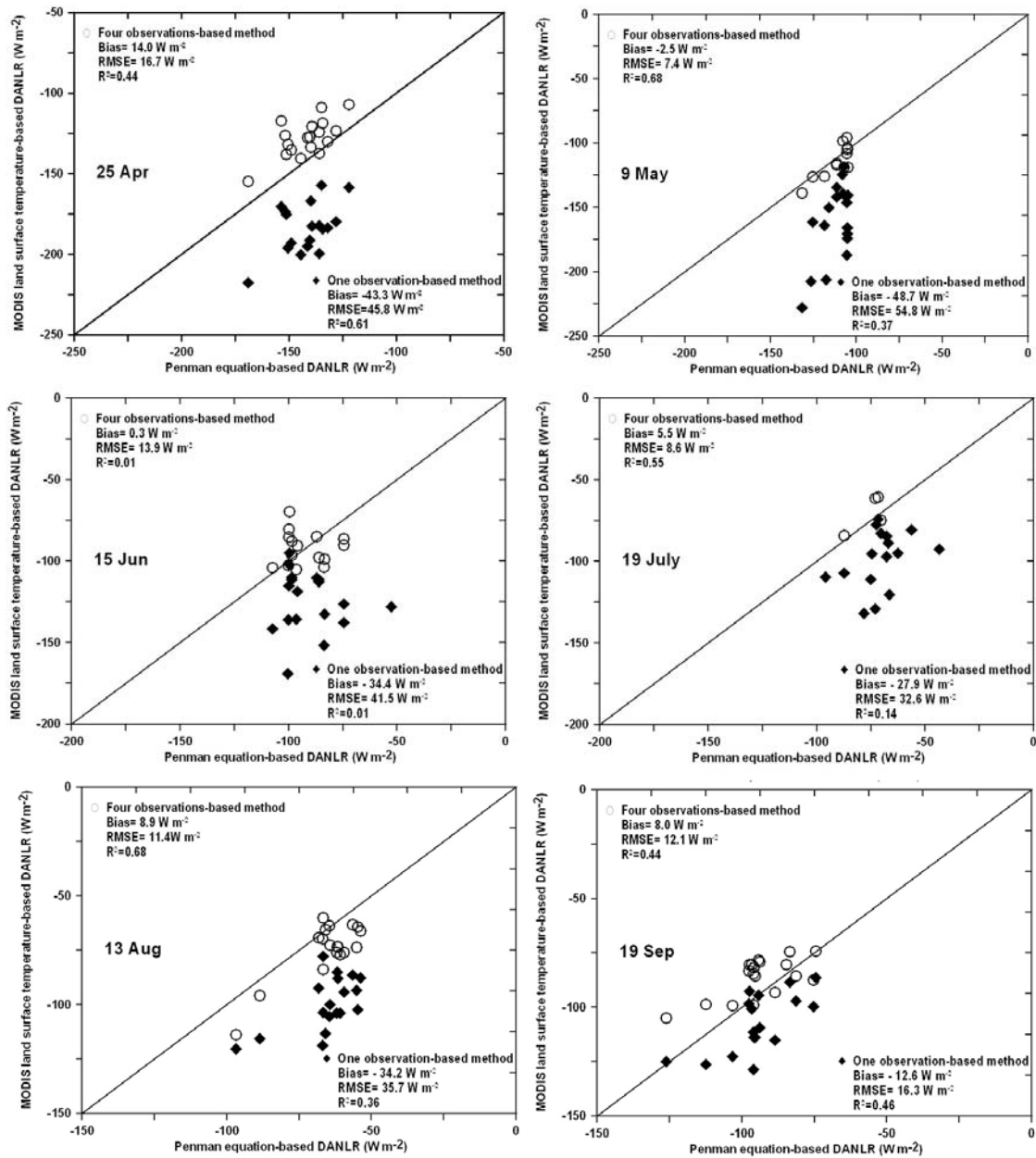


Figure 2.10 Comparison of estimates of DANLR (W m^{-2}) from the one observation-based method and the four observations-based method against the Penman equation across 18 weather stations over the Baiyangdian watershed for six clear sky days in the year 2007.

Table 2.4 Bias, RMSE, and coefficient of determination (R^2) for DANLR from using one observation of MOD11_L2 LST acquired around 10:30 a.m. and using four observations of MOD11A1 and MYD11A1 LST acquired on 10:30 a.m. and 10:30 p.m., and 1:30 a.m. and 1:30 p.m., respectively, relative to the Penman equation using meteorological data across 18 weather stations for six clear sky days in the year 2007

Calendar day (DOY)	Using one observation of MODIS LST			Using four observations of MODIS LST		
	Bias (W m^{-2})	RMSE (W m^{-2})	R^2 (W m^{-2})	Bias (W m^{-2})	RMSE (W m^{-2})	R^2 (W m^{-2})
Apr 25 (115)	-43.3	45.8	0.61	14.0	16.7	0.44
May 9 (129)	-48.7	54.8	0.37	-2.5	7.4	0.68
Jun 15 (166)	-34.4	41.5	0.01	0.3	13.9	0.01
July 19 (200)	-27.9	32.6	0.14	5.5	8.6	0.55
Aug 13 (225)	-34.2	35.7	0.36	-8.9	11.4	0.68
Sep 19 (262)	-12.6	16.3	0.46	8.0	12.1	0.44
Total	-33.3	39.6	0.70	2.7	12.8	0.81

Figure 2.11 shows a comparison for the two methods against the Penman equation across 18 weather stations for all tested clear sky days. It is clear that the one observation-based method showed a relatively larger bias and an RMSE on the order of -33.3 W m^{-2} and 39.6 W m^{-2} , respectively. However, the four observations-based method agrees reasonably well with the Penman equation, indicating a bias, RMSE and R^2 of 2.7 W m^{-2} , 12.8 W m^{-2} and 0.81, respectively. Accordingly, it can be concluded that the proposed method that combines four observations of MODIS LST with minimum meteorological data (T_a and e_a) is of the capability to reliably derive DANLR against the Penman equation that has been proven to be applicable to the study site based on extensive ground measurements.

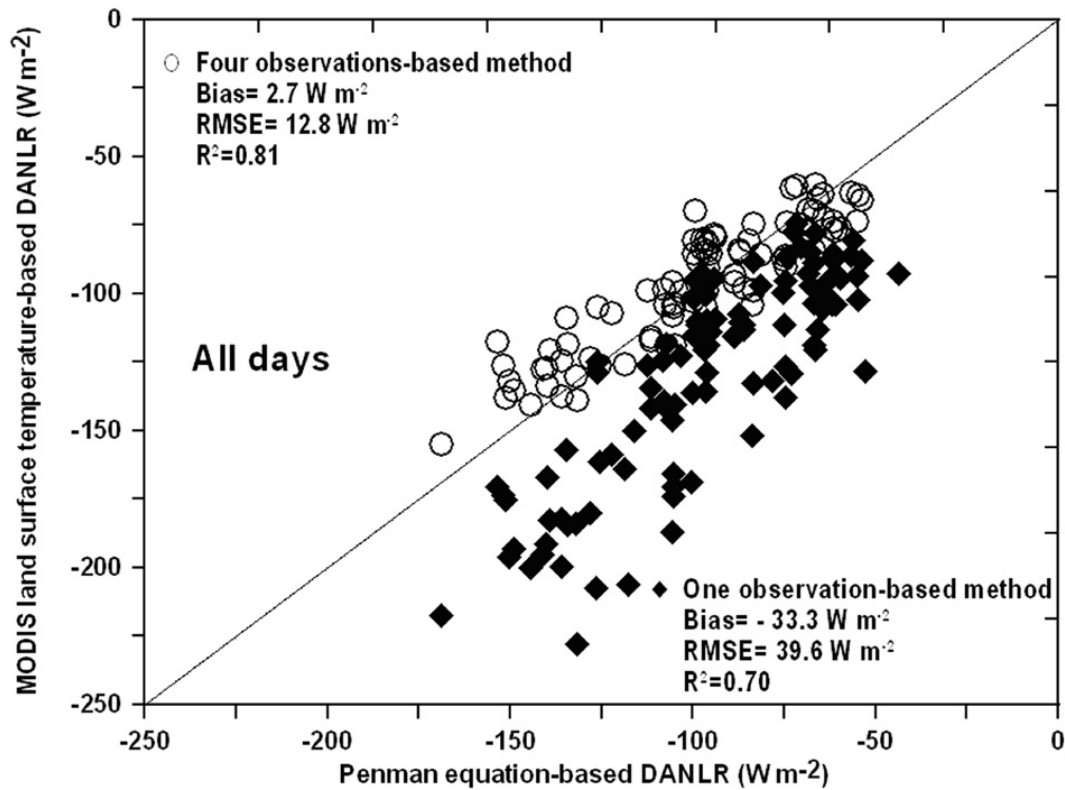


Figure 2.11 Comparison of estimates of DANLR (W m^{-2}) from the one observation-based method and the four observations-based method against the Penman equation across 18 sites over the Baiyangdian watershed for the whole study period.

2.4.5. Daily average net radiation

After obtaining each component of Eq. (2.1), DANR can be ultimately calculated over the study watershed (Fig. 2.12 and Table 2.5). It can be seen from the results that first, the mean of estimates of DANR increased from 25 April, peaked on 19 July with a maximum of 229.4 W m^{-2} , and then showed decreased, reaching a minimum of 131.1 W m^{-2} on September 19. The temporal variation in DANR can probably be ascribed to the solar declination which profoundly impacts DANSR. The closer to the summer solstice (June 22 in 2007), the larger radiation energy the land surface could receive under the

clear sky condition.

Second, although the spatial distribution of DANLR attenuates to some degree the effect of terrain factors on DANR for sloping land surfaces due to DANLR having no strong relationship with specific slopes and azimuths, an appreciable difference in DANR between mountainous and plains areas was still observed on April 25, May 9, August 13, and September 19, respectively. Estimates of DANR across the southeast plain were apparently larger than those in the northwest mountainous areas on June 15. This rests on the fact that the distribution of actual sunshine duration was not homogeneous on June 15, with the observations from the southeast sites showing larger values than those from the northwest. Owing to clouds obstructing some portions of LST images acquired on July 19, the Penman equation was thus used to produce DANLR to make up those portions, thereby showing relatively larger values compared with the entire scene.

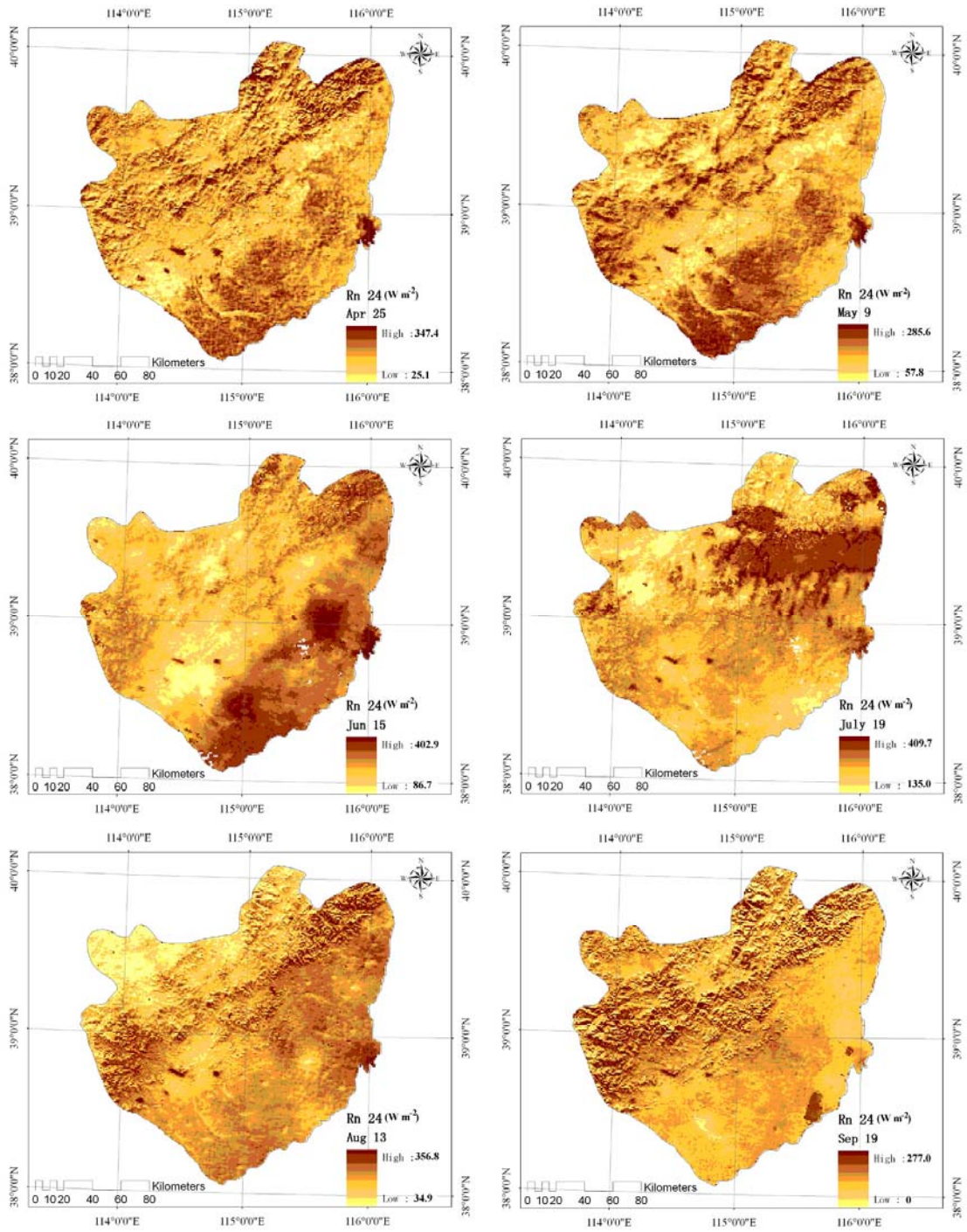


Figure 2.12 Simulated DANR (W m⁻²) over the Baiyangdian watershed for six clear sky days in the year 2007.

Table 2.5 Estimated DANR (W m^{-2}) over the Baiyangdian watershed for six clear sky days in the year 2007

Calendar day (DOY)	Maximum	Minimum	Mean	Standard deviation
Apr 25 (115)	347.4	25.1	140.7	21.6
May 9 (129)	285.6	57.8	142.6	24.1
Jun 15 (166)	402.9	86.7	183.1	27.0
July 19 (200)	409.6	135.0	229.4	23.0
Aug 13 (225)	356.8	34.9	178.2	20.1
Sep 19 (262)	277.0	0.0	131.1	20.6

The relationship between retrieved DANR and elevation was investigated to show how elevation influences macroscopic distribution of DANR throughout the entire study watershed. In general, atmospheric composites, temperature, humidity and LST may vary to different degrees with elevation, which could induce the variations in direct and diffuse solar radiation, atmospheric downwelling and surface upwelling longwave radiation, and eventually result in the variations in DANR and ET from plains to mountainous areas.

Fig. 2.13 shows the relationship between DANR and elevation for six clear sky days. Overall, DANR decreased slightly with an increase in elevation, showing a maximum amplitude of $-20 \text{ W m}^{-2} \text{ km}^{-1}$ on August 13 and a minimum amplitude of $-1.6 \text{ W m}^{-2} \text{ km}^{-1}$ on April 25, respectively, with the exception of September 19 showing a small amplitude of $2.5 \text{ W m}^{-2} \text{ km}^{-1}$ but an inverse variation trend. In addition, the coefficients of determination R^2 are generally low, implying that there is no direct relationship between DANR and elevation. This means that DANR basically remains

invariant with an increase in elevation. The variation trend in DANR with elevation appears to be determined by the combined effects of each component of DANSR and DANLR.

First, with an increase in elevation, the atmosphere tends to be rare, and the air density, dust, impurity and water content in atmosphere tend to reduce, therefore resulting in an increase in atmospheric transmissivity and direct solar radiation. However, diffuse solar radiation will reduce in terms of the findings from Fig. 2.4, thus restraining the increase in total shortwave radiation. Second, as to the variation in DANLR with elevation, the air temperature at the screen level and LST can decrease with an increase in elevation, resulting in reductions in atmospheric downwelling and surface upwelling longwave radiation simultaneously. Eventually, DANR remains relatively invariant. However, it shows very scattered points stemming from large differences in land cover types, terrain factors, and actual sunshine duration for a specific location.

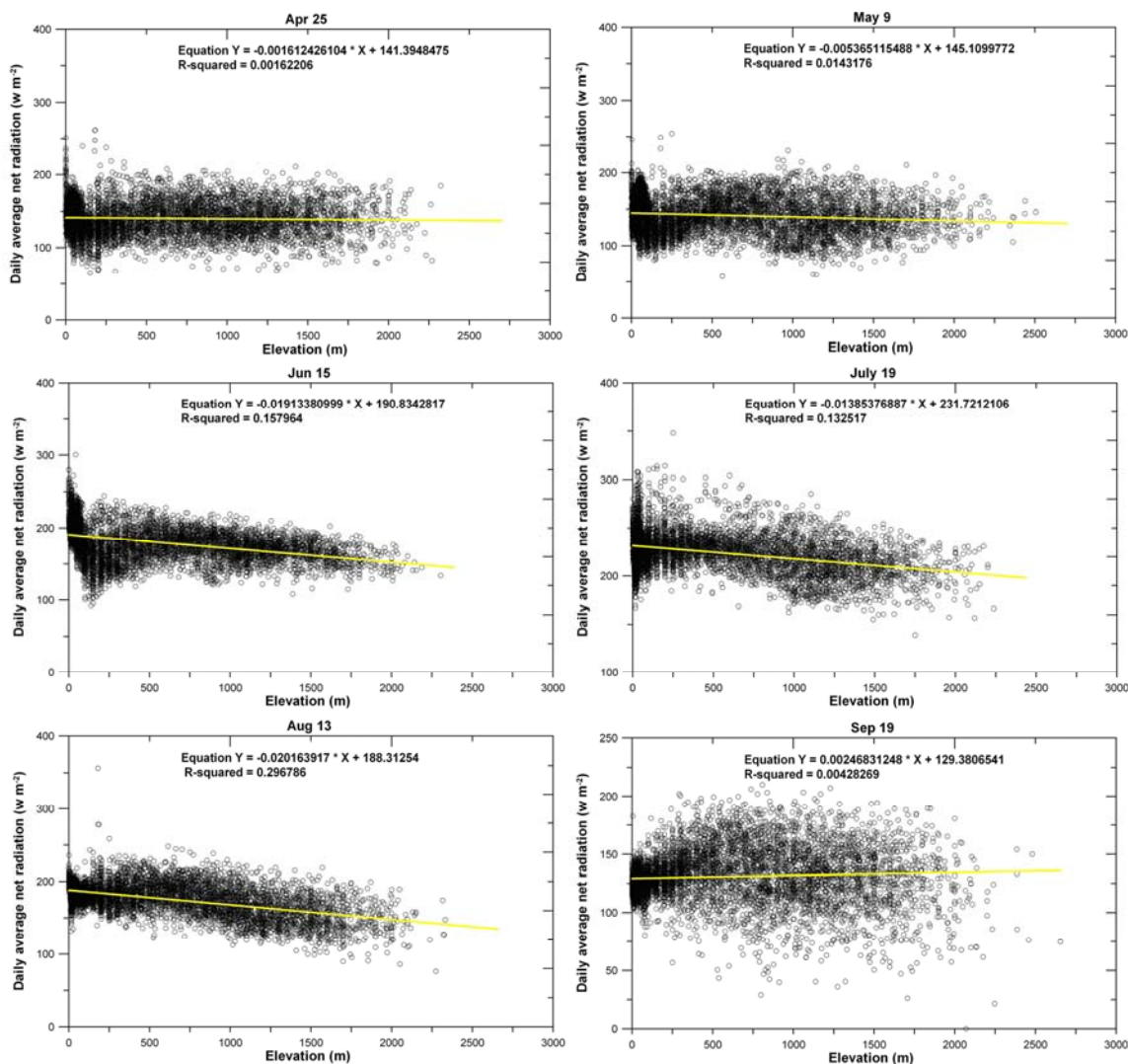


Figure 2.13 Relationship between DANR and elevation across the study watershed for six clear sky days in the year 2007.

It should be emphasized that our purpose is to retrieve DANR from MODIS data products and DEM in combination with minimum meteorological data at regional or watershed scales. Resulting estimates of DANR could not be directly compared with ground-based measurements for the dearth of radiation observations over this area. We acknowledge that the proposed method warrants further validation about the final

estimates of DANR. However, the parameterization schemes for each component of Eq. (2.1) do provide more reasonable estimates compared with existing parameterization schemes that do not account for the effect of terrain factors, particularly restoring realistic spatial variability in DANR across mountainous areas. The proposed scheme for estimating DANSR was validated against the Penman equation. On the other hand, although a handful of ground-based DANR would obtain, there are no universally acceptable methods to compare spatially distributed estimates with point-based ground observations due to the discontinuity, scale issues, and limited number of observations (Bisht et al., 2005; McCabe and Wood, 2006).

2.5. Conclusions

DANR is a critical variable linking instantaneous latent heat flux to daily ET. However, the existing parameterization schemes of DANR appear to be less than suitable for capturing its substantial distribution patterns across large heterogeneous areas, especially over mountainous areas because: (1) the parameterization scheme of DANSR does not involve some physical mechanism to characterize the heterogeneity in $S_{in,24}$ for sloping land surfaces, and (2) the applicability of the parameterization scheme of DANLR only using one observation of remotely sensed LST may vary with satellite platform systems, leading uncertainties to DANLR estimation due to different capabilities of near midday LST to represent the daily average LST.

In this chapter, $S_{in,24}$ is parameterized through taking into account the effects of terrain factors, such as slope, azimuth, and elevation on direct solar radiation.

Specifically, the sunrise and sunset angles for a given sloping surface are quantified. Besides, the physical mechanism governing the variation in diffuse solar radiation with solar zenith angle is investigated in order to involve $S_{d,24}$ in the calculation of DANSR. Results indicate that the geometric model has the capability to characterize the variability in $S_{in,24}$ over the entire study watershed, explicitly showing that the southwest and southeast azimuths have relatively larger magnitudes of direct solar radiation compared with other azimuths on April 25 and September 19, respectively, and there exist the hottest slopes for surfaces facing south.

Improvements in the spatial representation of $S_{in,24}$ would significantly improve the distributions and magnitudes of DANSR and DANR. Without incorporating terrain factors into the parameterization schemes, the difference in $S_{in,24}$ would be as large as 199.4 W m^{-2} and 204.6 W m^{-2} on April 25 and September 19, respectively. Furthermore, the steeper the slope, the larger difference would occur, implying the robustness of the parameterization schemes. DANSR can be ultimately derived from modeled $S_{in,24}$, $S_{d,24}$, and MODIS albedo products.

An approach to simulating DANLR is proposed through incorporating four observations of MODIS LST and surface emissivities from MOD11_L2, MOD11A1 and MYD11A1 in conjunction with minimum meteorological data, aiming at circumventing the deficiency in the use of only one observation of remotely sensed LST. The retrieval accuracy is evaluated on the basis of the Penman equation that has been shown to be able to provide reliable estimates of DANLR across the study site but needs relatively more meteorological data. Comparison of retrievals from the four observation-based

method and one observation-based method against the Penman equation is performed, showing a bias of 2.7 W m^{-2} and a RMSE of 12.8 W m^{-2} for the proposed method and a bias of -33.3 W m^{-2} and a RMSE of 39.6 W m^{-2} for the one observation-based method across 18 weather stations for six tested clear sky days.

We acknowledge that the proposed method does not involve a complex radiative transfer model. Nevertheless, it incorporates a sophisticated algorithm to quantify solar radiation for sloping surfaces. In addition, it adequately utilizes four observations of MODIS LST to improve the accuracy of DANLR retrievals. One can be confident that the improvements in DANSR and DANLR would significantly improve the accuracy of DANR estimates, particularly its spatial distribution across large heterogeneous areas. These contributions would be significant in operational regional ET estimation for water resources planning and management, hydrologic modeling, and further applications like antecedent soil water content and surface runoff estimation, and flood monitoring from remote sensing.

It should be noted that for cloudy days, DANSR can also be estimated from the proposed method with successive MODIS albedo products and observations of actual sunshine duration for calculating daily average atmospheric transmissivity ($a+bn/N$). Because of the absence of remotely sensed LST in cloudy days, DANLR could be estimated directly with the Penman equation and meteorological data. Atmospheric radiative transfer models or more sophisticated methods with profiles of atmospheric states could also be used to address daily average atmospheric transmissivity and DANLR for cloudy days (Forman and Margulis, 2009).

CHAPTER III

INTEGRATION OF THE GG MODEL WITH SEBAL TO PRODUCE ET TIME SERIES OF HIGH SPATIAL RESOLUTION AT WATERSHED SCALES

3.1. Introduction

Satellite-based models tend to generate latent heat flux of reasonable spatial representation due primarily to the incorporation of remotely sensed LST (Anderson et al., 2007a; Anderson et al., 2007b; Bastiaanssen et al., 2002; Batra et al., 2006; Gao and Long, 2008; Jiang and Islam, 2001; Krajewski et al., 2006; Kustas et al., 2007; Nishida et al., 2003; Zhang, 2009). Satellite images, in particular the images of the thermal infrared band, however, are often blurred or obstructed by clouds especially during rainy season. The restriction makes such models only work under cloud-free conditions. At most, they can offer temporally integrated daily ET by assuming instantaneous evaporative fraction (EF) to be fairly invariant during daytime and then utilizing the derived instantaneous EF to partition daily net radiation (Ahmad et al., 2006; Bastiaanssen, 2000; Bastiaanssen et al., 1998a; Bastiaanssen et al., 2005; Jiang and Islam, 2001; Norman et al., 2003; Su, 2002). Nevertheless, the latent heat flux or daily ET estimates under cloud-free conditions cannot satisfy the requirement of ET time series. In particular, monthly, seasonal, and yearly ET estimates are needed for quantifying total water consumption by agricultural crops and assisting professionals in water resources allocation and management (Ahmad et al., 2006; Allen et al., 2007).

We suggest that integration of the feedback method (Granger, 1989; Granger and

Gray, 1989), (hereinafter the GG model) with a remote sensing-based model has the potential to make reliable predictions of ET time series of high spatial resolution by simply using routine weather data. The point here is that for a specific region where the complementary relationship (hereinafter CR) between pan ET and actual ET has been shown to be valid, the ET time series would exhibit complementary features over time and space. If the integration approach has demonstrated skill in generating ET time series which are of CR features and high spatial resolution due to the incorporation of remotely sensed variables and/or fluxes, it would successfully extend remotely sensed information on cloud-free days to days without usable images. This technique would substantially improve the accuracy of ET time series estimates and greatly benefit a range of applications.

The GG model has been shown to be able to yield reliable magnitudes of ET over large areas in different regions throughout different climatic zones (Allen et al., 2007; Armstrong et al., 2008; Crago and Crowley, 2005; Liu et al., 2006; Xu and Singh, 2005). To account for departures from the saturated condition and obtain a more general expression for calculating actual ET, Granger and Gray (1989) introduced a concept of relative evaporation, G , (defined as the ratio of the actual evaporation to the potential evaporation) to this method. The potential evaporation is defined as the evaporation rate that would occur, given certain atmospheric conditions (e.g., wind and humidity), if the surface were saturated at the temperature of the surface. Moreover, they related G to the relative drying power of air, D , based on an assumption that meteorological variables (e.g., air temperature and vapor pressure) can be indicative of changes in soil moisture

status and thus potential and actual ET (Brutsaert, 1982; Morton, 1983). The GG model eliminates the need for surface variables like LST and surface vapor pressure in that D not only drives the actual ET but also reflects the effects of actual ET on regional advection (Hobbins et al., 2004). Furthermore, the GG model avoids a prior calculation of potential evaporation which has not been clearly defined in a universally accepted manner (Biftu and Gan, 2000; Granger and Gray, 1989; Wu et al., 2006).

It is noted that the relationship between D and G should be applied with caution. In Granger and Gray's original work (1989), limited data points (158) of actual ET and the values of G larger than 0.7 (the wet environment) did not allow for a more universally applicable functional relation over large heterogeneous areas. Later, Granger modified this relationship which is also an exponential function (Granger, 1996; Granger, 1998). Nevertheless, Biftu and Gan (2000) suggested that the modified relationship cannot represent heterogeneity in landscape properties governing the mechanisms of water-heat transfer either. Furthermore, it should also be noted that although the GG model has the capability to make reliable predictions of areal ET, its spatial representation has not yet been well examined.

It is logical that the spatial resolution of ET from the GG model relies largely on the spatial scale of meteorological forcing. The satellite-based models tend to produce ET estimates with reasonable spatial distribution over an entire scene on cloud-free days. Meanwhile, the GG model can yield reasonable ET magnitudes over large areas using routine meteorological data, provided an effective relationship between D and G is well established. The two approaches have important complimentary potential. If the

relationship between D and G can be established by the ET outputs from a satellite-based model of large heterogeneous areas with a range of atmospheric and surface conditions, the modified GG model would probably make reliable predictions of ET with reasonable magnitude and distribution throughout a study region by simply using routine meteorological data.

Of satellite-based models for simulating land surface fluxes, SEBAL has been one of commonly used tools to capture the spatial variability in ET at watershed/regional scales (Allen et al., 2007; Compaore et al., 2008; French et al., 2005b; Gao et al., 2008; Hong et al., 2009; Immerzeel and Droogers, 2008; Immerzeel et al., 2008; Kongo and Jewitt, 2006; Oberg and Melesse, 2006; Ramos et al., 2009; Teixeira et al., 2009a; Teixeira et al., 2009b). A watershed with a variety of land covers exhibiting distinct surface and atmospheric conditions can be selected as a study site, which would probably satisfy the prerequisite of the presence of two hydrological extremes, termed the hot and the cold pixels in SEBAL. Remote sensing sources come from MODIS land and atmospheric products which are widely used in regional ET estimation.

The objectives of this chapter were to (1) estimate actual ET of a selected watershed on cloud-free days using SEBAL; (2) re-establish the relationship between D and G in the GG model using the ET retrievals from SEBAL; (3) generate ET time series with the modified GG model; and (4) compare and contrast the performance of the evaporative fraction method, the crop coefficient method, and the proposed integration method to produce ET time series at watershed scales.

3.2. Critique of methods to generate ET time series

Existing methods to produce ET time series include: (1) the use of EF derived in cloud-free days as a surrogate to partition daily net radiation between satellite overpass dates or for days without usable images (Bastiaanssen et al., 2002; Farah, 2000; Farah et al., 2004) (hereinafter the evaporative fraction method), (2) the use of crop coefficients derived from remotely sensed actual ET and corresponding weather-based reference ET on days of image acquisition to partition reference ET on days without usable images (Allen et al., 2007; Li et al., 2008b; Mohamed et al., 2004; Mohamed et al., 2006; Oberg and Melesse, 2006; Singh et al., 2008) (hereinafter the crop coefficient method), and (3) the use of physically-based, distributed hydrological models to generate ET time series over large heterogeneous domains (Arnold et al., 1993; Bastiaanssen et al., 2002; Droogers and Bastiaanssen, 2002; Flerchinger et al., 1996; Gao and Long, 2008; Refsgaard, 1997; Schuurmans et al., 2003; Xu and Li, 2003).

3.2.1. Evaporative fraction method

Bastiaanssen et al. (2002) pointed out that there is a primary assumption in SEBAL that EF remains constant between satellite overpass dates. It may hold true when soil moisture and meteorological conditions do not significantly change. Farah (2000) stated that the accumulated ET for a period of around 10-20 days can be predicted satisfactorily from the remotely sensed EF amid the period. However, use of the EF retrieved for a particular day to predict ET for other days within a 10-day period fails. Bastiaanssen et al. (2002) implied that temporarily integrated ET from the temporal constancy of EF for

a week and or so can suffice for the accuracy, as systematic errors would cancel out over a relatively longer period of time:

$$ET_{\text{period}} = 86400 \sum_{i=b}^f \left[\frac{R_{n24i} \Lambda_d}{\lambda_i} \right] \quad (3.1)$$

where ET_{period} is the accumulated actual ET for a period beginning on day b and ending on day f , 86400 converts from seconds to 24 hours, Λ_d is the evaporative fraction derived on days with usable satellite images, R_{n24i} is the daily net radiation for day i , and λ_i is the daily latent heat of vaporization (J kg^{-1}). Uncertainties may exist in the extrapolated ET from the EF method in the presence of notable differences in soil moisture availability, daily net radiation, and meteorological conditions between clear sky satellite image dates.

3.2.2. Crop coefficient method

Allen et al. (2007) indicated that one satellite image per month can generally suffice for the construction of a reasonable crop coefficient curve for purposes of estimating seasonal ET. However, during periods of rapid vegetation change, a more frequent image interval may be required. Note that this approach assumes the actual ET for the entire area of interest to change in proportion to changes in the weather-based reference ET. This means that the larger the reference ET, the larger the actual ET given a constant crop coefficient:

$$ET_{\text{period}} = \sum_{i=b}^f \left[\frac{ET_d}{ET_{0d}} ET_{0i} \right] \quad (3.2)$$

where ET_d is the actual ET derived from days with usable images, ET_{0d} is the corresponding reference ET, and ET_{0i} is the reference ET for day i . In this study, the reference ET is calculated with the FAO56 equation (Allen, 2000):

$$ET_0 = \frac{0.408\Delta(R_{n,24} - G_s) + \gamma \frac{900}{T_a + 273} u_2 (e_s - e_a)}{\Delta + \gamma(1 + 0.34u_2)} \quad (3.3)$$

where ET_0 is the reference ET (mm d^{-1}), Δ is the slope of saturated vapor pressure ($\text{kPa}^\circ\text{C}^{-1}$), $R_{n,24}$ is the net radiation ($\text{MJ m}^{-2} \text{d}^{-1}$), and G_s is the soil heat flux ($\text{MJ m}^{-2} \text{d}^{-1}$). In applications having a 24-h calculation time step, G_s is assumed to be 0. γ is the psychrometric constant ($\text{kPa}^\circ\text{C}^{-1}$), T_a is the air temperature at a 2 m height ($^\circ\text{C}$), u_2 is the wind speed at 2 m height (m s^{-1}), and $e_s - e_a$ is the saturation vapor pressure deficit (kPa). ET_0 predicts ET from a hypothetical grass reference surface that is 0.12 m in height having a surface resistance of 70 s m^{-1} and albedo of 0.23. Sensitivity analysis (Fig. 3.1a) of Eq. (3.3) shows that $R_{n,24}$ is the most sensitive variable, with a 10% increase in $R_{n,24}$ resulting in around 7.5% increase in ET_0 . A 10% increase in $e_s - e_a$, T_a , and u_2 would result in a 2.5 %, 0.9%, and 0.8% increase in the resulting ET_0 , respectively.

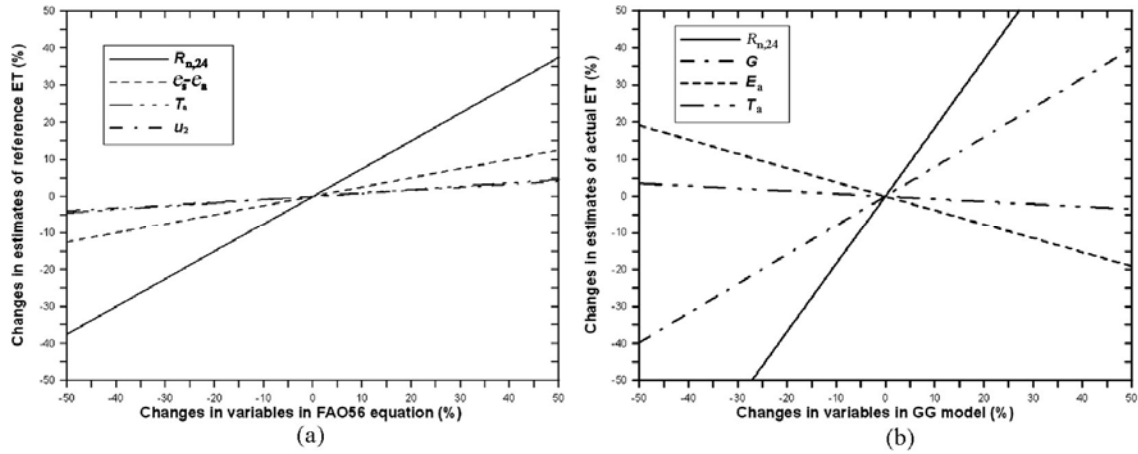


Figure 3.1 Sensitivity analysis of the FAO56 reference ET equation (a) and the GG model (b), with reference values: $R_{n,24}=17.28 \text{ MJ m}^{-2} \text{ d}^{-1}$, $e_s-e_a=1 \text{ kPa}$, $u_2=2 \text{ m s}^{-1}$, and $T_a=27 \text{ }^{\circ}\text{C}$.

3.3. Proposed integration method

Integration of the GG model with SEBAL is proposed to produce ET time series with high spatial resolution at watershed scales as the following steps: (1) the use of SEBAL to simulate spatially consistent and reasonably distributed ET for cloud-free days; (2) the ET output from SEBAL constitutes input into the GG model to invert G ; (3) the new relationship between D and G can be explored and reconstructed; and (4) the modified GG model with associated weather data and remotely sensed albedo and VI will generate ET time series.

3.3.1. SEBAL model

SEBAL is an energy balance-based method of modeling land surface fluxes with remotely sensed, i.e., LST, albedo, and emissivity, and less meteorological data, i.e., air temperature, vapor pressure, and wind velocity. The latent heat flux is calculated as the

residual term of the surface energy balance equation, which was intended to circumvent the need for surface vapor content and surface resistance that cannot be measured by satellite techniques at the current stage. Assuming advection and light energy for photosynthesis to be negligible, the energy balance equation can be expressed as

$$R_n = G_s + H + LE \quad (3.4)$$

where R_n denotes the instantaneous net radiation (W m^{-2}) (typically at the satellite overpass), G_s denotes the soil heat flux (W m^{-2}), H denotes the sensible heat flux (W m^{-2}), and LE denotes the latent heat flux (W m^{-2}).

R_n is the sum of the net shortwave radiation and the net longwave radiation, minus the reflected downwelling longwave radiation from the land and atmosphere system:

$$\begin{aligned} R_n &= (1-\alpha)S_d + (L_d - L_u) - (1-\varepsilon)L_d \\ &= (1-\alpha)S_d + \varepsilon\varepsilon_a\sigma T_a^4 - \varepsilon\sigma T_s^4 \end{aligned} \quad (3.5)$$

where $(1-\alpha)S_d$ is the net shortwave radiation, $(L_d - L_u)$ is the net longwave radiation, and $(1-\varepsilon)L_d$ is the reflected downwelling longwave radiation. α is the surface albedo (dimensionless) which can be derived from visible and near-infrared bands of satellite images, and S_d is the instantaneous shortwave radiation (W m^{-2}), which is a function of extraterrestrial solar radiation, solar zenith angle, and atmospheric transmissivity at the satellite overpass. Given that S_d varies greatly with terrain, S_d will be simulated by Eqs. (2.2)-(2.4) in Chapter II. L_d and L_u are the downwelling and upwelling longwave radiation (W m^{-2}), respectively, which can be calculated using the Stefan-Boltzmann law shown in the last two terms of the second line in Eq. (3.5). ε_a is the atmospheric

emissivity (dimensionless) which is primarily a function of air temperature and vapor pressure (Brutsaert, 1975), ε is the surface emissivity (dimensionless) which can be estimated using an empirical relationship with the Normalized Difference Vegetation Index (NDVI) derived from the red and near-infrared bands of satellite images (Bastiaanssen et al., 1998a), σ is the Stefan-Boltzmann constant ($5.67 \times 10^{-8} \text{ W m}^{-2} \text{ K}^{-4}$), T_a is the atmospheric temperature (K) at the screen level which can be obtained from weather stations and distributed T_a maps across a study site can be produced by a multivariate regression analysis of longitude, latitude, and elevation, and T_s is the land surface temperature (K) which can be retrieved by the thermal infrared band(s) of satellite measurements.

In SEBAL, G_s is taken to be a fraction of R_n (Bastiaanssen, 2000):

$$G_s = R_n (T_s - 273.15) (0.0038 + 0.0074\alpha) (1 - 0.98\text{NDVI}^4) \quad (3.6)$$

Parameterization of H is a key component of satellite-based ET models. SEBAL assumes the difference between the air temperature at a reference height and the aerodynamic temperature at the land surface to be linearly correlated with LST. Coefficients of the linear relationship are determined by two extreme pixels selected by the operator from satellite images. For the hot pixel, LE is assumed to be zero; and H is thus equal to its available energy ($R_n - G$). For the cold pixel, H is regarded as zero and its LE is equal to the available energy. The H algorithm in SEBAL can be expressed as

$$H = \rho c_p \frac{dT}{r_{ah}} = \rho c_p \frac{(a_0 T_s + b_0)}{r_{ah}} \quad (3.7)$$

where ρ is the air density (kg m^{-3}), c_p is the air specific heat at the constant pressure ($\text{J kg}^{-1} \text{K}^{-1}$), dT is the near-surface temperature difference between z_1 ($=0.1 \text{ m}$) and z_2 ($=2 \text{ m}$), a_0 and b_0 are the scene-specific coefficients of linear regression, and r_{ah} is the aerodynamic resistance for heat transfer (s m^{-1}), which is a function of friction velocity u_* (m s^{-1}) and stability correction factors for momentum transfer ψ_m (dimensionless) and sensible heat transfer ψ_h (dimensionless):

$$u_* = ku_{200} / [\ln(\frac{200}{z_m}) - \psi_{m(200)}] \quad (3.8)$$

$$r_{\text{ah}} = \frac{1}{ku_*} [\ln(\frac{z_2}{z_1}) - \psi_{h(z_2)} + \psi_{h(z_1)}] \quad (3.9)$$

where k is the von Karman constant ($=0.41$), u_{200} is the wind velocity (m s^{-1}) at an assumed blending height (200 m), which can be inferred using the observed wind velocity at a weather station within a study area of interest, z_m is the roughness length for momentum transfer (m), which can be related to remotely sensed VI or Leaf Area Index (LAI), and expressions of ψ_m and ψ_h can be found in Allen et al. (2007).

In terms of the assumption regarding extreme pixels in SEBAL, a_0 and b_0 can be expressed as

$$a_0 = \frac{r_{\text{ah,hot}}}{\rho_{\text{hot}} c_p} \cdot \frac{R_{\text{n,hot}} - G_{\text{hot}}}{T_{\text{s,hot}} - T_{\text{s,cold}}} \quad (3.10)$$

$$b_0 = -\frac{r_{\text{ah,hot}}}{\rho_{\text{hot}} c_p} \cdot \frac{(R_{\text{n,hot}} - G_{\text{hot}})T_{\text{s,cold}}}{T_{\text{s,hot}} - T_{\text{s,cold}}} \quad (3.11)$$

where subscripts hot and cold denote the hot and cold pixels, respectively. Since both ψ_m

and ψ_h are a function of H , Eqs. (3.7)-(3.11) have to be solved for in an iterative manner. After R_n , G_s , and H are computed, LE can be obtained using Eq. (3.4). EF ($=LE/(R-G_s)$) is made use of by SEBAL as a link between the instantaneous LE and the daily ET (in the unit of mm d^{-1}):

$$\text{ET} = 86400 \frac{R_{n,24} \text{EF}}{\lambda} \quad (3.12)$$

where λ is the latent heat of vaporization (J kg^{-1}). There are two critical assumptions in Eq. (3.12) that EF keeps fairly invariant throughout a day in the absence of significant regional advection (Bastiaanssen, 2000; Bastiaanssen et al., 1998a; Su, 2002). $R_{n,24}$ is a key variable for determining the magnitude of ET given an EF estimate. Parameterization of $R_{n,24}$ has been elaborated in Chapter II.

3.3.2. GG model

The GG model (Granger and Gray, 1989) is intended to estimate terrestrial actual ET at large spatial scales with routine meteorological data. This model was derived based on energy budget and aerodynamic principles, similar in form to the Penman equation but differs in the inclusion of the relative evaporation, G . ET in this model is driven primarily by two components: $R_{n,24}$ and the drying power of air, E_a :

$$\text{ET} = 86400 \left(\frac{\Delta G}{\Delta G + \gamma} \frac{R_{n,24}}{\lambda} + \frac{\gamma G}{\Delta G + \gamma} E_a \right) \quad (3.13)$$

$$E_a = f(u)(e_a^* - e_a) \quad (3.14)$$

where e_a^* is the saturated vapor pressure at the daily average temperature (kPa), e_a is the

daily average vapor pressure (kPa), and $f(u)$ is a function of wind speed:

$$f(u) = \frac{0.622k^2 \rho u}{P \left[\ln\left(\frac{z-d}{z_m}\right) \right]^2} \quad (3.15)$$

where P is the atmospheric pressure (Pa), u is the wind velocity at the reference height (m s⁻¹), z is the reference height (m), and d is the zero plane displacement (m). $f(u)$ does not call for stability corrections at daily and longer time steps by assuming that the atmospheric stability is, on average, neutral.

Granger and Gray (1989) related G to a concept of the relative drying power of air, D , through experimental data, and established an exponential relationship between G and D :

$$G = \frac{1}{1 + ae^{bD}} \quad (3.16)$$

$$D = \frac{E_a}{E_a + R_{n,24} / \lambda} \quad (3.17)$$

where a and b are the regression coefficients. In the first formulation (1989) of the GG model (hereinafter GG 1989), a is 0.028 and b is 8.045 derived from 158 experimental samples. As indicated by Granger and Gray (1989), the lack of measurements from the wet environments ($G > 0.7$) does not allow for the development of a functional relation between D and G that can be treated with confidence over the full range of G . As a result, its utility should be further investigated when applied to a broad range of soil wetness conditions and landscapes. Granger (1996) modified Eq. (3.16) with an updated set of a and b of 0.2 and 4.902, respectively (hereafter GG 1996):

$$G = \frac{1}{0.793 + ae^{bD}} + 0.006D \quad (3.18)$$

Sensitivity analysis of GG 1989 was performed in order to examine how inputs of the GG model affect the resulting ET estimates (Fig. 3.1b). Results suggest that a 10% increase in $R_{n,24}$ can lead to about an 18.4% increase in the ET estimates. A 10% increase in G , D , and daily mean temperature can result in an 8.0 %, -3.8%, and -0.7% variation in the resulting ET, respectively. It is clear that G is positively correlated with ET estimates. Re-establishing the functional relationship between D and G is critical to improving the spatial representation of the ET time series estimates. Fig. 3.2 shows the flow chart of the GG model.

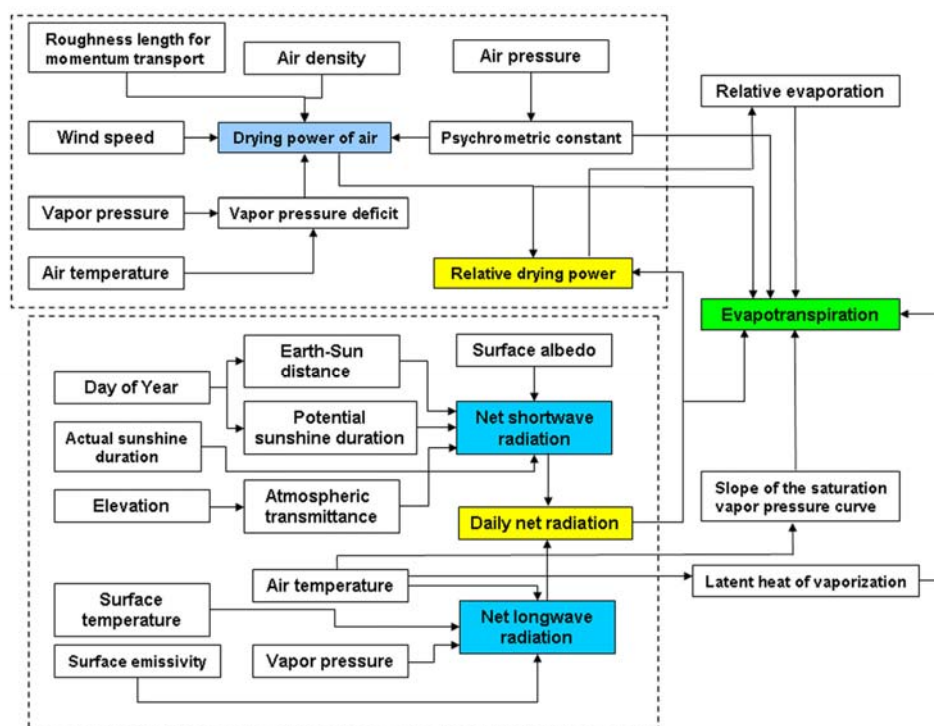


Figure 3.2 Flow diagram of inputs and outputs of the GG model.

3.4. Application

3.4.1. Study site

Validation of the proposed integration method was conducted in the Baiyangdian watershed in North China (illustrated in Section 2.2.1 in Chapter II). It is noted that the Bouchet's CR between potential and actual evaporation (Bouchet, 1963) has been shown to be valid over the non-humid region in North China under the condition of elevation lower than 1000 m (Qiu et al., 2004; Yang et al., 2006; Yu et al., 2009). The characteristic of this watershed creates an opportunity to interpret and estimate watershed/regional actual ET in a different way.

3.4.2. Data description

A data set encompassing hydrometeorological data, remote sensing data, DEMs, and ancillary parameters in year 2007 was built to simulate daily ET by SEBAL and GG, and ET time series by the evaporative fraction method, the crop coefficient method, and the proposed integration method.

Hydrometeorological data

Meteorological data on a daily basis, e.g., daily maximum, minimum, and mean T_a , e_a , and P were obtained by averaging *in-situ* measurements from 18 weather stations within the study watershed (see Fig. 2.1a) and Section 2.2.2. Maps of these variables were produced using multiple linear regression analysis of longitude, latitude, elevation, and observations. In simulation of instantaneous surface fluxes by SEBAL,

instantaneous P , T_a and e_a observed at 16 weather stations were obtained by a sinusoidal model which used 4 observations of the respective variable observed at 2:00 a.m., 8:00 a.m., 14:00 p.m., and 20:00 p.m. throughout the day to infer the values at the time of satellite overpass. For Baoding and Fuping stations, the instantaneous counterparts were estimated by linear interpolation between two measurements on an hourly basis. Instantaneous u was linearly interpolated by two observations recorded on the hour for the 18 weather stations.

Observations of precipitation on a daily basis from 18 weather stations, streamflows at 12 gauging stations, reservoir storage change, and groundwater observation well levels in the watershed were jointly used to estimate water budget for the entire watershed in year 2007. Daily pan ET measurements from 18 weather stations were used to interpret trends in the ET time series estimates.

Remote sensing data

Remote sensing data for this study were obtained from MODIS land and atmospheric data products (<http://modis.gsfc.nasa.gov/>). MODIS data products involved in this study are shown in Table 3.1. Section 2.2.2 details the composition of each MODIS data product.

Table 3.1 MODIS data products used in this study and their associated properties

Name	Used variables	Temporal resolution	Spatial resolution	Platform
MOD11_L2	LST & Emissivity	5 Min	1000 m	Terra
MOD11A1	LST & Emissivity	Daily	1000 m	Terra
MYD11A1	LST & Emissivity	Daily	1000 m	Aqua
MCD43A3	Albedo	16days	500 m	Terra & Aqua
MOD13A2	NDVI	16days	500 m	Terra
MOD15A2	Leaf area index	8 days	1000 m	Terra
MOD04_L2	Aerosol depth	Daily	10 km	Terra

DEM and ancillary data

SRTM DEMs for the study site were obtained from the U.S. Geological Survey Earth Resources Observation and Science Center. Terrain variables (e.g., slope, azimuth, and elevation) can be extracted from DEMs for use in simulating terrain-dependent S_d for SEBAL and simulating $S_{in,24}$ for SEBAL and GG on the basis of the algorithms presented in Chapter II. Ancillary parameters comprised day of year (DOY) and satellite overpass time.

3.4.3. Daily ET modeling by SEBAL

As LST is the most critical remotely sensed variable required by SEBAL, we selected one day having LST of the best quality from MOD11_L2 in each month in year 2007 for modeling surface fluxes and then re-establishing relationships between D and G . It is noted that for some months in spring and winter (e.g., January, February, March, November, and December) and rainy season in summer (e.g., June, July, and August), the scarcity in usable MODIS LST products due to cloud contamination makes reconstruction of ET time series only by satellite-based models infeasible. Images covering the study watershed obtained in January, February, March, November, December, and July were inevitably contaminated by clouds to varying degrees.

Correctly selecting the hot and cold pixels is critical in SEBAL. However, these extremes are visually identified by the operator from images. We selected the extreme pixels by virtue of scatterplots of LST and NDVI (Fig. 3.3) and a land use map for the study watershed (see Fig. 2.1b).

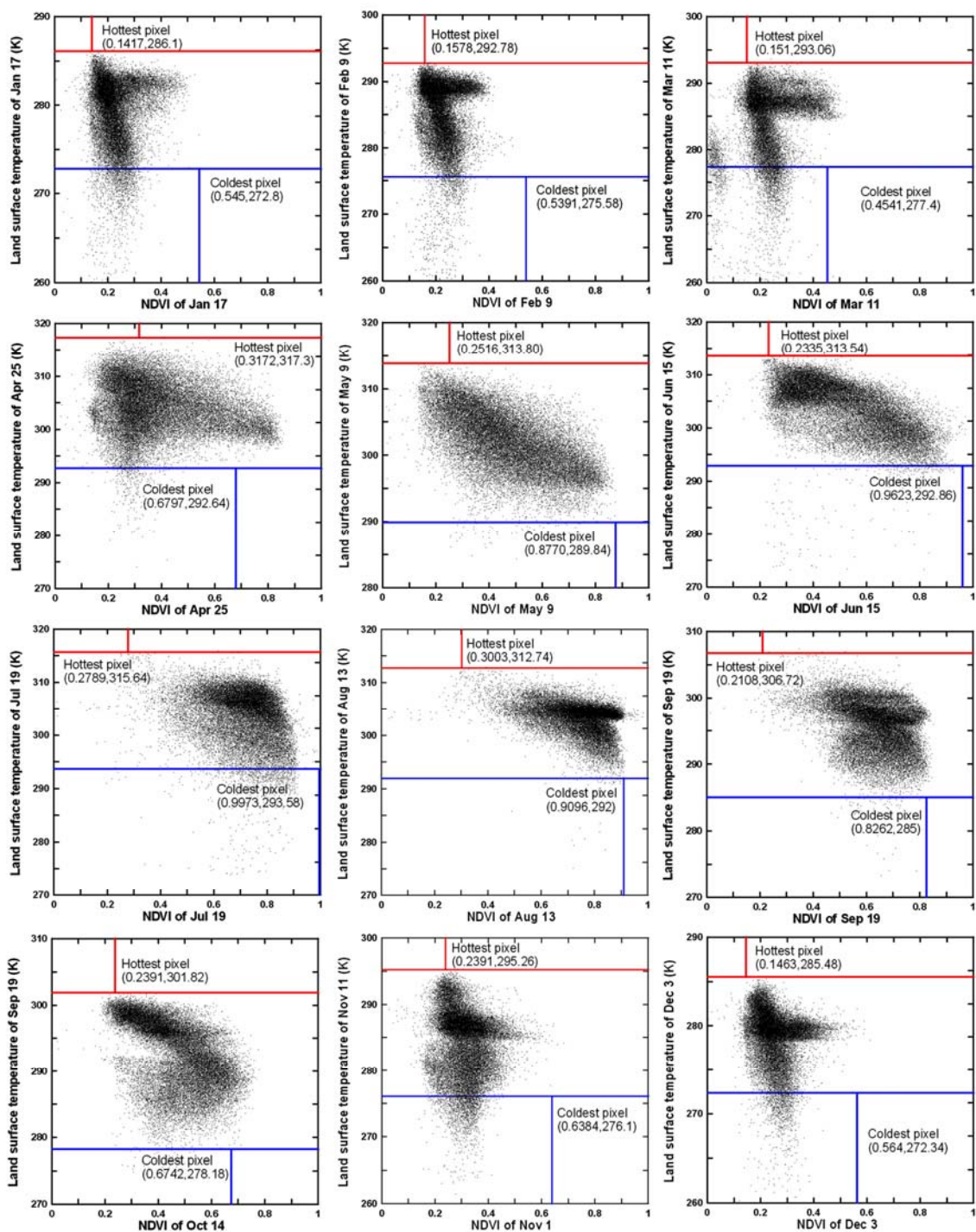


Figure 3.3 Selection of hot and cold pixels from the contextual map of NDVI and LST for simulating daily ET by SEBAL under cloud-free days.

The hot pixel was selected by the following procedures: (1) pixels with a group of high temperature values and relatively low NDVI values were selected and saved; (2) the land cover map was used to discriminate land cover types for these selected hot pixel candidates. It appears that the hot pixel tends to occur on the bare soil surface, sandy land, or dry land; and (3) the hot pixel candidates which corresponded to these land covers were refined, from which the one with the highest LST value was taken as the hot pixel.

Regarding the selection of the cold pixel, it is shown in Fig. 3.3 that a small group of pixels scattered on the lower portion of these scatterplots are indicative of contamination by clouds and sloping terrains. To eliminate the erroneous effects of LST retrievals on extreme cold pixel selection, the MOD11_L2 LST quality product was used to exclude all pixels that may be influenced by clouds or other factors. Then, the pixel with the lowest temperature value could be regarded as the cold pixel. Combining the selected extremes with other variables described in Section 3.3.1, daily ET for typical cloud-free days was simulated based on the SEBAL algorithm.

3.4.4. Reconstruction of the GG model

ET estimates from SEBAL constitute input to the GG model to invert G based on Eq. (3.13). D values were calculated based on Eq. (3.17) using meteorological forcing and remotely sensed albedo and LAI. Scatterplots of D and G on typical cloud-free days are shown in Fig. 3.4. Table 3.2 provides statistics of regression analysis.

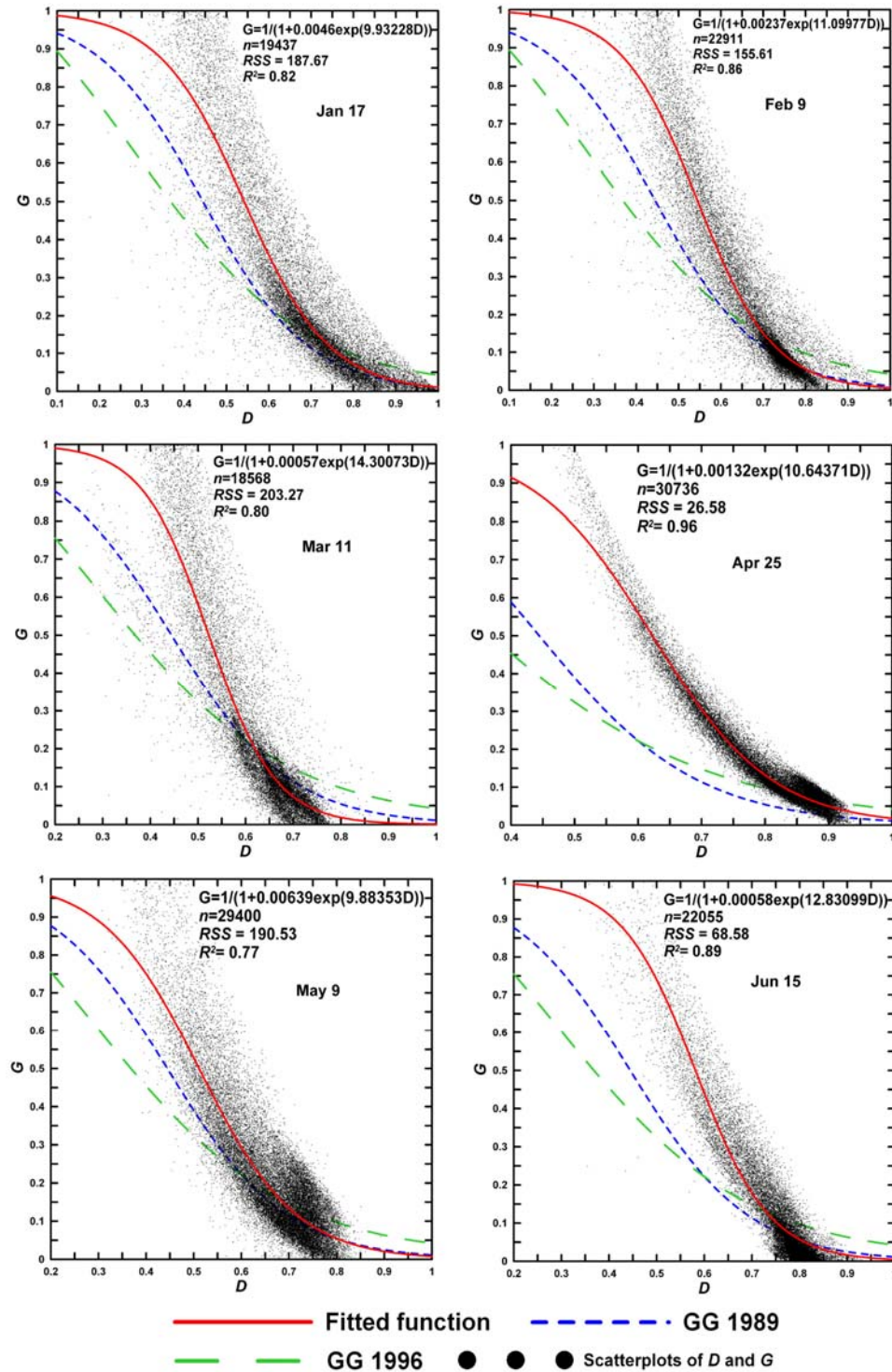


Figure 3.4 Calibration of the functional relationship between D and G in the GG model using SEBAL-based ET estimates for the Baiyangdian watershed on 12 cloud-free days in year 2007, with showing GG 1989 and GG 1996.

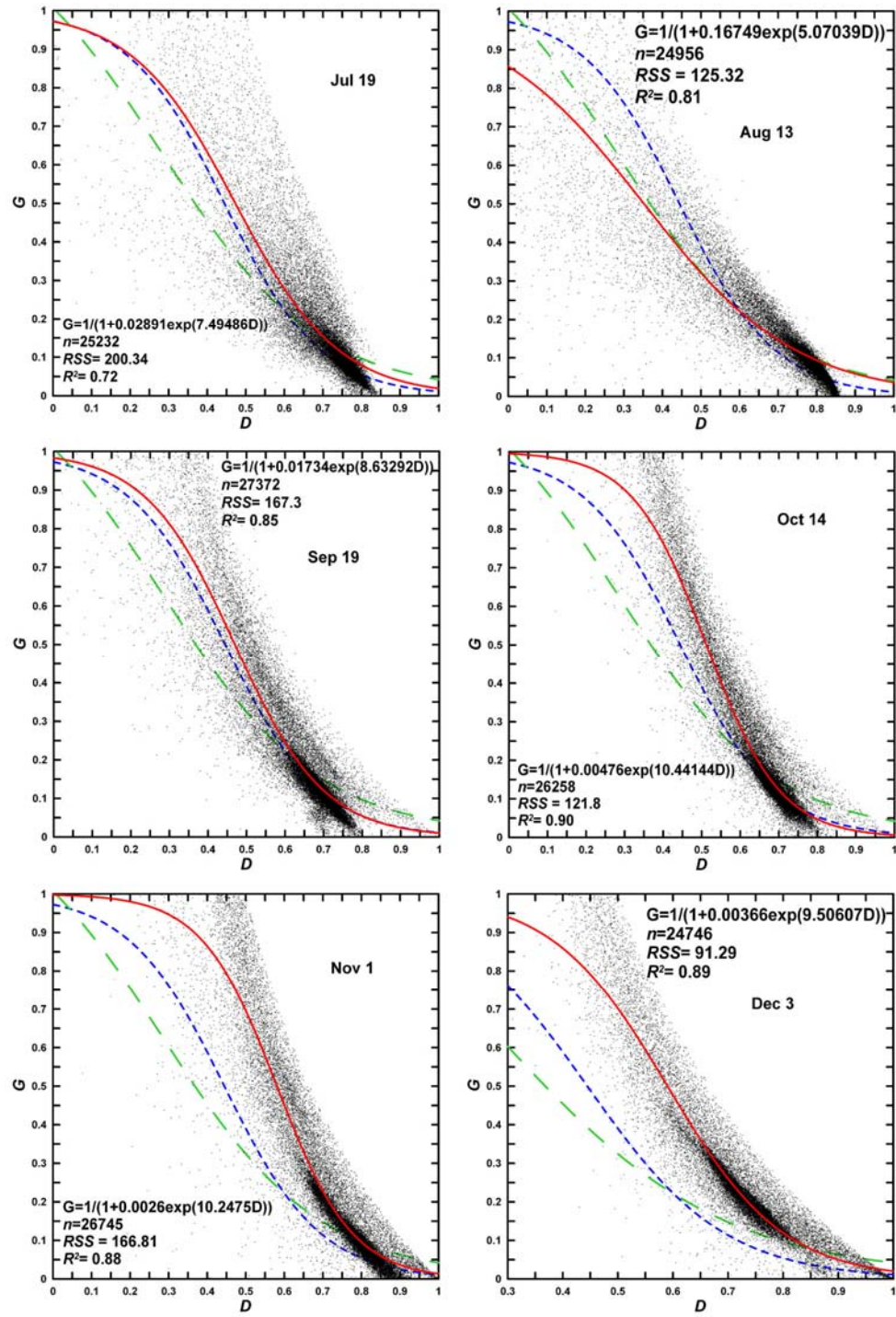


Figure 3.4 Continued.

Table 3.2 Regression coefficients of the exponential relationship between D and G and associated statistics (n is the number of samples, RSS is the residual sum of squares and R^2 is the coefficient of determination)

Date	a	b	n	RSS	R^2
Jan 17	0.00460	9.93228	19437	187.67	0.82
Feb 9	0.00237	11.09977	22911	155.61	0.86
Mar 11	0.00057	14.30073	18568	203.27	0.80
Apr 25	0.00132	10.64371	30736	26.58	0.96
May 9	0.00639	9.88353	29400	190.53	0.77
Jun 15	0.00058	12.83099	22055	68.58	0.89
July 19	0.02891	7.49486	25232	200.34	0.72
Aug 13	0.16749	5.07039	24956	125.32	0.81
Sep 19	0.01734	8.63292	27372	167.30	0.85
Oct 14	0.00476	10.44144	26258	121.80	0.90
Nov 1	0.00260	10.24750	26745	166.81	0.88
Dec 3	0.00366	9.50607	24746	91.29	0.89

Results clearly show that G decreases nonlinearly with increasing D , which is consistent with the finding reported by Granger and Gray (1989). They used the actual ET calculated as the residual term in a soil water balance model applied at field sites to derive the relationship between D and G . The relationship between D and G is generally curvilinear and fitted using an exponential function. The highest and lowest R^2 were found to be 0.96 on April 25 and 0.77 on May 9, respectively (Table 3.2). It is observed that with decreasing D (e.g., $D < 0.6$), the points tend to be scattered. This tendency may be as a result of the weakening CR effect at high altitudes, which suggests that the SEBAL-based ET estimates are of more variability than the GG model. Nevertheless, the relationship between D and G can be essentially depicted by the fitted functions.

3.5. Results and discussion

ET time series on a daily basis from the evaporative fraction method, the crop

coefficient method, and the proposed integration method for the study watershed in year 2007 were generated. There were in total 28 cloud-free days selected for generating daily evaporative fractions and crop coefficients. The simulated daily evaporative fractions and crop coefficients were then employed to extrapolate daily counterparts and ET for all cloudy days based on Eq. (3.1) and Eq. (3.2), respectively. The integration method yielded ET time series in terms of the modified relationship between D and G (Table 3.2) and routine meteorological data.

3.5.1. ET time series from the evaporative fraction method

Evaporative fractions and crop coefficients of the entire watershed on the 28 cloud-free days are shown in Fig. 3.5. The evaporative fraction curve varies irregularly throughout the year, with a mean of about 0.518. This demonstrates that there was no regular variation trend in EF during the year. The daily EF was, to a large extent, influenced by the combined effect of soil moisture and energy availability, and vegetation and metrological states on that day, considerably varying from one day to another. The evaporative fraction method suffers significantly from theoretical and technical limitations in producing ET time series.

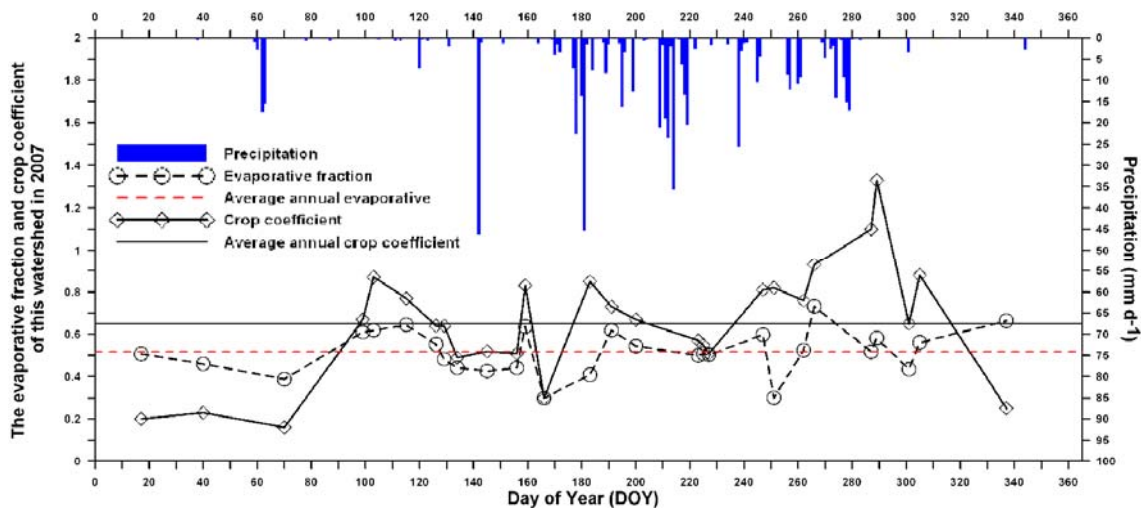


Figure 3.5 Evaporative fractions and crop coefficients from SEBAL of the Baiyangdian watershed on 28 cloud-free days in year 2007, with showing corresponding daily precipitation and mean values of these estimates.

First, usable images, in particular LST products, were rarely obtained in January, February, March, November, and December, with only one day in each month being selected for EF and crop coefficient simulation. In the worst case, there are no usable images available for routine ET estimation, especially during rainy season when soil water content is ample and the actual ET is likely to be large between rain events. Therefore, the use of the satellite-deduced EF on a cloud-free day in each month to extrapolate ET time series for the month would lead to large uncertainties in the resulting ET. The applicability of the evaporative fraction method depends largely on the frequency and distribution of images acquired.

Second, one may obtain several scenes of usable images within consecutive cloud-free days (e.g., August 11, 13, and 15 in this study) when the EF for the entire watershed probably shows similar patterns. These closely-spaced images, however,

cannot capture variations in EF for a relatively longer period during rainy season which is likely to exhibit considerable variations in soil moisture, energy availability, and ET. Hence, there is somewhat of a tradeoff between the frequency of usable images and their distribution over time. This means that even though sufficient usable images are obtained, such images are probably centered on a short period of cloud-free days exhibiting similar EF patterns and magnitudes. As such, the evaporative fraction method does not seem to be capable of estimating ET for a longer period of time when EF and ET change greatly over time. The case of sufficient satellite images regularly spaced over time rarely occurs in applications.

Third, there exist large differences in EF during rainy season (e.g., from May to September in this study). For instance, the estimates of EF for the entire watershed were 0.441, 0.636, and 0.300 on June 5, 8, and 15, respectively. The use of any of the EF estimates to extrapolate ET for a period centered on the day of image acquisition would give rise to large uncertainties.

In summary, EF estimates for the study watershed are significantly variable over time and space. The usefulness of the evaporative fraction method depends largely on the quantity of usable satellite images and the distribution of image acquisition dates, and variations in energy and soil moisture availability. Uncertainties in the evaporative fraction method would introduce gross errors in the resulting ET time series at watershed scales.

3.5.2. ET time series from the crop coefficient method

Reference ET was first calculated using Eq. (3.3) at 18 weather stations on a daily basis. Variations in daily reference ET, pan ET, and precipitation for the Anxin, Fuping, Yixian, and Anguo stations in year 2007 are shown in Fig. 3.6. It is illustrated that trends in the daily reference ET are highly consistent with that of pan ET. Moreover, the reference ET and pan ET during rainy season (June to August) are both relatively lower than during May, showing general decreasing trends in the rainy season. The trends in the reference and pan ET during rainy season can be ascribed to essentially large $R_{n,24}$ but relatively smaller $e_s - e_a$ compared with May.

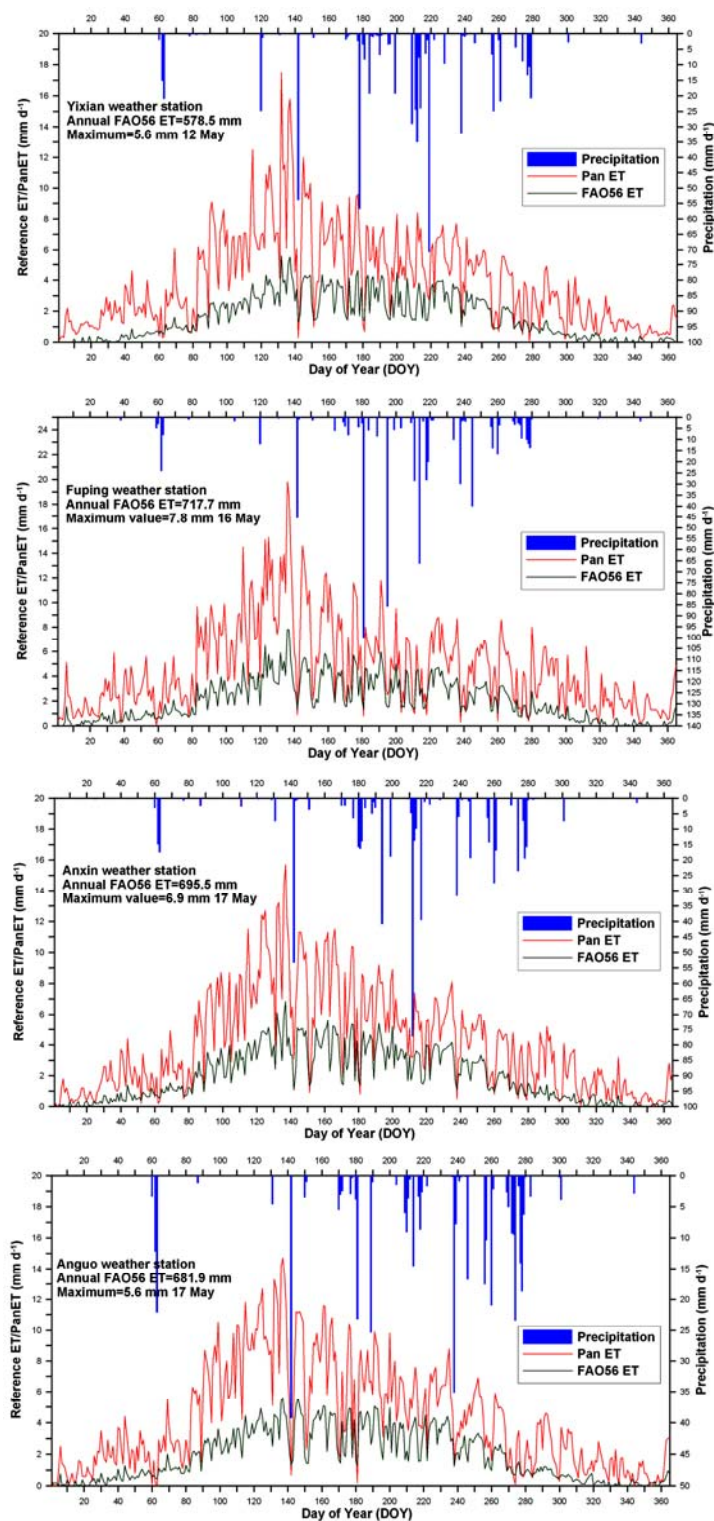


Figure 3.6 Variations in the FAO56-based reference ET, pan ET, and precipitation of the Baiyangdian watershed for the Anxin, Fuping, Yixian, and Anguo stations in year 2007.

It is observed that there does not exist a distinct inter-monthly low-and high-variation in the crop coefficient throughout the year, showing a mean crop coefficient of 0.651 (Fig. 3.5). It is apparent that the crop coefficient of the entire watershed from January to March is relatively small because of the underdeveloped vegetation and crops combined with small $R_{n,24}$. With increasing irrigation water supply in the four irrigation districts in April, water consumption by crops increased dramatically and therefore resulted in a marked increase in the crop coefficient. The crop coefficient continued increasing during the growing seasons and peaked in July, showing the largest value of around 0.85 on July 2.

It should, however, be noted that the estimated crop coefficients shown in August appear to be counter-intuitively smaller than September and October, which is not consistent with field experiment results from Chen et al. (1995) over the North China Plain. The erroneous crop coefficient estimates may be due to an overestimation of the reference EF in August and/or an underestimation of the reference ET in September and October. It seems difficult to construct a consistent and realistic crop coefficient curve from a few scenes of satellite images especially during periods of rapid vegetation change. In this case, a more frequent image interval may be desirable (Allen et al., 2007). However, it rarely comes true in applications.

In summary, limited usable satellite images only cover a fraction of the crop coefficient cycle during a year. The crop coefficient method cannot offer a realistic and consistent crop coefficient curve due primarily to insufficient satellite images especially during periods of rapid development of vegetation and crops.

3.5.3. ET time series from the integration method

ET time series at the watershed scale from the evaporative fraction method, the crop coefficient method, and the proposed integration method are shown in Fig. 3.7. It should be noted that the estimates of the ET time series from the evaporative fraction and crop coefficient methods were produced by extrapolating corresponding variables from 28 discrete image dates based on Eq. (3.1) and Eq. (3.2), respectively. In contrast, the ET time series from the integration method was generated on a daily basis.

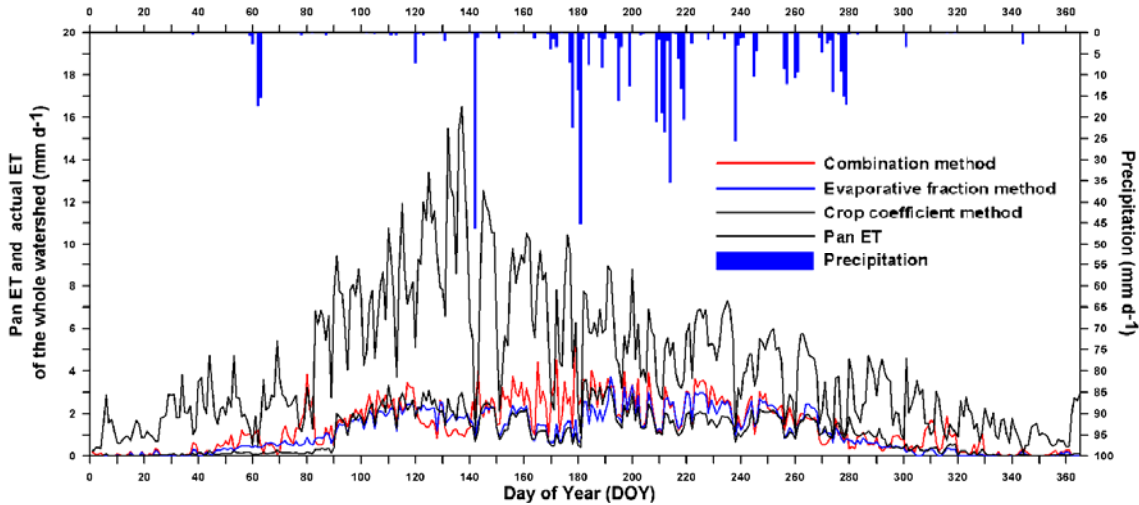


Figure 3.7 ET Time series from the evaporative fraction method, the crop coefficient method, and the proposed integration method of the Baiyangdian watershed in year 2007, showing corresponding observations of daily precipitation and pan ET.

In general, the ET time series from the three methods were lower than the corresponding pan ET except rainy days when the pan ET data were suspected to be systematically overestimated and thus set to zero.

It is interesting to note that exploring the relationship between pan evaporation and actual terrestrial ET at the watershed scale on a daily basis would help clarify and test the validity of different approaches to yielding ET time series. Some published studies indicated that there exists a CR across the study areas (Qiu et al., 2004; Yang et al., 2006; Yu et al., 2009). It is therefore logical that if the generated ET time series and the corresponding pan ET measurements show a complementary behavior at watershed scales, this would lend support to the credence of the proposed method. Fig. 3.8 graphically displays data pairs of the estimates of daily ET from the three tested methods of the entire watershed against pan ET observations in an ascending order of pan ET for days with $R_{n,24} > 100 \text{ W m}^{-2}$. The inclusion of only days with $R_{n,24} > 100 \text{ W m}^{-2}$ was intended to ensure a similar radiative energy condition so as to unravel the underlying CR features.

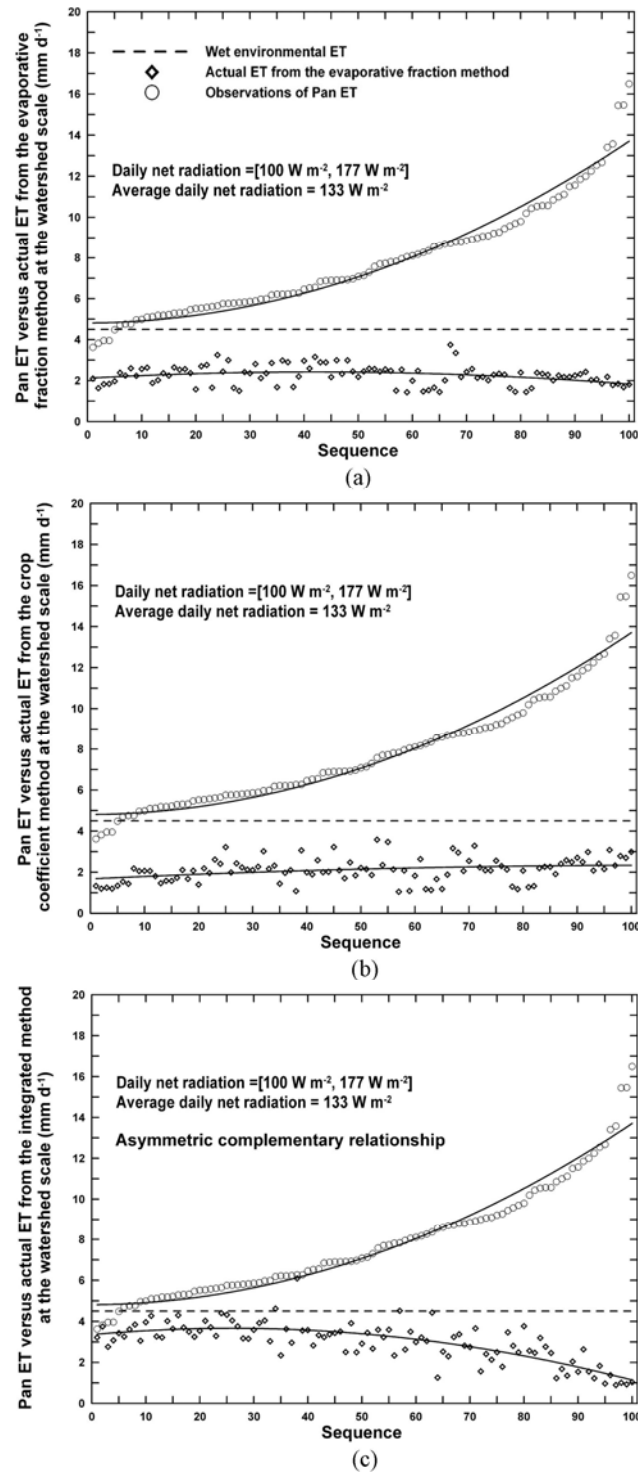


Figure 3.8 Observations of the pan ET and actual ET estimates from the evaporative fraction method (a), the crop coefficient method (b), and the proposed integration method (c) of the Baiyangdian watershed for days with $R_{n,24} > 100 \text{ W m}^{-2}$.

Results suggest that the pan ET observations and the simulated daily actual ET from the integration method show a pronounced asymmetric CR. An increase in pan ET generally evidences a decrease in the actual ET estimates. In particular, for days with relatively larger pan ET observations emerging in mid May, the simulated actual ET from the integration method was relatively low. This might be related to relatively large $e_s - e_a$ and u in the period, both contributing to a large magnitude of D and thus small G and actual ET in terms of the sensitivity analysis performed in Section 3.3.2. Conversely, for days with relatively small pan ET observations, overall, they show relatively large actual ET estimates, which approach the wet environmental ET of around 4.5 mm for this watershed (Fig. 3.8c). Relatively large soil moisture and energy availability and small D were likely to jointly contribute to the large estimates of actual ET for these days. It is apparent that the pan ET observations and the actual ET estimates from the evaporative fraction and the crop coefficient methods do not diverge from each other, which could be considered a significant limitation in the two methods of producing ET time series at watershed scales.

The asymmetric CR from the integration method is essentially in accord with what Kahler and Brutsaert (2006) found. They demonstrated that the scaled pan ET and locally observed actual ET at the daily timescale show a distinct CR. It is noted that although pan ET observations in our study were not scaled, the inclusion of pan ET on days with $R_{n,24} > 100 \text{ W m}^{-2}$ and the corresponding actual ET from the integration method of the entire watershed can generally exhibit a CR.

It is highlighted that the modified GG model departs from GG 1989 and 1996 in

adjusting the D and G relationship by satellite-based ET estimates for different time periods (e.g., one month). However, GG 1986 and 1996 take advantage of only one set of D and G relationship. The attribute of the modified GG model makes it show more characteristics of energy balance-based approaches.

It can be concluded that evolution of ET estimates from the proposed integration method seems to be more reasonable than other extrapolation techniques. The finding that the energy balance-based method tends to yield complementary features between the actual ET estimates and the pan ET observations lends support to the CR at watershed scales and daily timescale. By contrast, ET time series from the evaporative fraction and crop coefficient methods do not seem to be able to produce similar complementary features as does the integration method. Simply extrapolating or interpolating EF and crop coefficients based on a few scenes of images which are probably spaced irregularly over time would destruct the temporal patterns of ET time series at watershed scales.

3.5.4. Validation

Daily ET validation versus SEBAL

To evaluate the performance of the modified GG model, it was used to produce daily estimates of ET for typical cloud-free days which were not involved in the reconstruction of the D and G relationship. The estimates from the modified GG model were then compared with SEBAL-based ET predictions (Fig. 3.9 and Table 3.3). Results indicate that the modified GG model generally shows consistency with SEBAL, with $R^2 > 0.6$ (the highest R^2 was 0.8 on June 5) and relative error smaller than -22.8% (the lowest relative error was -0.5% on April 9) except August 15. However, GG 1989 generates systematically lower ET estimates, showing larger relative errors versus SEBAL. As for ET estimates on August 15, SEBAL may have provided relatively low ET estimates due to erroneously large H estimates across bare surfaces and built-up land (larger than $R_n - G$). As a result, estimates of ET for these areas were postprocessed into zero. This treatment makes the ET estimates of the entire watershed be underestimated. Given this specific case, the relative error with respect to SEBAL would be smaller than 35.4% on August 15.

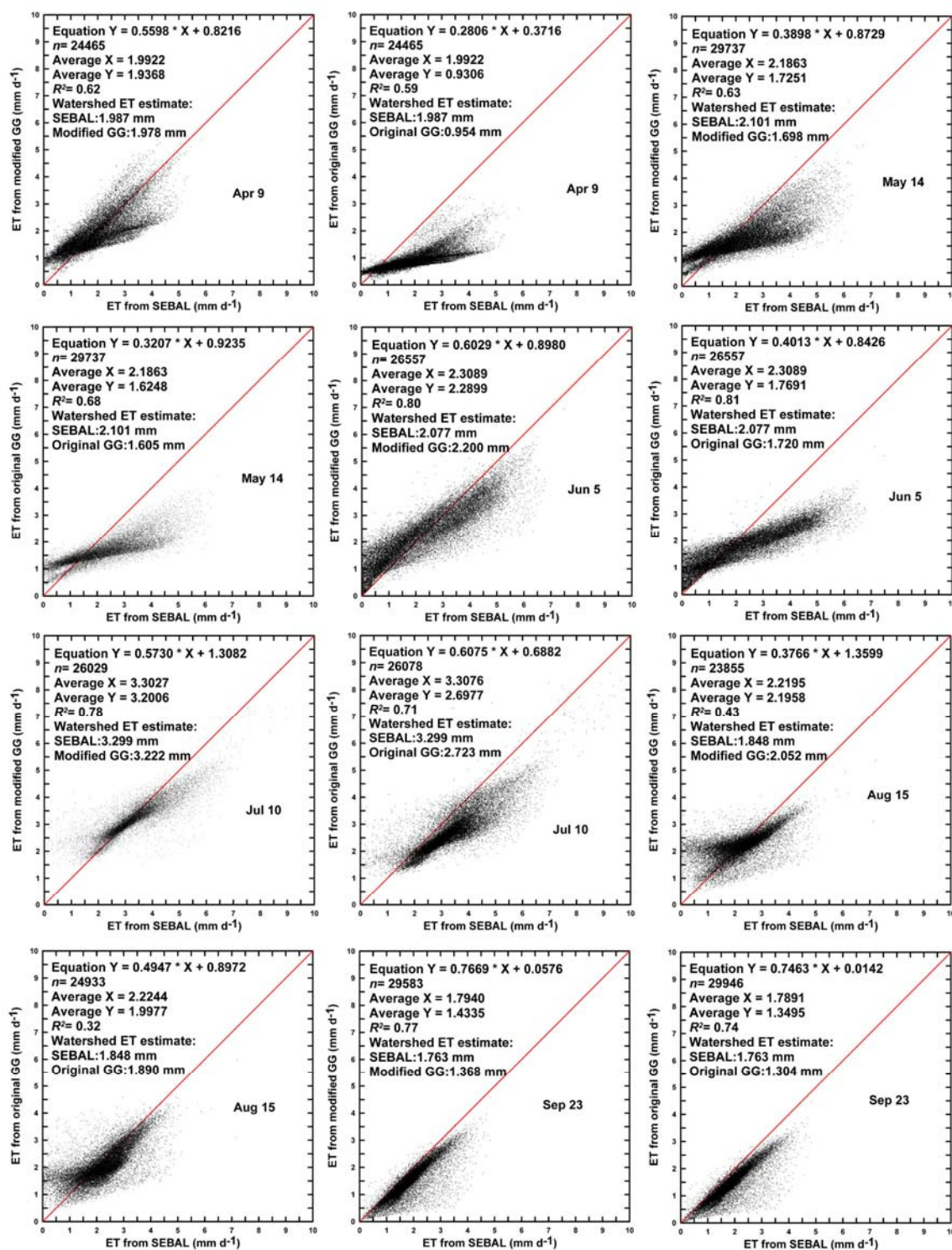


Figure 3.9 Comparison of predictions of daily ET from the modified GG and GG 1989 for the Baiyangdian watershed in year 2007 and SEBAL-based counterparts.

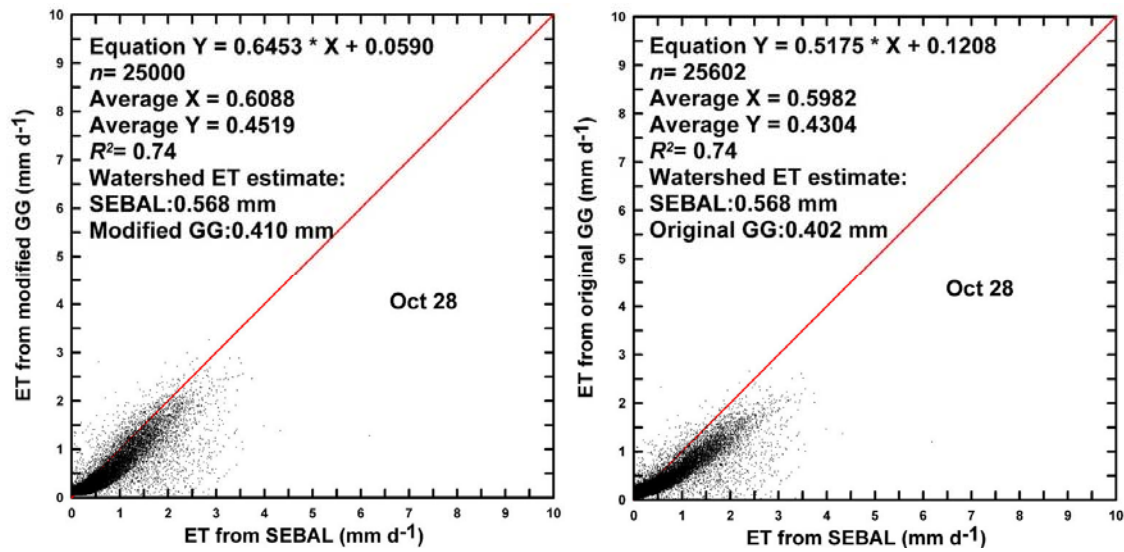


Figure 3.9 Continued.

Table 3.3 Statistics of the estimates of ET from GG 1989 and the modified GG model versus SEBAL-based ET predictions

Date	Original GG R^2	Modified GG R^2	Original GG ET (mm)	Relative error	Modified GG ET (mm)	Relative error	SEBAL ET (mm)
Apr 9	0.59	0.62	0.954	-4.6%	1.978	-0.5%	1.987
May 14	0.68	0.63	1.605	-23.6%	1.698	-19.2%	2.101
Jun 5	0.81	0.80	1.720	-17.2%	2.200	5.9%	2.077
Jul 10	0.71	0.78	2.723	-17.5%	3.222	-2.3%	3.299
Aug 15	0.32	0.43	1.890	2.3%	2.052	35.4%	1.848
Sep 23	0.74	0.77	1.304	-26.0%	1.368	-22.4%	1.763
Oct 28	0.74	0.74	0.402	-29.3%	0.410	-27.8%	0.568

Even though the GG model shows less variability in ET under the small D condition, the areal mean and essential spatial characteristic of the ET estimates can be generally captured by the modified GG model. Fig. 3.10 clearly illustrates that the modified GG model can offer a more realistic distribution of ET across the entire watershed compared with GG 1989 and GG 1996, showing a larger standard deviation of

0.909 mm and a closer mean watershed ET estimate of 2.943 mm on April 25, 2007 relative to the estimates from SEBAL. GG 1989 and 1996 systematically underestimate ET, indicating relatively lower averaged ET estimates of 1.453 mm and 2.359 mm, and standard deviations of 0.499 mm and 0.434 mm, respectively. The differences in the spatial distribution of ET between the modified GG, GG 1989 and 1996 suggests that GG 1989 and 1996 are not sensitive to variations in surface wetness, land cover, and actual ET at the study watershed. The deficiencies in GG 1989 and 1996 may result from a different hydrologic condition these models are based on. GG 1989 was derived for a semi-arid climatic zone of western Canada, which may have led to a relatively small magnitude of G and thus low predictions of ET. However, the modified relationship between D and G in this study was developed in a semi-humid climatic zone in North China, suggesting a relatively larger magnitude of G given the same D . The remotely sensed ET from SEBAL at watershed scales provides the potential to derive a more universal functional relationship between D and G .

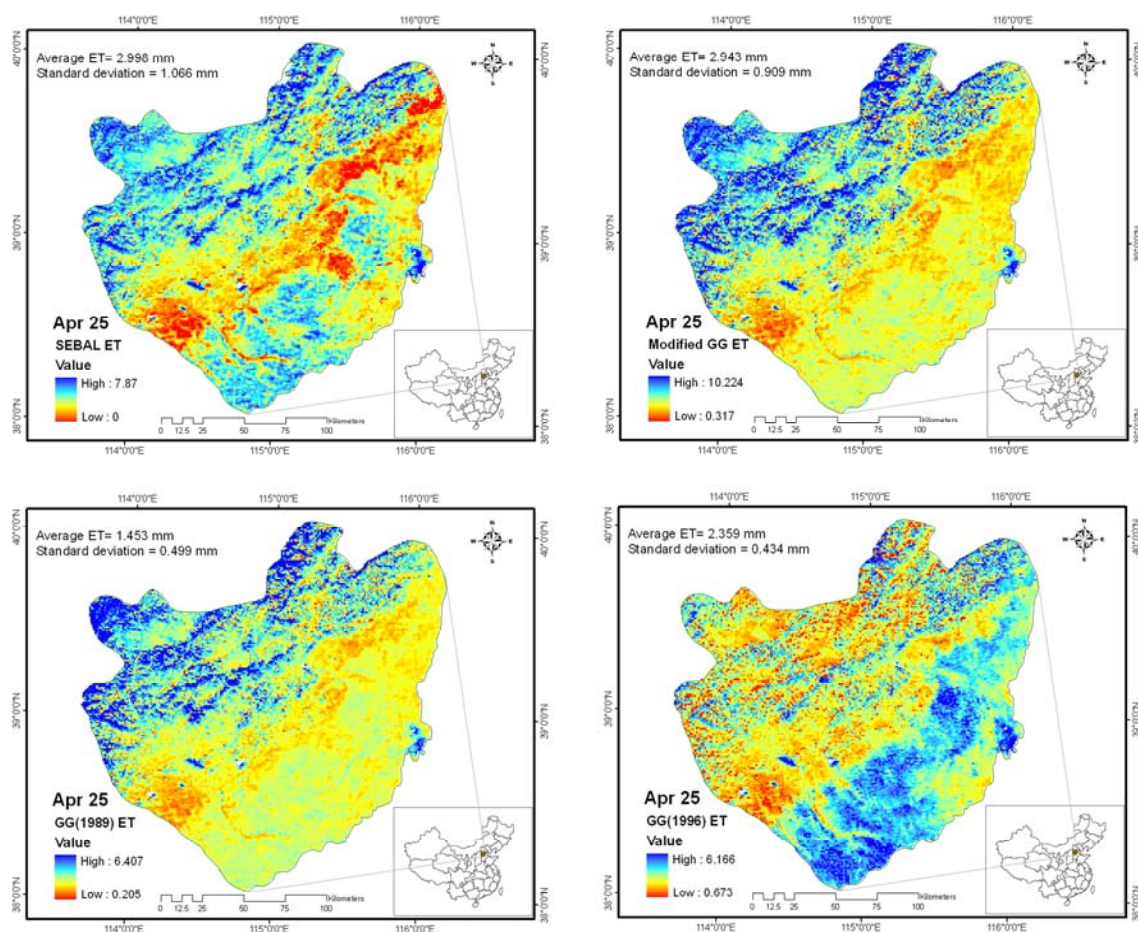


Figure 3.10 Spatial distributions of ET estimates from SEBAL, the modified GG model, GG 1989 and 1996 of the Baiyangdian watershed on April 25, 2007.

Annual ET validation based on water budget calculations

Hydrologic budget calculation for the Baiyangdian watershed in year 2007 was performed to independently generate annual ET for evaluating the overall accuracy of the ET time series estimates from the three techniques under investigation. The water balance equation plays a fundamental role in hydrologic modeling and has been widely used to perform model validation in satellite-based ET estimation (Bastiaanssen et al., 2002; Gao and Long, 2008; Mohamed et al., 2006):

$$ET = P - R - \frac{dS}{dt} - \frac{dG}{dt} - \frac{dW}{dt} \quad (3.19)$$

where P is the annual precipitation for a watershed (mm), which can be obtained from meteorological stations. The Thiessen polygon interpolation method was adopted to provide the areal mean precipitation. R is the streamflow (mm), which can be obtained from the gauging station at the outlet. dS/dt is the surface water storage change (mm), which can be estimated from records of large reservoirs in a watershed. dG/dt is the ground water storage change (mm), which can be estimated from phreatic records. dW/dt is the soil water storage change (mm). The ground outflow was neglected in Eq. (3.19) in this study.

The precipitation of the Baiyangdian watershed in year 2007 was estimated to be 570.0 mm on the basis of records of 18 weather stations. There have not been natural streamflow into the outlet, Baiyangdian Lake, due to enormous usage of water resources from irrigation, industrial and municipal use, and reservoir regulation in recent years. The change in surface water storage was roughly 10.2 mm from reservoir storage data within this watershed. The groundwater storage change was calculated using data from groundwater observation wells and the inverse distance weighting method, showing an increase of about 10 mm across the plain areas. In addition, the groundwater storage change over mountainous areas and the soil water storage change were assumed negligible. The actual ET of this watershed in 2007 was calculated as 549.8 mm. The evaporation method, crop coefficient method, and integration method show annual ET estimates with relative errors of -25.4%, -32.3%, and -7.5%, respectively.

3.6. Summary and conclusions

The lack of usable satellite images due to cloud contamination especially in rainy season and to the schedule of satellite significantly degrades ET time series predictions at watershed scales from satellite-based ET models. This limitation greatly hampered satellite-based operational ET estimation for use in estimating water consumption by agricultural crops, formulating irrigation scheduling, as well as facilitating water resources planning, allocation, and management.

In this chapter, we integrate the large-scale feedback GG model with satellite-based SEBAL, with the objective to generate ET time series of high spatial resolution and reasonable temporal resolution. The point here is that for a specific region where the complementary relationship between the pan ET and the actual ET shows to be valid, the ET time series would exhibit complementary features at certain timescales and spatial scales. It is expected that the integration method is capable of extending remotely sensed information on cloud-free days to days without usable images only using routine weather data.

Results suggest that the modified GG model that has incorporated remotely sensed information can reproduce ET of high resolution at watershed scales. GG 1989 and 1996 systematically underestimate areal ET at watershed/regional scales due to the deficiencies in the original relationship between D and G . The usefulness of the evaporative fraction method and crop coefficient method depends largely on the quantity of satellite images and their intervals. ET time series estimates from the three techniques for days with $R_{n,24}$ larger than 100 W m^{-2} and the corresponding pan ET show that the

integration method seems to exhibit an asymmetric complementary relationship at the watershed scale and daily timescale. Extrapolation or interpolation of evaporative fractions or crop coefficients derived from a few scenes of images to the whole time period would destruct the underlying complementary features which would have shown. Validation based on hydrologic budget calculations performed in the Baiyangdian watershed in North China indicates that the proposed integration method generates an annual estimate of ET with the smallest error amongst all techniques being studied.

CHAPTER IV

A TWO-SOURCE TRAPEZOID MODEL FOR ET (TTME) USING SATELLITE IMAGERY

4.1. Introduction

Combined with precipitation and runoff, ET, a key component in the water cycle, determines the water availability and partitioning of turbulent energy fluxes on the Earth's surface (McCabe and Wood, 2006). Satellite remote sensing of surface fluxes and soil water content at a variety of spatial and temporal scales has emerged since the attraction and utility of the thermal infrared remote sensing was recognized in the 1980s (Kalma et al., 2008). This has resulted in a series of modeling schemes with varying mechanisms and degrees of complexity. In general, they can be categorized into the one-source scheme (Bastiaanssen et al., 1998a; Su, 2002) and the two-source scheme (Kustas and Norman, 1999; Norman et al., 1995), differing in treating a landscape as a mixture of soil and vegetation or independent sources of energy turbulent fluxes.

There is another type of modeling scheme unique in interpreting the contextual relationship between remotely sensed VI or NDVI and radiative temperature (T_{rad}). VI and NDVI have been widely recognized as promising indicators to capture vegetation information on the land surface. T_{rad} , as a proxy reflecting water and heat states at the interface between the land surface and the lower atmosphere, has been used to deduce ET and surface soil moisture. Previous studies have shown that in such a space, a high NDVI value generally corresponds to a low T_{rad} value for a pixel where large

evaporation rates would occur and *vice versa*. If there exist sufficient pixels representing a broad range of soil wetness and f_c in an image, and outliers (e.g., clouds, sloping terrain, and shading) are removed, the envelope of these pixels could constitute a physically meaningful triangle or trapezoid.

The triangle or trapezoid model infers evaporative fraction within a modeling domain, without parameterizing the networks of aerodynamic and surface resistances involved in one-source and two-source models that require excessive data and/or intractable parameters on vegetation physiology and micrometeorology, e.g., vegetation height, leaf area index, leaf size, and wind velocity at a height above the soil surface (Carlson et al., 1994; Carlson et al., 1995b; Carlson and Ripley, 1997; Gillies and Carlson, 1995; Gillies et al., 1997; Jiang and Islam, 1999; Jiang and Islam, 2001; Jiang and Islam, 2003; Lambin and Ehrlich, 1996; Nemani et al., 1993; Nemani and Running, 1989; Owen et al., 1998; Price, 1990).

Jiang and Islam (2001) and Sandholt et al. (2002) proposed a similar triangle scheme to estimate EF/Temperature Vegetation Dryness Index (TVDI) over large areas. Venturini et al. (2004) and Batra et al. (2006) applied Jiang and Islam (2001)'s model to National Oceanic and Atmospheric Administration-Advanced Very High Resolution Radiometer (NOAA-AVHRR) and MODIS sensors over South Florida and the Southern Great Plains, respectively, achieving a root mean square difference (RMSD) of the order of 50 W m^{-2} relative to ground-based latent heat fluxes. Wang et al. (2006) made use of the day-night LST difference (ΔT_s) instead of T_{rad} to constitute the NDVI- ΔT_s space to deduce EF over the Southern Great Plains under the Atmospheric Radiation

Measurement (ARM) Program, demonstrating a relative error of about 17% of EF retrievals. Stisen et al. (2008) substituted a non-linear power function interpolation for a linear interpolation of parameter ϕ describing the combined effects of the Priestley-Taylor parameter and surface temperature on EF in Jiang and Islam's model (2001), obtaining EF estimates with a bias of 0.13 and LE estimates with an RMSD of 41.45 W m^{-2} from the high-temporal resolution geostationary MSG-SEVIRI sensor.

In general, the triangle model was intended to overcome difficulties traditionally in (1) the initialization of the land surface model with atmospheric measurements that are not readily available over large areas, (2) complex parameterization of aerodynamic and surface resistances for water and heat transfer (Jiang et al., 2009), and (3) accurate absolute radiometric calibration of satellite-based T_{rad} retrievals (Carlson, 2007; Jiang and Islam, 2003).

However, there are several critical issues involved in the triangle framework: (1) most of triangle models pertain to the one-source scheme. This means their inability to discriminate vegetation transpiration from soil surface evaporation, which affects crop/vegetation water use by decreasing the air vapor pressure deficit and reducing the overall evaporative demand. In particular, water consumption by crops and transpired by vegetation are more meaningful in agricultural applications and assimilation into water balance models as a metric for root zone moisture conditions (Crow et al., 2008); (2) there exist completely wet surfaces evaporating at potential rates, and extremely dry surfaces with negligible ET in an image; (3) aerodynamic and physiological effects of the surface on H are not explicitly incorporated into the triangle scheme, and assumed to

be encapsulated in the NDVI- T_{rad} space; (4) determination of warm and cold edges involves subjectivity (Carlson, 2007). In particular, the cold edge is often poorly demarcated because of clouds, sloping terrain, and shading; and (5) there is an assumption of linearity of variations in EF across the NDVI- T_{rad} space.

There has been significant research performed to further derive information contained in the NDVI- T_{rad} space. Carlson (2007) comprehensively reviewed the development of the triangle scheme. Their simulations and observations show that there exist isopleths of soil surface moisture availability within the triangle space. Each isopiestic line has the same soil moisture availability and therefore soil temperature. However, interpretation of the triangle precludes analysis of the variability in water stress on vegetation. This means that within the triangle framework the temperature of vegetation is assumed to be invariant regardless of soil moisture content. Moran et al. (1994) developed a trapezoid framework to derive the crop water stress index (CWSI), which appears to be more suited for depicting the realistic contextual space of NDVI- T_{rad} but requires extensive ground-based measurements to determine four vertices of the trapezoid.

Nishida et al. (2003) proposed a two-source triangle model to separately parameterize EF for soil by an NDVI- T_s relationship-based method (Gillies et al., 1997) and EF for vegetation based on the complementary relationship. They showed EF and LE estimates with an RMSD of 0.17 and 45 W m⁻², respectively, at 13 AmeriFlux stations. However, the calculation of vegetation transpiration requires a wealth of data on vegetation physiology, which seems to impede application of the algorithm to large-scale

areas (Petropoulos et al., 2009). In addition, the derivation of the maximum soil surface temperature necessitates spatially homogeneous meteorological forcing given a study site. However, this model was applied to continental scales, which might exaggerate its applicability.

The objective of this chapter was to develop a robust and operational two-source ET model from satellite imagery based on the trapezoid framework. T_{rad} is partitioned into temperature components (T_s and T_c) using the concept of isopleths of soil surface moisture availability within the trapezoid framework. Evaporation from the soil surface and vegetation transpiration are then separately parameterized. The proposed model will be compared with one-source and two-source models using the same data set to provide an insight into the performance of a range of models. Section 4.2 presents the model formulation. Study site, data description, and variable derivation are shown in Section 4.3, followed by results in Section 4.4 and discussion in Section 4.5. Concluding remarks are given in Section 4.6.

4.2. Model formulation

4.2.1. Two-source scheme

The proposed Two-source Trapezoid Model for Evapotranspiration (TTME) partitions turbulent energy fluxes for a mixed landscape using a patch configuration, i.e., contributions of evaporation and transpiration to LE of a mixed landscape are weighted by f_c as

$$\text{LE} = f_c \text{LE}_c + (1 - f_c) \text{LE}_s \quad (4.1)$$

where subscripts c and s denote vegetation and soil hereafter, respectively; LE_c is the vegetation transpiration ($W\ m^{-2}$); and LE_s is the evaporation from the soil surfaces ($W\ m^{-2}$).

Energy balance equations for vegetation and soil components can be written as

$$Q = f_c Q_c + (1 - f_c) Q_s \quad (4.2)$$

$$R_n = f_c R_c + (1 - f_c) R_s \quad (4.3)$$

$$Q_c = R_c = H_c + LE_c \quad (4.4)$$

$$Q_s = R_s - G = (1 - c) R_s = H_s + LE_s \quad (4.5)$$

where Q is the available energy for a pixel ($W\ m^{-2}$); Q_c and Q_s are the components of available energy ($W\ m^{-2}$); R_n is the net radiation for a mixed pixel ($W\ m^{-2}$); R_c and R_s are the components of net radiation ($W\ m^{-2}$); H_c and H_s are the components of sensible heat flux ($W\ m^{-2}$); and G is the soil heat flux ($W\ m^{-2}$), which can be taken as a fraction (c) of R_s . The LE components can also be written in terms of EF components as

$$LE_c = Q_c EF_c \quad (4.6)$$

$$LE_s = Q_s EF_s \quad (4.7)$$

where EF_c and EF_s are the EF components. Substituting Eqs. (4.6) and (4.7) into Eq. (4.1) and dividing by Q yield a representative EF for a mixture of two sources in terms of the EF_c and EF_s components:

$$EF = f_c q_c EF_c + (1 - f_c) q_s EF_s \quad (4.8)$$

where q_c is equal to Q_c/Q and q_s is equal to Q_s/Q . Determination of EF and q components within the trapezoid framework will be elaborated in the following sections.

4.2.2. Interpretation of the trapezoid framework and decomposition of T_{rad}

TTME is based on the interpretation of the f_c - T_{rad} space. To parameterize LE_c and LE_s for a pixel, temperature components (T_c and T_s) will be first derived by interpreting the f_c - T_{rad} space. Fig. 4.1(a) illustrates the f_c - T_{rad} space and concepts of soil surface moisture isopleths superimposed, and Fig. 4.1(b) shows procedures of decomposing T_{rad} into T_c and T_s .

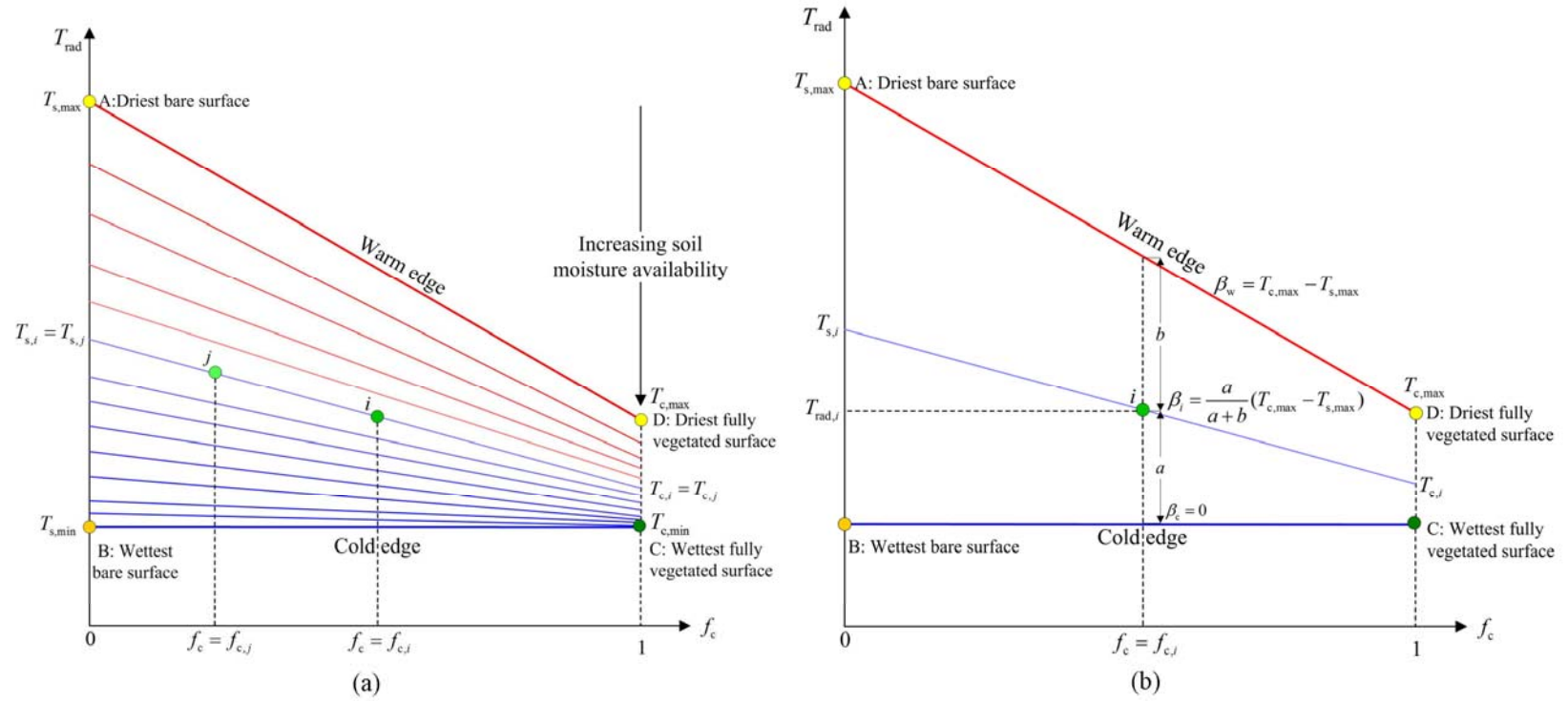


Figure 4.1 A sketch (a) of the trapezoid f_c - T_{rad} space involved in TTME and (b) illustrates the decomposition of T_{rad} into T_s and T_c .

Theoretically there are four critical points within the trapezoid framework ABCD. Point A ($f_c=0$, $T_{\text{rad}}=T_{s,\text{max}}$) represents the driest bare surface with the highest surface temperature $T_{s,\text{max}}$, point B ($f_c=0$, $T_{\text{rad}}=T_{s,\text{min}}$) represents the wettest bare surface with the lowest temperature $T_{s,\text{min}}$, point C ($f_c=1$, $T_{\text{rad}}=T_{c,\text{min}}$) represents the fully vegetated surface with the lowest temperature $T_{c,\text{min}}$, and point D ($f_c=1$, $T_{\text{rad}}=T_{c,\text{max}}$) represents the fully vegetated surface with the highest temperature $T_{c,\text{max}}$. Warm edge AD represents surfaces with the largest water stress for the full range of f_c ; thus LE of these surfaces is equal to zero. Analogously, cold edge BC represents surfaces without water stress at equilibrium ET rates, i.e., EF=1. It is noted that the warm and cold edges are the boundary conditions of TTME. An assumption of TTME is that the boundary conditions can theoretically be met, given certain meteorological conditions and surface characteristics. This is different from some satellite-based ET models that determine boundary conditions by selecting extreme pixels (Allen et al., 2007) or specifying limiting edges (Jiang and Islam, 2001) from satellite images.

In general, with increasing f_c , T_{rad} decreases because sunlit vegetation is generally cooler than sunlit bare soil (Carlson, 2007; Price, 1990). Numerous studies (Carlson et al., 1995a; Carlson et al., 1994; Price, 1990; Sandholt et al., 2002) have demonstrated that there exist isopleths of soil surface moisture availability/Temperature-Vegetation Dryness Index (TVDI) within the f_c - T_{rad} space. As superimposed in Fig. 4.1 (a), each isopiestic line reflects the same soil surface moisture availability and then has the same T_s . It is assumed that T_{rad} is a weighted sum of vegetation and soil temperatures (Anderson et al., 2007a; Norman et al., 1995)

$$T_{\text{rad}}(\theta) \approx f_c(\theta)T_c(\theta) + (1 - f_c(\theta))T_s(\theta) \quad (4.9)$$

$$f_c(\theta) = 1 - \left(\frac{\text{NDVI}_{\text{max}} - \text{NDVI}}{\text{NDVI}_{\text{max}} - \text{NDVI}_{\text{min}}} \right)^a \quad (4.10)$$

where θ denotes a viewing angle; a is a function of canopy architecture; NDVI_{max} and NDVI_{min} represent the maximum and minimum values of NDVI within a scene, respectively.

Considering variations in T_{rad} with f_c for each isopiestic line by re-writing Eq. (4.9) as $T_{\text{rad}}(\theta) \approx f_c(\theta)(T_c - T_s) + T_s$, it is clear that T_s and $T_c - T_s$ are the intercept and the slope of this function, respectively. As such, T_c is also the same for an isopiestic line. Variation in T_{rad} for each isopiestic line results essentially from the variation in f_c , the independent variable. T_s of a mixed surface can be deduced as T_{rad} of the bare surface on the same isopiestic line, i.e., the intercept; T_c of the mixed surface can be deduced as T_{rad} of the fully vegetated surface on the same isopiestic line, i.e., Eq. (4.9) intersecting with $f_c=1$.

It is assumed that the slope of each isopiestic line can be derived by interpolating the slope of the warm edge AD, i.e., $\beta_w = T_{c,\text{max}} - T_{s,\text{max}}$ and the slope of the horizontal cold edge BC, i.e., $\beta_c = 0$, in terms of the T_{rad} difference between the pixel and the cold edge, a , and the T_{rad} difference between the pixel and the warm edge, b (see Fig. 4.1 (b)). To that end, vertices of trapezoid ABCD play a critical role in configuring the isopleths of soil surface moisture availability and subsequently in decomposing T_{rad} in TTME.

4.2.3. Determination of theoretical boundary conditions of TTME

Determination of $T_{s,max}$

The idea is to solve radiation budget and energy balance equations for $T_{s,max}$. The radiation budget and energy balance equations specifically for the soil component can be expressed as Eqs. (4.11) and (4.12), respectively:

$$\begin{aligned} R_s &= (1 - \alpha_s)S_d + (L_d - L_u) - (1 - \varepsilon_s)L_d = (1 - \alpha_s)S_d + \varepsilon_s L_d - L_u \\ &= (1 - \alpha_s)S_d + \varepsilon_s \varepsilon_a \sigma T_a^4 - \varepsilon_s \sigma T_s^4 \end{aligned} \quad (4.11)$$

$$R_s - G = H_s + ET_s = \rho c_p \left(\frac{T_s - T_a}{r_{a,s}} \right) + LE_s \quad (4.12)$$

where α_s is the albedo for the soil surface (dimensionless); S_d is the downwelling shortwave radiation (W m^{-2}); L_d and L_u are the downwelling and upwelling longwave radiation (W m^{-2}), respectively, which can be calculated by the Stefan-Boltzmann law; and ε_s is the broadband (8-14 μm) emissivity of the soil surface (e.g., 0.95), which can vary with soil moisture (Mira et al., 2007; Rubio et al., 2003). If there is no measurement of ε_s , some representative values can be used according to look-up tables from Rubio et al. (2003); ε_a is the emissivity of the atmosphere (dimensionless), which is a function of air temperature T_a (K) and water vapor pressure e_a (hPa) (Brutsaert, 1975); ρ is the air density (kg m^{-3}); c_p is the air specific heat at the constant pressure ($\text{J kg}^{-1} \text{K}^{-1}$); and $r_{a,s}$ is the aerodynamic resistance for the soil surface (s m^{-1}). In TTME, $r_{a,s}$ is computed with Kondo (1994)'s formula in conjunction with Paulson (1970) and Webb's (1970) formulas for stability corrections:

$$r_{a,s} = \frac{1}{0.0015u_{1m}} \quad (4.13)$$

$$u = \frac{u_*}{k} \left[\ln \frac{(z_m - d)}{z_{om}} - \psi_{m(1)} + \psi_{m(z_{om})} \right] \quad (4.14)$$

A) Unstable conditions ($L < 0$):

$$\psi_{m(1)} = 2 \ln \left(\frac{1 + x_{(1)}}{2} \right) + \ln \left(\frac{1 + x_{(1)}^2}{2} \right) - 2 \arctan(x_{(1)}) + 0.5\pi \quad (4.15)$$

$$\psi_{m(z_{om})} = 2 \ln \left(\frac{1 + x_{(z_{om})}}{2} \right) + \ln \left(\frac{1 + x_{(z_{om})}^2}{2} \right) - 2 \arctan(x_{(z_{om})}) + 0.5\pi \quad (4.16)$$

$$x_{(1)} = \left(1 - 16 \frac{1}{L} \right)^{0.25} \quad (4.17)$$

$$x_{(z_{om})} = \left(1 - 16 \frac{z_{om}}{L} \right)^{0.25} \quad (4.18)$$

$$L = - \frac{\rho c_p u_*^3 T_a}{kg H_s} \quad (4.19)$$

B) Stable conditions ($L > 0$):

$$\psi_{m(1)} = -5 \left(\frac{1}{L} \right) \quad (4.20)$$

$$\psi_{m(z_{om})} = -5 \left(\frac{z_{om}}{L} \right) \quad (4.21)$$

where u_{1m} is the wind velocity at 1 m height above the bare soil surface (m s^{-1}); Eq. (4.14) is the logarithmic wind profile function, in which u_* is the friction velocity (m s^{-1}), k is von Karman's constant (0.41), z_m is the reference height for wind velocity observations (1 m for the bare soil surface), d is the zero plane displacement (m) (0 for the bare soil

surface), and z_{om} is the roughness length for momentum transfer (m). For the bare soil surface z_{om} can be typically taken as 0.005 m (Allen et al., 2007; Nishida et al., 2003). $\Psi_{m(1)}$ and $\Psi_{m(z_{0m})}$ are the stability correction factors at 1 m and 0.005 m height for the bare soil surface (dimensionless), respectively. L is the Monin-Obukhov length (m), and g is the acceleration of gravity (9.8 m s^{-2}).

Substituting Eq. (4.11) into Eq. (4.12), it is clear that T_s is implicitly involved. To explicitly express T_s , the first two terms of the Taylor series of L_u at T_a can be written as

$$L_u = \varepsilon_s \sigma T_s^4 \approx \varepsilon_s \sigma T_a^4 + 4\varepsilon_s \sigma T_a^3 (T_s - T_a) \quad (4.22)$$

Substituting Eq. (4.22) into Eq. (4.11) one obtains

$$\begin{aligned} R_s &= (1 - \alpha_s) S_d + \varepsilon_s \varepsilon_a \sigma T_a^4 - \varepsilon_s \sigma T_s^4 \\ &\approx (1 - \alpha_s) S_d + \varepsilon_s \varepsilon_a \sigma T_a^4 - \varepsilon_s \sigma T_a^4 - 4\varepsilon_s \sigma T_a^3 (T_s - T_a) \end{aligned} \quad (4.23)$$

Let $(1 - \alpha_s) S_d + \varepsilon_s \varepsilon_a \sigma T_a^4 - \varepsilon_s \sigma T_a^4$ be $R_{s,0}$, which is the net radiation for the soil surface in which T_s is approximated by T_a in L_u . Combining $R_{s,0}$, Eqs. (4.12) and (4.23), and let $G = cR_s$ where c is a calibrated proportionality coefficient (0.35), one obtains

$$T_s = \frac{R_{s,0} - LE_s / (1 - c)}{4\varepsilon_s \sigma T_a^3 + \rho c_p / [r_{a,s} (1 - c)]} + T_a \quad (4.24)$$

It is apparent from Eq. (4.24) that $T_{s,max}$ for the theoretical driest bare surface (point A) can be derived by setting $ET_s=0$, given certain meteorological conditions and surface characteristics:

$$T_{s,max} = \frac{R_{s,0}}{4\varepsilon_s \sigma T_a^3 + \rho c_p / [r_{a,s} (1 - c)]} + T_a \quad (4.25)$$

$T_{s,\max}$ can be eventually derived by solving for the system of nonlinear Eqs. (4.11)-(4.21) and (4.25) in an iterative manner. It is noted that the derivation of $T_{s,\max}$ requires spatially homogeneous meteorological fields (T_a , u_* , and S_d) for a study site.

Determination of $T_{c,\max}$

In a similar vein, $T_{c,\max}$ at point D can be derived by solving for radiation budget Eq. (4.26) and energy balance Eq. (4.27) for the vegetation component:

$$\begin{aligned} R_c &= (1 - \alpha_c)S_d + (L_d - L_u) - (1 - \varepsilon_c)L_d = (1 - \alpha_c)S_d + \varepsilon_c L_d - L_u \\ &= (1 - \alpha_c)S_d + \varepsilon_c \varepsilon_a \sigma T_a^4 - \varepsilon_c \sigma T_c^4 \end{aligned} \quad (4.26)$$

$$R_c = H_c + ET_c = \rho c_p \left(\frac{T_c - T_a}{r_{a,c}} \right) + LE_c \quad (4.27)$$

where α_c is the albedo for vegetation (dimensionless); ε_c is the emissivity of vegetation (e.g., 0.98), which can be obtained from look-up tables of Rubio et al. (2003) in the case of the absence of measurements (Rubio et al., 2003; Sanchez et al., 2008); and $r_{a,c}$ is the aerodynamic resistance above the canopy ($s\ m^{-1}$) expressed as

$$r_{a,c} = \frac{\ln\left(\frac{z_T - d}{z_{oh}}\right) - \psi_{h(z_T)} + \psi_{h(z_{oh})}}{u_* k} \quad (4.28)$$

$$u = \frac{u_*}{k} \left[\ln\left(\frac{z_m - d}{z_{om}}\right) - \psi_{m(z_m)} + \psi_{m(z_{om})} \right] \quad (4.29)$$

A) Unstable conditions ($L < 0$):

$$\psi_{m(z_m)} = 2 \ln\left(\frac{1 + x_{(z_m)}}{2}\right) + \ln\left(\frac{1 + x_{(z_m)}^2}{2}\right) - 2 \arctan(x_{(z_m)}) + 0.5\pi \quad (4.30)$$

$$\psi_{m(z_{om})} = 2 \ln\left(\frac{1+x_{(z_{om})}}{2}\right) + \ln\left(\frac{1+x_{(z_{om})}^2}{2}\right) - 2 \arctan(x_{(z_{om})}) + 0.5\pi \quad (4.31)$$

$$\psi_{h(z_T)} = 2 \ln\left(\frac{1+x_{(z_T)}^2}{2}\right) \quad (4.32)$$

$$\psi_{h(z_{oh})} = 2 \ln\left(\frac{1+x_{(z_{oh})}^2}{2}\right) \quad (4.33)$$

$$x_{(z_m)} = \left(1 - 16 \frac{z_m}{L}\right)^{0.25} \quad (4.34)$$

$$x_{(z_{om})} = \left(1 - 16 \frac{z_{om}}{L}\right)^{0.25} \quad (4.35)$$

$$x_{(z_{oh})} = \left(1 - 16 \frac{z_{oh}}{L}\right)^{0.25} \quad (4.36)$$

$$L = -\frac{\rho c_p u_*^3 T_a}{kg H_c} \quad (4.37)$$

B) Stable conditions ($L > 0$):

$$\psi_{m(z_m)} = -5\left(\frac{z_m}{L}\right) \quad (4.38)$$

$$\psi_{m(z_{om})} = -5\left(\frac{z_{om}}{L}\right) \quad (4.39)$$

$$\psi_{h(z_T)} = -5\left(\frac{z_T}{L}\right) \quad (4.40)$$

$$\psi_{h(z_{oh})} = -5\left(\frac{z_{oh}}{L}\right) \quad (4.41)$$

where, z_T is the reference height for temperature observation, which is taken to be 2 m for the study site. It is assumed that the driest fully vegetated surface has a vegetation height $h_c=1$ m. The zero plane displacement d , z_{om} , and z_{oh} for the hypothesized

vegetated surface can be taken as $d=2h_c/3$, $z_{om}=h_c/10$, and $z_{oh}=z_{om}/7$ (Folhes et al., 2009).

It is noted that if u^* that has been corrected by $\Psi_{m(zm)}$ and $\Psi_{m(zom)}$ is obtained from weather stations, Eq. (4.29) is just needed to perform the stability correction by $\Psi_{h(zT)}$ and $\Psi_{h(zoh)}$.

Combining Eqs. (4.26) and (4.27), and rewriting L_u at T_a for vegetation canopy in terms of the first two terms of the Taylor series yield the general expression of T_c as:

$$T_c = \frac{R_{c,0} - LE_c}{4\varepsilon_c \sigma T_a^3 + \rho c_p / r_{a,c}} + T_a \quad (4.42)$$

where $R_{c,0}$ is the radiation for vegetation in which L_u is calculated using T_a instead of T_c .

Let $LE_c=0$ in Eq. (4.42), $T_{c,max}$ can then be expressed as:

$$T_{c,max} = \frac{R_{c,0}}{4\varepsilon_c \sigma T_a^3 + \rho c_p / r_{a,c}} + T_a \quad (4.43)$$

Likewise, the system of non-linear Eqs. (4.26)-(4.41), and (4.43) can be solved for in an iterative manner. It is noted that numerically solving radiation budget and energy balance Eqs. (4.11)-(4.21) for $T_{s,max}$, and Eqs. (4.26)-(4.41) for $T_{c,max}$ without first simplifying L_u in terms of its Taylor series would provide more accurate solutions of $T_{s,max}$ and $T_{c,max}$.

Determination of cold edge

Areas evaporating at high rates could be detected as pixels with relatively low T_{rad} . These pixels are likely to occur in inland wetlands, storage reservoirs, or dense vegetation stands (Jiang and Islam, 1999; Jiang et al., 2009). Sandholt et al. (2002)

suggested that the cold edge can be taken as the lowest T_{rad} value in an image. Derivation of the cold edge, however, suffers somewhat from subjectivity. Erroneous effects introduced by clouds and terrains can cause uncertainties in the specification of the cold edge from satellite imagery (Gillies et al., 1997; Nemani et al., 1993). In most cases, even the visually inspected cloud-free images could be contaminated by cirrus clouds. In addition, the use of T_{rad} of water bodies might not ensure an appropriate specification of the lowest T_{rad} due to possible clouds over water bodies.

The surface at the largest evaporation/transpiration rate would correspond to the smallest difference between T_c/T_s and T_a . Observed T_a has been used to represent the lowest T_{rad} for a study region, i.e., equilibrium evapotranspiration, forming the horizontal cold edge of the triangle model (Jiang and Islam, 1999). In TTME, observed T_a within a study site is taken to be the horizontal cold edge, i.e., the lower boundary condition. This requires relatively homogeneous atmospheric conditions. If there are slight differences in the observed T_a among different weather stations or flux towers, the mean T_a observations can be taken as the cold edge. The use of T_a as the cold edge of TTME can operationally eliminate the effects of clouds and terrains.

4.2.4. Determination of LE_s , LE_c , and LE

Hereto, the configuration ($T_{s,\text{max}}$, $T_{c,\text{max}}$, and the cold edge) of the trapezoid is uniquely determined given certain meteorological conditions and surface characteristics. Combining Eqs. (4.24) and (4.25), and taking T_a to be $T_{s,\text{min}}$ yield the following relation

$$\frac{T_{s,\max} - T_s}{T_{s,\max} - T_{s,\min}} = \frac{T_{s,\max} - T_s}{T_{s,\max} - T_a} = \frac{LE_s}{R_{s,0}(1-c)} \quad (4.44)$$

Let $R_{s,0}(1-c)$ be $Q_{s,0}$, in combination with Eqs. (7) and (4.44), one obtains

$$EF_s = \frac{T_{s,\max} - T_s}{T_{s,\max} - T_a} \cdot \frac{Q_{s,0}}{Q_s} \quad (4.45)$$

In a similar vein, EF_c can be derived by combining Eqs. (4.6), (4.42), and (4.42) as:

$$EF_c = \frac{T_{c,\max} - T_c}{T_{c,\max} - T_a} \cdot \frac{Q_{c,0}}{Q_c} \quad (4.46)$$

Combining Eqs. (4.8), (4.45) and (4.46), EF for a mixed landscape can be further expressed as

$$EF = f_c \frac{Q_{c,0}}{Q} \cdot \frac{T_{c,\max} - T_c}{T_{c,\max} - T_a} + (1 - f_c) \frac{Q_{s,0}}{Q} \cdot \frac{T_{s,\max} - T_s}{T_{s,\max} - T_a} \quad (4.47)$$

In summary, LE_c can be calculated by Eqs. (4.6), (4.11), and (4.45); LE_s can be calculated by Eqs. (4.7), (4.26), and (4.46). LE for a mixed landscape can be calculated by Eq. (4.1). It is emphasized that TTME does not use observed extreme temperatures selected/specified from the f_c - T_{rad} space as triangle and other spatial variability models do. Instead, TTME makes use of the theoretical boundary conditions illustrated in Sections 4.2.2 and 4.2.3 to decompose T_{rad} and parameterize LE_c and LE_s , which can reduce large uncertainties in the use of observed boundary conditions.

4.2.5. Estimation of α_c and α_s

A primary feature of TTME is its two-source scheme. In addition to decomposing T_{rad} into T_s and T_c within the theoretical boundary conditions, separate parameterization of Q_s (Q_{s0}) and Q_c (Q_{c0}) plays a prominent role in determining the magnitudes of LE_s and LE_c . Albedo components, α_s and α_c for a generic surface, and albedo of two particular surfaces, $\alpha_{s,\text{max}}$ and $\alpha_{c,\text{max}}$ in Eqs. (4.11) and (4.26), are essential to partitioning S_d .

The shortwave radiation reaching a sensor for a simplified landscape is taken as the weighted sum of the radiation coming from the vegetation and soil components (Sanchez et al., 2008; Zhang et al., 2005). The surface albedo for a pixel is therefore assumed to be the weighted sum of albedo components:

$$\alpha_m = f_c \alpha_c + (1 - f_c) \alpha_s \quad (4.48)$$

where α_m is the albedo for a composite pixel; and α_c and α_s are the albedo for vegetation and soil surfaces, respectively. Differentiating α_m with respect to f_c , one obtains

$$\frac{d\alpha_m}{df_c} = \alpha_c - \alpha_s \quad (4.49)$$

Combining Eqs. (4.48) and (4.49), one gets

$$\alpha_c = \alpha_m + (1 - f_c) \frac{d\alpha_m}{df_c} \quad (4.50)$$

$$\alpha_s = \alpha_m - f_c \frac{d\alpha_m}{df_c} \quad (4.51)$$

It is clear from Eqs. (4.50) and (4.51) that partitioning of α_m into α_c and α_s depends

on f_c and slope of the variation in α_m with f_c . The slope of each pixel can be linearly interpolated by the slopes of warm and cold edges of the f_c - α_m space (Zhang et al., 2005).

We propose that warm and cold edges of the f_c - α_m space can be determined by the following steps. First, the full range of f_c is divided into n intervals (e.g., 100). Second, the maximum and minimum values of α_m for each f_c interval are selected and saved. Third, to capture the fundamental features of the two critical edges, outliers of the selected data pairs of α_m and f_c are discarded if the extreme α_m values fall outside the range $[\mu_\alpha - \sigma_\alpha, \mu_\alpha + \sigma_\alpha]$ (μ_α and σ_α are the mean and standard deviation of the saved α_m extreme values). Fourth, linear regression analysis for the refined data pairs is performed to derive the slopes of the two edges. $\alpha_{s,\max}$ and $\alpha_{c,\max}$ can be deduced by the warm edge intersecting with $f_c=0$ and $f_c=1$, respectively.

Inputs, intermediate variables, outputs, and computation procedures of TTME are summarized in Fig. 4.2.

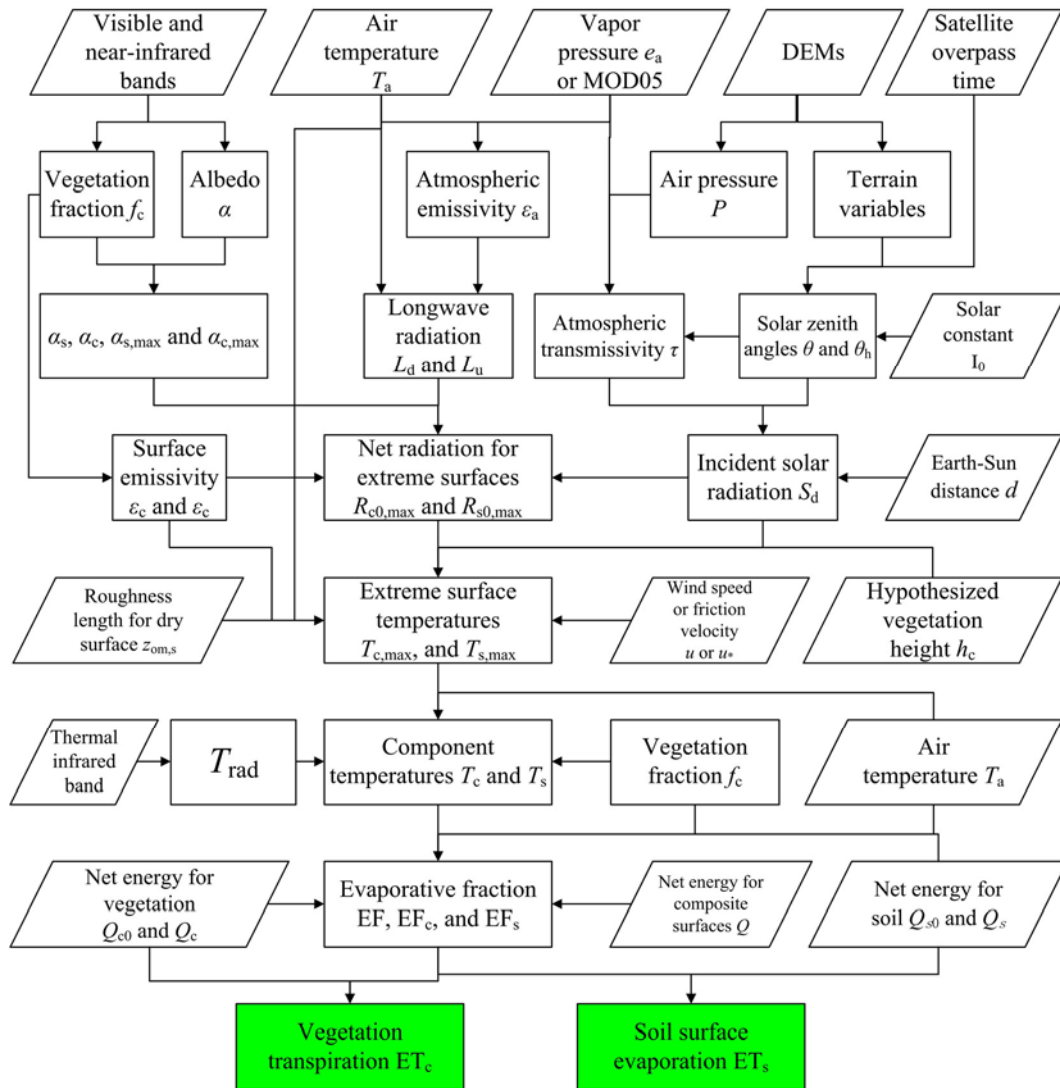


Figure 4.2 Flow chart of TTME.

4.3. Study site and data processing

4.3.1. Study site

The Soil Moisture-Atmosphere Coupling Experiment (SMACEX) campaign was conducted in an area ranging in latitude between 41.87°N and 42.05°N and in longitude between -93.83°W and -93.39°W, covering a grid box around 10 km north-south by 30 km east-west (Fig. 4.3). It was primarily focused on the Walnut Creek (WC) watershed, just south of Ames in central Iowa (IA), U.S., during the period from 15 June (DOY 166) through 8 July (DOY 189) in 2002, designed to provide extensive measurements of soil, vegetation, and meteorological properties and states to understand how horizontal heterogeneities in vegetation cover, soil moisture, and other land surface variables influence surface flux exchanges with the atmosphere (Kustas et al., 2005). The dominant land cover across the WC watershed comprises rainfed corn and soybean fields, accounting for approximately 80% in relatively equal proportions of the watershed. During the course of campaign, crops and vegetation grew rapidly. The surface soil moisture changed from dry to wet from rainfall events in early July.

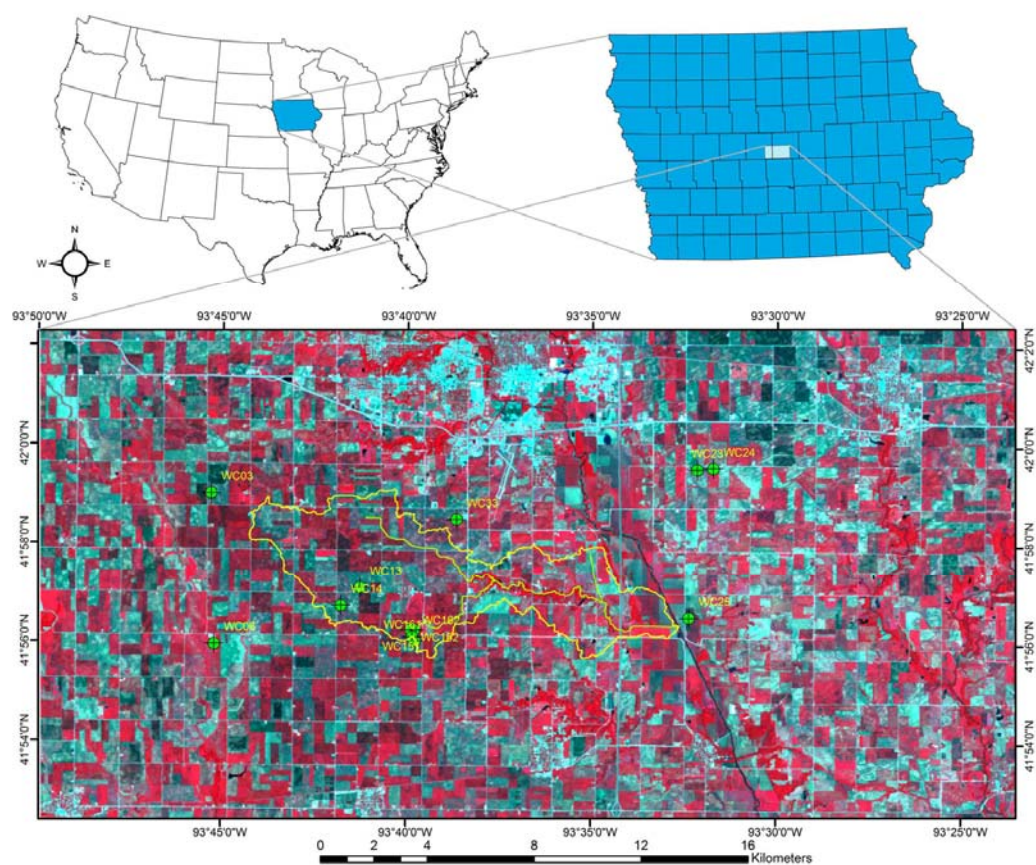


Figure 4.3 Location and the false color composite of Landsat TM imagery acquired on June 23, 2002, of the SMACEX study site at Ames, central Iowa, U.S.

A mean annual rainfall of 835 mm falls in this region, which can be classified as a humid climate. Precipitation during the SMACEX campaign occurred a few days prior to 15 June (DOY 166), with a minor rainfall event of 0-5 mm on 20 June (DOY 171). This was followed by a rain-free period for the WC watershed until 4 July (DOY 185). In a typical growing season, the most rapid growth in corn and soybean crops is observed in June and July. Elevation of the SMACEX site ranges from 256 m to 354 m, with a mean of 302 m. The topography is characterized by low relief and poor surface drainage.

4.3.2. Flux tower measurements

A network consisting of 14 meteorological-flux (METFLUX) towers (12 were fully operational during the campaign) was deployed within or in the vicinity of the WC watershed (WC03, 06, 23, 24, 25, and 33 were outside the watershed), employing eddy covariance (EC) systems at 12 field sites, in which 6 sites were corn and 6 sites were soybean. These towers were instrumented with a variety of sensors for measuring turbulent fluxes of latent and sensible heat, as well as radiation components (incoming and outgoing shortwave and longwave radiation) and soil heat fluxes at 30-min intervals. It is noted that relatively large LE fluxes and small H fluxes were observed on DOY 189. WC 3, 6, 14, and 24 tower flux sites (Fig. 4.3) even showed negative H , which might be indicative of the presence of advection on that day. Additional *in situ* hydrometeorological observations encompassed 10-min averaged temperature, relative humidity, and wind speed and direction, etc. Observed fluxes for three image acquisition dates were used to validate the TTME model. Details about these sensors and processing of the measurements can be found in (Kustas et al., 2005; Prueger et al., 2005).

4.3.3. Energy balance closure

The eddy covariance systems have been found to underestimate LE and H , i.e., $R_n - G > LE + H$, due to mismatched source areas of LE and H , inhomogeneous surface cover and soil characteristics, and flux divergence or dispersion, etc.; therefore the measured LE and H need to be adjusted for energy balance closure (Twine et al., 2000). Fig. 4.4 compares observed $LE + H$ with $R_n - G$ at the Landsat overpass for three image

acquisition dates, illustrating that in general the observed $LE+H$ fluxes are less than R_n-G except for the observed $LE+H$ being significantly larger than R_n-G at WC 25 on DOY 182. The averaged closure ratio $[CR=(LE+H)/(R_n-G)]$ for all observations was found to be 0.85.

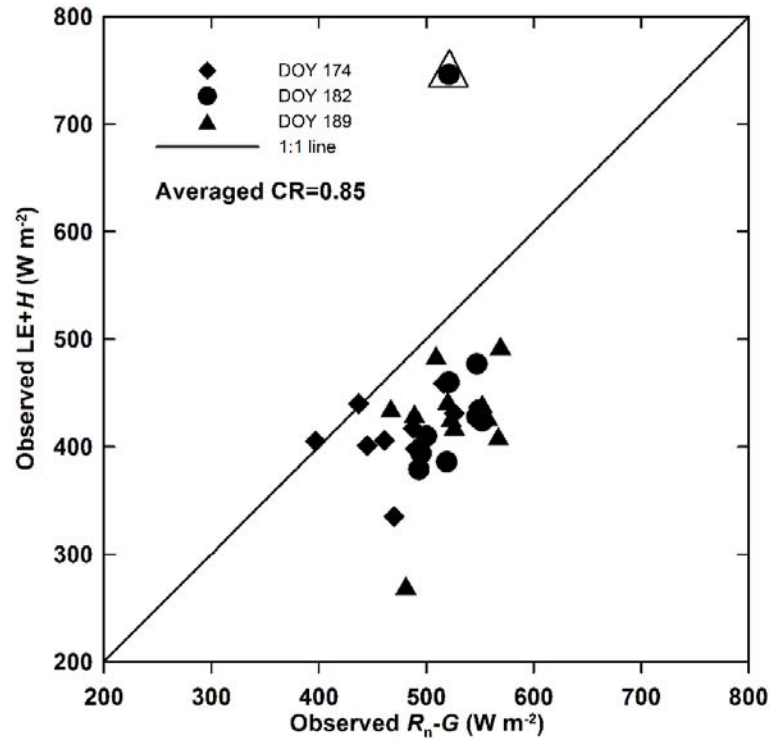


Figure 4.4 Comparison of the observed energy availability (R_n-G) and the sum of observed sensible and latent heat fluxes ($LE+H$), showing the averaged closure ratio (CR) of 0.85.

Twine et al. (2000) have stated that the preferred method of energy balance closure is to maintain the Bowen ratio (H/LE) and partition the measured available energy (R_n-G), since there was no compelling evidence to discard the measured LE as the residual closure does. They also compared the measured LE after forcing closure by the

Bowen ratio and residual techniques with that from water budget calculations, indicating that the Bowen ratio method showed a closer agreement with the water balance results. Anderson et al. (Anderson et al., 2005) found that the observed LE after forcing closure by the Bowen ratio method agreed well with aircraft counterparts for the SMACEX site. French et al. (2005b) performed the Bowen ratio closure in validation of Two-source Energy Balance (TSEB) and Surface Energy Balance Algorithm for Land (SEBAL) at the SMACEX site. As such, we performed a closure of the measured LE and H fluxes by the Bowen ratio technique.

4.3.4. Remote sensing sources and ancillary data

There were three cloud-free scenes of Landsat TM/ETM⁺ imageries acquired across the campaign period, i.e., Landsat TM on DOY 174 spanning vegetated canopy cover from 50% to 75%, Landsat ETM⁺ on DOY 182 from 75% to 90%, and Landsat ETM⁺ on DOY 189 from 85% to essentially full cover. Basic information regarding these imageries is shown in Table 4.1.

Table 4.1 Parameters of Landsat imageries covering the SMACEX site for three study days in 2002

Date (DOY)	Landsat	Path/Row	Overpass time (local)	Solar elevation angle (°)	Solar azimuth angle (°)
June 23 (174)	TM	26/31	10:29 a.m.	61.50	121.88
July 1 (182)	ETM ⁺	26/31	10:42 a.m.	62.93	126.30
July 8 (189)	ETM ⁺	27/31	10:45 a.m.	62.24	126.73

Digital Elevation Models (DEMs) were obtained from the National Elevation Dataset (NED) produced and distributed by the U.S. Geological Survey (<http://seamless.usgs.gov/index.php>), with a spatial resolution of 1 arc-second (about 30 m). Terrain variables (e.g., elevation, slope, and aspect) were extracted directly from the DEMs.

4.3.5. Variable derivation

Derivation of α_m

Albedo of a composite pixel α_m was derived from visible and near-infrared bands of Landsat imagery using calibrated atmospheric transmittance and path reflectance functions developed by Tasumi et al. (2008). The atmospheric transmittance and path reflectance are functions of fitted satellite-dependent constants, the solar zenith angle for a horizontal flat surface, satellite view angle, atmospheric pressure, and precipitable water in the atmosphere. The former four parameters and variables can be specified or determined readily, whereas the precipitable water in the atmosphere requires an

empirical relationship with observed near-surface vapor pressure. The empirical relationship between precipitable water and near-surface pressure was derived using monthly mean atmospheric precipitable water and near-surface vapor pressure data for 82 sites in the U.S. (Garrison and Adler, 1990). It is noted that this relationship should be used with caution on the instantaneous timescale and in regions outside the U.S.

We recommend that the use of MODIS atmospheric products, MOD05_L2, providing the total precipitable water vapor, be able to retain the spatial characteristic of precipitable water content and improve the accuracy of α_m retrievals. We compared α_m retrievals from observed near-surface vapor pressure and MOD05_L2, respectively, with observed ones. The observed albedo was obtained from the observed outgoing shortwave radiation over the observed incoming shortwave radiation from the CNR1 at towers 3, 6, 24, 25, 33, 152 and 162, and the Radiation and Energy balance (REBS) Q*7 series at towers 13, 14, 23, 151, and 161. Results (Fig. 4.5) indicate that in general α_m simulations using near-surface vapor pressure and MOD05_L2 both show reasonable agreement with observations. The use of MOD05_L2 precipitable water content resulted in slightly improved accuracy of α_m retrievals in terms of a bias of -0.0024 and an RMSD of 0.0065 for the three study days. The α_m retrievals from using observed vapor pressure showed a bias of -0.0036 and an RMSD of 0.0069. The advantages of the use of MOD05_L2 will be manifested when simulating α_m over large heterogeneous areas and/or the absence of near-surface vapor pressure measurements.

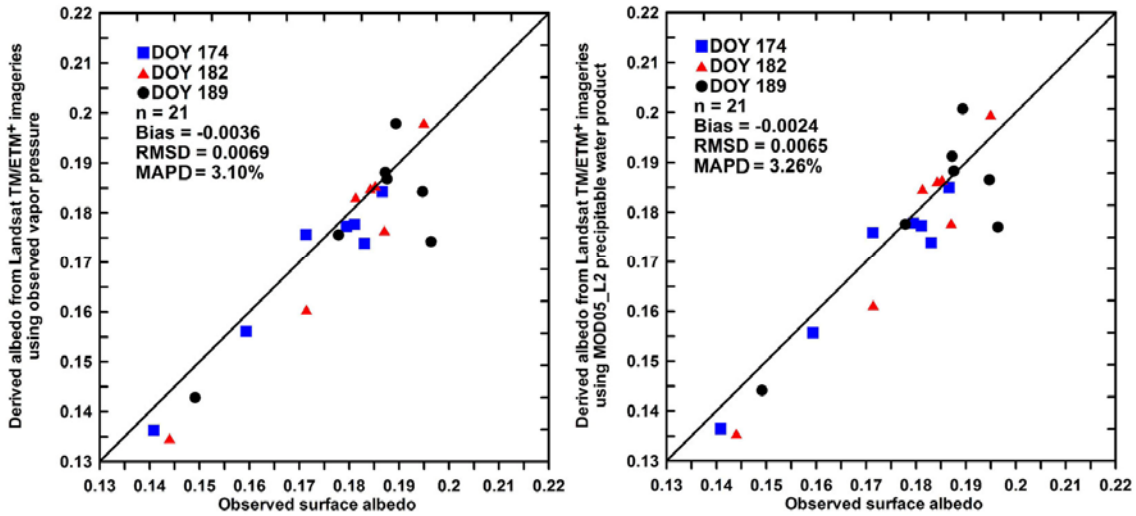


Figure 4.5 Comparison of surface albedo retrievals from Landsat TM/ETM⁺ imagery using observed near-surface vapor pressure and MOD05_L2 precipitable water products, respectively.

Derivation of T_{rad}

T_{rad} is derived from the thermal infrared band of Landsat imagery. Prior to retrieving T_{rad} , atmospheric corrections for the at-sensor spectral radiance should be performed using atmospheric radiation transfer simulation models (e.g., MODTRAN) in combination with radiosounding data, ground-based measurements, and/or remotely sensed sources (e.g., MOD05_L2). The atmospherically corrected radiance can be converted into T_{rad} using the Planck equation (Allen et al., 2007; Li et al., 2004). Li et al. (2004) performed atmospheric corrections for the thermal bands of 4 scenes of Landsat TM/ETM⁺ imagery acquired during the SMACEX campaign, providing the simulated atmospheric transmittance, spectral radiance added by the atmosphere, and the downwelling sky radiance from the atmosphere. We took advantage of such coefficients to retrieve T_{rad} for the SMACEX site on DOY 174, 182 and 189.

Retrievals of T_{rad} require surface emissivity for the thermal band of the wavelength of 10.45-12.42 μm and 10.31-12.36 μm for Landsat TM and ETM⁺, respectively. Given the relatively homogenous and flat study site, we adopted the formula proposed by Sobrino et al. (1990) to estimate surface emissivity, in which the term associated with the cavity effect is taken to be zero.

Derivation of S_d

Downwelling shortwave radiation S_d is the largest contributor of net radiation, largely determining the magnitudes of H and LE. It is a function of solar constant I_0 (1367 W m^{-2}), solar zenith angle θ , the relative Earth-Sun distance d (dimensionless), and broad-band atmospheric transmissivity τ (dimensionless):

$$S_d = \frac{I_0}{d^2} \cos(\theta) \tau \quad (4.52)$$

The solar zenith angle θ for a surface can be computed in terms of the geometric relationship between the incident beam and the sloping surface described in Section 2.3.1 in Chapter II. As demonstrated in Section 2.3.1, S_d is most sensitive to τ . Accurate determination of τ calls for radiosounding data about atmospheric composite, water content, and temperature of the atmospheric profile using radiative transfer models (e.g., MODTRAN). In practice, we can estimate τ using the formula provided by Allen et al. (2007).

4.4. Results

4.4.1. Surface flux and EF estimates from TTME

Energy balance components (R_n , G , H , and LE) simulated by TTME were compared with tower-based flux measurements which were adjusted for energy balance closure using the Bowen ratio method (Fig. 4.6 and Table 4.2). The simulated fluxes were averaged over the estimated upwind source-area/footprint (1~2 pixels/~120 m) for each flux tower using the approach proposed by Li et al. (2008a). Results indicate that in general retrievals of all four components of the energy balance equation agree reasonably well with tower-based measurements. The model reproduced measured R_n with good accuracy at all sites for the three days, yielding an RMSD of 27.1 W m^{-2} , an MAPD of 3.6%, and a bias of 14.2 W m^{-2} . The overestimation of R_n would be probably due to an underestimation of T_{rad} and consequently an underestimation of the outgoing longwave radiation. The R_n retrievals showed the highest accuracy in terms of the overall MAPD of 3.6% for the three days compared with other energy balance components.

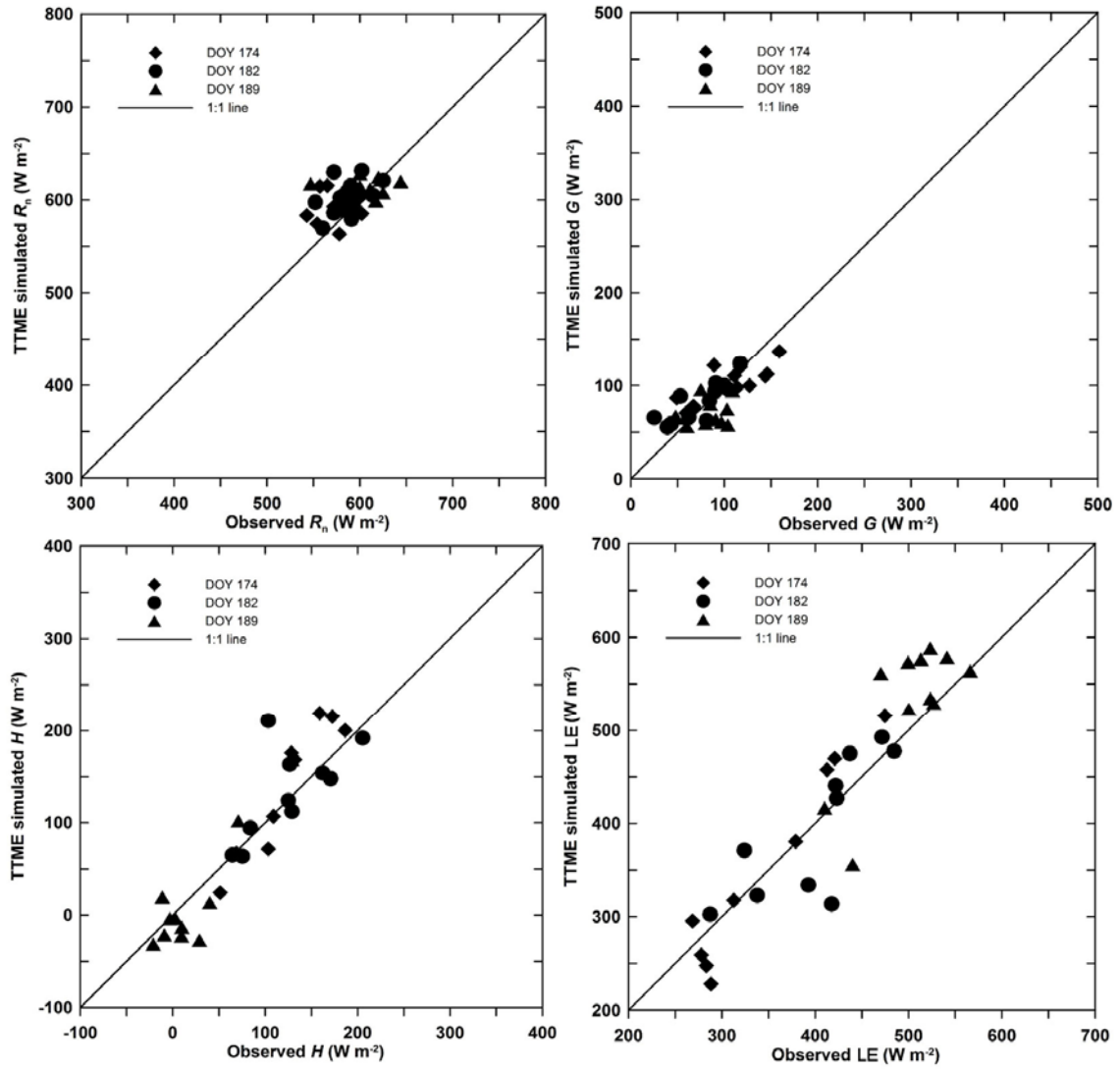


Figure 4.6 Comparison of R_n , G , H , and LE fluxes (W m^{-2}) from TTME with corresponding eddy covariance tower-based measurements (W m^{-2}) at the SMACEX site on DOY 174, 182 and 189 in 2002.

Table 4.2 Statistics on discrepancies between the simulated energy balance components from TTME, and the eddy covariance energy and heat fluxes in the SMACEX site for three test dates. The observed fluxes are corrected by the Bowen ratio (BR) technique.

Flux and date		Observation number	Observed average (W m^{-2})	Simulated average (W m^{-2})	Bias (W m^{-2})	RMSD (W m^{-2})	MAPD (%)
R_n	DOY174	12	572.4	590.5	18.1	28.6	4.1
	DOY182	12	586.5	602.5	16.0	26.0	3.5
	DOY189	11	606.4	614.2	7.9	26.5	3.2
	Overall	35	587.9	602.1	14.2	27.1	3.6
G	DOY174	12	104.1	101.7	-2.4	23.4	21.8
	DOY182	12	74.1	83.1	9.0	18.4	30.8
	DOY189	11	82.7	70.4	-12.3	24.4	24.5
	Overall	35	87.1	85.5	-1.6	22.1	25.7
LE	DOY174	9	346.6	352.4	5.8	36.6	9.2
	DOY182	10	399.8	395.7	-4.1	43.7	8.4
	DOY189	11	501.3	527.4	26.1	53.2	8.5
	Overall	30	421.0	431.0	10.0	45.6	8.7
H	DOY174	9	123.4	138.6	15.1	34.7	24.7
	DOY182	10	124.6	132.7	8.1	37.7	20.1
	DOY189	11	22.4	16.4	-5.9	28.8	145.7
	Overall	30	86.8	91.8	5.0	33.8	67.5
EF	DOY174	9	0.73	0.71	-0.02	0.06	8.7
	DOY182	10	0.76	0.74	-0.01	0.07	6.8
	DOY189	11	0.96	0.97	0.01	0.06	5.0
	Overall	30	0.82	0.82	-0.01	0.06	6.7

The G retrievals were taken to be a fraction ($=0.35$) of R_s , showing an RMSD of 22.1 W m^{-2} and an MAPD of 25.7% compared with tower-based measurements. A fixed fraction for G might be the principal reason for the discrepancies in the G estimates. Calibration of the fraction would improve the agreement.

LE appeared to be well reproduced by TTME, demonstrating an overall RMSD of 45.6 W m^{-2} and an MAPD of 8.7% for the three study dates, in which DOY 189 implied a relatively larger RMSD of 53.2 W m^{-2} . This is likely related to the presence of advection under high soil wetness conditions on that day.

The H estimates for the three dates showed an RMSD of 33.8 W m^{-2} and an MAPD of 67.5%. It is noted that a larger MAPD of up to 145.7% for the H estimates occurred on DOY 189, which could be ascribed to the negative and relatively small magnitudes of the H measurements due to advection. Of the 11 sites having H measurements on DOY 189, 4 sites showed negative H measurements on the order of $10\sim 20 \text{ W m}^{-2}$. For the other two dates, the H retrievals were in greater agreement with the tower-based measurements, showing an RMSD of 34.7 W m^{-2} and 37.7 W m^{-2} , and an MAPD of 24.7% and 20.1% for DOY 174 and 182, respectively.

It is important to note that unlike other types of energy-balance models, TTME does not directly compute H ; it takes H as the residual term of the energy balance equation. All uncertainties in R_n , G , and LE are therefore encapsulated into the H estimates. Even though a great discrepancy of H retrievals would take place in some cases (e.g., advection), the most interesting component, LE, can be well reproduced.

For further examining the utility and mechanisms of TTME, we isolated uncertainties in R_n and G retrievals from the resulting LE estimates by evaluating the EF estimates for the three days. Results (Table 4.2 and Fig. 4.7) show that there is a fairly close agreement between the EF retrievals and the tower-based measurements, showing an RMSD of 0.06 and an MAPD of 6.7%. This means that if the EF estimates from TTME are combined with net energy ($R_n - G$) measurements, it will produce LE estimates with higher accuracy. On the other hand, there is still room for improving the parameterization of R_n and G in TTME.

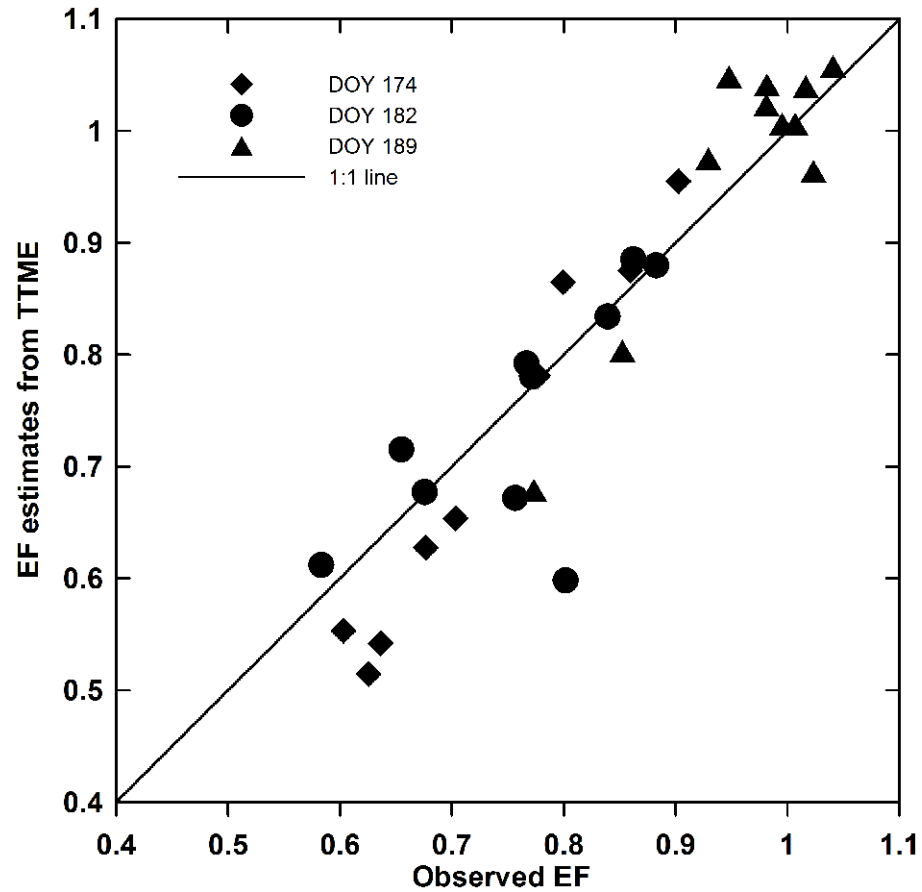


Figure 4.7 Comparison of EF from TTME with corresponding eddy covariance tower-based EF at the SMACEX site on DOY 174, 182 and 189 in 2002.

Fig. 4.8 shows the spatial distributions of LE_c and LE_s of the SMACEX site for the three study days. Evolution of LE_c and LE_s estimates for the three days is primarily determined by the evolution of T_{rad} and f_c . Because of the varying discriminating ability of thermal bands for Landsat TM and ETM sensors, the spatial resolution of LE_c and LE_s retrievals are apparently different. The LE_c and LE_s estimates for DOY 189 show low values across the central portion of the modeling domain, with values generally becoming large from the centre.

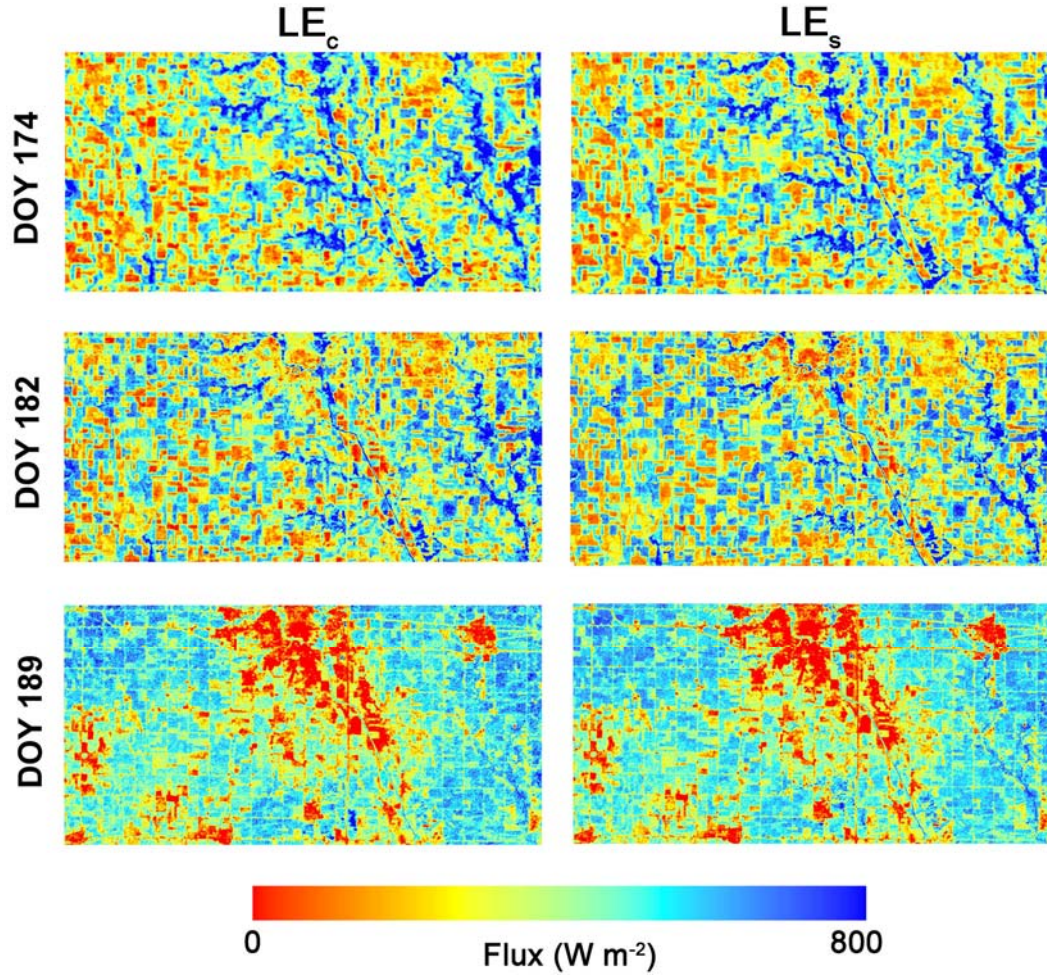


Figure 4.8 Spatial distribution of LE_c ($W m^{-2}$) and LE_s ($W m^{-2}$) from TTME at the SMACEX site on DOY 174, 182 and 189 in 2002.

In summary, TTME seems to be capable of reproducing surface fluxes under dry and wet conditions with model-measurement errors on the order of RMSD within $45 W m^{-2}$ for energy balance components and 0.06 for EF. Even though a relatively large uncertainty in the H estimates would occur due to advection and uncertainties in R_n , G , and LE estimates, LE can be well reproduced. The retrievals of EF are in close agreement with tower-based measurements.

4.4.2. Sensitivity analysis of TTME

Model sensitivity analysis plays a fundamental role in understanding the contributions of variables and parameters to model outputs and consequently provides an insight into the mechanisms of error propagation and uncertainty of the model. In this study, the sensitivity S_i of the most interesting output, LE, from TTME to an input i is used, which can be expressed as

$$S_i = \left(\frac{LE_{\pm} - LE_0}{LE_0} \right) \cdot 100 \quad (4.53)$$

where LE_{\pm} represents the LE estimates when an input variable is increased (+) or decreased (-) with respect to the reference values (original inputs); and LE_0 is the LE estimates based on the reference values. Given the retrieval accuracy of T_{rad} , perturbations of T_{rad} were specified as $[-2\text{K}, 2\text{K}]$, with a variation step of 0.5 K. Perturbations of T_a were also specified as $[-2\text{K}, 2\text{K}]$, even though uncertainty in T_a observations might not be as large as the specified range. Perturbations of the other variables were specified as $[-20\%, 20\%]$, with a variation step of 5%. The reference

values were obtained from the SMACEX data set on DOY 174, which showed a range of soil moisture and f_c conditions. DOY 182 and 189 showed relatively homogeneous soil moisture and f_c conditions, which might make the model sensitivity be conservatively estimated.

Sensitivity to T_{rad} and T_a

Results (Table 4.3 and Fig. 4.9a) show that T_{rad} is negatively correlated with LE, but T_a is positively correlated with LE. An increase in T_{rad} is a signal of surfaces moving to the warm edge within the trapezoid framework; therefore the LE estimates tend to decrease. Analogously, an increase in T_a is primarily indicative of surfaces moving towards the cold edge, thereby resulting in increases in the LE estimates. Additionally, T_{rad} and T_a can also influence the calculation of net radiation components. However, the contributions of T_{rad} and T_a to net radiation are considerably smaller than that to the resulting LE estimates.

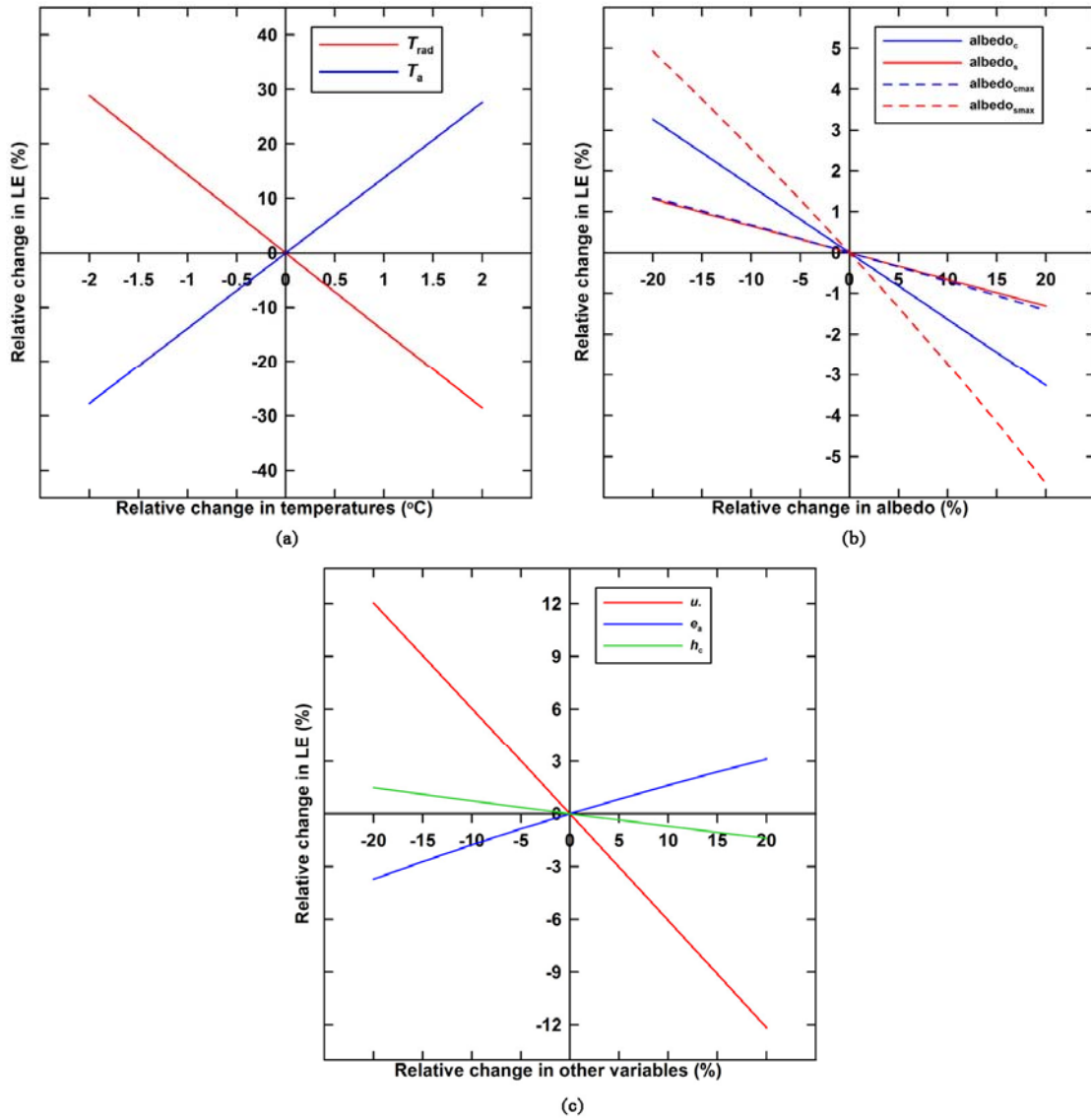


Figure 4.9 Sensitivity analysis of TTME to T_{rad} and T_a in (a), α_c , α_s , $\alpha_{c,max}$, and $\alpha_{s,max}$ in (b), and u_* , e_a , and h_c in (c).

Table 4.3 Relative sensitivity S_i (%) of LE estimates from TTME to each input variable at the SMACEX site on three study days, variations of T_a and T_{rad} are in K and variations of the other variables are in percentage (%)

Variation (%/K) Variable	-20 (-2)	-15 (-1.5)	-10 (-1)	-5 (-0.5)	5 (0.5)	10 (1)	15 (1.5)	20 (2)
T_{rad}	28.9	21.6	14.4	7.2	-7.2	-14.3	-21.5	-28.6
T_a	-27.7	-20.8	-13.9	-6.9	6.9	13.8	20.7	27.6
α_s	1.3	1.0	0.7	0.3	-0.3	-0.7	-1.0	-1.3
α_c	3.3	2.4	1.6	0.8	-0.8	-1.6	-2.4	-3.3
$\alpha_{s,max}$	4.9	3.8	2.5	1.3	-1.3	-2.7	-4.2	-5.7
$\alpha_{c,max}$	1.4	1.0	0.7	0.3	-0.3	-0.7	-1.1	-1.4
u^*	12.0	9.0	6.0	3.0	-3.0	-6.1	-9.1	-12.2
e_a	-3.7	-2.7	-1.8	-0.9	0.8	1.6	2.4	3.1
h_c	1.5	1.1	0.7	0.4	-0.4	-0.7	-1.1	-1.4

A 1 K increase in T_{rad} and T_a could result in a 14.3% decrease and a 13.8% increase in the LE estimates. A 2 K increase in T_{rad} and T_a could result in a 28.6% decrease and a 27.6% increase in the LE estimates. This means that T_{rad} and T_a play a critical role in determining the relative displacement of pixels to the boundary conditions of LE, and in demarcating the boundary conditions of TTME. To that end, restraining errors of TTME lies in controlling uncertainty in the T_{rad} retrievals.

In fact, all satellite-based ET models take advantage of T_{rad} to calculate H , e.g., SEBAL, Surface Energy Balance System (SEBS), and TSEB, or to directly deduce EF, e.g., triangle models. Sensitivity analysis performed by Timmermans et al. (2007) indicated that a 2.5 K increase in T_{rad} would result in a 74% increase in the H estimates from TSEB. Given that TTME and TSEB have the similar retrieval accuracies of R_n and G shown in Section 4.1, TTME would show less sensitivity to T_{rad} than TSEB. On the other hand, uncertainty in T_a observations can be generally small. The use of T_a to be the

lower boundary condition of LE seems to circumvent the uncertainty in determining the lower boundaries by specifying end-member T_{rad} as the SEBAL model does.

Sensitivity to albedo components

It is noted that remotely sensed α_m for a composite pixel should be decomposed into α_c and α_s to compute R_c and R_s in terms of algorithms illustrated in Section 4.2.5. In addition, $\alpha_{c,\text{max}}$ and $\alpha_{s,\text{max}}$ deduced from the f_c - α_m space can also influence the magnitudes of $T_{c,\text{max}}$ and $T_{s,\text{max}}$. Since these albedo components are derived/deduced by the TTME algorithm, we investigated the sensitivity of TTME to them.

Results (Table 4.3 and Fig. 4.9b) show that in general, all albedo components are negatively correlated with the LE estimates. This can be explained by radiation budget and energy balance equations. With increasing α_c or α_s , the net radiation will be reduced and therefore LE_c or LE_s and LE tend to be reduced. In a similar vein, with increasing $\alpha_{c,\text{max}}$ or $\alpha_{s,\text{max}}$, $T_{c,\text{max}}$ or $T_{s,\text{max}}$ tends to decrease, which corresponds to the upper boundary condition of TTME moving downward, therefore leading to decreasing LE. A 20% increase in α_c , α_s , $\alpha_{c,\text{max}}$, and $\alpha_{s,\text{max}}$ can result in -3.3%, -1.3%, -1.4%, and -5.7% decreases in the LE estimates, respectively. TTME appears to have the largest sensitivity to $\alpha_{s,\text{max}}$ in all albedo components.

Sensitivity to other variables

u/u_* is involved in the calculation of the aerodynamic resistance of the driest bare surface and the driest fully vegetated surface. e_a is involved in the estimation of L_u . The model sensitivity to the two meteorological inputs was investigated. Furthermore, the model sensitivity to a hypothesized h_c for the driest fully vegetated surface was also examined. Results (Fig. 4.9c) suggest that e_a is positively correlated with the LE estimates, and u_* and h_c are negatively correlated with the LE estimates. A 20% increase in e_a would lead to a 3.1% increase in the LE estimates due to an enhanced effect of L_u , thereby causing a slightly larger LE estimate. A 20% increase in u_* and h_c would result in -12.2% and -1.4% decreases in the LE estimates. This means that TTME is not greatly sensitive to meteorological observations. More importantly, the hypothesized h_c for the theoretical driest fully vegetated surface of the trapezoidal framework would not result in large uncertainty in the model.

In summary, TTME is most sensitive to T_{rad} and T_{a} . It is noted that T_{rad} is the most critical input in all satellite-based ET models. TTME shows less sensitivity to T_{rad} than TSEB. The hypothesized h_c for the driest fully vegetated surface could not result in large uncertainty in the TTME algorithm. TTME is not sensitive to albedo components, which can be derived or specified appropriately and therefore would not result in large uncertainty in the LE estimates. The TTME model does not seem sensitive to meteorological observations of u^* and e_a .

4.5. Discussion

4.5.1. Comparison with other models

The SMACEX data set has been extensively used to perform model validation and comparison. The performance of SEBAL, Mapping Evapotranspiration at high Resolution with Internalized Calibration (METRIC), SEBS, TSEB, and the triangle model at this site has been reported in the literature. Table 4.4 lists statistics of the discrepancies between surface flux retrievals and flux tower measurements from published studies.

Table 4.4 Statistics on discrepancies between flux estimates from SEBAL, SEBS, and TSEB, against eddy covariance-based measurements for the SMACEX site in the literature. Closure techniques involve residual (RE) and Bowen ratio (BR) methods. Hyphen (-) denotes null value. The unit of bias and RMSD is W m^{-2} and MAPD is percentage (%)

Model	Study	Satellite imagery	DOY	Closure technique/ α_c	ET ($\text{W m}^{-2}/\%$)	H ($\text{W m}^{-2}/\%$)	R_n ($\text{W m}^{-2}/\%$)	G ($\text{W m}^{-2}/\%$)
SEBAL	(French et al., 2005a)	ASTER	182	BR	Bias:-82	Bias: 63	Bias: -31	Bias: -12
METRIC	(Choi et al., 2009)	Landsat TM/ETM+	174 and 182	BR	Bias:19; RMSD: 55	Bias: -29; RMSD: 57	Bias: -10 RMSD: 19	Bias: 0 RMSD: 19
	(Choi et al., 2009)	Landsat TM/ETM+	174 and 182	RE	Bias:53; RMSD: 75	–	–	–
	(Gonzalez-Dugo et al., 2009)	Landsat TM/ETM+	174, 182, and 189	RE	Bias: 1 RMSD: 42	Bias: -1 RMSD: 42	–	–
Range	–	–	–	–	Bias:-82~53 RMSD:42~75	Bias: -29~63 RMSD:42~57	Bias: -31~-10 RMSD: 19	Bias: -12~0 RMSD: 19
TSEB	(Li et al., 2005)	Landsat TM/ETM+	167, 174, 182, and 189	BR/1.3	RMSD: 46 MAPD: 12	RMSD: 49 MAPD: 35	RMSD: 20 MAPD: 3	RMSD: 20 MAPD: 3
	(Li et al., 2005)	Landsat TM/ETM+	167, 174, 182, and 189	RE/1.3	RMSD: 45 MAPD: 9	–	–	–
	(French et al., 2005a)	ASTER	182	BR/ \square	Bias: 8	Bias: -20	Bias: 0	Bias: 12
	(Choi et al., 2009)	Landsat TM/ETM+	174 and 182	BR/1.26	Bias: 4; RMSD: 53	Bias: 39; RMSD: 62	Bias: 21 RMSD: 30	Bias: -22 RMSD: 32
	(Choi et al., 2009)	Landsat TM/ETM+	174 and 182	RE/1.26	Bias: 37; RMSD: 60	–	–	–
	(Gonzalez-Dugo et al., 2009)	Landsat TM/ETM+	174, 182, and 189	RE/1.26	Bias: 17 RMSD: 30	Bias: 17 RMSD: 30	–	–
Range	–	–	–	–	Bias:4~37 RMSD: 30~60	Bias:-20~39 RMSD: 30~62	Bias:0~21 RMSD: 20~30	Bias:-22~12 RMSD: 20~32

Table 4.4 Continued.

Model	Study	Satellite imagery	DOY	Closure technique/ α_c	ET (W m ⁻² /%)	H (W m ⁻² /%)	R_n (W m ⁻² /%)	G (W m ⁻² /%)
SEBS	(McCabe and Wood, 2006)	Landsat ETM+	182	–	Bias: -6	–	–	–
	(McCabe and Wood, 2006)	ASTER	182	–	Bias: 18	–	–	–
	(McCabe and Wood, 2006)	MODIS	182	–	Bias: -57	–	–	–
Triangle	(Choi et al., 2009)	Landsat TM/ETM+	174 and 182	BR	Bias: -93 RMSD: 115	Bias: -93 RMSD: 108	Bias: 21 RMSD: 26	Bias: 14 RMSD: 24
	(Choi et al., 2009)	Landsat TM/ETM+	174 and 182	RE	Bias: 133 RMSD: 146	–	–	–

Different studies using the same data set seem to show generally comparable accuracy of surface flux retrievals for the same type of model. Overall, the TSEB models (both parallel and series configurations) appear to be capable of reproducing LE and H fluxes with a higher accuracy compared with one-source models (SEBAL, METRIC, SEBS, and the triangle model). Bias of the LE retrievals from TSEB ranges between 4 W m^{-2} and 37 W m^{-2} and RMSD ranges between 30 W m^{-2} and 60 W m^{-2} . Similarly, the TSEB models generate H fluxes with bias ranging between -20 W m^{-2} and 39 W m^{-2} , and RMSD ranging between 30 W m^{-2} and 60 W m^{-2} .

SEBAL suggests a bias of LE up to 82 W m^{-2} . As a variant of SEBAL, METRIC reproduces LE with RMSD ranging between 42 and 75 W m^{-2} , and H with RMSD ranging between 42 and 57 W m^{-2} , both of which are slightly larger than that of TSEB and TTME. Neither the one-source models are designed to discriminate between soil surface evaporation and vegetation transpiration, nor can they reproduce surface fluxes at a handful of towers with higher accuracy than TSEB and TTME. Operability, data requirements, and objectives in practical applications would be the primary considerations for model selection. It is important to note that TTME generally shows a comparable accuracy as TSEB, implying a bias of 10 W m^{-2} , an RMSD of 45.6 W m^{-2} , and an MAPD of 8.7% for LE from TTME. In addition, retrievals of R_n and G from TTME also suggest similar magnitudes of RMSD on the order of $20\sim 30 \text{ W m}^{-2}$ as TSEB.

It is noted that the LE retrievals from TSEB generally show a positive bias (French et al., 2005a; Gonzalez-Dugo et al., 2009; Li et al., 2005) (some studies do not provide bias but provide the averaged LE estimates and averaged measurements) compared with

observed LE after forcing closure by both the residual and Bowen ratio techniques. This means that TSEB has a tendency to overestimate LE. In fact, there is a critical assumption involved in TSEB that the Priestley-Taylor formula (Priestley and Taylor, 1972) with a parameter α of ~ 1.3 applies for both stressed and unstressed vegetation and agricultural crops (French et al., 2005b), but there is no mechanism in the model to capture the condition of $\alpha_c < 1.26$ and $ET_s > 0$ (Agam et al., 2010). Only through the initial assumption about canopy transpiration formulated by the Priestley-Taylor formula can the model be triggered to partition T_{rad} into T_c and T_s and energy fluxes between soil and vegetation. However, as Agam et al. (2010) stated, parameter α built in the TSEB model varies to some extent with LAI, water stress status, vegetation type, and vapor pressure deficit. Parameter $\alpha = 1.3$ has been found large for stressed, large vapor pressure deficit, and naturally vegetated conditions, where a conservative value (e.g., 1 or less than 1) might be more suitable. That is to say, TSEB tends to overestimate LE under less soil wetness, large drying power of air, and natural vegetation cover conditions.

In addition, the LE outputs from these models can be evaluated by the observed LE after forcing closure by the residual method or the Bowen ratio method. The difference should be considered in comparing model accuracy. Furthermore, some studies, e.g., (Gonzalez-Dugo et al., 2009), utilized measured R_n and G to facilitate the simulation of H and LE, which tends to increase the accuracy of LE if the measured R_n and G are of less uncertainty than the modeled counterparts.

4.5.2. Advantages of TTME

The most significant attribute of TTME is its capability to discriminate vegetation transpiration from soil surface evaporation based on the two-source scheme. This attribute seems to be more beneficial in effective water use in agricultural crops and water resources management compared with one-source models. Validation of TTME against flux tower measurements across the SMACEX site on three Landsat TM/ETM⁺ imagery acquisition days in 2002 demonstrates that TTME appears to be capable of reproducing EF and LE on the order of MAPD within 10%. The EF estimates even show a smaller discrepancy in terms of an MAPD of 6.7%. This means that TTME shows comparable or even higher accuracy compared with TSEB, given the overestimation of vegetation transpiration using the Priestley-Taylor equation and the determination of the Priestley-Taylor parameter of somewhat subjectivity. In particular, TTME enjoys the following advantages:

(1) TTME is unique in its two-source scheme compared to one-source models. Also, it deviates from TSEB in explicitly accommodating soil water stress on vegetation transpiration. In TSEB, the vegetation transpiration is parameterized by the Priestley-Taylor equation for decomposing T_{rad} . The parameterization assumes canopy to transpire at potential rates regardless of f_c at the first approximation of the canopy temperature. Only when LE_s is attained with a nonphysical solution, i.e., $LE_s < 0$ corresponding to daytime condensation at the soil surface, can the Priestley-Taylor parameter α be manually lowered to account for soil moisture stress on LE_c (Crow et al., 2008; Kustas and Anderson, 2009). If a physical solution is otherwise obtained (i.e.,

$LE_s > 0$) and parameter α is not reduced, overestimates of LE could occur.

(2) TTME circumvents parameterization of the resistance networks involved in TSEB and the two-source model proposed by Nishida et al. (2003), and consequently the specification of variables and parameters (e.g., wind velocity field, canopy height, leaf size, leaf perimeter, and LAI) in surface and canopy resistances. The resistance networks seem difficult to handle across large areas. In TTME, only two theoretically hypothesized extreme surfaces require the computation of aerodynamic resistance. As the two extreme cases necessarily show some simplified physiological and surface properties, e.g., typical values of roughness length for the bare surface range from 0.005-0.02 m, the determination of aerodynamic resistance for the two extreme surfaces can be appropriately dealt with. This attribute allows TTME to effectively restrain uncertainties in the computation of resistance across large heterogeneous areas where the vegetation height, leaf width, and soil surface roughness are difficult to specify.

(3) TTME reduces uncertainties arising from the specification of warm and cold edges/pixels involved in one-source models by deriving the theoretical boundary conditions of EF. The configuration of the trapezoid f_c - T_{rad} space is dependent on three critical temperatures, i.e., $T_{s,max}$, $T_{c,max}$, and T_a , which can be derived by solving for energy balance and radiation budget equations. By contrast, the boundary conditions of SEBAL, METRIC, and the triangle model should be selected by the operator or derived from the NDVI- T_{rad} space, which involves large subjectivity and is dependent on the size and resolution of satellite imagery being used.

(4) TTME isolates uncertainties in R_n , G , and H from LE to a certain degree. Many

remote sensing-based models calculate LE as the residual term of the energy balance equation. Uncertainties in R_n , G , and especially H retrievals have to be encapsulated into the resulting LE estimates. In contrast, TTME directly calculates EF and LE without calculating H first. Uncertainties in the simulation of H are considerably mitigated by the TTME algorithm.

(5) TTME is robust in terms of model sensitivity. The most sensitive variables of TTME are T_{rad} and T_a , which can be retrieved or obtained with reasonable accuracy. Furthermore, TTME is not sensitive to some hypothesized physiologic parameters, e.g., h_c , or deduced surface properties, e.g., $\alpha_{c,\text{max}}$ and $\alpha_{s,\text{max}}$.

(6) TTME requires relatively fewer inputs compared with TSEB. Overall, TTME encompasses three types of inputs (see Fig. 4.2). The first type is remotely sensed variables, i.e., T_{rad} , f_c and α . The three surface characteristic variables are involved in most of the satellite-based models for surface flux and LE simulations. The second type is atmospheric variables at the satellite overpass, including T_a , e_a , and u/u^* . It is noted that T_a and e_a are indispensable variables for estimating radiant energy involved in models aimed at reproducing LE. In addition, MOD07_L2 atmospheric products provide remotely sensed T_a and dew point temperature (can be converted to e_a), which might be useful for being incorporated into TTME in the case of the absence of ground-based measurements. The wind velocity u or friction velocity u^* , involved in most one-source models (e.g., SEBAL and SEBS) and two-source models (e.g., TSEB), is also required to estimate the aerodynamic resistance for only two extreme surfaces in TTME. The third type of input consists of DEM, time related parameters (i.e., DOY and satellite overpass),

and surface properties (I_0 , h_c , $\alpha_{c,\max}$ and $\alpha_{s,\max}$), which can be readily obtained or appropriately specified. The input requirement of TTME has been substantially reduced as compared with other two-source models and even one-source models (e.g., SEBS).

4.5.3. Limitations of TTME

As other types of satellite-based ET models, TTME has its own applicability and limitations due to its assumptions:

(1) Linear weighted sum of temperatures: $T_{\text{rad}} = f_c T_c + (1 - f_c) T_s$. It is noted that the assumption is also used in the series-TSEB, e.g., Eq. (A5) in (Norman et al., 1995) and Eq. (A1) in (Anderson et al., 2007a). As long as the temperature difference between T_c and T_s is small compared with T_{rad} , this equation would be generally valid (Nishida et al., 2003a; Price, 1990). However, the use of the nonlinear combination of temperatures would be able to more accurately depict reality. This will be discussed in the future, and is beyond the scope of this study.

(2) Effects of advection on partitioning of turbulent energy fluxes are not explicitly accounted for. The use of T_a to be the cold edge of TTME would overestimate/underestimate surface temperatures of the wettest surfaces. In fact, pixels scattered below the cold edge of the trapezoid space might be indicative of the presence of advection, i.e., negative temperature gradients between the land surface and the lower atmosphere. Taking T_a to be the limit of $EF=1$ is, however, an operational way to demarcate the lower boundary condition. If there is advection for all wet surfaces with varying f_c , then determining the lower boundary seems to be infeasible.

(3) Derivation of the theoretical boundary conditions of TTME necessitates relatively homogeneous meteorological conditions (e.g., T_a , S_d , and u/u_*) over the entire scene. It could be deduced that the more heterogeneous the meteorological conditions, often corresponding to larger areas, the larger the uncertainties in the configuration of the trapezoidal boundary conditions. Over large areas, TTME would be applicable by geographical stratification. This means that a large study area could be partitioned into multiple sub-areas with relatively homogeneous meteorological conditions. Surface fluxes could then be simulated for each sub-area. Additional attention is paid to the applicability of TTME to semi-arid and arid areas, where soil surface evaporation dominates ET and groundwater recharge. Addressing these issues forms the foundation of our ongoing work.

4.6. Concluding remarks

The study presented in this chapter is primarily motivated by developing a more operational two-source remote sensing-based model for ET estimation, which is capable of reproducing surface fluxes with reasonable accuracy but requires less data than the existing two-source models and substantially reduces subjectivity involved in one-source models. A Two-source Trapezoid Model for Evapotranspiration (TTME) using satellite imagery has been developed. TTME is based on interpreting the f_c - T_{rad} space and the concept of isopleths of soil surface moisture availability superimposed in the space. The upper boundary condition ($T_{s,\text{max}}$ and $T_{c,\text{max}}$) of the model is derived by solving for radiation budget and energy balance equations for the hypothesized driest bare surface

and the driest fully vegetated surface. Air temperature T_a constitutes the lower boundary of the model. Determination of these theoretical boundary conditions is dependent on less meteorological forcing and surface property parameters, which can be obtained with reasonable accuracy or appropriately specified. Radiative temperature T_{rad} of a pixel is decomposed into temperature components T_c and T_s by interpolating the slopes of the theoretical boundaries for the isopiestic line going across the pixel. Subsequently, vegetation transpiration and soil surface evaporation can be separately parameterized. TTME is applied to the SMACEX site in central Iowa, U.S., on three Landsat TM/ETM⁺ imagery acquisition dates during the period of rapid growth in corn and soybean crops in 2002. Results indicate that the model is capable of reproducing EF and LE with an MAPD of 6.7% and 8.7% and an RMSD of 0.06 and 45.6 W m⁻², respectively. Comparison of TTME with other one-source and two-source models using the same data set suggests that TTME shows comparable accuracy as TSEB, but requires relatively fewer inputs and does not need to compute the resistance networks. In addition, the most sensitive variables of TTME, T_{rad} and T_a , can be retrieved or obtained with reasonable accuracy. Compared with other one-source models, TTME substantially reduces subjectivity in determining boundary conditions, i.e., extreme pixels/edges. Additional efforts will be made to validate the model in the semi-arid and arid environments. Geographic stratification would make the model applicable to large river basins or regional scales.

CHAPTER V

SENSITIVITY OF SEBAL TO CHANGES IN INPUT VARIABLES, DOMAIN SIZE AND SATELLITE SENSOR

5.1. Introduction

SEBAL (Bastiaanssen et al., 1998a; Bastiaanssen et al., 1998b) was designed to simulate surface fluxes across areas with sufficiently large hydrologic contrast by incorporating remotely sensed variables and a minimum of ground data. This model has been widely used for estimation of water consumption by agricultural crops and natural vegetation, crop water productivity and water depletion in a river basin, formulation of appropriate irrigation schedules, and assisting in water resources management (Allen et al., 2007; Bastiaanssen et al., 2002; Bastiaanssen et al., 2005; Teixeira et al., 2009a). In hydrologic and atmospheric modeling, SEBAL-based ET can be utilized to quantify the impact of expanding irrigated agriculture on the regional water balance (Teixeira et al., 2009b) and to improve the spatial representation of water balance components in hydrologic models (Droogers and Bastiaanssen, 2002; Immerzeel and Droogers, 2008; Schuurmans et al., 2003). Bastiaanssen et al. (2005) summarized the overall accuracy of SEBAL-based ET in terms of its application in more than 30 countries to a variety of climates and ecosystems at different spatial scales. They asserted that for a range of soil wetness and plant community conditions, typical accuracy at the field scale was 85% for 1 day and it increased to 95% on a seasonal or annual basis (Bastiaanssen et al., 2010).

SEBAL is based on a set of formulas involved in each component of the energy

balance equation. How different variables/parameters in these equations interact with each other and vary with the domain scale would largely determine the mechanism of error propagation and the magnitude of error in the resulting surface flux estimates. The domain scale is defined here as the size of satellite images being used/modeling domain being considered. The domain dependence is referred to as the dependence of the magnitude and distribution of retrievals from a model on the domain scale.

SEBAL assumes the difference between the aerodynamic temperature and the air temperature to be linearly proportional to remotely sensed LST. Linear coefficients a and b (a_0 and b_0 in Chapter III) should be derived from two extreme pixels selected by the operator from images. The selection procedure is, however, influenced somewhat by subjectivity (Gao et al., 2008; Timmermans et al., 2007; Winsemius et al., 2008). The output of SEBAL would depend on domain scales in that the two extreme pixels would be identified at different locations with disparate characteristic variables (e.g., $T_{s,hot}$ and $T_{s,cold}$) on varying domain scales. Varying spatial coverage and quality of satellite images available and different considerations of the domain of interest would result in different extremes. Some studies have reported that it is difficult to properly select pixels representing extreme hydrologic conditions; improper selection may cause large uncertainties in the resulting surface flux estimates (Bastiaanssen et al., 2010; Singh et al., 2008; Timmermans et al., 2007). However, the uncertainty arising from the selection procedure has not been systematically quantified.

On the other hand, satellite-based ET algorithms are typically developed and tested at the resolution scale of a certain sensor based on the assumption of homogeneity within the

pixel resolution. Here the resolution scale is defined as the spatial resolution of satellite images being used. Similarly, the resolution dependence is referred to as the dependence of the magnitude and distribution of retrievals from a model on the resolution scale. There is a tendency to directly apply the algorithms developed at a finer scale to a coarser scale (Gebremichael et al., 2010). For instance, SEBAL was first developed and tested on the resolution scale of Landsat TM images. However, it was asserted that the model can handle thermal infrared images at resolutions between a few meters to a few kilometers (Bastiaanssen, 1995; Bastiaanssen et al., 1998a) being applied to a variety of satellite platforms, e.g., ASTER (Gebremichael et al., 2010), NOAA-AVHRR (Bastiaanssen et al., 2002; Bastiaanssen and Chandrapala, 2003), and MODIS (Compaore et al., 2008; Kongo and Jewitt, 2006). A noteworthy concern associated with the resolution dependence is: Are the resulting estimates from coarse resolution data combined with the algorithm developed at a fine-resolution scale reliable? Are there differences in the magnitude and distribution between those estimates?

It is noted that the resolution dependence of a model is primarily a consequence of the resolution of inputs; uncertainty in the outputs are propagated in a large part by the resolution of the input rather than the model physics. However, uncertainties arising from the resolution dependence in SEBAL might also result in the alteration of the model physics by changing coefficients a and b . This means that the resolution dependence of SEBAL would be compounded by its domain dependence.

There have been some studies on the resolution dependence of ET retrievals from satellite-based models (e.g., TSEB and SEBS) across a variety of satellite platforms (e.g.,

Landsat TM/ETM⁺, ASTER, and MODIS) (Brunner et al., 2008; Kustas et al., 2004; Li et al., 2008a; McCabe and Wood, 2006; Su et al., 2007). These studies provide insights into variations in ET retrievals at varying resolutions. They are greatly helpful in building an understanding of heterogeneity in coarse resolution image-based retrievals. However, a few published studies have addressed the domain and resolution dependencies of SEBAL, which have not restrained the misuse of this model in operational ET estimation.

Allen et al. (2007) developed a satellite-based image-processing model for mapping ET, METRIC, in which the key component for computing H inherits substantially from SEBAL. Sensitivity analysis can identify the most sensitive variables/parameters for quantifying model uncertainty, and consequently provide valuable insight into the degree of effort that should be made to constrain errors of a model. If the sensitive variables of a model are domain and/or resolution dependent, variations in the model outputs on a variety of scales can be quantified. The sensible heat flux (H) appears to be the most critical component in the energy balance-based approach in terms of the proportion of H in the energy balance and the complexity of parameterization. However, the sensitivity of H estimates from SEBAL to the model input has not yet been fully examined.

Wang et al. (2009) performed a sensitivity analysis of SEBAL on full, half, and sparse cover conditions. We suggest that the application of SEBAL does not depend on cover conditions and land use types; the three cover conditions, as a matter of fact, only provide three initial value conditions for running the model. A more comprehensive sensitivity analysis of SEBAL can therefore be achieved by varying inputs under a

broader range of initial value conditions. Marx et al. (2008) performed an uncertainty analysis of SEBAL-based H estimates using the Gaussian error propagation, indicating that the computed total relative uncertainty in H was 15% for the Tamale site and 20% for the Ejura site (both in the central part of West Africa). Nevertheless, they did not quantify the effect of extreme pixels in SEBAL, which would not allow a thorough understanding of the sensitivity of SEBAL.

The critical issues mentioned above have significantly hindered a better understanding of the behavior of SEBAL and its proper application. If the model sensitivity and domain and resolution dependencies were not fully understood, the user would not be able to achieve the expected accuracy of model output by properly restraining the sources of errors either from input or the model physics.

In this chapter, a detailed sensitivity analysis on the H algorithm of SEBAL was first performed, on the basis of which the domain and resolution dependencies of SEBAL were investigated by applying it to the Baiyangdian watershed and its sub-watersheds in North China, and to Landsat TM and MODIS imageries. Through a theoretical investigation into the model physics, it is expected that SEBAL would be better understood and more properly applied to hydrologic modeling and water resources management. If the output of SEBAL does change with domain and/or resolution scales, the model output derived at the scale where the performance is poor should be used with caution, or scale-independent models can be considered. If it does not change with scale, the model can be applied in more circumstances. Section 5.2 presents remotely sensed and meteorological data used and a description of the study watersheds. Section 5.3 provides sensitivity analysis of the

H algorithm of SEBAL. Section 5.4 discusses problems and procedures for selection of extreme pixels in SEBAL. Discussion on the domain dependence and resolution dependence of SEBAL are presented in Sections 5.5 and 5.6, respectively, followed by concluding remarks of this chapter in Section 5.7.

5.2. Study site, data and variable derivation

5.2.1. Study site

The Baiyangdian watershed is described in Section 2.2.1 (hereafter watershed I). The Zhulong River watershed (hereafter watershed II, Fig. 5.1) with the outlet at the Beiguocun hydrologic station was delineated from watershed I, covering an area of around 8550 km². Elevation ranges from roughly 28.0 m to 2784.3 m, with a mean value of 478.9 m. There are three weather stations within watershed II, approximately distributed in the upper, middle, and lower reaches of the watershed (Fig. 5.1). The mean annual precipitation of around 608.7 mm falls in watershed II, showing a generally decreasing trend from the upper to the lower reaches. The Sha River watershed (hereafter watershed III) with the outlet located at the Wangkuai Reservoir is located in the upper reaches of watershed II, covering an area of 3770 km² (Fig. 5.1). The Fuping hydrologic station is located in the middle reaches of watershed III. Elevation of watershed III ranges between 180.0-2784.3 m, with a mean annual precipitation of 676.9 mm being observed at the Fuping hydrologic station. There is a weather station located in Fuping, providing routine meteorological data.

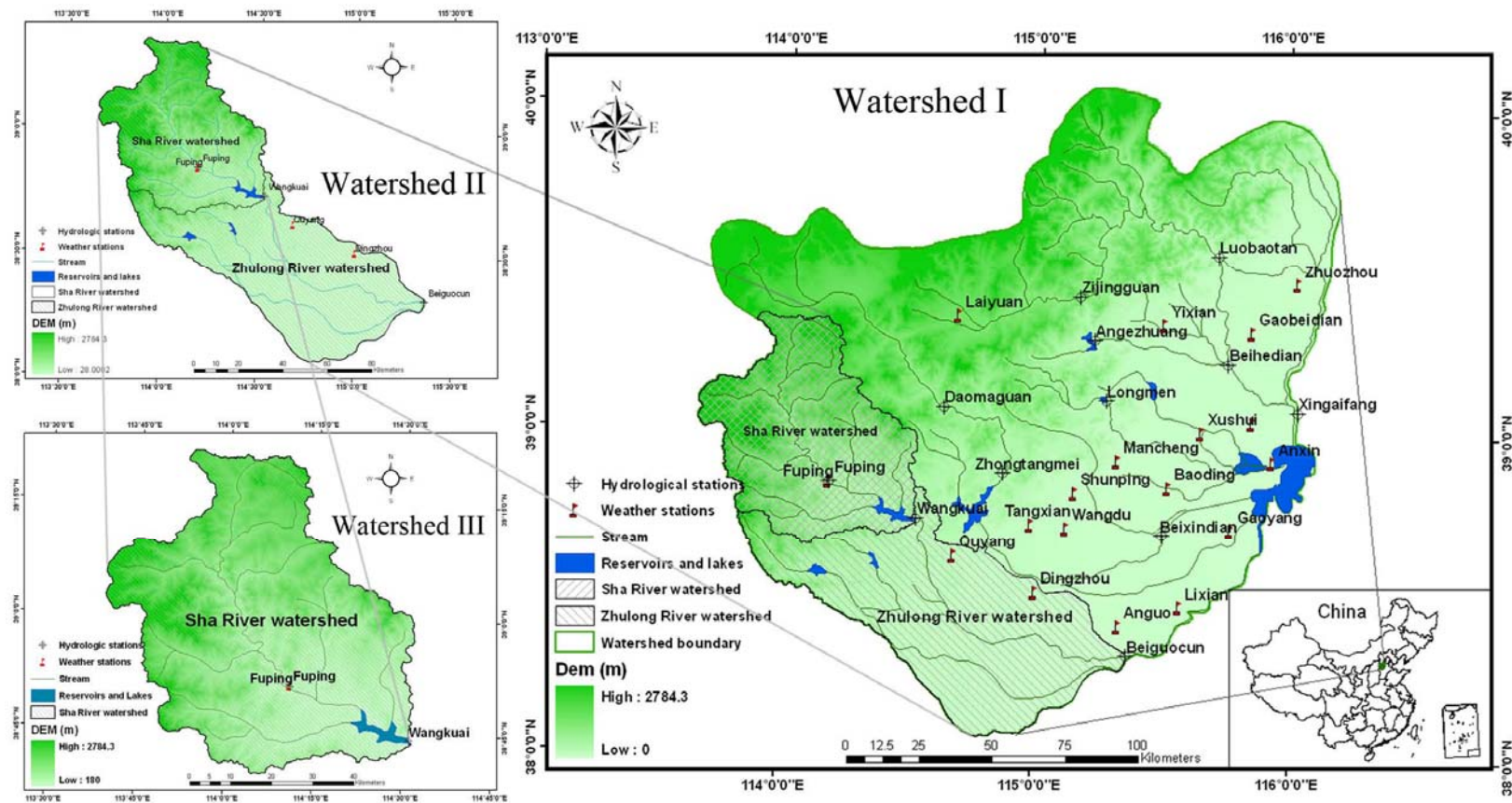


Figure 5.1 The Baiyangdian watershed (watershed I) with its sub-watersheds, the Zhulong River watershed (watershed II) and the Sha River watershed (watershed III) and relevant facilities, North China.

5.2.2. Data

Meteorological data and MODIS data products are described in sections 2.2.2 and 3.4.2. For investigating the resolution dependence of SEBAL, a scene of Landsat TM imagery (path/row 124/33) acquired at 10:54 a.m. (local time) on May 19, 2007 was used, with a solar azimuth angle of 130.94° and a solar elevation angle of 63.64° . A set of MODIS data products within the spatial coverage of the Landsat TM imagery were also obtained. One swath of MOD11_L2 covering about 90% of watershed I was obtained at 10:25 a.m. on May 19, 2007, and the other swath of MOD11_L2 covering about 10% of watershed I was obtained at 12:05 a.m. (local time). Note that the Landsat imagery was almost cloud-free except for minor contamination by cirrus clouds; there was about 10% cloud cover contamination for the MODIS LST products. Effects of differences in the time of image acquisition between Landsat TM and Terra-MODIS on surface flux retrievals were assumed to be negligible.

5.2.3. Variable derivation

For Landsat TM imagery, much more preprocessing work (e.g., geometric and radiometric corrections) should be done before retrieving surface variables and then simulating surface fluxes by SEBAL. Surface albedo was derived from the visible and near-infrared bands (band 1-5, 7). The at-sensor radiance is first converted into at-sensor bidirectional reflectance (Chander et al., 2009), on the basis of which the narrowband at-surface reflectance and broadband surface albedo can be derived using calibrated atmospheric transmittance and path reflectance formulas at the time of satellite overpass

(Tasumi et al., 2008). In Tasumi et al. (2008)'s algorithms, vapor pressure, atmospheric pressure, and the turbidity coefficient at satellite image time are required to estimate atmospheric transmittance and path reflectance. In this study, vapor pressure and atmospheric pressure were obtained from meteorological stations within watershed I. A value of 1.0 for the turbidity coefficient indicates clean air and a value of 0.5 indicates extreme turbidity. We took it as 1 in this study based on observed meteorological conditions on that day.

The brightness temperature was retrieved from band 6 of Landsat TM imagery (Chander et al., 2009), which was further processed by atmospheric and emissivity corrections to be converted into LST using the algorithm proposed by Jimenez-Munoz and Sobrino (2003). In the algorithm, precipitable water content and thermal infrared band emissivity were required for LST retrieval. In the absence of radiosounding data depicting the atmospheric profile, the precipitable water content can be obtained from the MOD05_L2 product. The precipitable water content can be determined with errors typically ranging between 5-10% under no-hazy conditions (visibilities less than 10 km corresponding to hazy conditions) (Gao and Kaufman, 2003). The visibility over the entire watershed I on May 19, 2007, was observed to be approximately 20 km, which could be indicative of high confidence in the accuracy of the MOD05_L2 precipitable water content product. The thermal infrared band emissivity can be estimated using the NDVI thresholds method (Sobrino and Raissouni, 2000).

5.3. Sensitivity analysis of H

Recall that SEBAL estimates H in two steps. The first step is to derive linear regression coefficients a and b from the characteristic variables of extreme pixels, i.e., $R_{n,hot}$, G_{hot} , $T_{s,hot}$, $T_{s,cold}$, $z_{om,hot}$, and ρ_{hot} . In this chapter, such variables are defined as local variables hereafter for the convenience of discussion in the following sections. The second step is to compute H for the remaining pixels except for the extreme pixels in an image in terms of their respective characteristic variables, i.e., T_s , z_{om} , ρ , and the derived a and b from the first step. The characteristic variables of the remaining pixels are termed global variables hereafter. It is noted that u_{200} is involved in both the first step to derive a and b and in the second step to derive u^* for other pixels.

There were 28 sets of reference values selected from 28 cloud-free days in year 2007 spanning a broad range of atmospheric, soil moisture, and land cover conditions. These reference values provided 28 sets of initial value conditions for initialization of the H algorithm of SEBAL. The model sensitivity was performed by varying each variable/parameter under a given set of reference values at a step of 5% (perturbation) with the upper and lower limits of $\pm 50\%$ (a 0.5 K perturbation and the upper and lower limits of ± 5 K for LST given variations as large as $\pm 50\%$ for LST would not occur in reality). Variations in the resulting H estimates due to the variations in inputs were then evaluated. This is a general way to perform sensitivity analysis of remote sensing-based ET models (Sanchez et al., 2008; Timmermans et al., 2007).

It is noted that variations in the resulting H estimates are a function of both the initial value condition (reference values) and the perturbation of each variable/parameter. Each

perturbation can be taken as an integrated effect of uncertainties in model input under certain soil moisture and meteorological conditions. As indicated in Section 3.3.1, H can be obtained in an iterative manner. The iterative process was terminated as the absolute value of the difference between the last two estimates of a , b , and H over the estimates next to the last was less than 1%. It is apparent that the number of iterations is not necessarily equal to five as indicated by Bastiaanssen (2000), relying on the specified termination condition for the iterative process.

5.3.1. Sensitivity to local variables

In general, all local variables, except $R_{n,hot}$, associated with the characteristics of hot and cold pixels are negatively correlated with the H estimates. Coefficient a has a positive value and coefficient b has a negative one. It is critically important to note that the H estimates exhibit the highest sensitivity to $T_{s,hot}$ and $T_{s,cold}$. Fig. 5.2 graphically illustrates the maximum, minimum, and mean variations in the averaged H estimates of the entire scene for the 28 sets of reference values at each perturbation of $T_{s,hot}$ and $T_{s,cold}$, respectively. Results indicate that a 2 K increase in $T_{s,hot}$ is likely to result in a 9.3% increase but a 9.1% decrease in a and b , respectively, and an average of 11.8 % decrease in H . Likewise, a 2 K increase in $T_{s,cold}$ can cause an 11.7% increase and a 12.5% decrease in a and b , respectively, and an average of around 14.6% decrease in H estimates (also see Table 5.1). Furthermore, with increasing perturbation in $T_{s,hot}$, the first-order derivative of the curve between the perturbation in $T_{s,hot}$ and the variation in H estimates tends to decrease. By contrast, $T_{s,cold}$ exhibits an opposite trend, with increasing perturbation in

$T_{s,cold}$ corresponding to an increase in the first-order derivative.

Table 5.1 Sensitivity of SEBAL to all local and global variables for 28 sets of reference values for the Baiyangdian watershed in 2007. Variations of the variables and H estimates are in percentage and variations of land surface temperatures are in K. Min, Max, and Mean represent the minimum, maximum, and mean variations in H estimates, respectively

Variations % (K) Variable		-50 (-5)	-40 (-4)	-30 (-3)	-20 (-2)	-10 (-1)	10 (1)	20 (2)	30 (3)	40 (4)	50 (5)
$T_{s,hot}$	Min	32.1	24.2	17.2	10.9	5.2	-9.6	-17.6	-24.4	-30.2	-35.3
	Max	96.1	66.2	43.4	25.7	11.5	-4.7	-9.0	-13.0	-16.6	-20.0
	Mean	49.2	36.0	24.8	15.3	7.1	-6.3	-11.8	-16.8	-21.3	-25.3
$T_{s,cold}$	Min	14.9	12.3	9.5	6.6	3.4	-12.4	-26.1	-41.3	-57.9	-76.0
	Max	47.3	39.5	30.9	21.5	11.3	-3.6	-7.6	-11.8	-16.4	-21.4
	Mean	27.3	22.7	17.6	12.2	6.4	-7.0	-14.6	-22.9	-32.1	-42.2
$R_{n,hot}$	Min	-72.2	-57.5	-42.9	-28.5	-14.2	11.7	23.4	35.0	46.5	57.9
	Max	-60.7	-48.2	-35.9	-23.8	-11.8	14.1	28.2	42.2	56.2	70.2
	Mean	-67.1	-53.1	-39.5	-26.2	-13.0	12.9	25.6	38.2	50.7	63.2
G_{hot}	Min	12.4	9.9	7.4	5.0	2.5	-4.5	-9.1	-13.6	-18.2	-22.8
	Max	22.6	18.1	13.6	9.0	4.5	-2.5	-5.0	-7.5	-10.0	-12.5
	Mean	18.1	14.5	10.9	7.3	3.6	-3.6	-7.3	-11.0	-14.7	-18.4
ρ_{hot}	Min	84.0	56.7	36.8	21.7	9.7	-8.8	-16.2	-22.4	-27.8	-32.4
	Max	95.6	63.9	41.2	24.1	10.7	-8.0	-14.8	-20.6	-25.6	-30.0
	Mean	90.0	60.5	39.2	23.0	10.3	-8.5	-15.6	-21.6	-26.8	-31.4
$z_{om,hot}$ ($z_{oh,hot}$ =0.1)	Min	-1.8	-1.2	-0.8	-0.5	-0.2	-0.7	-1.4	-2.0	-2.6	-3.2
	Max	4.7	3.5	2.5	1.6	0.8	0.2	0.4	0.5	0.6	0.7
	Mean	1.7	1.3	1.0	0.6	0.3	-0.3	-0.6	-0.9	-1.2	-1.4
$z_{om,hot}$ ($z_{oh,hot}$ = 0.1 $z_{om,hot}$)	Min	18.1	13.1	9.1	5.6	2.6	-4.1	-7.7	-10.9	-13.8	-16.4
	Max	33.4	23.9	16.3	10.0	4.6	-2.3	-4.5	-6.4	-8.1	-9.8
	Mean	25.1	18.1	12.4	7.7	3.6	-3.1	-6.0	-8.5	-10.8	-12.9
T_s	Min	-84.7	-70.8	-55.7	-38.8	-20.2	9.2	18.7	28.3	38.1	48.1
	Max	-43.1	-34.9	-26.5	-17.9	-9.1	21.8	45.1	69.8	96.0	123.5
	Mean	-59.8	-49.1	-37.7	-25.7	-13.1	13.6	27.7	42.3	57.4	72.8
z_{om} ($z_{oh}=0.1$)	Min	-6.9	-5.2	-3.7	-2.4	-1.1	0.2	0.4	0.7	0.9	1.1
	Max	-1.0	-0.8	-0.6	-0.4	-0.2	1.1	2.1	3.0	3.9	4.8
	Mean	-4.5	-3.4	-2.4	-1.6	-0.8	0.7	1.4	2.0	2.7	3.2
z_{om} ($z_{oh}=0.1z_{om}$)	Min	-26.2	-20.4	-14.9	-9.7	-4.8	2.6	5.0	7.4	9.6	11.8
	Max	-16.2	-12.4	-8.9	-5.7	-2.8	4.6	9.1	13.4	17.7	21.8
	Mean	-21.1	-16.2	-11.8	-7.6	-3.7	3.5	6.9	10.2	13.4	16.4
u_{200}	Min	-21.7	-16.7	-12.1	-7.7	-3.7	0.9	1.8	2.5	3.2	3.8
	Max	-5.7	-4.5	-3.3	-2.1	-1.0	3.5	6.8	9.9	12.8	15.5
	Mean	-14.0	-10.6	-7.5	-4.8	-2.3	2.0	3.9	5.5	7.0	8.4

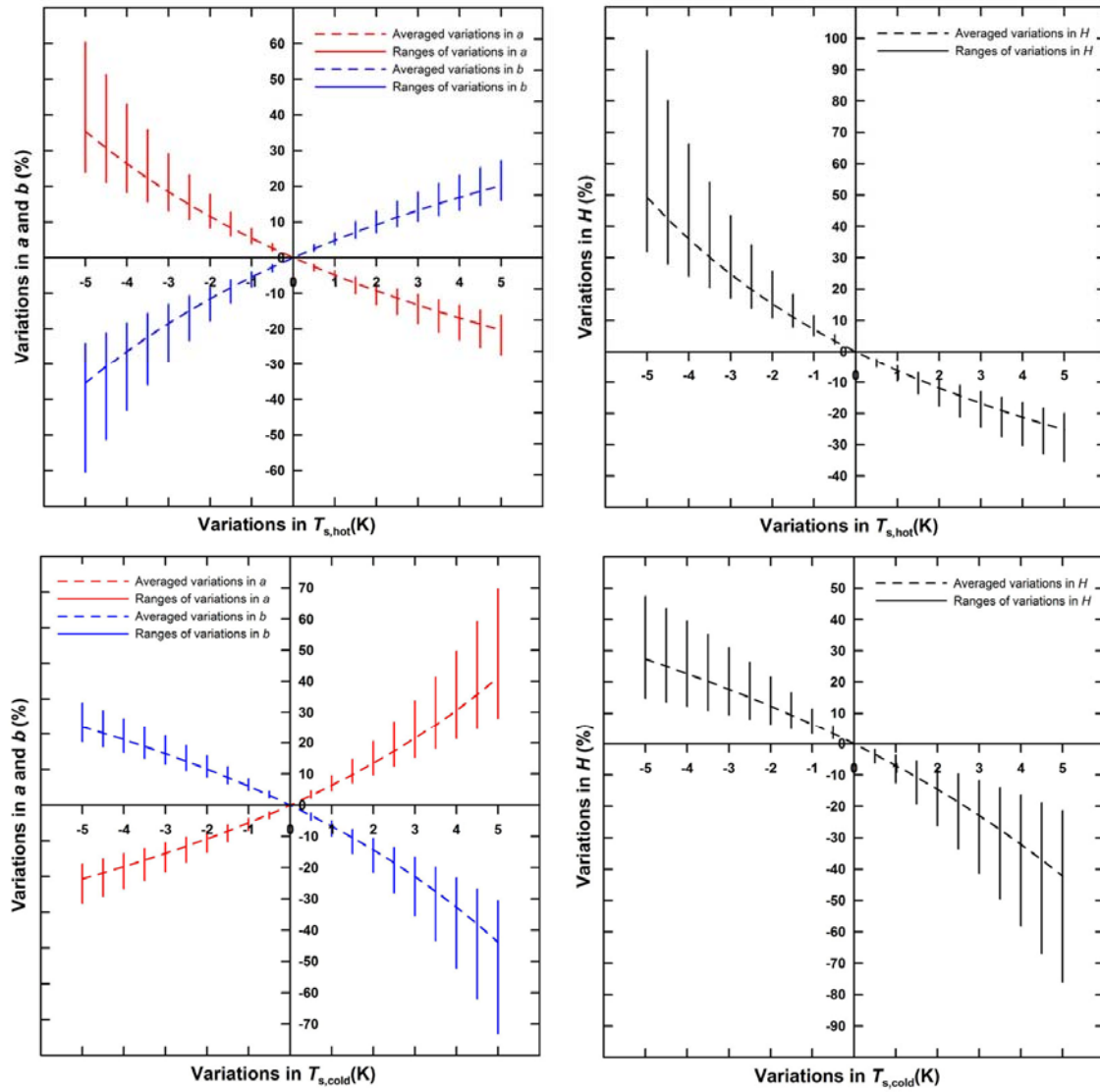


Figure 5.2 Sensitivity analysis of a , b , and H estimates to $T_{s,hot}$ and $T_{s,cold}$ for 28 initial value conditions, with the maximum, minimum, and mean variations for the 28 sets of reference values at each perturbation of $T_{s,hot}$ and $T_{s,cold}$ (0.5 K with the limits of ± 5 K). High-low lines on each plot represent the maximum and minimum variations. Dashed lines represent the mean variation.

$R_{n,hot}$ is closely related to the determination of H in SEBAL, which has not received much attention in previous studies. Fig. 5.3 illustrates the maximum, minimum, and mean variations in the averaged H estimates of the entire scene for the 28 sets of

reference values at each perturbation of $R_{n,hot}$ and $G_{n,hot}$, respectively. It is found that a 10% increase in $R_{n,hot}$ can lead to a 9.7% increase and a 9.7% decrease in a and b , respectively, and an average of 12.9% increase in H . As such, the energy availability ($R_{n,hot}-G_{hot}$) for the hot extreme contributes largely to the resulting H estimates following extreme temperatures. This further underlines the relevance of the selection of extreme pixels in SEBAL. In particular, the hot pixel is of more importance than the cold pixel.

5.3.2. Sensitivity to global variables

Sensitivity analysis of the resulting H estimates to the global variables given each pair of coefficients a and b derived for each set of reference values was performed. Results (Table 5.1) indicate that the model is most sensitive to T_s , with a 2 K increase in T_s yielding an average of 27.7% increase in the H estimates. It is apparent that ρ is linearly correlated with the resulting H estimates with a correlation coefficient of 1. Fortunately, this physical quantity can be readily estimated without causing large uncertainty.

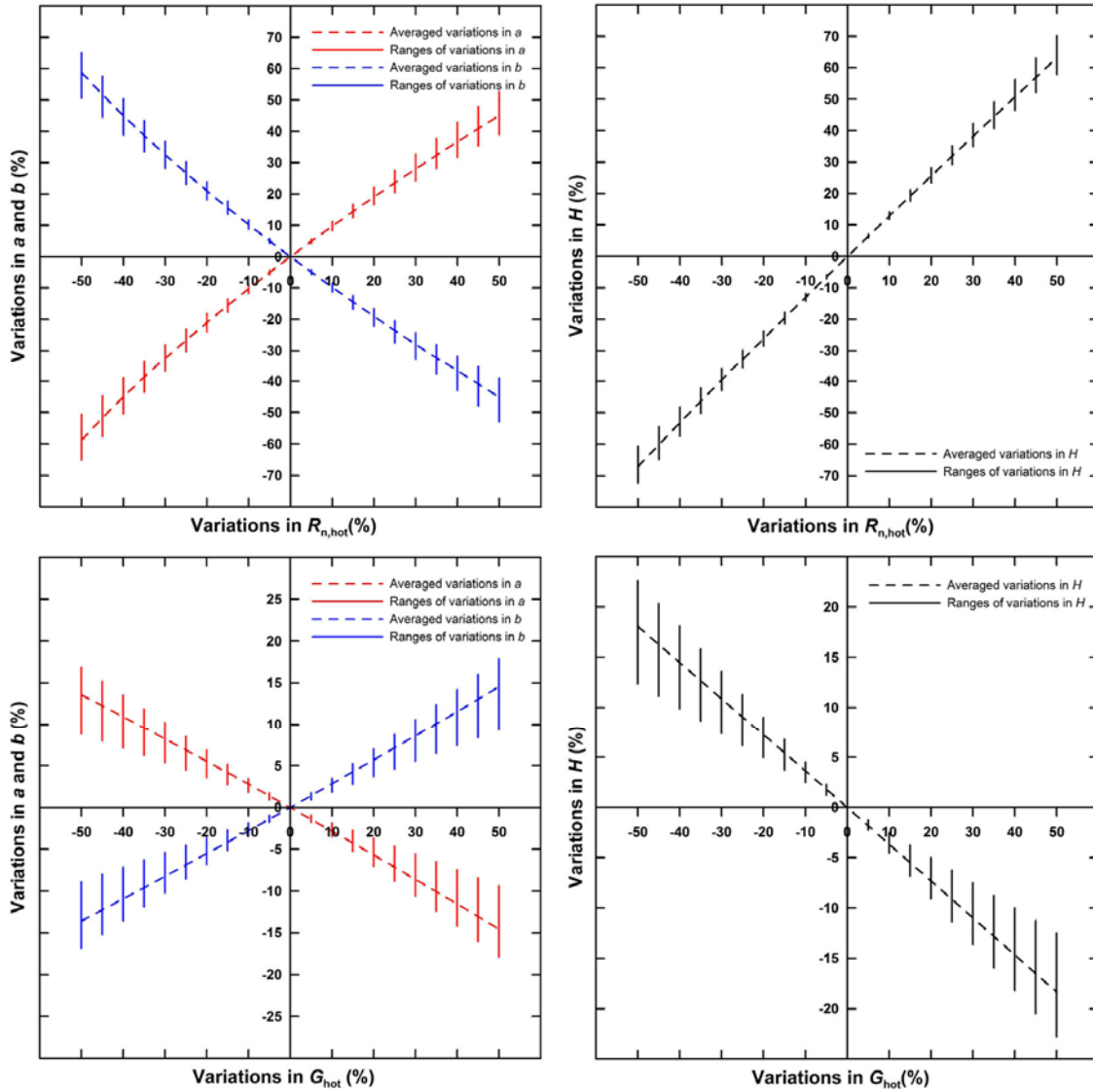


Figure 5.3 Sensitivity analysis of a , b , and H estimates to $R_{n,hot}$ and G_{hot} for 28 initial value conditions, with the maximum, minimum, and mean variations for the 28 sets of reference values at each perturbation of $R_{n,hot}$ and G_{hot} (5% with the limits of $\pm 50\%$). High-low lines on each plot represent the maximum and minimum variations. Dashed lines represent the mean variation.

5.3.3. Sensitivity to z_{om} and z_{oh}

It is noted that there are two versions of the treatment of z_{om} and z_{oh} (z_1 in SEBAL).

First, z_{oh} is taken to be a fixed value of 0.1 m. Second, z_{oh} is taken to be $0.1z_{om}$

corresponding to a kB^{-1} parameter of 2.3. Sensitivity analysis of the H algorithm to z_{om} under the two conditions was performed. It is found that the resulting H estimate appears to be insensitive to $z_{\text{om,hot}}$ under both conditions (Fig. 5.4 and Table 5.1). Under the first condition, a 10% increase in $z_{\text{om,hot}}$ can only lead to a 0.2% decrease but a 0.2% increase in a and b , respectively, and an average of 0.3% decrease in H estimates. Under the second condition, a 10% increase in $z_{\text{om,hot}}$ can result in a 2.6% decrease but a 2.6% increase in a and b , respectively, and an average of 3.1% decrease in H estimates. Taking a fixed value of $z_{\text{oh}}=0.1$ m has shown a small effect on the resulting H estimates compared with taking a kB^{-1} of 2.3.

Note that the hot pixel often corresponds to a bare soil surface. If accurate calibration or measurements are not available, a typical value of 0.005 m for $z_{\text{om,hot}}$ can be used (Allen et al., 2007). This obviates the specification of $z_{\text{om,hot}}$ for determining a and b .

Regarding the global variable z_{om} for the remaining pixels in an image, results show that under the condition of $z_{\text{oh}}=0.1$ m, a 10% increase in z_{om} can only result in an average of 0.7% decrease in the H estimate. Similarly, under the condition of $\text{kB}^{-1}=2.3$, a 10% increase in z_{om} only introduces an average of 3.7% decrease in the H estimate.

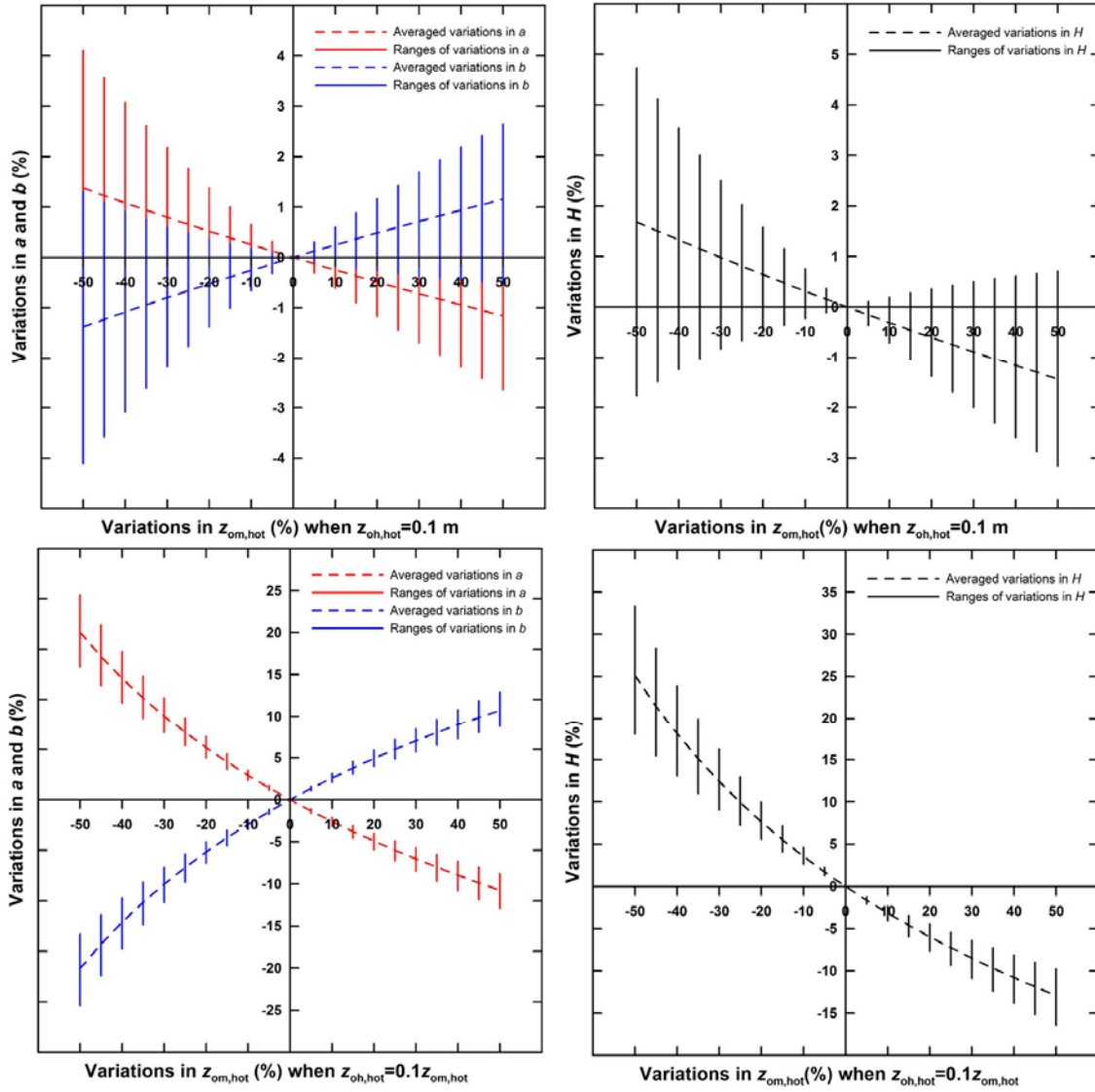


Figure 5.4 Sensitivity analysis of a , b , and H estimates to $z_{om,hot}$ under the conditions of $z_{oh,hot}=0.1$ m and $z_{oh,hot}=0.1z_{om,hot}$ for 28 initial value conditions, respectively, with maximum, minimum, and mean variations for the 28 sets of reference values at each perturbation of $z_{om,hot}$ (5% with the limits of $\pm 50\%$). High-low lines on each plot represent the maximum and minimum variations. Dashed lines represent the mean variation.

In summary, the effects of $z_{om,hot}$ and z_{om} have been substantially reduced in SEBAL under both conditions of $z_{oh,hot}$ or $z_{oh}=0.1$ m and $kB^{-1}=2.3$. The H estimates are not

strongly dependent on $z_{om,hot}$ and z_{om} , which can be specified as 0.005 m in terms of the characteristic of the bare surface or appropriately estimated by remotely sensed vegetation index or LAI. However, the two different treatments do result in different H estimates, suggesting an MAPD of 36.0%. It is noted that more studies on SEBAL have used $z_{oh}=0.1$ m (Allen et al., 2007; Bastiaanssen et al., 2002; Bastiaanssen et al., 2005), rather than introducing the kB^{-1} of 2.3 (Bastiaanssen, 2000; Kalma et al., 2008; Timmermans et al., 2007). Investigation of other local and global variables here is based on $z_{oh,hot}$ and $z_{oh}=0.1$ m.

5.3.4. Sensitivity to u_{200}

It is noted that u_{200} is defined here both as a local variable determining $r_{ah,hot}$ and a global variable determining r_{ah} for the remaining pixels in that a constant value of u_{200} over the entire scene is used in SEBAL. A 10% increase in u_{200} can only result in a 1.6% decrease but a 1.6% increase in a and b , respectively, and a 2.0% decrease in H estimates (see Fig. 5.5). In SEBAL, u_{200} is inferred using a logarithmical wind profile function combined with observations of wind velocity at a weather station within or near a study site. Sensitivity analysis indicates that u_{200} plays an immaterial role in the SEBAL algorithm.

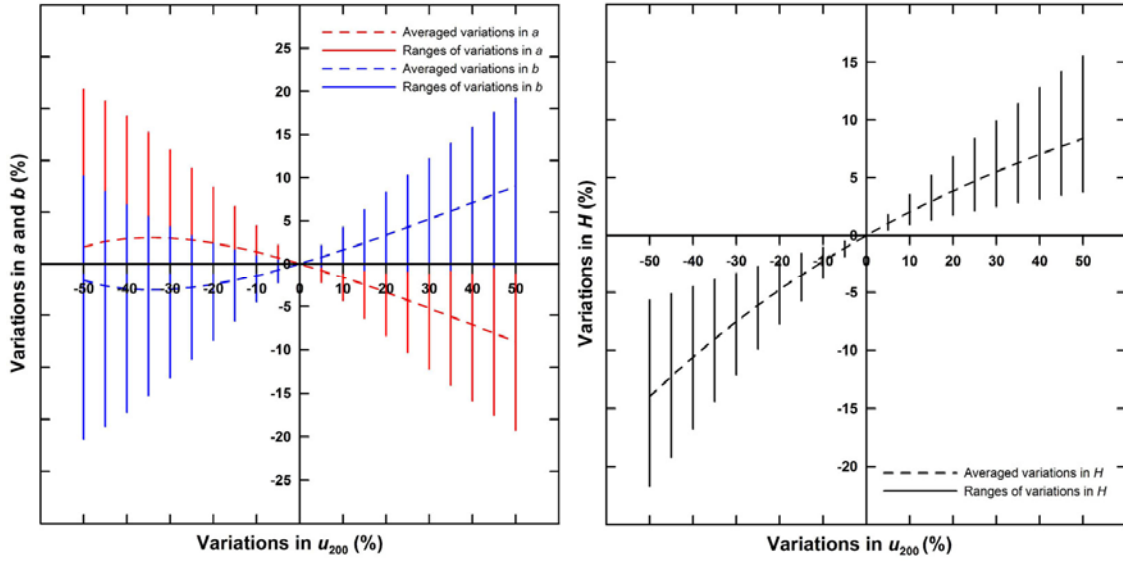


Figure 5.5 Sensitivity analysis of a , b , and H estimates to u_{200} for 28 initial value conditions, with maximum, minimum, and mean variations for the 28 sets of reference values at each perturbation (5% with the limits of $\pm 50\%$). High-low lines on each plot represent the maximum and minimum variations. Dashed lines represent the mean variation.

It is noted that for all of these local variables, only $T_{s,hot}$, $R_{n,hot}$, and G_{hot} show certain dependence. An increase in $T_{s,hot}$ would result in a decrease in $R_{n,hot}$ due to an increase in outgoing longwave radiation and result in an increase in G_{hot} , both of which contribute to decreases in H as discussed in Section 5.3.1. However, fixing $R_{n,hot}$ and G_{hot} to perform the sensitivity of H to $T_{s,hot}$ also shows that an increase in $T_{s,hot}$ could result in a decrease in H . This means that the sensitivity of SEBAL to $T_{s,hot}$ performed here tends to be conservative given certain dependence of $T_{s,hot}$, $R_{n,hot}$, and G_{hot} . In reality, the SEBAL algorithm would show a larger sensitivity to $T_{s,hot}$.

5.4. Selection of extreme pixels

In terms of the sensitivity analysis performed in Section 5.3, selection of two

extremes, particularly the hot pixel, plays a vital role in determining regression coefficients a and b and subsequently shows a great impact on the H estimates. Investigating the domain scale behavior of SEBAL requires a thorough investigation into change in the distribution of extreme pixels due to varying domains.

5.4.1. Problems in selection of extremes

There seems to be no consensus on how to select the hot pixel (Compaore et al., 2008; Marx et al., 2008; Timmermans et al., 2007) and the cold pixel; or it is not clear how the two extremes are identified in the calculation of the a and b coefficients and then H . (French et al., 2005b; Hong et al., 2009; Kongo and Jewitt, 2006; Ramos et al., 2009; Teixeira et al., 2009a). A few published studies have addressed procedures for identifying the extreme pixels. Most studies related to SEBAL only state the hypothesis of extreme pixels and/or provide spatial representation of the resulting fluxes that is highly correlated with the distribution of LST.

In addition to the difficulty of appropriately determining extreme pixels, it is suggested that there exist various uncertainties in the distribution of extreme pixels resulting from the modeling domains being considered. It is expected that the location and characteristic variables of extreme pixels are likely to vary with different domains. This problem would be frequently encountered due to a variety of cases below.

First, pixels satisfying the assumptions in SEBAL would largely rely on the quality of remotely sensed images. Good quality images for cloud-free days are not always available for operational ET estimation. Contamination of clouds would make portions of an image

blurred or obstructed, resulting in a reduction in the domain of interest and thus the shrinking of the range of LST. It seems that selection of the cold pixel tends to be largely impacted by clouds in that a cloud pixel might be mistakenly taken as the cold pixel (Gao et al., 2008; Marx et al., 2008).

Second, pixels satisfying the assumptions in SEBAL would be dependent on surface hydrologic contrast (dry and wet land surfaced types) that may vary substantially with the modeling domain (French et al., 2005b). If a study watershed is primarily characterized by crops or vegetated areas, the possibility of the presence of the hot pixel with negligible ET in an image would be largely reduced. Likewise, for a study site where bare soil surfaces or impervious areas prevail, the likelihood that the cold pixel with zero H could be successfully identified would be decreased.

Third, even though images for absolute clear skies are available, the resulting surface flux estimates would vary with the actual size of images being used. One would derive a subset of an image specifically for a study site, take the entire scene of the image, or even merge multiple scenes of images. This means that varying sizes of images would be used because of emplacement of the study watershed/region in different hierarchical river basin systems. In this case, the locations and the corresponding physical and geomorphological features of extremes would probably be different.

Fourth, the resolution of satellite images would be another major factor affecting the distribution of extreme pixels. High-spatial resolution images (e.g., Landsat TM/ETM⁺ and ASTER) can provide more details of the thermal properties of the surface but are limited in longer revisit time and coverage. High-temporal resolution images (e.g., GOES and MODIS) have adequate coverage but generally provide less detailed information of LST and consequently are less useful for identifying the extreme pixels than images with high spatial resolution. There is, therefore, a tradeoff between the coverage of an area of interest and the spatial resolution of satellite images being used.

5.4.2. Selection of extremes for varying domains

We selected extreme pixels using scatterplots of LST and NDVI maps (Fig. 5.6), a land use map for watershed I (Fig. 2.1b), and geomorphologic features of certain land covers obtained from field investigations. Criteria for selection of extremes are described in Section 3.4.3.

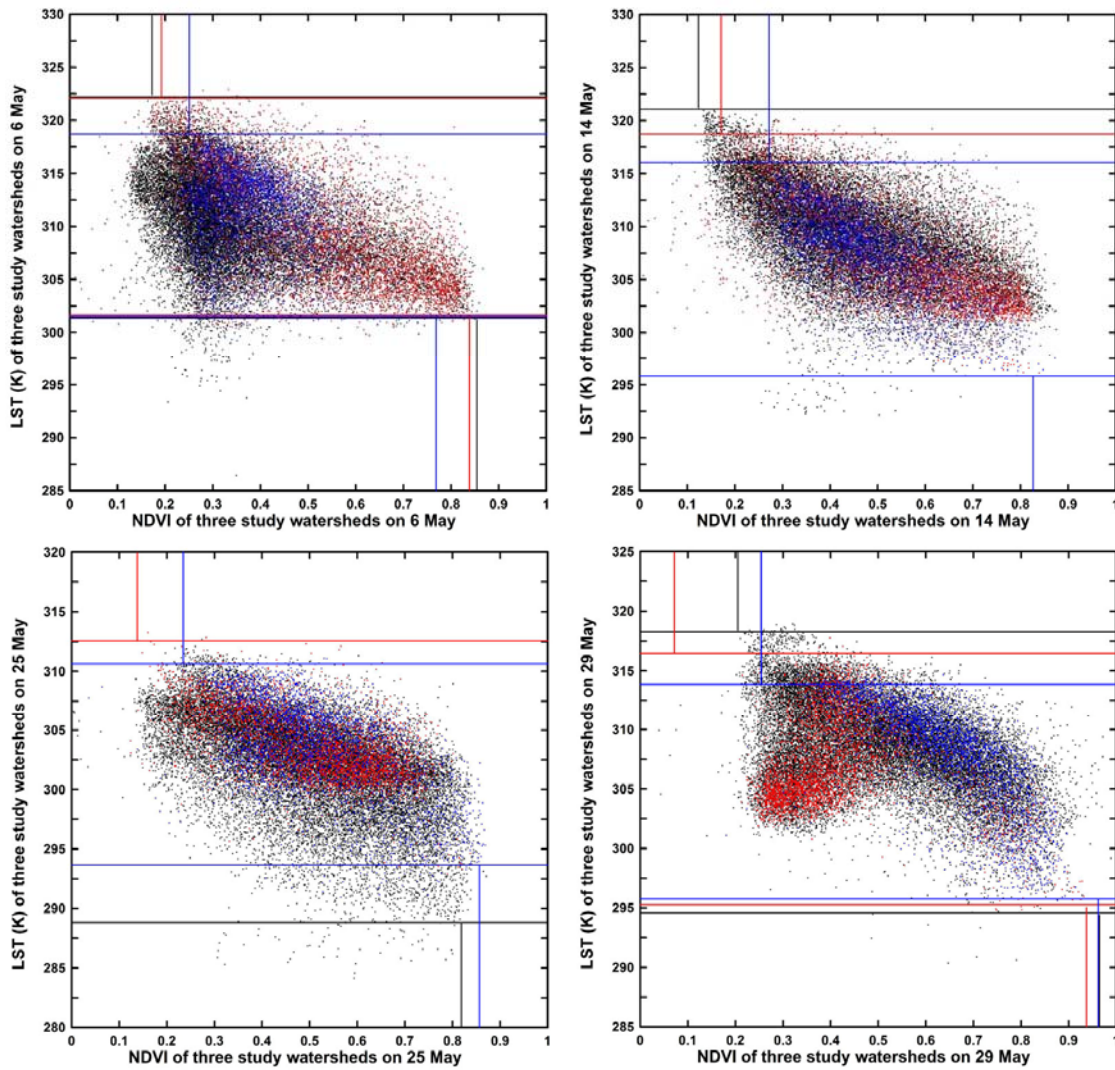


Figure 5.6 Selection of extreme pixels for watersheds I, II, and III, respectively, on May 6, 14, 25, and 29, 2007 based on scatterplots of NDVI and LST. Black dots represent scatterplots for watershed I, red dots for watershed II, and blue dots for watershed III. Points of the intersection of black, red, and blue lines show the identified extreme pixels for watersheds I, II, and III, respectively.

5.5. Domain scale effect

5.5.1. Shift of extreme pixels within watersheds

Extreme pixels for watersheds I, II, and III on May 6, 14, 25, and 29 in 2007, respectively, were selected to investigate the domain dependence of SEBAL. The four

days had highest quality MODIS data products in the study year. Results clearly show that both the hot and cold pixels vary with the domain of the study watersheds (see Fig. 5.7 and Table 5.2). For instance, the hot pixel for watershed I on May 6, 2007, was identified on a dry surface on the boundary of watershed II, whereas it moved to another dry surface within watershed II when just accounting for watershed II. For watershed III, the hot pixel moved to a dry surface near the outlet of the watershed. Similarly, the cold pixels for the three watersheds differed from each other, all being at wet surfaces in the irrigation districts or in densely forested land surfaces. The largest difference in LST of the hot pixels on May 6, 2007, was up to 3.5 K for watershed I and watershed III, whereas the differences in LST of the cold pixels were small (see columns 5 and 6 in Table 5.2). With varying locations, the characteristic variables for extreme pixels varied to some extent. For instance, the largest difference in $R_{n,hot}$ between watersheds I and III on May 14, 2007, was as large as 72.6 W m^{-2} (see column 3 in Table 5.2). It is apparent that different locations of extremes would probably show different characteristic variables, thereby resulting in different magnitudes of coefficients a and b and then different H estimates (see Table 5.2).

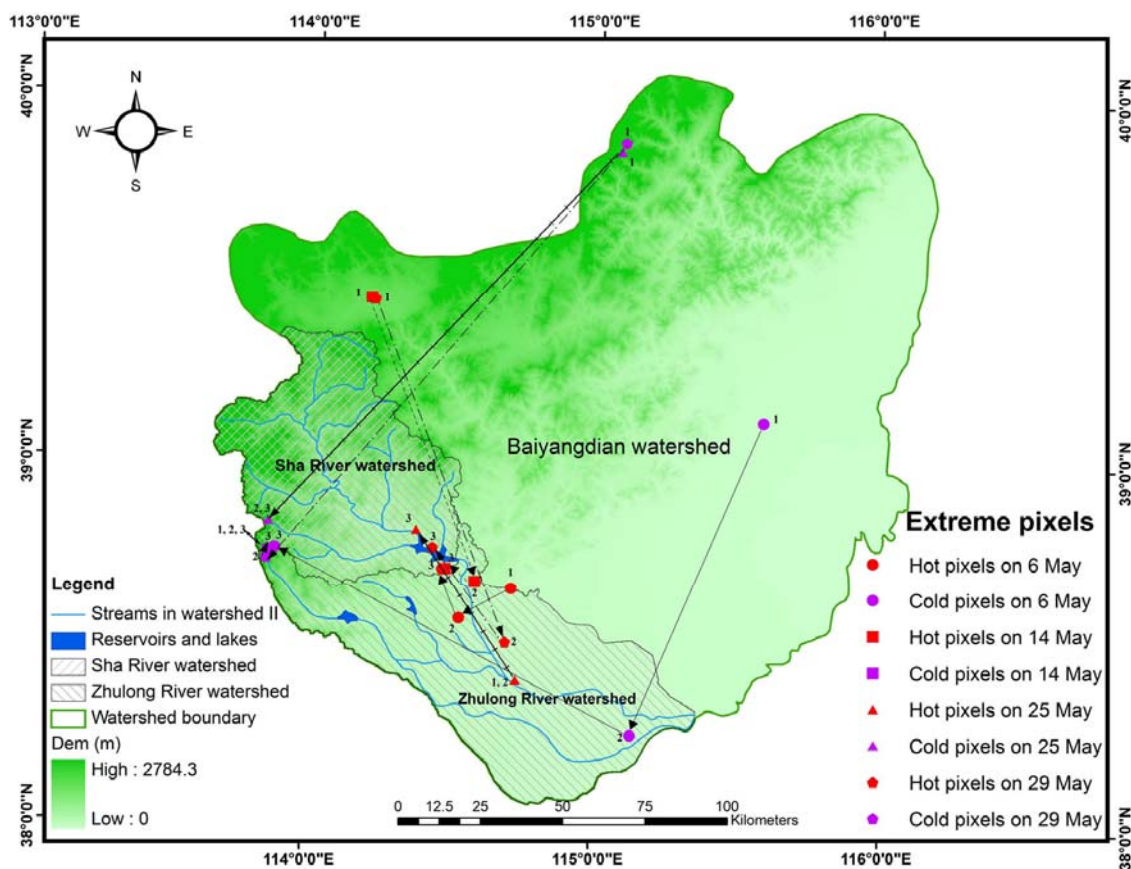


Figure 5.7 Shift of extreme pixels within watersheds I (1), II (2), and III (3) on 6, 14, 25, and 29 May 2007. Numbers along the symbols represent extreme (s) for each watershed (s). Shift of extreme pixels within watersheds for the same day is represented with the same line style.

Table 5.2 Characteristic variables of extreme pixels for watersheds I, II, and III on May 6, 14, 25, and 29, 2007 for investigating the domain dependence of SEBAL

Date	Watershed	$R_{n,hot}$ (W m ⁻²)	G_{hot} (W m ⁻²)	$T_{s,hot}$ (K)	$T_{s,cold}$ (K)	ρ_{hot} (kg m ⁻³)	u_{200} (m s ⁻¹)	$z_{om,hot}$ (m)	a (-)	b (K)	Number of iterations	Averaged H (W m ⁻²)	σ of H (W m ⁻²)
May 6	Watershed I	463.4	134.3	322.2	301.4	1.178	3.0	0.015	0.2431	-73.2620	15	115.3	65.7
	Watershed II	468.1	130.2	322.1	301.6	1.179	2.5	0.022	0.2516	-75.8957	18	101.0	74.2
	Watershed III	488.0	125.1	318.7	301.5	1.178	4.4	0.037	0.2879	-86.8066	14	175.1	83.5
May 14	Watershed I	519.5	150.5	321.1	295.8	1.061	3.5	0.015	0.2297	-67.9535	15	169.8	70.6
	Watershed II	577.0	167.2	318.7	295.8	1.148	3.8	0.015	0.2557	-75.6496	14	177.3	83.4
	Watershed III	592.1	151.8	316.0	295.8	1.140	4.6	0.037	0.2868	-84.8302	14	210.8	91.3
May 25	Watershed I	583.3	162.2	312.6	288.8	1.159	4.9	0.022	0.2336	-67.4519	13	223.1	74.8
	Watershed II	583.3	162.2	312.6	293.6	1.159	4.2	0.022	0.3027	-88.8771	14	190.7	75.3
	Watershed III	643.9	165.1	310.5	293.6	1.137	5.8	0.037	0.3402	-99.8691	13	239.9	115.3
May 29	Watershed I	542.3	163.8	318.3	294.6	1.069	2.9	0.007	0.2489	-73.3237	15	193.2	68.4
	Watershed II	576.3	136.4	316.4	295.3	1.162	2.0	0.052	0.2920	-86.2275	27	200.0	87.3
	Watershed III	598.5	188.5	313.8	295.8	1.151	3.2	0.100	0.3131	-92.6269	20	222.6	94.9

It is interesting to note that on the one hand, extreme pixels vary with the domain under consideration. On the other hand, extreme pixels generally center on particular patches or fields for a particular watershed. First, the hot pixel primarily concentrates on extreme dry surfaces around the middle reaches of watershed II, and dry surfaces in the Laiyuan basin located in northwestern watershed I. As for the cold pixel, it is generally identified in wet surfaces in irrigation districts or densely forested land surfaces (Fig. 5.7).

To sum up, even though extreme pixels often show different locations over watersheds of varying domains, they tend to concentrate on certain surfaces for a given watershed. The more *a priori* knowledge on land cover, terrain, and geomorphology for a study site, the more uncertainties in the selection of the extreme pixels could be reduced.

5.5.2. Comparison of H estimates between different domain sizes

Comparison of H estimates between different domains was performed by the procedures: (1) estimates of H for watersheds I, II, and III were generated by SEBAL, respectively, based on coefficients a and b (see Table 5.2) derived from extreme pixels within the domain of each watershed; and (2) comparison of the H estimates for pixels within the domain of the smaller watershed between watersheds I and II, watersheds I and III, and watersheds II and III was performed (Fig. 5.8)

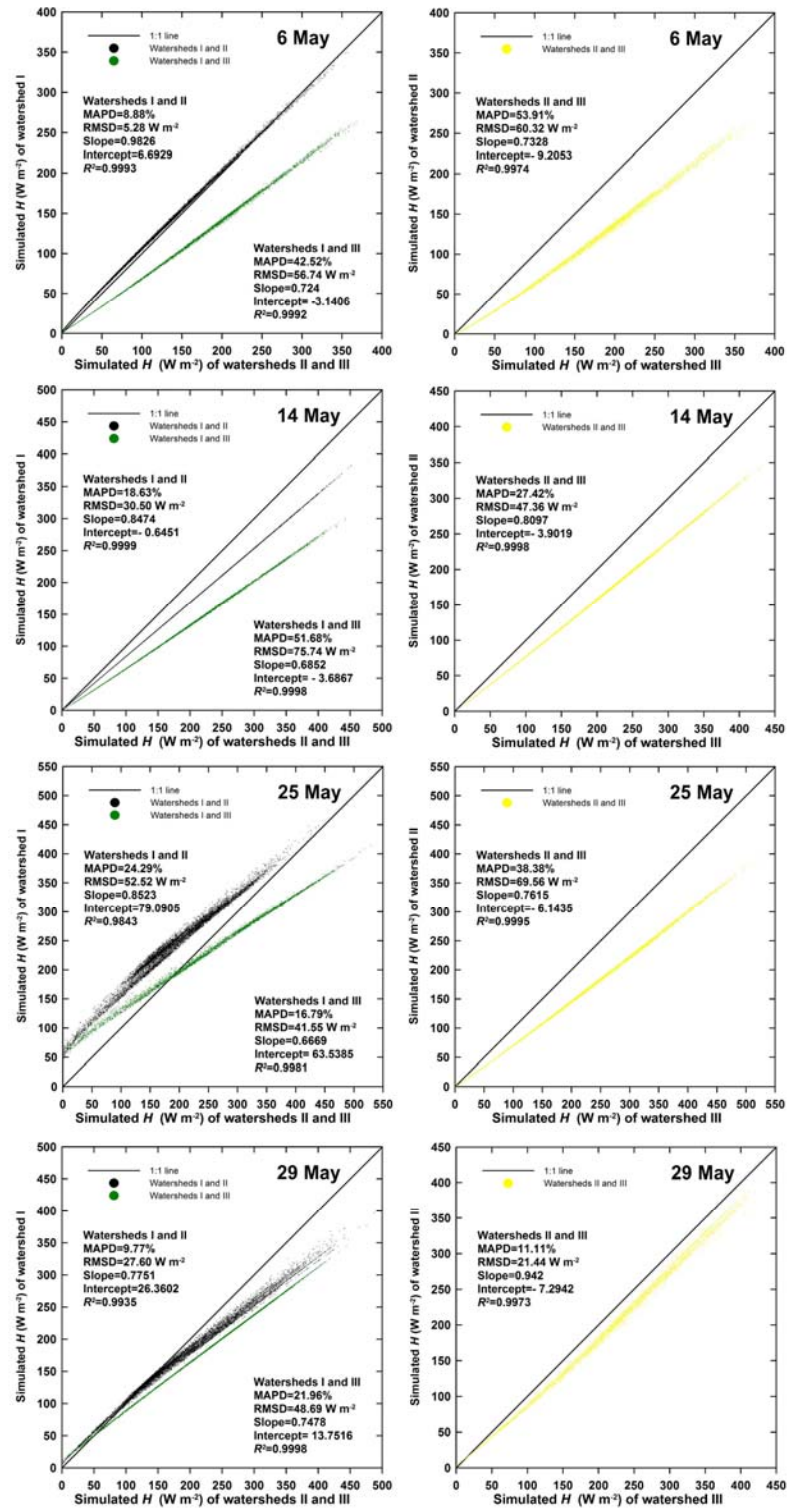


Figure 5.8 Comparison of H estimates between watersheds I, II, and III on May 6, 14, 25, and 29, 2007, MAPD, RMSD, slope, intercept, and R^2 .

Results indicate that estimates of H for watersheds II and III are quite different from that derived for watershed I as a whole. The largest difference in the estimates of H between watersheds I and II was observed on May 25, 2007, showing an MAPD and an RMSD of 24.29% and 52.52 W m^{-2} , respectively. This corresponds to the largest difference in LST for the cold pixel up to 4.8 K (see column 6 in Table 5.2). Also, the largest difference in the estimates of H for watershed III with reference to watershed I was observed on May 14, 2007, yielding an MAPD and an RMSD of 51.68% and 75.74 W m^{-2} , respectively. The largest difference in the estimates of H for watershed III relative to watershed II was shown on May 25, 2007, indicating an RMSD of 69.56 W m^{-2} . Still, the largest MAPD of 53.91% for watershed III with reference to watershed II occurred on May 6, 2007. These discrepancies are considered significant in surface flux modeling. Only the estimates of H for watershed II on May 6, 2007, were almost consistent with that for watershed I, showing an MAPD and an RMSD of 8.88% and 5.28 W m^{-2} , respectively. This is primarily due to the fairly similar extreme pixels selected for the two watersheds, showing the LST values for the hot pixels of 322.2 K and 322.1 K, and that for the cold pixels of 301.4 K and 301.6 K for watersheds I and II, respectively (see columns 5 and 6 in Table 5.2).

Overall, with decreasing domains of watersheds, the range of LST could decrease, corresponding to a potential decrease in the LST for the hot pixel and an increase in the LST for the cold pixel. According to the sensitivity analysis performed earlier in Section 5.3, estimates of H by SEBAL for a smaller watershed could be larger than that from a larger watershed if the LST for the hot pixel decreases with decreasing domain and the

LST for the cold extreme remains substantially invariant. The magnitudes of the differences in the H estimates depend primarily upon the variations in $T_{s,hot}$, $T_{s,cold}$ and $R_{n,hot}$ for the selected extremes. Cloud cover, surface hydrologic contrast, and the size of modeling domain are the major factors affecting variations in $T_{s,hot}$, $T_{s,cold}$ and $R_{n,hot}$. Therefore, the domain dependence of SEBAL may be confusing to the user when estimating surface fluxes.

However, one would be more confident with SEBAL when applied to a relatively large watershed under absolute clear sky days and spatially homogeneous meteorological conditions (i.e., u_{200} and T_a). For such a case, the presence of surfaces with sufficiently large hydrologic contrast would greatly reduce uncertainty in the selection of the two extremes. However, if the study domain is too large, the assumption of a linear relationship between T_s and dT inherent in SEBAL would break down. Demarcating the boundary of a study site within which there exists “sufficiently large hydrologic contrast” really poses a big challenge for the appropriate use of SEBAL.

5.6. Resolution scale effect

5.6.1. Comparison of H estimates from Landsat TM and MODIS imageries

After obtaining R_n and G (G is G_s in Chapter III) using the SEBAL algorithm in conjunction with the retrieved surface albedo and LST from Landsat TM imagery, H can be simulated by first specifying two extreme pixels. It is particularly important to note that the extreme pixels would exhibit different spatial distributions due to different resolutions of the thermal infrared bands used to retrieve LST, i.e., 1 km for MODIS imagery and 120

m for Landsat TM image. The extremes identified from the Landsat TM image would show a wider range of LST due to a higher discriminating capability.

Extreme pixels from Landsat TM and MODIS imageries based on scatterplots of NDVI and LST are shown in Fig. 5.9. It is clear that the Landsat-based scatterplot of NDVI and LST exhibits a wider LST range. It seems difficult to appropriately determine the cold pixel from the Landsat-based contextual map in that a group of pixels are influenced by cirrus cloud contamination, showing the temperatures of clouds rather than the land surface. This phenomenon frequently occurs, in particular for applications at regional or watershed scales. The difficulty in specifying the cold pixel appears to be serious in terms of the sensitivity analysis performed previously, which is considered a significant limitation when using Landsat images to retrieve ET by SEBAL. Even though some studies on SEBAL-based ET estimation using Landsat TM data indicate a prerequisite of the ‘absolute’ clear skies, it is extremely hard to determine if the seemingly cloud-free Landsat images are influenced by thin clouds. Here, the LST for the cold pixel for the Landsat platform was technically taken as the lowest LST value for an irrigation district in watershed I.

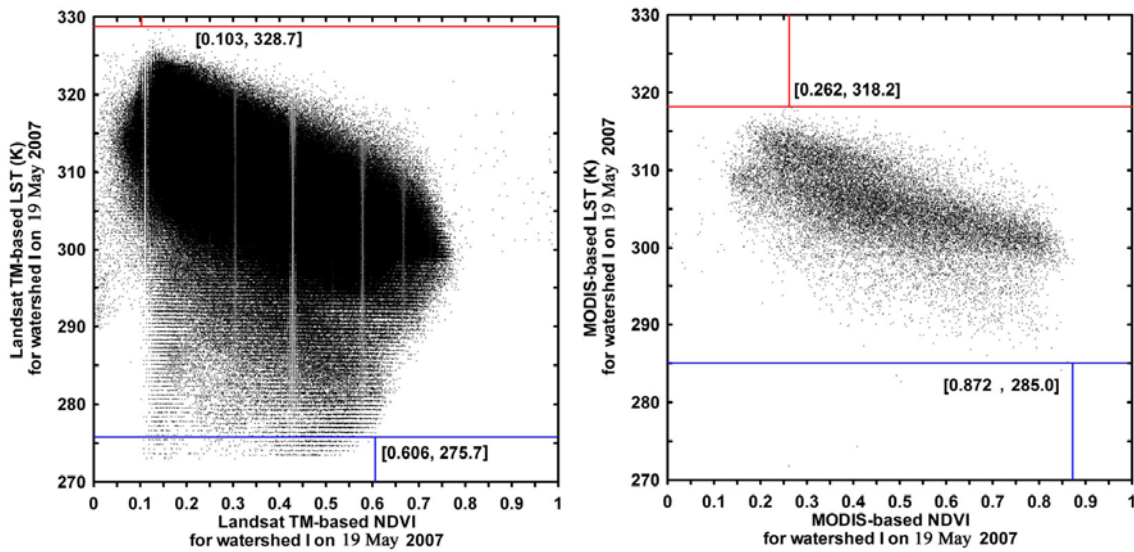


Figure 5.9 Extreme pixels from Landsat TM-based and MODIS-based contextual maps of NDVI and LST for watershed I on May 19, 2007, points of the intersection of red lines represent the locations of the hot pixels and blue lines represent the locations of the cold pixels.

It is indicated that the effect of shifting from using finer resolution images to coarser ones can be analogous to the case applying SEBAL from a larger watershed to a sub-watershed because of the shrinking of the LST range. The LST for the hot pixel decreases from 328.7 K for the Landsat TM to 318.2 K for the MODIS images. Analogously, the LST for the cold pixel increases from 275.7 K for the Landsat TM to 285.0 K for the MODIS images. Given these initial value conditions, regression coefficients a and b for the Landsat TM and MODIS data were derived as 0.1109 and -30.5898 K, and 0.1495 and -42.6148 K, respectively.

Fig. 5.10 compares the Landsat- and MODIS-based H estimates. The Landsat-based H estimates at 120 m resolution were aggregated to 960 m resolution estimates using an 8×8 moving window with a bilinear resampling method. The output up-scaling scheme

(i.e., aggregating outputs) adopted here would result in a better representation of the H estimates compared with the input up-scaling scheme (i.e., aggregating inputs first and then computing H) (Hong et al., 2009). Results indicate an RMSE as large as 52.3 W m^{-2} and a bias of 26.5 W m^{-2} . These discrepancies are considered greater than negligible in surface flux modeling. It is noted that the areal averaged H estimates for Landsat TM and MODIS data were found to be relatively close, being 201.9 W m^{-2} and 228.4 W m^{-2} , respectively. The MODIS-based averaged H estimate shows a larger value and also a slightly larger standard deviation (61.73 W m^{-2} for MODIS-based H estimates and 58.15 W m^{-2} for Landsat-based H estimates, Fig. 5.11).

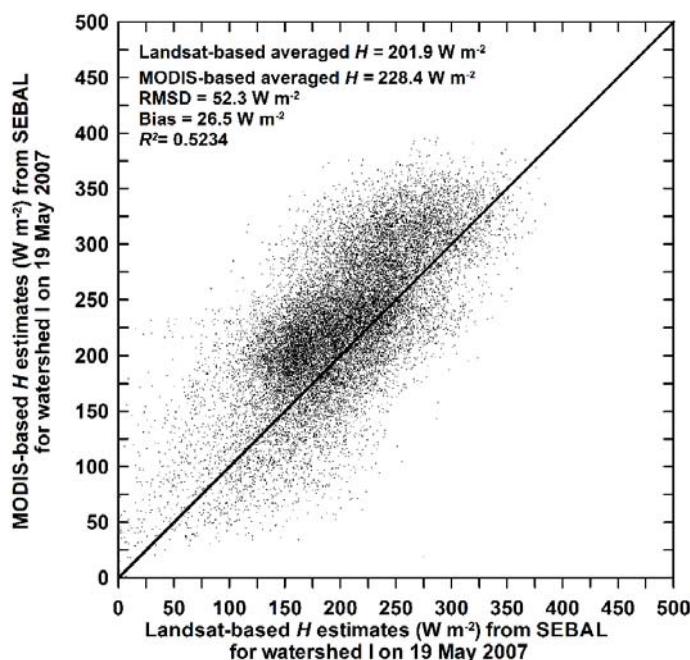


Figure 5.10 Comparison of H estimates from Landsat TM and MODIS images of watershed I on May 19, 2007. Landsat TM-based estimates of a 120 m resolution are aggregated to that of a 960 m resolution.

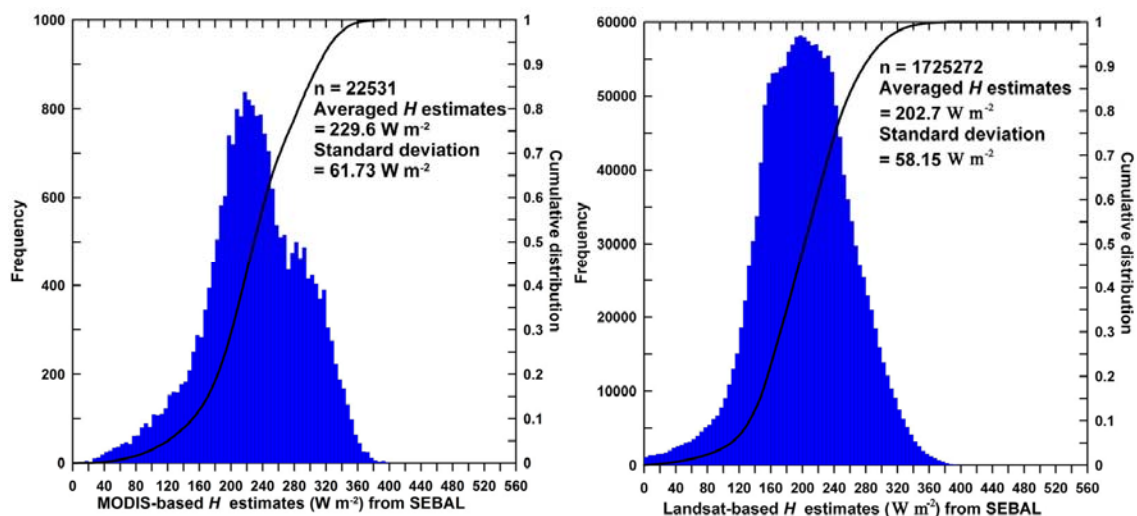


Figure 5.11 Frequency distributions and relevant cumulative distributions of H estimates from Landsat TM and MODIS images of watershed I on May 19 2007. A bin size is set to 5 W m^{-2} .

5.6.2. Discussion

These findings are contrary to what McCabe and Wood (2006) have found. In their work, ASTER, Landsat, and MODIS data are used to simulate ET by SEBS, demonstrating that finer resolution images could capture more detailed ET across the entire study area. The difference between these findings is likely due to different mechanisms of ET estimation models used. Given that the MODIS-based flux estimates for the two studies both suffer resolution scale effects, SEBAL-based flux estimates are additionally impacted by the dependence of model parameters on image resolution. Contradictions even occur in studies on investigating the resolution scale effect of SEBAL. Hong et al. (2009) examined differences in SEBAL-based LE estimates using Landsat ETM⁺ and MODIS images, indicating that the LE estimates from Landsat ETM⁺ show a greater standard deviation and greater maximum and smaller minimum values of

the resulting estimates. Gebremichael et al. (2010) performed a similar study as Hong et al. (2009), implying that ET estimates of the MODIS-based resolution (1000 m) aggregated by ASTER data (90 m for the thermal infrared band) have a greater standard deviation compared to the original ASTER-based estimates. Gebremichael et al. (2010) and Hong et al. (2009) tended not to examine in detail the fundamental reasons for the differences in variations in the standard deviations of the resulting estimates from SEBAL, which are probably caused by the resolution dependence of SEBAL.

Through our theoretical analysis and simulations, it can be concluded that the difference in the standard deviation of the resulting flux estimates from SEBAL using different satellite platforms results from the range and magnitude of LST of extreme pixels. The use of high resolution LST can result in a higher $T_{s,hot}$ value and a lower $T_{s,cold}$ value. If the absolute magnitude of the increase in $T_{s,hot}$ exceeds that of the decrease in $T_{s,cold}$, it could lead to a smaller coefficient a compared with that from using coarse resolution LST retrievals, and consequently a somewhat smaller standard deviation and magnitudes of the H estimates.

It should also be suggested that the magnitude of the pixel-based H estimates using coarse images might not be accurate; however, the areal averaged H estimates over the study area using fine and coarse images tend to be comparable. Even though the pixel-based flux estimates from SEBAL have large uncertainties due to the domain and resolution dependencies, information contained in the frequency domain of these estimates might be meaningful and requires further study.

5.7. Concluding remarks

Numerous satellite-based algorithms have been developed to estimate ET over large heterogeneous areas. However, outputs of some of these algorithms may depend on the size of satellite images being used/the modeling domain being considered, which is referred to as the domain dependence. In addition, these algorithms are typically developed and validated at the spatial resolution of a certain sensor based on the assumption of homogeneity within a pixel. Their performance may also be dependent on the spatial resolution of satellite images being used, here defined as the resolution dependence. The domain and resolution dependencies are considered a significant obstacle to the accurate derivation of ET on large scales and an enhanced understanding of sub-pixel variations in ET retrievals using coarse satellite images. First, sensitivity analysis of SEBAL to the input is performed, indicating that the H estimate is most sensitive to the temperatures of hot and cold pixels and the available energy of the hot pixel. Second, the domain and resolution dependencies of SEBAL are investigated by applying SEBAL to varying modeling domains in the Baiyangdian watershed in North China, and to Landsat TM and MODIS sensors. The range of LST can decrease or increase to varying degrees due to cloud cover and variation in the domain of interest/the spatial coverage of satellite images. This uncertainty can lead to varying temperatures of extremes and therefore disparate H estimates. The largest MAPD and RMSD in the H estimates between different modeling domains could be as large as 53.91% and 75.74 W m^{-2} , respectively, for all study days. In addition, the MODIS-based H estimates showed an RMSD of 52.3 W m^{-2} and a bias of 26.5 W m^{-2} relative to the Landsat TM-based

counterparts. Unlike other models, the standard deviation of H estimates from SEBAL using high spatial resolution images could be smaller than that using low spatial resolution images. Such differences are caused by the resolution dependence compounded by the domain dependence due to the inadequacies in the SEBAL physics. Retrievals of H and LE from SEBAL tend to vary with the size of the modeling domain and the satellite platform. The study presented in this chapter can provide a clearer picture of the performance of SEBAL under a range of circumstances the user often encounters, and help correctly interpret the model outputs. In addition, it can also serve as a basis for examining scale effects of other remote sensing-based approaches (e.g., TSEB and triangular or trapezoidal schemes) and provide meaningful implications for refining those scale-dependent models.

CHAPTER VI

A MODIFIED SURFACE ENERGY BALANCE ALGORITHM FOR LAND (M-SEBAL) BASED ON A TRAPEZOIDAL FRAMEWORK

6.1. Introduction

SEBAL has been developed and widely used to estimate ET at varying spatial and temporal scales over the past 15 years (Bastiaanssen et al., 1998a; Pelgrum and Bastiaanssen, 1996). However, the applicability and operability of SEBAL remain controversial in the operational ET estimation community due to its one-source parameterization scheme and selection of hot and cold extremes involved in the calculation of H . Many researchers and practitioners have explored the application of SEBAL to estimate ET for improving water use efficiency, water resources allocation and management, as well as efficacies of distributed hydrologic models (Bastiaanssen et al., 2005). However, the majority of these studies and applications appear to fall short of rigorous validation due in large part to the lack of expensive field instruments (Compaore et al., 2008; Courault et al., 2009; Karatas et al., 2009; Li and Zhao, 2010; Wu et al., 2010; Yao et al., 2010); or only compare the daily ET estimates based on the assumption of fairly invariant EF at the satellite overpass with daily ET measurements from lysimeters (Allen et al., 2007; Ramos et al., 2009), reference ET-crop coefficient based calculations (Ahmed et al., 2010; Bashir et al., 2009; Gao et al., 2008; Oberg and Melesse, 2006; Zwart et al., 2010), or from limited number of Bowen ratio or eddy covariance towers (Folhes et al., 2009; Wang et al., 2009; Zwart and Bastiaanssen, 2007);

or compare longer timescale ET estimates (e.g., monthly and seasonal ET estimates) with counterparts from water balance approaches (Bastiaanssen et al., 2002; Mohamed et al., 2004; Mohamed et al., 2006).

We argue that as daily, monthly, or seasonal accumulated ET estimates are a function of SEBAL-based EF or crop coefficient at the satellite overpass and daily net radiation, errors involved in H and LE estimates at the satellite overpass could be cancelled out in the integrated ET estimates over a relatively longer timescale. In other words, even though the ET estimates from SEBAL show agreement with some integrated counterparts or measurements on a daily or a longer timescale, there is still a possibility that the most critical outputs of H and LE at the time of image acquisition involve a large uncertainty. Furthermore, the spatial distribution of LE may have been distorted due to the inadequacies of model physics.

There are indeed some relatively rigorous studies addressing validation of SEBAL by comparing SEBAL-based estimates at the time of imaging with measurements of eddy covariance towers, Bowen ratio techniques, or large aperture scintillometers (Kleissl et al., 2009; Marx et al., 2008; Singh et al., 2008; Teixeira et al., 2009a). Nevertheless, these studies seem to be less than adequate in examining errors in the model outputs from the perspective of model physics, e.g., the highly consistent overestimation of H in Melesse and Nangia (2005) and Teixeira et al. (2009a), and the consistent underestimation of H in Kleissl et al. (2009), Marx et al. (2008), and Singh et al. (2008) are not well expounded, or they presumably attribute all errors and uncertainties to two extremes and the one-source parameterization scheme adopted by

SEBAL.

Timmermans et al. (2007) performed an insightful comparison between SEBAL and TSEB using the Southern Great Plains '97 and Monsoon '90 data sets. Meticulous selection of end-members of T_{rad} for one image acquisition date under 5 cases and a preliminary sensitivity analysis help with greater understanding of SEBAL. However, this study mistakenly takes $kB^{-1}=2.3$ as part of SEBAL; in fact, SEBAL does not use the fixed kB^{-1} parameter, but rather takes z_{oh} as 0.1 m. Therefore, Timmermans et al. (2007) appeared to exaggerate the effect of z_{oh} in SEBAL, attributing in part the discrepancies of the model outputs to incorrect causes. French et al. (2005b) conducted a comparison between SEBAL and TSEB at the SMACEX site in central Iowa, U.S., for one image acquisition day (DOY 182) using one pair of extreme pixels for running SEBAL. They obtained significantly larger H estimates from SEBAL compared with that from TSEB and eddy covariance towers. We suggest that a more complete picture of the performance of SEBAL would be obtained by increasing the number of quasi hot and cold extremes and combinations thereof. In Chapter V, the sensitivity of SEBAL to its inputs and the domain and resolution dependencies inherent in the model physics were comprehensively investigated, indicating that increases in the temperatures of extremes will decrease the resulting H estimates, and *vice versa*. Increases in $R_{\text{n,hot}}-G_{\text{hot}}$ will also increase the H estimates.

It is critically important to note that almost all studies pertaining to SEBAL, particularly that of the model developers (Allen et al., 2007; Bastiaanssen et al., 2010), recognize the key role of extremes in the resulting estimates; large uncertainty in the

model outputs would be introduced by differing extremes identified by the user. The consensus on the difficulty of correctly selecting extremes, compounded by limited ground-based measurements of surface fluxes which are rarely available for most developing countries, seems to hinder further insights into the deficiencies of model physics and a substantial improvement in the critical selection procedures involved in the model.

The objective of this chapter was to systematically explore the deficiencies in the formulation of SEBAL, and develop a new framework to replace the intractable step of selection of two extremes. The performance of the newly developed Modified Surface Energy Balance Algorithm for Land (M-SEBAL) will be compared with SEBAL at the SMACEX site with a dense flux tower network, which provides an excellent data set for validating the two models and comparing and contrasting their advantages and limitations. Section 6.2 addresses the deficiencies in SEBAL formulation and the formulation of M-SEBAL. Section 6.3 presents the results from SEBAL and M-SEBAL and comprehensively compares and contrasts the two models. Section 6.4 provides a summary of advantages and disadvantages of SEBAL and M-SEBAL, followed by concluding remarks in Section 6.5.

6.2. Model formulation

6.2.1. Trapezoidal framework of M-SEBAL

Modifications to SEBAL and illustrations of the deficiencies in SEBAL will take advantage of the trapezoid framework illustrated in Chapter IV. For the triangle method

based on the contextual space of f_c - T_{rad} , EF is linearly correlated with T_{rad} for each class i of f_c :

$$\text{EF} \propto \frac{T_{\text{radi,max}} - T_{\text{rad}}}{T_{\text{radi,max}} - T_{\text{radi,min}}} \quad (6.1)$$

where $T_{\text{radi,max}}$ and $T_{\text{radi,min}}$ are the temperatures of extreme edges of the triangle space at the class i of f_c . With increasing f_c , $T_{\text{radi,max}}$ will decrease, forming a slanting hot edge.

Fig. 6.1 is a schematic of the scatterplot of remotely sensed f_c and T_{rad} . The scatterplot of f_c and T_{rad} constitutes essentially a quadrangle AB'CD, whose sides and vertices are the real physical limits of EF. In AB'CD, point A ($f_c=0$, $T_{\text{rad}}=T_{\text{s,max}}$) is the bare surface with the largest water stress, i.e., EF=0, point B' ($f_c=0$, $T_{\text{rad}}=T_{\text{s,min}}$) is the bare surface without water stress, i.e., EF=1, point C ($f_c=1$, $T_{\text{rad}}=T_{\text{c,min}}$) is the fully vegetated surface without water stress, i.e., EF=1, and point D ($f_c=1$, $T_{\text{rad}}=T_{\text{c,max}}$) is the fully vegetated surface with the largest water stress, i.e., EF=0. Side AD is called the warm edge of the f_c - T_{rad} space, i.e., EF is zero for pixels on this edge for a full range of f_c . Side B'C is referred to as the cold edge of the f_c - T_{rad} space, i.e., there is no water stress for pixels on this edge.

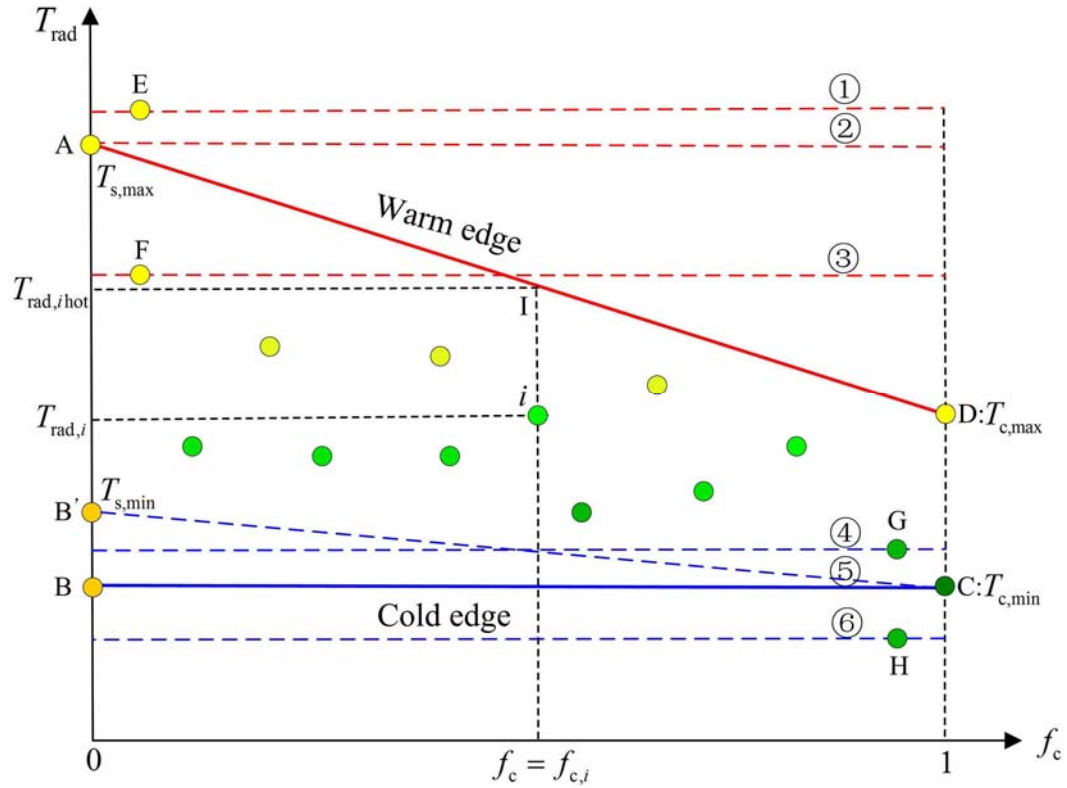


Figure 6.1 A schematic of the scatterplot of remotely sensed f_c and T_{rad} , colored circles represent pixels with varying f_c and T_{rad} . Quadrangle $AB'CD$ represents real physical limits of the f_c - T_{rad} space. Point A represents the bare surface with the largest water stress (i.e., $EF=0$), point B' represents the bare surface without water stress (i.e., $EF=1$), point C represents the fully vegetated surface without water stress (i.e., $EF=1$), and point D represents the fully vegetated surface with the largest stress (i.e., $EF=0$). Trapezoid $ABCD$ represents the reasonably simplified framework of quadrangle $AB'CD$, in which point B represents the bare surface without water stress ($EF=1$). Side AD is the warm edge representing surfaces of $EF=0$ for a full range of f_c , and side BC is the horizontal cold edge representing surfaces of $EF=1$ for a full range of f_c . Red dashed lines (①-③) represent hot extremes, which could be selected, involved in SEBAL, corresponding to points E, A, and F. Blue dashed lines (④-⑥) represent cold extremes, which could be selected, involved in SEBAL, corresponding to points G, C, and H.

Quadrangle $AB'CD$ is also referred to as the theoretical envelope of the f_c - T_{rad} space, given certain meteorological conditions. As vertices of quadrangle $AB'CD$ appear difficult to determine in some cases, quadrangle $AB'CD$ can be simplified as a trapezoid

ABCD as shown in Chapter IV or triangle framework, with the aim to make a determination of EF and ET feasible without significantly compromising the accuracy in practice.

It is important to note that the trapezoidal framework involved in M-SEBAL is the theoretical boundary condition, given certain meteorological conditions and surface property parameters. This is different from the determination of the triangle framework directly from the scatterplot of f_c and T_{rad} . The latter suffers somewhat from subjectivity and uncertainty of outliers of T_{rad} retrievals.

6.2.2. Rectangular framework of SEBAL

SEBAL involves a critical step to visually identify a hot extreme and a cold extreme from images, and assumes linearity between T_{rad} and dT throughout a scene. There are three possibilities that the hot extreme is selected: (1) point E (Fig. 6.1) whose T_{rad} is larger than point A; (2) point A; and (3) point F whose T_{rad} is lower than point A. Similarly, the cold extreme is likely to be identified as point G, C, and H, respectively, where the T_{rad} of G is larger than $T_{c,\text{min}}$ and the T_{rad} of H is smaller than $T_{c,\text{min}}$.

For any combination of the selected hot and cold pixels, the two extreme pixels, as a matter of fact, can be analogous to two horizontal extreme edges throughout a scene, i.e., a “rectangular” framework. This means that the two identified extremes do not vary with f_c in SEBAL. All T_{rad} values in an image will be compared with $T_{\text{rad,hot}}$ and $T_{\text{rad,cold}}$ to deduce their dT values. EF from SEBAL for a given class i of f_c can be written as

$$EF_i = \frac{\Delta E_i - H_i}{\Delta E_i} = 1 - \frac{\rho c_p}{\Delta E_i} \cdot \frac{aT_{\text{rad}} + b}{r_{\text{ah},i}} \quad (6.2)$$

where EF_i is EF for a pixel at a given f_c value or f_c at class i , $f_{c,i}$; ΔE_i is the net energy (W m^{-2}) for the pixel at $f_{c,i}$; and $r_{\text{ah},i}$ is the aerodynamic resistance (s m^{-1}) at $f_{c,i}$. For unraveling the essential relationship between T_{rad} and EF_i in SEBAL, we simulated the variation in EF_i with T_{rad} for $f_c=0.2, 0.4$, and 0.6 , respectively. It is noted that for the same f_c value or the same class of $f_{c,i}$, variation in $r_{\text{ah},i}$ can be negligible because $r_{\text{ah},i}$ is a function z_{om} and u_{200} in SEBAL; both play immaterial roles in determining H as illustrated in Sections 5.3.3 and 5.3.4. For the same $f_{c,i}$, NDVI, h_c , and consequently z_{om} remain essentially invariant. ΔE_i is determined in part by T_{rad} in the calculation of L_u and G . However, the magnitudes of L_u and G are both relatively small compared with the shortwave radiation component.

Fig. 6.2 shows that EF_i from SEBAL is highly correlated with T_{rad} , suggesting a quasi-linear relationship and EF_i decreasing with increasing T_{rad} . In addition, it is apparent that EF_i is zero at hot extreme and 1 at cold extreme for each $f_{c,i}$. This means that SEBAL is, in fact, of the substantially similar form of EF_i as the triangle or trapezoid methods (Eq. 6.1). The only marked difference between SEBAL and the triangle framework lies in extreme edges they adopt which fundamentally determine the slope of the linear variation in EF_i with T_{rad} . Extremes in SEBAL are both horizontal edges; however, the triangle and trapezoid frameworks take advantage of the physically meaningful slanting edge shown in Fig. 6.1, which has been observed empirically and demonstrated theoretically by a multitude of studies (Carlson, 2007).

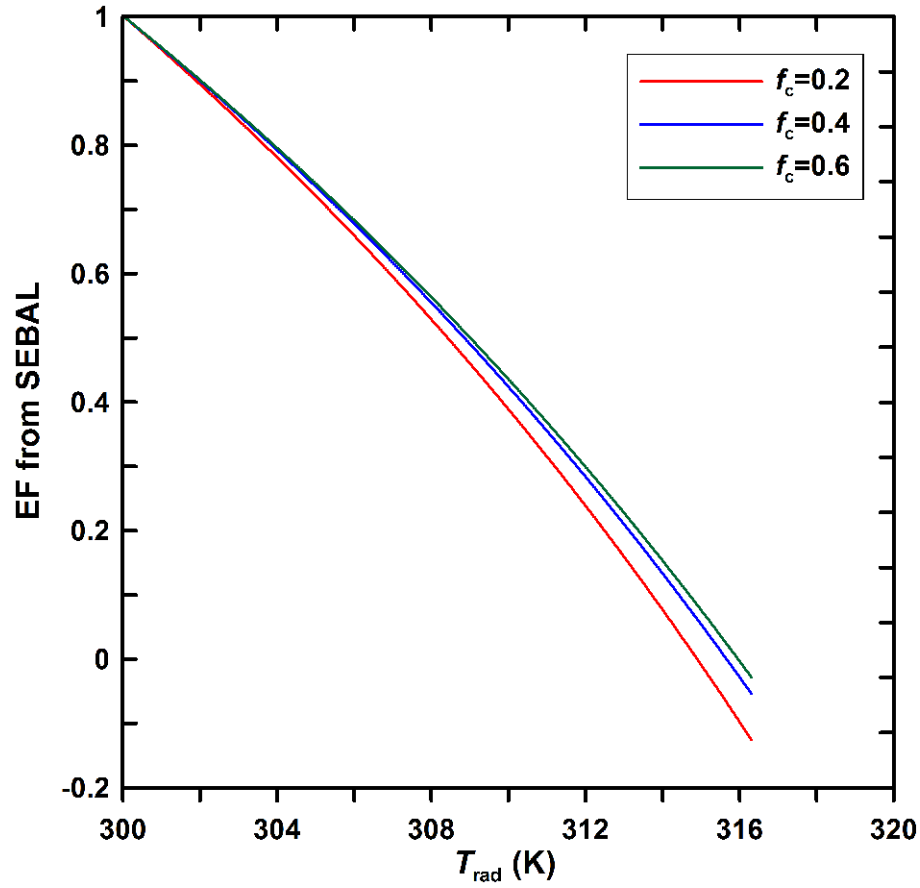


Figure 6.2 Variation in EF with T_{rad} in SEBAL for $f_c=0.2$, 0.4, and 0.6, respectively, given a set of coefficients a ($=0.27$) and b ($=-80.35$ K) derived from $T_{\text{rad,hot}}=316.3$ K and $T_{\text{rad,cold}}=300.1$ K and other characteristic variables, and typical values involved in ΔE_i .

6.2.3. Uncertainty in SEBAL

SEBAL is significantly beset by the selection of extremes from images (Choi et al., 2009; French et al., 2005b; Timmermans et al., 2007). As shown in Fig. 6.1, each selected extreme forms a limiting edge of the rectangular framework, with points E, A, F, G, C, and H corresponding to horizontal limiting edges of 1-6, respectively. It is important to state here that the rectangular framework intrinsic in SEBAL is far less than satisfactory in approximating the quadrangle AB'CD, which would be the key reason for

unrealistic spatial distributions of the H and LE estimates from SEBAL.

Recall that with increases in $T_{\text{rad,hot}}$ and/or $T_{\text{rad,cold}}$ in SEBAL, the H estimates will decrease and then the LE estimates will increase. With decreases in $T_{\text{rad,hot}}$ and/or $T_{\text{rad,cold}}$, the H estimates will increase and consequently the LE estimates will decrease. Let us first assume that the realistic cold edge, i.e., cold edge 5, can be correctly selected. In this case, if hot edge 1 is selected, it will result in a consistent overestimation of T_{rad} for hot extreme throughout the space compared with the realistic warm edge, thereby resulting in underestimation of H and then overestimation of LE. Furthermore, discrepancies will be exacerbated with increasing f_c . If hot edge 2 is selected, even though hot extreme A at $f_c=0$ is in accordance with the realistic one, the hot edge is generally over the real physical warm edge, yet causing an underestimation of H and consequently an overestimation of LE. Particular attention needs to be paid to hot edge 3 that if f_c is less than the intersection of the realistic warm edge and hot edge 3, the rectangular framework tends to overestimate H and then underestimate LE; however, when exceeding the intersection, H will be underestimated as in the previous two cases.

In a similar vein, if cold edge 6 and hot edge 1 or 2 are selected, the underestimation of H could be alleviated or even overestimation of H would occur due to the significantly downward shift of cold edge 6. If cold edge 4 and hot edge 1 or 2 are selected, the rectangular framework is overall moved upward, thereby resulting in underestimation of H and overestimation of ET. If cold edge 6 and hot edge 3 are identified, under the condition of f_c being less than the intersection of hot edge 3 and the realistic warm edge, H will be overestimated; when f_c is larger than the intersection, the

overestimation would be lessened due to hot edge 3 being over the realistic warm edge.

The combination of hot edge 3 and cold edge 4 becomes more complicated, because the overestimation of H due to a lower hot extreme and underestimation of H due to a higher cold edge before the intersection of the realistic warm edge and hot edge 3 appear to offset each other. But after exceeding the intersection, this case tends to underestimate H and consequently overestimate LE. Overestimation or underestimation of surface fluxes depends largely on the relative magnitudes of discrepancies of selected extremes relative to the corresponding realistic extremes for certain f_c ranges.

In summary, for any combinations of the selected extremes in SEBAL, the horizontal extreme edges seem to distort the realistic distribution of EF to varying degrees across a range of f_c . The rectangular framework intrinsic in SEBAL can result in overestimation or underestimation of fluxes and EF induced by the selected extreme pixels of large uncertainty. The magnitudes of discrepancy in fluxes and EF depend largely on the relative differences between the horizontal extremes and the trapezoidal boundary conditions. This attribute would be the most significant inadequacy in SEBAL.

6.2.4. Formulation of M-SEBAL

M-SEBAL has the same formulation of R_n and G components as SEBAL. It is noted that most of the remote sensing-based models share the same formulation of R_n . The most significant attribute or difference involved in remote sensing-based ET models rests on the parameterization scheme of H . Norman et al. (2006) indicate that several linear relationships between T_{rad} and dT with significantly different slopes can in fact

exist within a given landscape. Here, M-SEBAL takes advantage of the trapezoidal framework and replaces the rectangular framework intrinsic in SEBAL. We assume that coefficients a and b for determining dT in the calculation of H vary with f_c but remain invariant for the same f_c or f_c class i given as

$$a_i = \frac{r_{ahi,hot}}{\rho_{i,hot} c_p} \cdot \frac{R_{ni,hot} - G_{i,hot}}{T_{radi,hot} - T_{radi,cold}} \quad (6.3)$$

$$b_i = -a_i T_{radi,cold} \quad (6.4)$$

where subscript i denotes the class i for f_c . The other variables in Eqs. (6.3) and (6.4) are the corresponding characteristic variables for hot and cold extremes on the realistic warm and cold edges involved in the trapezoidal framework. Pixels with the same f_c value or same class of $f_{c,i}$ use a_i and b_i to infer their temperature gradient dT_i and subsequently calculate H .

In Eq. (6.3), the aerodynamic resistance of point I in Fig. 6.1 $r_{ahi,hot}$ can be determined using u_{200} deemed constant across an image and z_{om} specific for $f_{c,i}$. The air density of point I can also be readily specified. $T_{radi,hot}$ and $T_{radi,cold}$ can be located on the theoretical warm and cold edges at $f_c=f_{c,i}$. Determination of the theoretical limiting edges are illustrated in Sections 4.2.3. The available energy of hot extreme at $f_{c,i}$, i.e., $R_{ni,hot}-G_{i,hot}$ ($\Delta E_{i,hot}$) can be determined by the low envelope of the f_c - ΔE space, considering that (1) for extremely dry surfaces, i.e., EF=0, the largest T_{rad} contributes to relatively large outgoing longwave radiation; (2) the extremely dry surfaces often show relatively large albedo, which contributes to relatively small net shortwave radiation; and (3) the largest T_{rad} contributes to the largest G for the same $f_{c,i}$. All the three contributions

would favor the smallest $\Delta E_{i,\text{hot}}$ for the hot extreme at $f_{c,i}$, thereby taking the low envelope of the f_c - ΔE space.

6.3. Results and discussion

6.3.1. Results from M-SEBAL

M-SEBAL was applied to the SMACEX site on DOY 174, 182, and 189 in 2002 when three cloud-free Landsat TM/ETM⁺ images were acquired. Descriptions of the study site, ground-based measurements, satellite imageries, and variable derivation are given in Section 4.3. Energy balance components simulated by M-SEBAL were compared with tower-based flux measurements. The simulated fluxes were averaged over the estimated upwind source-area/footprint (1~2 pixels/~120 m) for each flux tower using the approach proposed by Li et al. (2008a). Results (Table 6.1 and Fig. 6.3) indicate that M-SEBAL seems to be capable of reproducing surface fluxes with reasonable accuracy at the SMACEX site for three test days in 2002. The most interesting output of M-SEBAL, LE, shows discrepancies between the retrievals and the tower-based measurements in terms of an RMSD of 41.1 W m⁻² and an MAPD of 8.9%, respectively. These discrepancies are generally within the intrinsic uncertainty in tower-based measurements. The retrieval accuracy of M-SEBAL seems to be comparable to TSEB models (both series and parallel configurations) which have been applied to the study site in a series of validation and comparison studies (Choi et al., 2009; French et al., 2005b; Gonzalez-Dugo et al., 2009; Li et al., 2005). Furthermore, R_n and G can be reproduced reasonably well, showing RMSD on the order of 20~30 W m⁻²

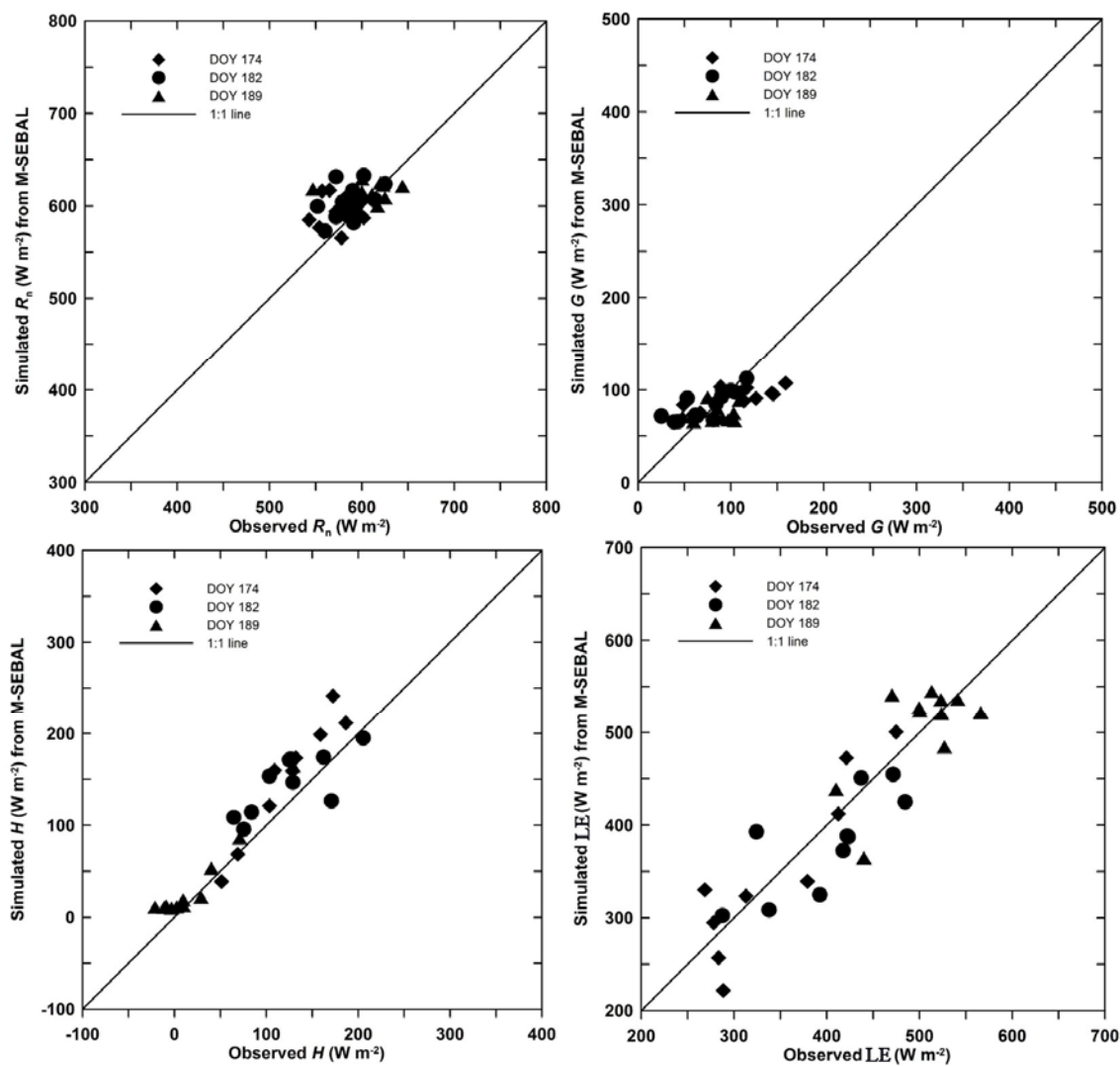


Figure 6.3 Comparison of R_n , G , H , and LE fluxes (W m^{-2}) from M-SEBAL with corresponding eddy covariance tower-based measurements (W m^{-2}) for the SMACEX site on DOY 174, 182 and 189 in 2002.

Table 6.1 Statistics on discrepancies between simulated energy balance components from M-SEBAL, and the eddy covariance energy and heat fluxes at the SMACEX site for three test dates in 2002. The observed fluxes are corrected by the Bowen ratio (BR) technique.

Flux and date		Observation number	Observed average (W m^{-2})	Simulated average (W m^{-2})	Bias (W m^{-2})	RMSD (W m^{-2})	MAPD (%)
R_n	DOY174	12	572.4	592.4	20.0	29.7	4.3
	DOY182	12	586.5	604.6	18.1	27.1	3.6
	DOY189	11	606.4	615.2	8.7	26.7	3.3
	Overall	35	587.9	603.7	15.8	27.9	3.8
G	DOY174	12	104.1	90.4	-13.6	31.0	25.5
	DOY182	12	74.1	85.0	10.9	21.0	36.4
	DOY189	11	82.7	73.9	-8.8	21.7	23.7
	Overall	35	87.1	83.4	-3.7	25.1	28.7
LE	DOY174	9	346.6	350.2	3.7	39.8	10.3
	DOY182	10	399.8	380.9	-19.0	43.3	9.8
	DOY189	11	501.3	503.6	2.3	40.1	6.8
	Overall	30	421.0	416.7	-4.4	41.1	8.9
H	DOY174	9	123.4	152.5	29.1	37.6	24.8
	DOY182	10	124.6	145.9	21.3	35.5	30.6
	DOY189	11	22.4	37.6	15.2	19.2	144.4
	Overall	30	86.8	108.2	21.4	31.3	70.6
EF	DOY174	9	0.73	0.69	-0.04	0.07	7.4
	DOY182	10	0.76	0.72	-0.04	0.07	8.5
	DOY189	11	0.96	0.93	-0.03	0.04	3.4
	Overall	30	0.82	0.79	-0.04	0.06	6.3

To isolate uncertainties in R_n , G , and H retrievals from LE retrievals, we computed EF for all sites having all measurements of R_n , G , H , and LE. The EF retrievals from M-SEBAL show closer agreement with ground-based measurements compared with LE retrievals (Table 6.1 and Fig. 6.4), suggesting an RMSD of 0.06 and an MAPD of 6.3%, respectively.

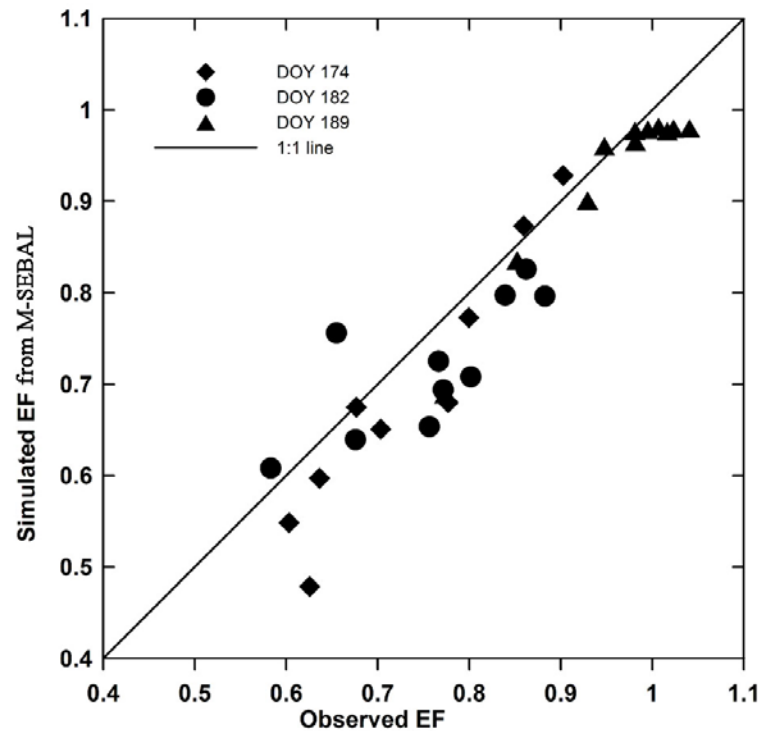


Figure 6.4 Comparison of EF from M-SEBAL with corresponding eddy covariance tower-based EF for the SMACEX site on DOY 174, 182 and 189 in 2002.

It is noted that the H estimates from M-SEBAL suggest a relatively larger discrepancy compared with the estimates of other energy balance components, even showing an MAPD of up to 144.4% for DOY 189. This could be a consequence of relatively small magnitudes of the H observations and the presence of advection on that day which led to negative H observations for sites 3, 6, 14, and 24. Since M-SEBAL is based on energy conservation in the vertical direction of the Earth's surface, advective energy which may have arisen on DOY 189 was not detected by the M-SEBAL algorithm. However, this effect seems to marginally influence the LE estimates, showing an RMSD of 40.1 W m^{-2} and an MAPD of 6.8% on DOY 189, respectively, due primarily to the relatively small contribution of the H estimates to the energy balance on

that day.

In addition, M-SEBAL appears to overestimate R_n , showing a bias of 15.8 W m^{-2} for the three days. This might be related to an underestimation of T_{rad} , consequently an underestimation of L_u and an overestimation of R_n . Note that H fluxes were overestimated by M-SEBAL to certain degrees for all three days, showing an overall bias of 21.4 W m^{-2} . This may result from the horizontal cold edge formulated in the trapezoidal framework. In fact, the realistic cold edge would be slanting and essentially above the horizontal one under low f_c conditions (i.e., side B'C in Fig. 6.1), with the two cold edges intersecting at point C. The downward displaced horizontal cold edge of trapezoid ABCD would lead to decreasing cold extremes, thereby an increase in H estimates and a decrease in LE estimates. However, substitution of the horizontal cold edge for the slanting one is motivated primarily by circumventing the specification of the temperature for the bare surface without water stress (point B in Fig. 6.1). This simplification would not significantly compromise the retrieval accuracy of LE during the growing season. Most importantly, it can greatly reduce uncertainty and subjectivity involved in SEBAL to visually identify the cold pixel which is often influenced by cloud contamination and other outliers.

6.3.2. Implementation of SEBAL

Numerous studies have indicated that the performance of SEBAL is largely influenced by selected hot and cold extremes from satellite imagery. However, less rigorous validation has been performed to systematically investigate how the

performance of SEBAL varies with these selected extremes. Most applications pertaining to SEBAL presumably ascribe all uncertainties or errors to the selected extremes and relevant procedures. It is particularly important to note that correctly implementing a model is critical to accurately examining its advantages and limitations in the model physics. Some validation work related to SEBAL did not take adequate measures to select pixels which are able to well satisfy the hypothesis of extremes; the larger the deviations from the hypothesis of SEBAL, the less the possibility of gaining a full understanding of the model performance and the mechanisms of error propagation. This can, however, be treated in part as the inadequacy of the model formulation; in practice, it is not necessarily feasible to successfully locate two extremes under all circumstances.

On the other hand, a majority of validation studies of SEBAL were conducted by comparing 24-h integrated ET retrievals (mm/d) with ground-based counterparts (e.g., lysimeter). However, the accumulated ET is also determined largely by daily net radiation; errors involved in the H and LE retrievals (or EF) at the time of imaging may be cancelled out during the diurnal cycle, even though the accumulated ET shows good agreement with ground-based daily measurements. This has hindered a more rigorous validation of SEBAL with respect to its core algorithm aimed at generating H and LE typically at the satellite overpass.

Fig. 6.5 shows the f_c - T_{rad} space at the SMACEX site derived from Landsat imageries acquired on DOY 174 and DOY 182 in 2002, respectively, which can facilitate the selection of extremes required by SEBAL. Meanwhile, we extracted coordinates of

these selected extremes to check their land cover types on color-infrared composite images. It is plausible that there are several options to locate hot and cold extremes with varying characteristic variables (i.e., $T_{\text{rad,hot}}$, $T_{\text{rad,cold}}$, and $R_{\text{n,hot}}-G_{\text{hot}}$) for the two days.

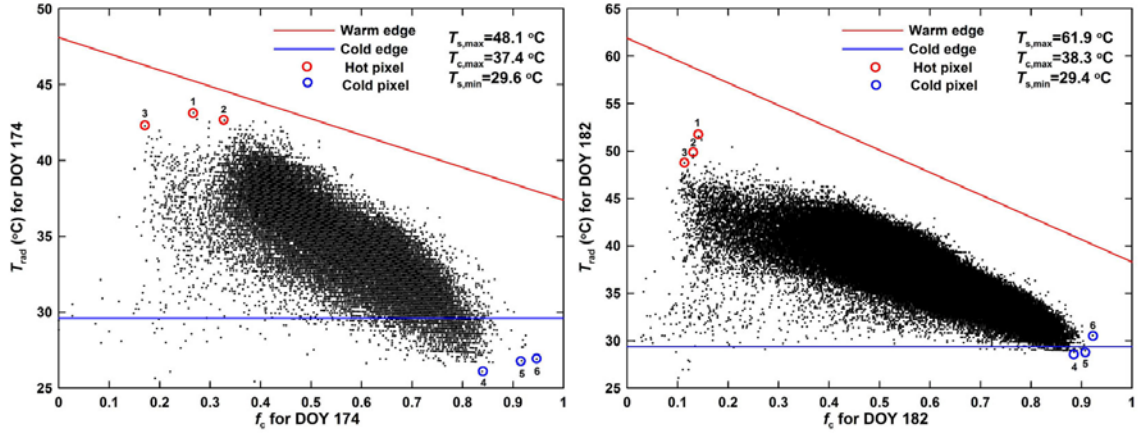


Figure 6.5 Scatterplots of f_c and T_{rad} for the SMACEX site for DOY 174 and 182 in 2002, numbered red circles represent hot extreme candidates, and numbered blue circles represent cold extreme candidates. Red and blue lines represent limiting edges of the trapezoidal framework, showing $T_{s,\text{max}}$, $T_{c,\text{max}}$, and $T_{s,\text{min}}(T_a)$ for both days.

Three hot extremes with relatively high T_{rad} and low f_c values likely corresponding to late plantings of soybean crops, and three cold extremes with relatively low T_{rad} and high f_c values corresponding to full canopy covers were located for the two days, respectively. It is noted that the identified hot extremes were not completely bare surfaces, showing f_c values ranging between 0.17 and 0.33 and ~ 0.14 for the two days, respectively. For a rainfed area particularly during the period of rapid growth in crops, a pure bare surface without ET seems to be non-existent, making the selection of hot extreme which completely satisfies the hypothesis from satellite imagery impossible. On the other hand, temperatures of the identified cold extremes are generally smaller than T_a

at the time of imaging. In fact, there are a certain group of pixels whose temperatures are generally lower than T_a , particularly for DOY 174 (Fig. 6.5). This might not necessarily result from advection, but rather from uncertainty in T_{rad} retrievals or cloud effects.

Taking several quasi hot and cold extremes exhibiting certain degrees of variation in their characteristic variables would be helpful for capturing the variability mechanisms of the performance of SEBAL with different anchor points. There are in total 9 combinations of a hot extreme and a cold extreme from 3 hot extreme candidates and 3 cold extreme candidates, which constitute inputs along with other characteristic variables of these extremes to invert coefficients a and b for calculating H for each day. Characteristic variables of these extreme pairs are shown in Table 6.2 For each day, 9 combinations of hot and cold extremes resulted in 9 pairs of coefficients a and b . Subsequently, they constituted inputs to SEBAL for computing H and LE for all remaining pixels in the images.

Table 6.2 Extreme pixels with their characteristic variables as inputs of SEBAL at the SMACEX site for DOY 174 and 182 in 2002, cases 1-9 represent all combinations of three hot pixels (numbering 1-3) and three cold pixels (numbering 4-6) selected from the satellite imagery

Case	$T_{s,hot} (^{\circ}\text{C})$		$(R_n-G)_{hot}$ (W m^{-2})		$f_{c,hot} (-)$		$T_{s,cold} (^{\circ}\text{C})$		$f_{c,cold} (-)$	
	174	182	174	182	174	182	174	182	174	182
1 (1, 4)	43.1	51.5	467.0	442.5	0.27	0.14	26.1	28.8	0.84	0.87
2 (2, 4)	42.6	49.6	478.3	440.9	0.17	0.13	26.1	28.8	0.84	0.87
3 (3, 4)	42.3	48.7	481.7	442.5	0.33	0.13	26.1	28.8	0.84	0.87
4 (1, 5)	43.1	51.5	467.0	442.5	0.27	0.14	26.8	29.0	0.92	0.90
5 (2, 5)	42.6	49.6	478.3	440.9	0.17	0.13	26.8	29.0	0.92	0.90
6 (3, 5)	42.3	48.7	481.7	442.5	0.33	0.13	26.8	29.0	0.92	0.90
7 (1, 6)	43.1	51.5	467.0	442.5	0.27	0.14	26.9	30.5	0.94	0.92
8 (2, 6)	42.6	49.6	478.3	440.9	0.17	0.13	26.9	30.5	0.94	0.92
9 (3, 6)	42.3	48.7	481.7	442.5	0.33	0.13	26.9	30.5	0.94	0.92

6.3.3. Results from SEBAL

Differences between the H and LE retrievals and tower-based measurements are listed in Table 6.3. Retrievals of all energy balance equation components under 9 different combinations of anchor points on DOY 174 and 182 are shown in Figs. 6.6 and 6.7, respectively. Results indicate that the SEBAL algorithm consistently overestimates H and underestimates LE on DOY 174, with RMSD and MAPD of the H retrievals ranging between 79~108.3 W m^{-2} and 65~92.6%, respectively, and RMSD and MAPD of the LE retrievals ranging between 55.4~81.2 W m^{-2} and 13.5~22.2%, respectively. SEBAL generally underestimates H and overestimates LE on DOY 182, suggesting RMSD and MAPD of the H retrievals ranging between 38.7~51.8 W m^{-2} , and 21.6~39.8%, respectively, and RMSD and MAPD of the LE retrievals ranging between 47.3~60.4 W m^{-2} and 9.8~13.3%, respectively.

Table 6.3 Statistics of discrepancies between the H and LE retrievals from SEBAL and tower-based measurements at the SMACEX site for DOY 174 and 182 in 2002 under 9 cases (1-9) representing different combinations of extreme hot pixels (numbering 1-3) and cold pixels (numbering 4-6) selected from Landsat TM imagery

Case (hot, cold)	H : RMSD (W m ⁻²)		H : MAPD (%)		H : bias (W m ⁻²)	
All days	174	182	174	182	174	182
1 (1, 4)	90.2	37.7	77.8	22.1	87.5	-11.2
2 (2, 4)	102.2	37.4	87.7	21.0	99.3	-1.0
3 (3, 4)	108.3	38.7	92.6	21.6	105.2	5.2
4 (1, 5)	80.4	38.6	66.7	22.9	77.0	-14.0
5 (2, 5)	92.2	37.7	76.2	21.6	88.5	-3.9
6 (3, 5)	98.2	38.6	81.0	21.7	94.2	2.2
7 (1, 6)	79.0	51.8	65.0	39.8	75.4	-36.3
8 (2, 6)	90.7	47.9	74.5	35.9	86.8	-27.7
9 (3, 6)	96.7	46.4	79.2	34.4	92.6	-22.4
Case (hot, cold)	LE: RMSD (W m ⁻²)		LE: MAPD (%)		LE: bias (W m ⁻²)	
All days	174	182	174	182	174	182
1 (1, 4)	64.4	46.6	16.6	10.2	-54.8	13.5
2 (2, 4)	75.5	46.2	20.3	10.0	-66.6	3.3
3 (3, 4)	81.2	47.3	22.2	9.8	-72.5	-2.9
4 (1, 5)	56.5	47.6	13.8	10.4	-44.2	16.3
5 (2, 5)	67.0	46.8	17.2	10.2	-55.7	6.2
6 (3, 5)	72.5	47.4	19.1	10.0	-61.5	0.1
7 (1, 6)	55.4	60.4	13.5	13.3	-42.7	38.6
8 (2, 6)	65.8	57.1	16.8	12.4	-54.1	30.0
9 (3, 6)	71.2	55.9	18.6	12.2	-59.8	24.7

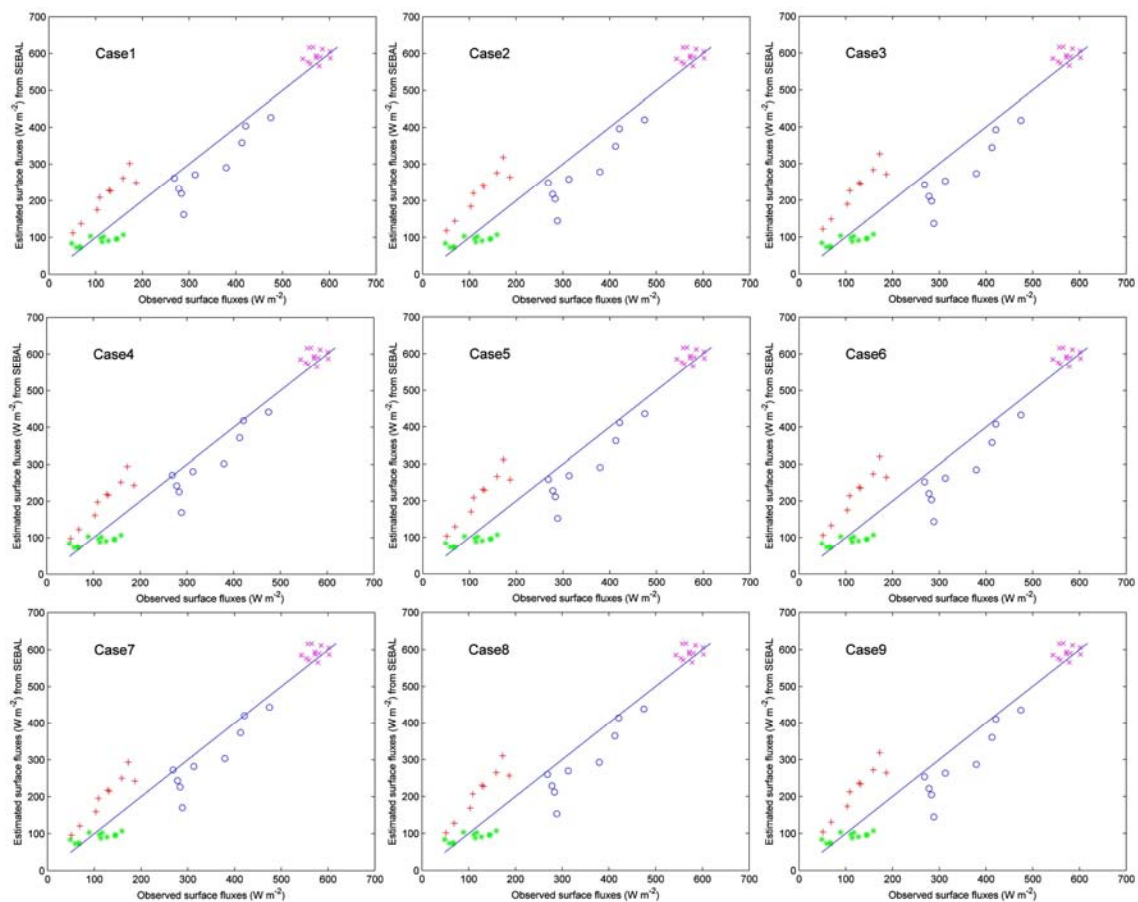


Figure 6.6 Estimates of R_n (magenta cross), G (green asterisk), H (red cross), and LE (blue circle) from SEBAL for 9 cases of combinations of selected extremes at the SMACEX site for DOY 174.

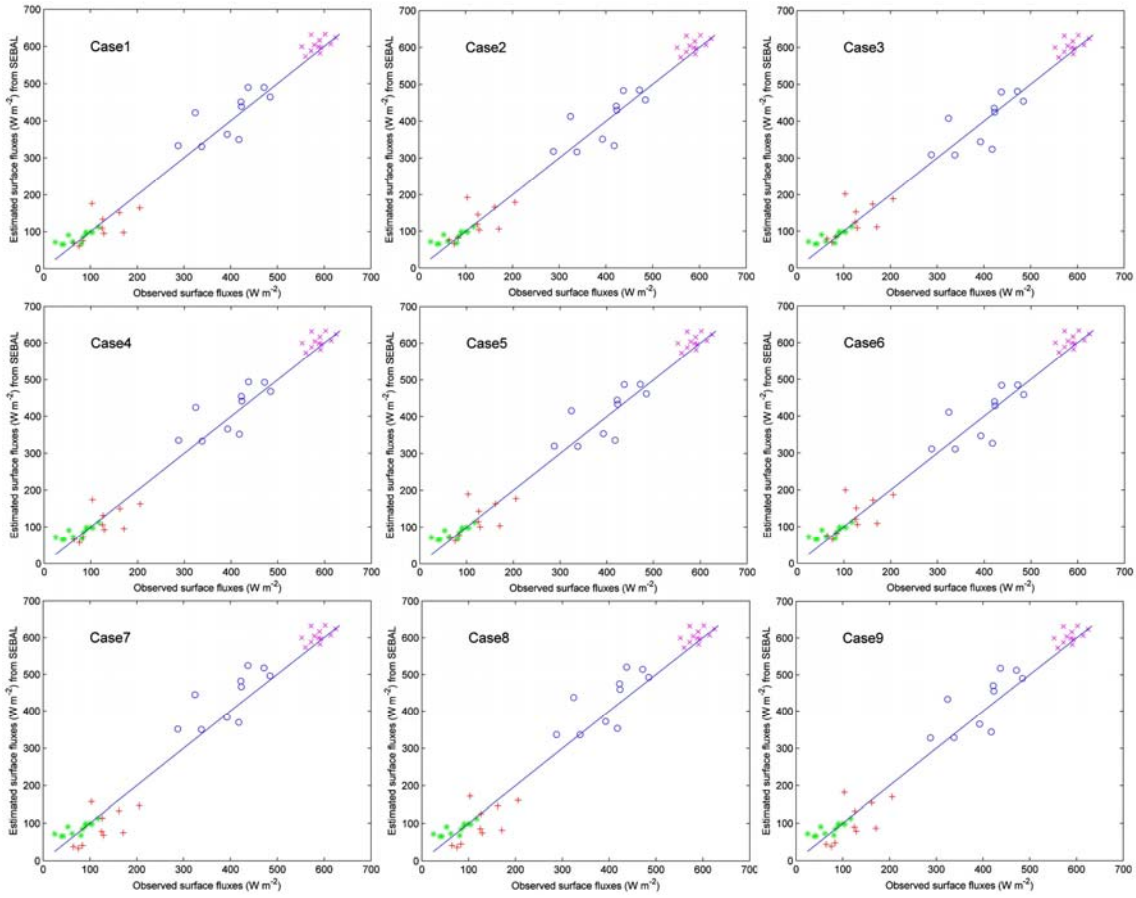


Figure 6.7 Estimates of R_n (magenta cross), G (green asterisk), H (red cross), and LE (blue circle) from SEBAL for 9 cases of combinations of selected extremes at the SMACEX site for DOY 182.

These differences are essentially large when compared with RMSD and MAPD of 39.8 W m^{-2} and 10.3% for the LE retrievals on DOY 174, and that of 43.3 W m^{-2} and 9.8% on DOY 182, respectively, from M-SEBAL, except the LE retrievals from SEBAL on DOY 182 under case 3 displaying a similar retrieval accuracy with the M-SEBAL algorithm and even slightly closer agreement with ground-based measurements for the H estimates from SEBAL. It is apparent that the H and LE retrievals from SEBAL are of great uncertainty, varying with selected extremes.

Furthermore, it is noted that the highest accuracy of H and LE retrievals from SEBAL for DOY 174 occurs under case 7 consisting of hot pixel 1 and cold pixel 6, which show the highest T_{rad} values in the three respective extreme candidates. The lowest accuracy of H and LE retrievals from SEBAL corresponds to case 3 composed of hot pixel 3 and cold pixel 4 which show the lowest T_{rad} values in the three respective extreme candidates. By contrast, the highest accuracy of H and LE retrievals from SEBAL for DOY 182 takes place under case 3 but the lowest accuracy under case 7.

From the perspective of the contextual relationship between f_c and T_{rad} , the two anchor points in SEBAL represent essentially two “horizontal” limiting edges of the f_c - T_{rad} space. SEBAL assumes a positive linear correlation of its H estimates with T_{rad} throughout a scene, which, as a matter of fact, corresponds to the quasi negative linear correlation of its EF estimates with T_{rad} at a specific f_c interval as demonstrated in Section 6.2.2. The most marked difference of these spatial variability approaches (i.e., SEBAL and the triangle model) lies in the configuration of limiting edges of the f_c - T_{rad} space or determination of extremes. Downward movement of warm and/or cold edges indicated by a reduction in the temperatures of extremes tends to result in increasing H estimates and consequently decreasing LE estimates. On the contrary, upward movement of the limiting edge (s) has a tendency to lead to decreasing H estimates and therefore increasing LE estimates.

The relative displacement of the rectangular framework intrinsic in SEBAL with respect to the trapezoidal framework adopted in M-SEBAL can explain the overestimated H from SEBAL for DOY 174 and the generally underestimated H for

DOY 182. For DOY 174, two horizontal extremes in SEBAL, i.e., the rectangular envelope of the f_c - T_{rad} space, are generally shifted downward with reference to the trapezoidal framework. Case 7 consisting of hot pixel 1 and cold pixel 6 forms a rectangle showing the least deviation from the trapezoidal framework, thereby suggesting the least discrepancies of the H and LE retrievals. Case 3 consisting of hot extreme 3 and cold extreme 4 shows the largest deviation from the trapezoidal framework, therefore leading to the largest discrepancies of model outputs. The same explanation could be applied to DOY 182 that the SEBAL-based rectangular framework under case 3 approximates the trapezoid best, particularly for the range of high f_c values where the eddy covariance towers were located, resulting in the least discrepancies of H and LE retrievals compared with ground-based measurements.

6.3.4. Relationship between error and f_c for SEBAL and M-SEBAL

For unraveling the mechanisms of error propagation of SEBAL and M-SEBAL, we investigated the relationship between the relative error (simulated H -observed H) in the H estimates from both models and the corresponding f_c values at all eddy covariance sites for DOY 174 and 182 (see Fig. 6.8), respectively. SEBAL was run under the case of the combination of extreme pixels for which it performed best, i.e., case 7 for DOY 174 and case 3 for DOY 182. Results indicate that for DOY 174, the relative error in the H estimates from SEBAL generally decreases with increasing f_c . This is caused principally by its rectangular framework and its extreme edges. Cold and warm edges of SEBAL are essentially lower than that of the trapezoid framework for DOY 174, resulting in

increased H and decreased LE estimates. However, with increasing f_c after exceeding the intersection of the realistic warm edge and the selected hot edge, the selected horizontal hot edge of SEBAL becomes higher than the slanting one of M-SEBAL, with the overestimation of H from SEBAL being mitigated to a certain degree. On the other hand, even though the H estimates from M-SEBAL also tend to be larger than the measurements, the errors are decreased appreciably compared with those of SEBAL. This demonstrates that the use of the trapezoidal framework is capable of more realistically reflecting variations in LE with f_c and T_{rad} .

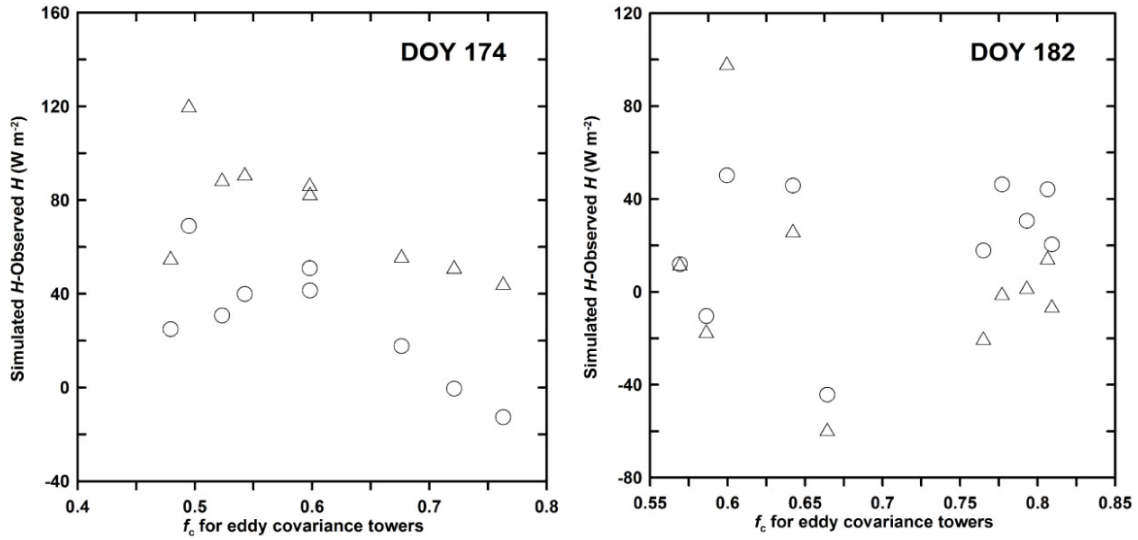


Figure 6.8 Variation of relative errors of H retrievals from SEBAL (triangle) and M-SEBAL (circle) with f_c for DOY 174 and 182, respectively.

For DOY 182, unfortunately, the whole picture of the mechanisms of error propagation of SEBAL cannot be completely reflected because of limited f_c values generally ranging from 0.55 to 0.8 at all eddy covariance sites. The errors in the H

estimates from SEBAL for high f_c values (i.e., larger than 0.75, five sites) tend to be smaller than those of M-SEBAL, which might result from a well approximation of the rectangular framework to the realistic quadrangular one. However, errors in the H estimates from SEBAL are generally larger than those of M-SEBAL for f_c lower than 0.7 (five sites).

6.3.5. Spatial distribution of H and LE Retrievals from SEBAL and M-SEBAL

We mapped surface fluxes by SEBAL and M-SEBAL for the entire SMACEX site for DOY 174 and 182. Figs. 6.9 and 6.10 show spatial distributions and frequencies of the H and LE estimates, respectively, from SEBAL and M-SEBAL for DOY 174 and 182. Results explicitly show that SEBAL generates significantly larger H estimates than does M-SEBAL, showing areal mean values of the H estimates from SEBAL and M-SEBAL of 208.5 W m^{-2} and 166.2 W m^{-2} , and 306.4 W m^{-2} and 164.6 W m^{-2} for DOY 174 and 182, respectively. The overestimation of H estimates from SEBAL is due primarily to the rectangular framework intrinsic in its hypothesis. The downward shift of cold edge for DOY 174 and downward shift of hot edge for DOY 182 of SEBAL could be responsible for the overestimation of areal H estimates, particularly for lower f_c areas. In fact, there was about 5.4% area of the study site showing the H estimates from SEBAL larger than the available energy ($R_n - G$) (see the cumulative distribution of LE in row 3 in Fig. 6.10). This was taken to be erroneous H retrievals from SEBAL, even under the condition of overestimation of R_n and underestimation of G of SEBAL; thereby the LE retrievals from SEBAL were artificially set to zero for these pixels. To

that end, some portions of the LE map from SEBAL for DOY 182 have to suffer somewhat from this artifact.

On the other hand, there were around 4% pixels whose H retrievals from M-SEBAL for DOY 174 were zero (see the cumulative distribution of H in row 2 in Fig. 6.9), which results from the cold edge of M-SEBAL being taken as T_a . There are a group of pixels whose temperatures lower than T_a at the satellite overpass due to clouds, sloping terrain, and other effects. However, their H estimates were mistakenly derived as small magnitudes by the SEBAL algorithm due to an unrealistic cold edge identified. In general, the LE estimates from SEBAL are essentially smaller than that of M-SEBAL for both days in large part due to the rectangular framework.

In summary, directly relating T_{rad} retrievals to LE throughout a scene based on a linear relationship in SEBAL could be unreasonable in generating large-scale LE/ET, even though good agreement between the estimates and measurements at a handful of sites is shown. Distributions of H and LE from SEBAL may have been distorted to varying degrees due to the oversimplified rectangular framework in previous applications; the degree of distortion depends on the real physical limits, visually identified extremes, and outliers in T_{rad} retrievals. Mapping ET from SEBAL seems to be less than satisfactory due to the oversimplified framework it involves and the determination of its limiting edges of large uncertainty. The M-SEBAL algorithm appears to be capable of reproducing reasonable LE distribution due to the integration of the trapezoidal framework.

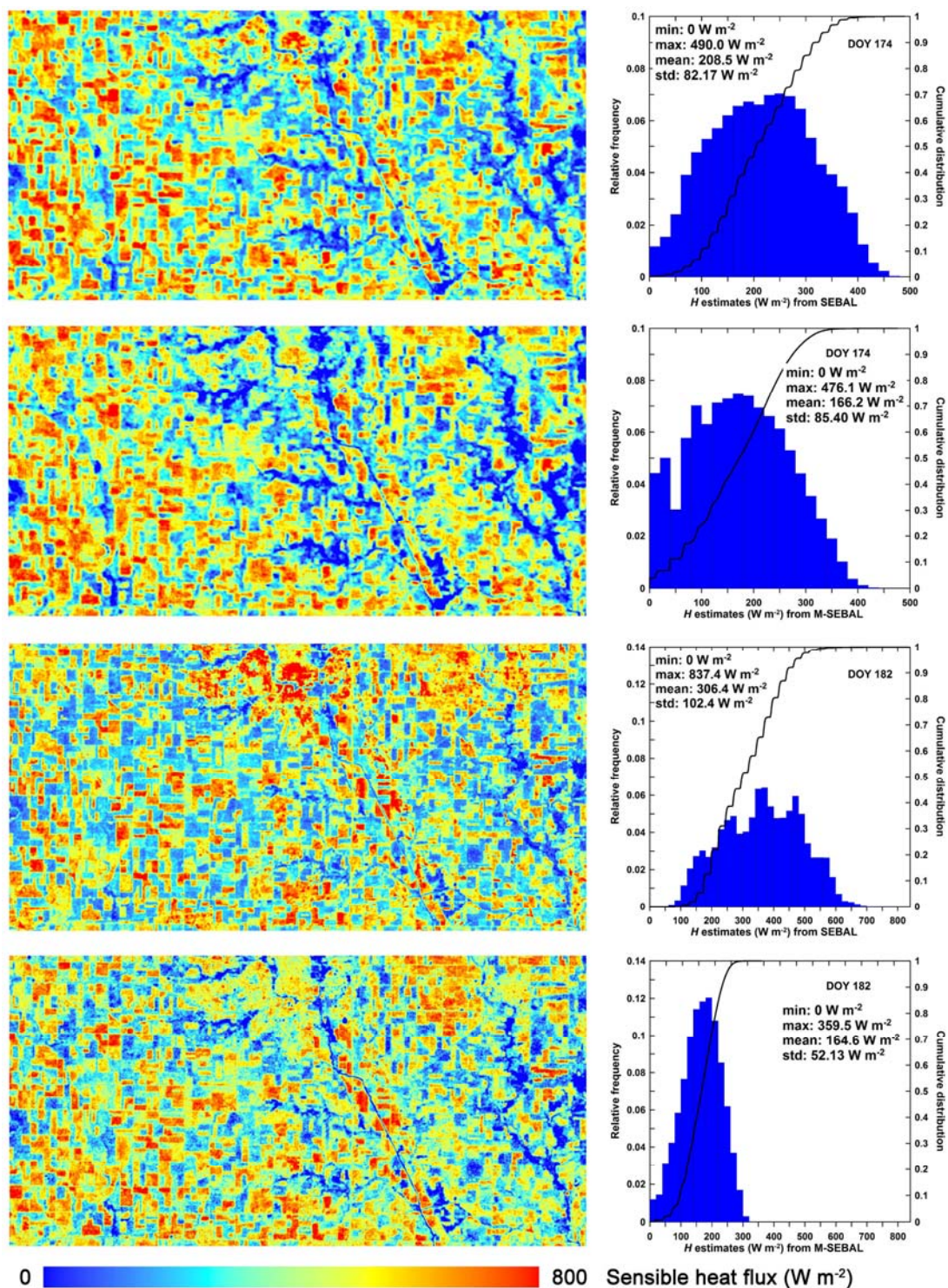


Figure 6.9 Spatial distributions of H estimates from SEBAL and M-SEBAL, frequency distributions (on the right of the H maps), and their cumulative curves for DOY 174 and 182.

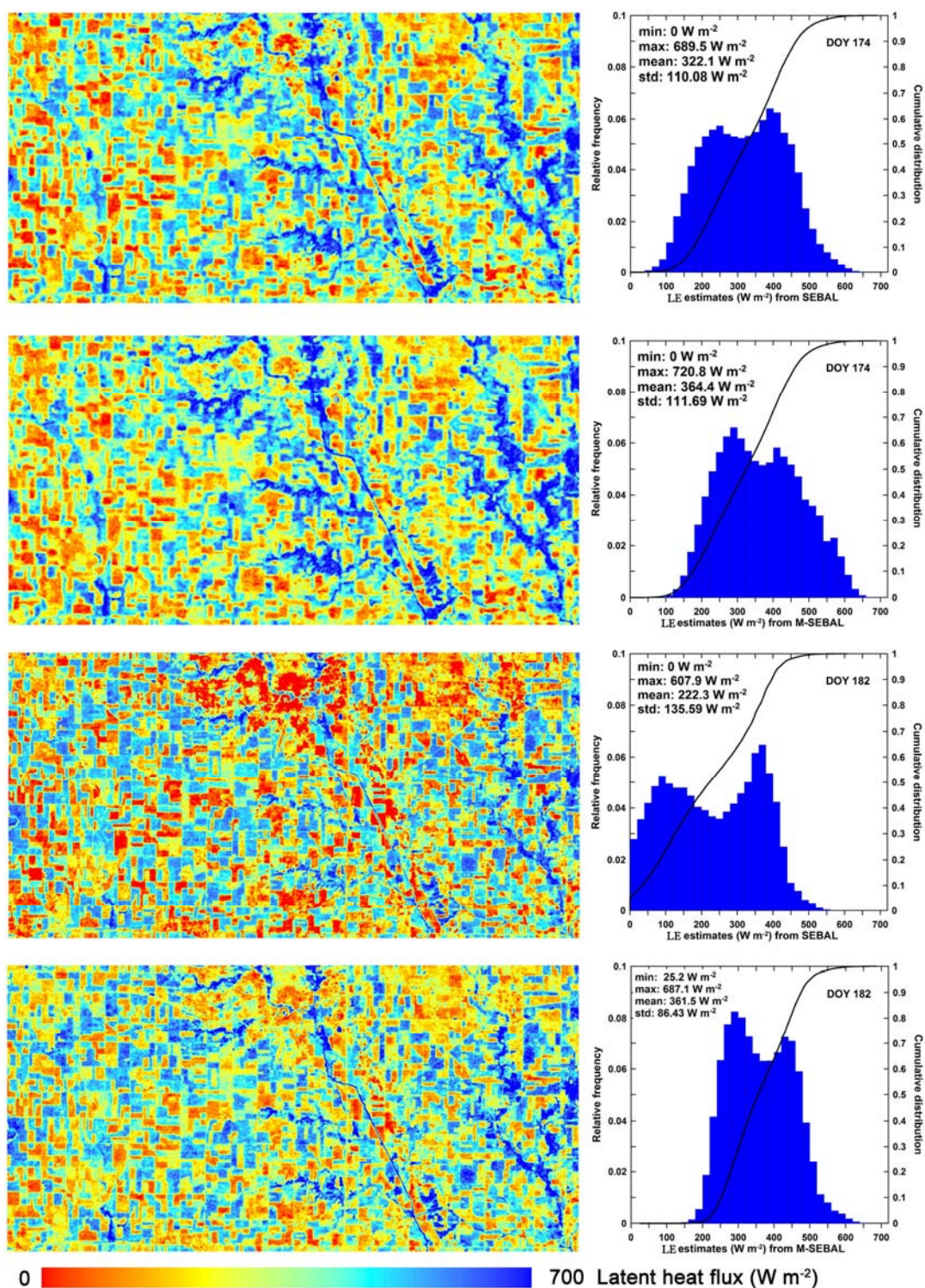


Figure 6.10 Spatial distributions of LE estimates from SEBAL and M-SEBAL, frequency distributions (on the right of the ET maps), and their cumulative curves for DOY 174 and 182.

6.4. Summary of model advantages and limitations

In summary, SEBAL tends to overestimate H and consequently underestimate LE/ET, if the hot extreme is significantly lower than the real physical limit of the warm edge which corresponds to the absence of extremely hot surfaces over areas dominated by vegetation or agricultural crops in the growing season or to the situation that there indeed exists the extreme surface but it is not able to precisely identified by the operator, and/or the cold extreme is significantly underestimated due to outliers incurred by cloud or terrain effects. Under the condition that both hot and cold extremes are occasionally close to the realistic ones, the horizontal hot extreme in SEBAL tends to be above the hypotenuse of the trapezoid with increasing f_c . This would lead to an underestimation of H and then an overestimation of LE. Under the condition that the hot extreme is overestimated, corresponding to an erroneous larger $T_{\text{rad,hot}}$, and the cold extreme is underestimated, corresponding to an erroneous smaller $T_{\text{rad,cold}}$ value (even smaller than T_a exhibited in DOY 174), the retrievals from SEBAL seem to be occasionally reasonable for certain f_c ranges because discrepancies caused by the two extremes offset each other.

In fact, the rectangular framework in the SEBAL algorithm seems to be inadequate to depict the realistic variability of the f_c - T_{rad} space. Instead, it should be a trapezoidal framework, or at least, a triangular framework observed by numerous studies. Moreover, determination of the rectangular framework (i.e., two anchor points) is beset with significant subjectivity and uncertainties involved in the T_{rad} retrievals. Outliers of T_{rad} retrievals may have been frequently mistakenly taken as extremes of SEBAL in a

majority of applications. The large dependence of two extremes of great uncertainty built on an oversimplified rectangular framework has been the major source of error of SEBAL.

It is important to note that METRIC modifies energy balances for two extremes by introducing a LE term to the hot extreme and an H term to the cold extreme, attempting to reflect not completely dry and not completely wet conditions. Nonetheless, this treatment does not mean the modification of the rectangular framework it involves and the manual selection of two extremes from images is still required. To that end, METRIC is of the similar inadequacies as SEBAL illustrated in this chapter.

The real physical limits of the quadrangular framework seem to be reasonably approximated by the trapezoidal framework involved in M-SEBAL, without largely compromising its accuracy. It is, however, noted that under low f_c conditions, M-SEBAL tends to overestimate H and consequently underestimate LE due to the use of the horizontal cold extreme. This is primarily due to the difficulty of demarcating cold edges directly from the contextual relationship between f_c and T_{rad} . Determination of vertices of the trapezoidal framework is feasible under certain assumptions on physiological properties for the fully vegetated surface without ET.

M-SEBAL has almost the same data requirements as SEBAL. In addition, M-SEBAL incorporates f_c into the contextual f_c - T_{rad} , f_c - α , and f_c - ΔE spaces to infer relevant variables and parameters. This gives full play to the inherent spatial information among remotely sensed surface variables and therefore creates an opportunity to reflect realistic EF and LE/ET across large areas with generally homogeneous meteorological

conditions.

6.5. Concluding remarks

SEBAL has been designed and widely used (misused) to estimate ET using remotely sensed surface variables and few meteorological data across varying spatial and temporal scales over the past 15 years. However, it is beset by manual identification of two extremes, hot pixel and cold pixel, to determine the temperature difference between the near surface and the reference height, which is assumed to be linearly related to remotely sensed T_{rad} throughout a scene. Aiming at unraveling the deficiencies in the SEBAL physics and replacing its core component of H scheme, this study demonstrates that SEBAL is, in fact, of a rectangular framework of the contextual f_c - T_{rad} space, which significantly distorts the spatial distributions of H and LE retrievals. In addition, determination of its limiting edges, i.e., two anchor points involved in SEBAL, suffers significantly from subjectivity.

SEBAL can overestimate or underestimate H and LE depending on the relative displacement between the rectangular framework and the real physical limits which indeed constitute a quadrangular framework and are approximated by a trapezoidal framework in the M-SEBAL. Determination of the trapezoidal framework is achieved by solving radiation budget and energy balance equations for temperatures of the bare surface with the largest water stress, and the fully vegetated surface with the largest water stress, given certain meteorological conditions. Coefficients of the linear relationship between T_{rad} and dT vary with f_c but are assumed essentially invariant within

the same f_c or f_c class in M-SEBAL.

SEBAL and M-SEBAL are applied to the SMACEX site in central Iowa, U.S. Results indicate that M-SEBAL is capable of reproducing EF and LE with relatively high accuracy, showing an overall RMSE of 0.06 and 41.1 W m⁻², and MAPD of 6.3% and 8.9%, respectively, for three Landsat TM/ETM⁺ imagery acquisition dates in 2002. The retrieval accuracy of SEBAL depends largely on the selected extremes. In addition, the spatial distributions of H and LE retrievals from SEBAL are significantly distorted due to its intrinsic rectangular framework. The use of the trapezoidal framework in M-SEBAL appears to ensure more reasonable distributions of H and LE across the study site.

CHAPTER VII

ADDRESSING THE SCALE DEPENDENCIES OF REMOTE SENSING-BASED TRIANGLE MODELS

7.1. Introduction

Amongst satellite-based models for ET estimation, the triangle models are unique in interpreting the contextual relationship between NDVI/f_c and T_{rad} to deduce EF and ET over large areas (Carlson et al., 1994; Gillies and Carlson, 1995; Jiang and Islam, 2001; Price, 1990; Sandholt et al., 2002). This type of models manifests advantages in utilizing spatial information of visible, near-infrared, and thermal infrared bands to deduce EF and ET without depending largely on ground observations, thereby facilitating initialization of land surface models.

There are, however, several common issues associated with triangle models that seem to be inadequately investigated and addressed over the past two decades. First, the triangle models have consistently underestimated (Choi et al., 2009; Jiang and Islam, 2003; Wang et al., 2006) or overestimated EF/ET (Batra et al., 2006; Jiang and Islam, 2001; Jiang et al., 2009) in the majority of published studies. However, reasons for these deviations have not been fully investigated and appropriately interpreted from a standpoint of model physics and scale effects. Second, most of triangle models are combined with moderate or low spatial resolution sensors, i.e., NOAA-AVHRR (Batra et al., 2006; Jiang and Islam, 2001; Sandholt et al., 2002), MODIS (Tang et al., 2010; Wang et al., 2006), and MSG-SEVIRI (Stisen et al., 2008), for estimating EF/ET over large areas. However, applications and investigations of triangle models using high resolution

imageries rarely appear in the literature. Determining effective techniques to make use of data from various sensors has been the focus of considerable research (McCabe and Wood, 2006).

Third, a recurring issue for the application of derived satellite data is whether techniques for one scale are appropriate to another (Carlson et al., 1995b). Methods to address spatial and temporal disparities between landscape heterogeneity and sensor and model resolution are limited, since an adequately developed theory of scale dependence or scaling in hydrology does not yet exist (Beven and Fisher, 1996). Particularly in surface flux estimation, little work has been performed to investigate differences in model outputs between using easily obtained moderate or low spatial resolution sensors and relatively infrequent high spatial resolution sensors, and in outputs between successively varying domains of satellite imagery. These issues have been perplexing surface flux estimation in the operational ET estimation and hydrological communities.

It is noted that there would be a significant domain scale effect intrinsic in triangle models. There exist two limiting edges constituting the envelopes of the f_c - T_{rad} space in triangle models. They play a paramount role in determining the magnitudes of EF and LE. The upper envelope is referred to as the warm edge, pixels on which are taken as surfaces with the largest water stress. By contrast, the lower envelope is called the cold edge, pixels on which represent surfaces without water stress, i.e., evaporating and transpiring at potential rates. EF and LE for a pixel at a specific NDVI/f_c interval are deduced by weighting extreme T_{rad} values within the interval in terms of T_{rad} of a pixel. To that end, warm and cold edges are essential to configuring the triangle space by

prescribing important boundary conditions of the contextual f_c - T_{rad} relationship and subsequently to determining EF and LE for pixels amid the limiting edges.

It is expected that the determination of warm and cold edges of the f_c - T_{rad} space would be dependent upon the domain of a study site being considered or the size of images being used. It is common that researchers and practitioners focus primarily on the study sites of interest, e.g., the SMACEX site of around 670 km² in central Iowa, U.S. (Choi et al., 2009), the Heihe River basin about 38,000 km² in northwestern China (Tang et al., 2010), and the Southern Great Plains site around 140,000 km², U.S. (Batra et al., 2006; Wang et al., 2006). Areas beyond a study site are rarely taken into account, especially for relatively small study sites. Nevertheless, a complete picture of the extreme edges and variations in EF with T_{rad} would rest on a larger domain. On the other hand, the thermal bands of a variety of satellite sensors have varying capacity to discriminate the thermal properties of the land surface and therefore to derive T_{rad} . In other words, the resolution of retrieved T_{rad} may also influence the definition and determination of limiting edges; varying spatial resolutions of imagery are likely to generate varying EF and LE for a given study site.

Carlson et al. (1995b) performed a preliminary investigation into the resolution scale effect of triangle models by linearly aggregating T_{rad} of high spatial resolution derived from the NS001 multispectral scanner (5 m) to mimic low spatial resolution data, with resolutions ranging from 20 m to 80 m to 320 m. They observed a successive movement of warm edges towards the cold edge with increasing pixel size, but concluded that the objectively determined warm edges coincided with the domain of soil

moisture availability isopleths and therefore the triangle with its warm edge was not substantially changed. Gillies et al. (1997) indicated that scale issues might influence EF and LE retrievals from triangle models, since low resolution data would not necessitate the definition of a cold and a warm edge (Gillies and Carlson, 1995). Batra et al. (2006) and Venturini et al. (2004) systematically compared and contrasted the utility of triangle models between the use of MODIS and AVHRR sensors, showing a similar contextual space of $\text{NDVI-}T_{\text{rad}}$ and EF estimates.

We suggest that exploring the utility of triangle models in combination with high spatial resolution imagery, e.g., Landsat TM/ETM⁺, and extensively comparing the performance of triangle models between the use of high and moderate or low spatial resolution sensors are imperative to reveal a complete picture of the resolution scale effect involved. Furthermore, conditions under which the triangle models may be applied need to be better defined (Goward et al., 2002). In most cases, researchers and practitioners apply triangle models without accounting for the size of a usable portion of imagery. Comparing the performance of triangles models within successively varying domains is the key to unravel the domain dependence of the triangle models. The resolution and domain dependencies may have resulted in a large uncertainty in the resulting EF and LE/ET estimates from triangle models. As such, much work needs to be undertaken to investigate the domain and resolution dependencies of the triangle methods. Mechanisms of addressing these scale effects and controlling errors therein are required to provide an accurate understanding of EF and ET distributions from the triangle models. We suggest that the physical limits of the $\text{NDVI-}T_{\text{rad}}$ space for a given

study site uniquely exist. Derivation of the physical limits would provide determinate solutions of the triangle models, which may be useful in restraining uncertainties arising from the domain and resolution dependencies of triangle models.

The objectives of this chapter therefore were to (1) explore the domain dependence of triangle models by applying them to varying domains and reveal the mechanisms of error propagation; (2) examine the resolution dependence of triangle models using MODIS and Landsat ETM⁺ imageries of the same overpass time; and (3) the use of the physical limits of the NDVI- T_{rad} space described in Chapter IV to control errors resulting from the domain and resolution dependencies intrinsic in triangle models and validate the proposed framework. Section 7.2 presents model formulation of triangle models and the framework to address the scale dependencies, followed by Section 7.3 providing a systematic analysis of the domain scale effect and Section 7.4 about the resolution scale effect of triangle models, along with the demonstration of the proposed framework to restrain error propagation. Major findings of this chapter are given in Section 7.5.

7.2. Model formulation

7.2.1. Formulation of triangle models

There are a series of triangle models (Batra et al., 2006; Jiang and Islam, 1999; Moran et al., 1994; Sandholt et al., 2002) developed which bear similarities in interpreting the contextual relationship between NDVI/f_c and T_{rad} . In general, the envelopes of the NDVI and T_{rad} space constitute a triangle or a trapezoid. The major differences of these models lie in the configuration of the space and determination of

limiting edges of the triangles. Fig. 7.1 illustrates the triangle space and their limiting edges.

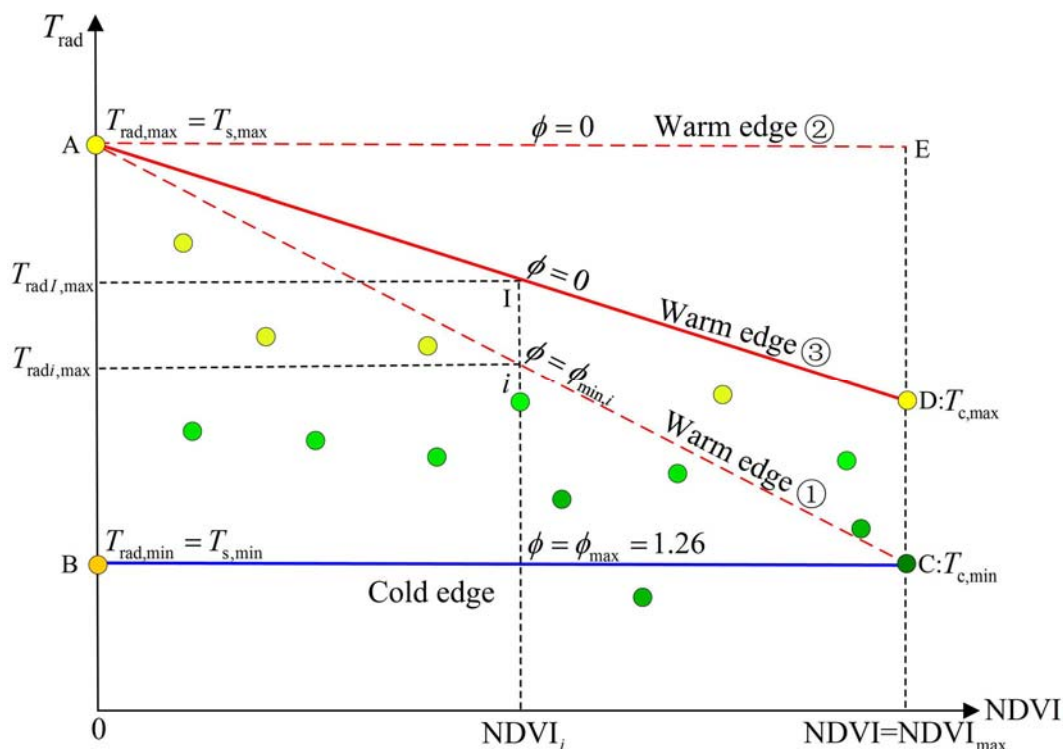


Figure 7.1 A schematic of the scatterplot of remotely sensed NDVI and T_{rad} , colored circles represent pixels with varying NDVI and T_{rad} . Side AC is the warm edge (①) of triangle ABC, whose ϕ values are equal to $\phi_{\text{min},i}$ for each NDVI value or NDVI class i . Side AE is the warm edge (②) of rectangle models (simplified from triangle models) whose ϕ value is equal to zero. Side AD is the warm edge (③) representing surfaces of $EF=0$ for a full range of NDVI in trapezoid model ABCD. Side BC is the horizontal cold edge representing surfaces of $EF=1$ for a full range of NDVI.

The triangle model (triangle ABC in Fig. 7.1) developed by Jiang and Islam (1999, 2001) makes use of parameter ϕ derived from a meaningful contextual space of NDVI and T_{rad} to partition net energy so as to estimate LE based on the Priestley-Taylor equation:

$$LE = \phi \left(\frac{\Delta}{\Delta + \gamma} \right) (R_n - G) \quad (7.1)$$

where parameter ϕ integrates the effects of soil moisture availability, aerodynamic and surface resistances on evaporative fraction, which is expressed as

$$\phi = \frac{T_{\text{radi,max}} - T_{\text{radi}}}{T_{\text{radi,max}} - T_{\text{radi,min}}} (\phi_{\text{max},i} - \phi_{\text{min},i}) + \phi_{\text{min},i} \quad (7.2)$$

where $T_{\text{radi,max}}$ and $T_{\text{radi,min}}$ are the maximum and minimum T_{rad} values for NDVI class i ; and T_{radi} is the T_{rad} value of a pixel in NDVI class i ; $\phi_{\text{max},i}$ is the maximum value of parameter ϕ (=Priestley-Taylor parameter of 1.26), i.e., the parameter ϕ for cold edge BC is equal to 1.26; $\phi_{\text{min},i}$ is the minimum value of parameter ϕ for NDVI class i , which is in fact the parameter ϕ for warm edge AC. Parameter $\phi_{\text{min},i}$ is assumed to be proportional to NDVI/f_c , i.e., $\phi_{\text{min},i} = 1.26 \text{NDVI}_i / \text{NDVI}_{\text{max}}$ where NDVI_{max} is the maximum value of NDVI for a scene. In terms of the assumption, parameter $\phi_{\text{min},i}$ is equal to 0 at $\text{NDVI}=0$ which is assumed to represent the direct bare surface and is equal to 1.26 at $\text{NDVI}=\text{NDVI}_{\text{max}}$, i.e., the point of intersection of AC and BC. Stisen et al. (2008) modified the linear correlation of $\phi_{\text{min},i}$ with NDVI as a power function with an exponent of two within the triangle framework. As such, $\phi_{\text{min},i}$ is nonlinearly correlated with NDVI, which accounts for a more rapid change of $\phi_{\text{min},i}$ for high NDVI values than that for low NDVI values along with the warm edge.

In the computation, $T_{\text{radi,max}}$ and $T_{\text{radi,min}}$ are both obtained from warm and cold edges derived from the $\text{NDVI}-T_{\text{rad}}$ space, respectively, which are a function of NDVI. Therefore, the value of parameter ϕ for a pixel can be uniquely determined by its T_{rad} and

NDVI values based on equation (7.2). Combining Eqs. (7.1) and (7.2), EF for a pixel can therefore be written as

$$EF = \left[\frac{T_{\text{radi,max}} - T_{\text{radi}}}{T_{\text{radi,max}} - T_{\text{radi,min}}} (\phi_{\text{max},i} - \phi_{\text{min},i}) + \phi_{\text{min},i} \right] \cdot \left(\frac{\Delta}{\Delta + \gamma} \right) \quad (7.3)$$

It is indicated in Eq. (3) that the quantity of $\Delta/(\Delta+\gamma)$ varies slightly with T_a ; therefore EF is largely determined by $T_{\text{radi,max}}$ and $T_{\text{radi,min}}$ for a given T_{radi} value in NDVI class i . It is particularly important to note that in reality, the contextual relationship between NDVI and T_{rad} rarely constitutes a triangle, but a trapezoid. To that end, $\phi_{\text{min},i}$ values in Eq. (7.3) for the observed warm edge are simplified as zero, which accounts for the effects of root zone water stress on vegetated surfaces for a full range of NDVI/ f_c (Choi et al., 2009).

7.2.2. Formulation of rectangle model

Jiang and his associates (Batra et al., 2006; Jiang et al., 2009) simplified parameter ϕ in Eq. (7.2) as

$$\phi = \frac{T_{\text{rad,max}} - T_{\text{rad}}}{T_{\text{rad,max}} - T_{\text{rad,min}}} \phi_{\text{max}} \quad (7.4)$$

where $T_{\text{rad,max}}$ and $T_{\text{rad,min}}$ are the global maximum and minimum T_{rad} throughout an entire scene. It is apparent from Eq. (7.4) that parameter ϕ on the warm edge, i.e., $\phi_{\text{min},i}$ in Eq. (7.3), is simplified as zero. The triangle ABC is indeed simplified as a rectangle ABCE in which $T_{\text{rad,max}}$ forms a horizontal warm edge of the rectangle model. Warm edge AE corresponds to the driest surfaces with EF=0 theoretically occurring for a range

of NDVI/f_c .

In the rectangle model, $T_{\text{rad,max}}$ is deduced by extrapolating the derived warm edge to intersect with $\text{NDVI}=0$, which is assumed to be the highest temperature over the bare soil (Batra et al., 2006). In triangle or rectangle models, $T_{\text{rad,min}}$ is determined by T_{rad} of the pixel with the largest NDVI value (Jiang and Islam, 2001), regression analysis as the warm edge (Sandholt et al., 2002; Stisen et al., 2008), or the use of T_a as the cold edge (Jiang and Islam, 2003). Consequently, ϕ values for the remaining pixels amid the limiting edges can be determined only by their T_{rad} values in terms of Eq. (7.4).

It is important to note that limiting edges involved in both the original version of Eq. (2) and the simplified version in Eq. (4) of triangle models are determined by the observed scatterplots of $\text{NDVI}-T_{\text{rad}}$. As such, these approaches are only valid when both minimum and maximum ET can be observed within the boundaries of the study area (Stisen et al., 2008). One important assumption is that the major differences in EF estimates are not introduced by atmospheric conditions and surface characteristics (e.g., u and h_c), but mainly contributed by variation in soil moisture availability. This necessitates a large or heterogeneous study area with a broad range of soil wetness conditions and at the same time relatively uniform atmospheric forcing.

Another assumption involved is that the use of triangle models does not allow the presence of water stressed full cover vegetation, since the triangle models create a singularity at point C (Fig. 7.1). Vegetation with a range of f_c transpires at near potential rates regardless of the surface soil water content; the triangle models do not account for water stress on vegetation (Carlson, 2007).

7.2.3. Formulation of trapezoid model

We argue that first, the real physical limits of the contextual space of NDVI- T_{rad} form neither a triangle nor a simplified rectangle in Batra et al. (2006) and Jiang et al. (2009), but in fact a trapezoid, i.e., ABCD in Fig. 7.1. This has been justified by Gillies et al. (1997), Moran et al. (1994), Tang et al. (2010), and Sandholt et al. (2002). In other words, the theoretical warm edge, on which parameter ϕ and EF are equal to zero, is above the hypotenuse of the triangle ABC but is in no way a horizontal edge in the simplified rectangle ABCE. This is because partially vegetated surfaces with the largest water stress would show lower temperatures than the driest bare surface (point A) as the sunlit vegetation is generally cooler than sunlit bare soil (Carlson, 2007). In this case, complete stomatal closure will theoretically occur for the vegetated part due to the largest water stress (Moran et al., 1994). Even though this is rarely observed for dense vegetation covers, the theoretical warm edge does provide a determinate limit for deducing EF across the NDVI and T_{rad} space, which obviates large uncertainties in the use of observed warm edges from satellite imageries and the determination of ϕ_{min} . In fact, the use of the horizontal warm edge in the rectangle model could result in an overestimation of EF/LE due to an overestimation of $T_{\text{radi,max}}$. This is virtually shown in the results of these studies (Batra et al., 2006; Jiang et al., 2009).

Second, $\phi_{\text{min},i}$ in triangle models is assumed to be correlated only with NDVI (Jiang and Islam, 2001; Stisen et al., 2008), with the largest value ($=1.26$) taking place on the fully vegetated surface without water stress and the smallest value ($=0$) on the driest bare surface. The assumed linear/nonlinear correlation between $\phi_{\text{min},i}$ and NDVI may be true

for the two extremes; however it might not be the case for the whole range of NDVI/f_c due to a more complex unknown relationship between $\phi_{\min,i}$ and other factors. More importantly, with varying observed warm edges due to the use of different sizes and resolutions of images, $\phi_{\min,i}$ for the warm edge cannot be uniquely determined.

We suggest that the derivation of the real physical limits (i.e., trapezoid ABCD) of the NDVI and T_{rad} space would be greatly useful in reducing uncertainty associated with the determination of ϕ_{\min} values for a full range of NDVI/f_c and the observed warm edge due to the use of different sizes and resolutions of images. Procedures for derivation of theoretical boundaries of the trapezoid framework are presented in Section 4.2.3.

After the theoretical boundaries are determined, EF from the proposed trapezoid model can be derived with the following equation

$$\text{EF} = \phi_{\max} \frac{T_{\text{rad},\max} - T_{\text{radi}}}{T_{\text{rad},\max} - T_{\text{rad},\min}} \cdot \frac{\Delta}{\Delta + \gamma} \quad (7.5)$$

where $T_{\text{rad},\max}$ and $T_{\text{rad},\min}$ are the temperatures of the physical limits (see Fig. 7.1) of the trapezoid model.

As demonstrated above, the rectangle framework of the NDVI- T_{rad} space seems to be inadequate to reflect the theoretical warm limit of EF and therefore estimate EF. To that end, the subsequent discussion on scale effects of broadly defined triangle models is based on the triangle model proposed by Jiang and Islam (2001). The performance of the proposed trapezoid model and the triangle model will be compared and contrasted in order to illustrate the capacity of the trapezoid model to address possible scale dependencies of the triangle model.

7.3. Domain scale effects

7.3.1. Four domains and three scenarios of limiting edges

The domain scale effects of triangle models were systematically examined by applying them to variable domains covering the SMACEX site within the coverage of Landsat TM/ETM⁺ imagery (a swath of 185 km) for DOY 174 and 182, respectively. It is mentioned that our original interesting area of LE distribution was focused on the SMACEX site, i.e., rectangle 1 with an aspect ratio of 2:1 shown in Fig. 7.2 (domain 1). It is postulated that warm and cold edges of the NDVI- T_{rad} space involved in the triangle models would vary with the domain being considered, even though these areas are relatively homogenous agricultural fields with low relief. To that end, we partitioned three other domains covering domain 1 and derived respective limiting edges and then EF with Eq. (7.3). Domains 2 and 3 are rectangles with the length and width being extended two times and four times relative to domain 1, respectively. Domain 4 is the entire coverage of the Landsat TM/ETM⁺ imageries acquired.

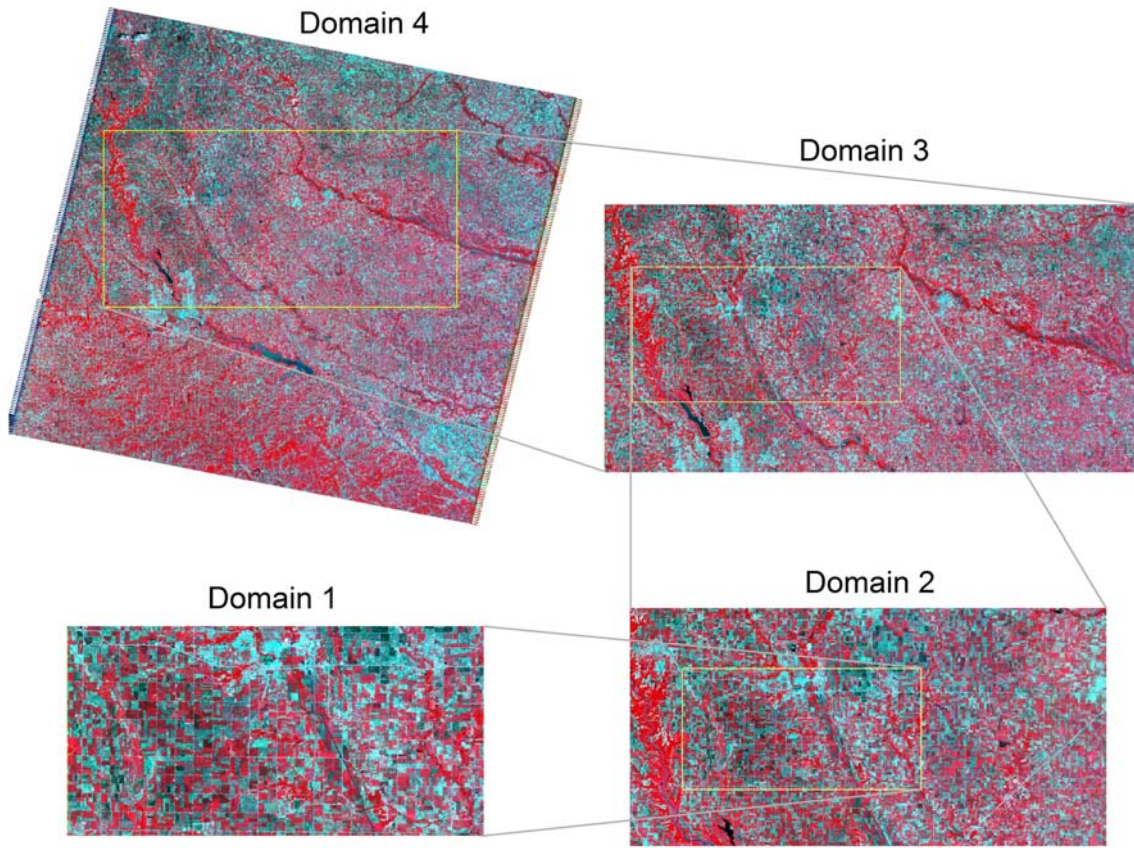


Figure 7.2 False color composite of Landsat TM imagery acquired on June 23, 2002, covering the SAMCEX site (domain 1), progressively enlarged domains 2 and 3, and the entire scene of the Landsat TM imagery (domain 4).

Three scenarios of the combinations of limiting edges for each domain were formulated. Scenario 1 makes use of extreme T_{rad} values (maximum and minimum) for each NDVI interval derived from each domain (outliers of the extremes are removed prior to subsequent processing) to perform regression analysis. The resulting limiting edges are also referred to as observed warm and cold edges of the f_c - T_{rad} space. This is a traditional way to determine limiting edges in triangle models (Jiang and Islam, 2001; Sandholt et al., 2002; Tang et al., 2010). Scenario 2 is a combination of the observed warm edge from scenario 1 and the cold edge formed by the average T_a (T_m) of domain 1.

Taking T_m as the cold edge is primarily motivated by obviating the difficulty of demarcating cold edges from the scatterplots of NDVI and T_{rad} due to relatively scattered points over low T_{rad} areas. Scenario 3 consists of the theoretical warm edge for domain 1 and the cold edge of T_m for domain 1. It is indicated that scenario 1 would result in varying warm and cold edges for different domains being considered. The cold edge in scenario 2 remains invariant due to the use of a constant T_m for domain 1, but the warm edge may be varying with the domain. Scenario 3 comprises the theoretical limiting edges specific for domain 1, which do not vary with the domain.

7.3.2. Variation in limiting edges and EF with domain

Appropriately deriving limiting edges is a prerequisite for using triangle models and examining their domain scale effects. Figs. 7.3 and 7.4 illustrate scatterplots of NDVI and T_{rad} derived from four domains with relevant limiting edges under three scenarios for DOY 174 and 182, respectively. Table 7.1 provides regression coefficients of the observed limiting edges for both days. It is apparent that the observed warm edges at different domain scales are relatively sharp; however, the observed cold edges are poorly demarcated, exhibiting many scattered points over areas with low NDVI and T_{rad} values, and the warm edges are better defined than the cold edges. The poor demarcation of cold edges is particularly exacerbated for domain 4 for both days. It could be concluded that with an enlarging domain where a triangle model is applied, the likelihood of effectively or automatically delineating the cold edge decreases, in particular from the scatterplots of f_c and T_{rad} of high spatial resolution imagery or imagery with large coverage. In fact,

many applications pertaining to triangle models make use of moderate or low spatial resolution data, e.g., MODIS, NOAA-AVHRR, or MSG-SEVIRI imageries for a given study site, e.g., (Batra et al., 2006; Stisen et al., 2008; Tang et al., 2010; Venturini et al., 2004; Wang et al., 2006), which may have circumvented the complexity arising from the use of high spatial resolution imageries, e.g., Landsat TM/ETM⁺. The difficulties of demarcating cold edges directly from the NDVI- T_{rad} space are primarily contributed by extraneous effects of T_{rad} retrievals for sloping terrain, shading, standing water, and clouds (Carlson, 2007; Gillies et al., 1997). This is also the reason why T_{m} was taken as the cold edge in Scenarios 2 and 3 to circumvent uncertainty in the derivation of cold edges. In general, the algorithms of deriving observed limiting edges involved in scenarios 1 and 2 seem to be effective for each domain except for the scatterplot of $f_{\text{c}}-T_{\text{rad}}$ for domain 4 on DOY 174. In this case, we substituted the observed cold edge derived from domain 3 for the erroneous observed cold edge derived from domain 4 for further calculation and discussion.

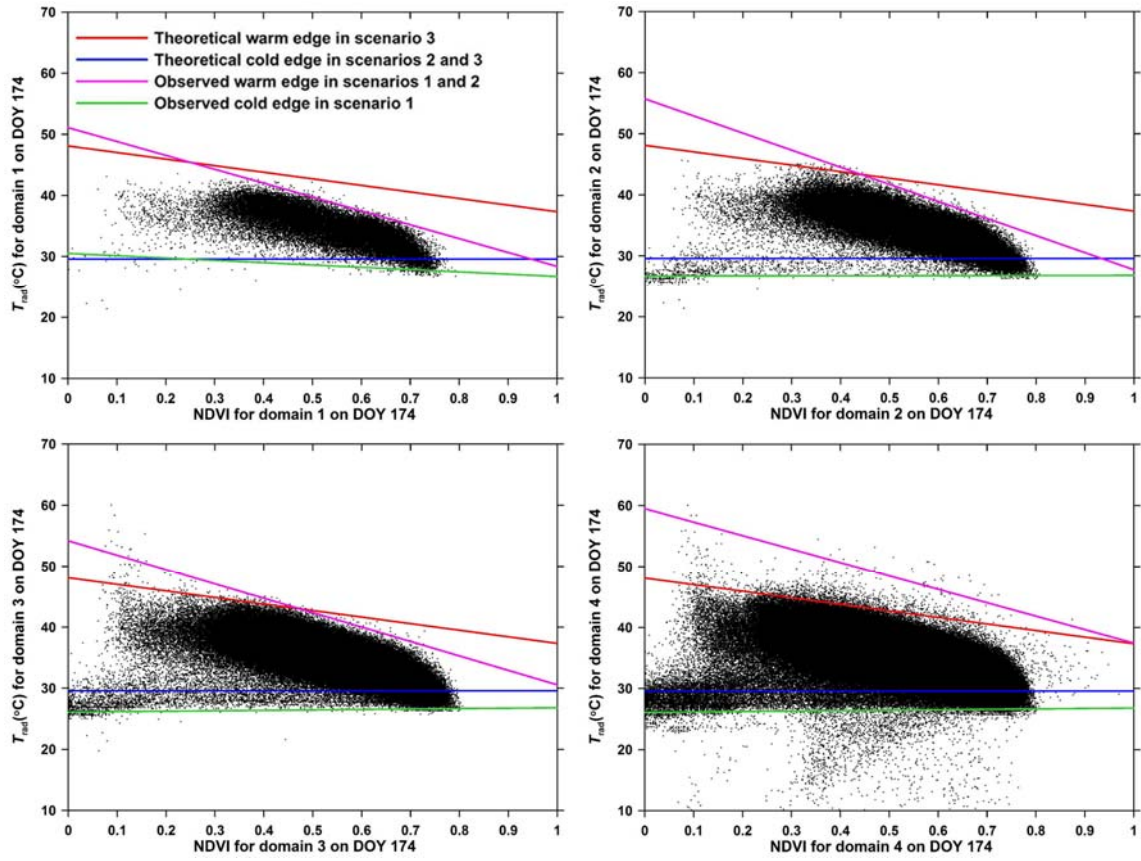


Figure 7.3 Scatterplots of NDVI and T_{rad} derived from Landsat TM imagery for four domains with relevant observed and theoretically derived limiting edges on DOY 174.

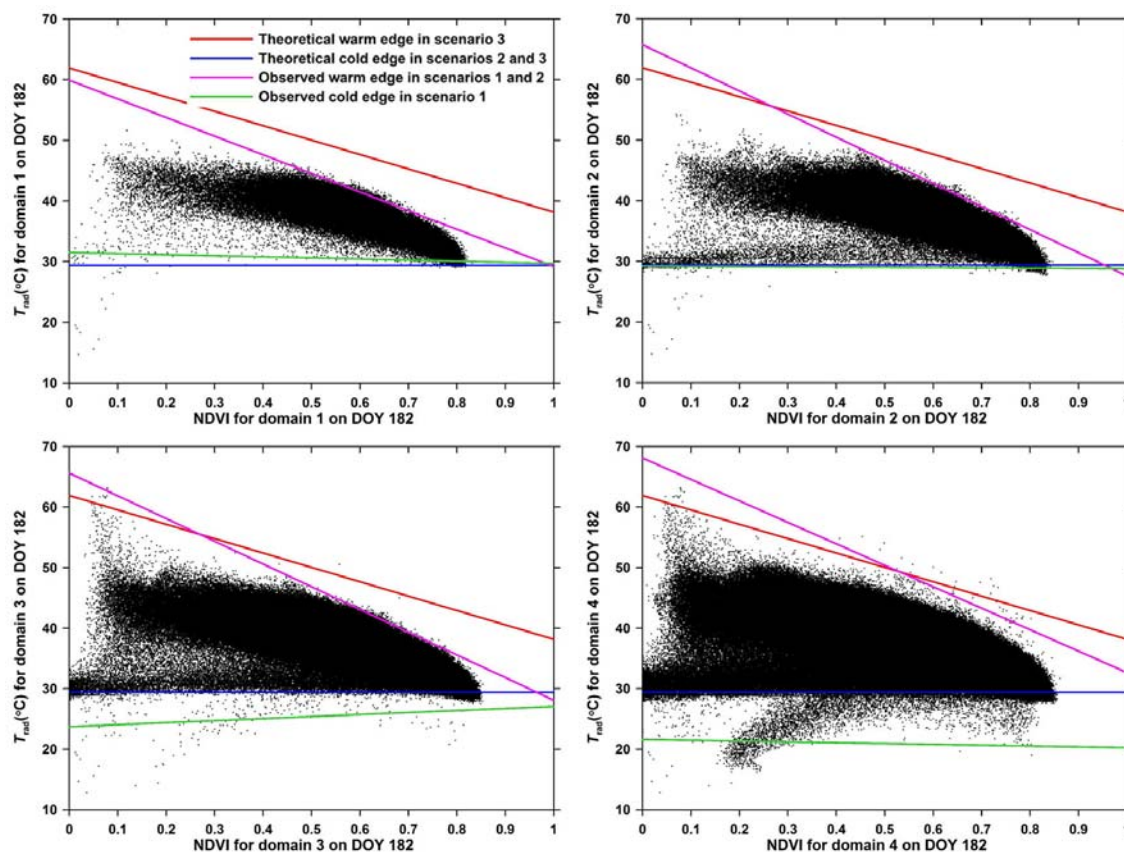


Figure 7.4 Scatterplots of NDVI and T_{rad} derived from Landsat ETM⁺ imagery for four domains with relevant observed and theoretically derived limiting edges on DOY 182.

Table 7.1 Regression coefficients of observed limiting edges derived from Landsat TM/ETM⁺ imagery for four domains around the SMACEX site on two study days in 2002

Domain	Warm edge				Cold edge			
	slope		intercept		slope		intercept	
	174	182	174	182	174	182	174	182
1	-22.71	-30.71	51.1	59.9	-3.77	-1.80	30.5	31.5
2	-27.97	-38.09	55.7	65.7	0.12	-0.42	26.7	29.2
3	-23.64	-37.53	54.2	65.6	0.70	3.35	26.1	23.7
4	-22.06	-35.45	59.5	68.1	0.70	1.35	26.1	21.6

We estimated EF with Eq. (7.3) and respective limiting edges for the four domains on DOY 174 and 182, respectively. The EF estimates were averaged over the estimated upwind source-area/footprint for each flux tower using the approach proposed by Li et al. (2008a), and then compared with measurements at each flux tower for both days. Figs. 7.5 and 7.6 give the EF estimates and the corresponding measurements for four domains under three scenarios on DOY 174 and 182, respectively. Fig. 7.7 and Table 7.2 illustrate variations in the difference between the estimates and the measurements (MAPD and RMSD) with domain. Results indicate that on DOY 174, the triangle model under scenarios 1 and 2 significantly underestimates EF within domains 1-3, suggesting an MAPD on the order of 30~40% and 20~30% for scenarios 1 and 2, respectively. However, emplacement of the triangle model with the observed limiting edges (i.e., scenarios 1 and 2) within domain 4 can reproduce EF with acceptable accuracy, showing an MAPD of 15.5% and 3.04% for scenarios 1 and 2, respectively.

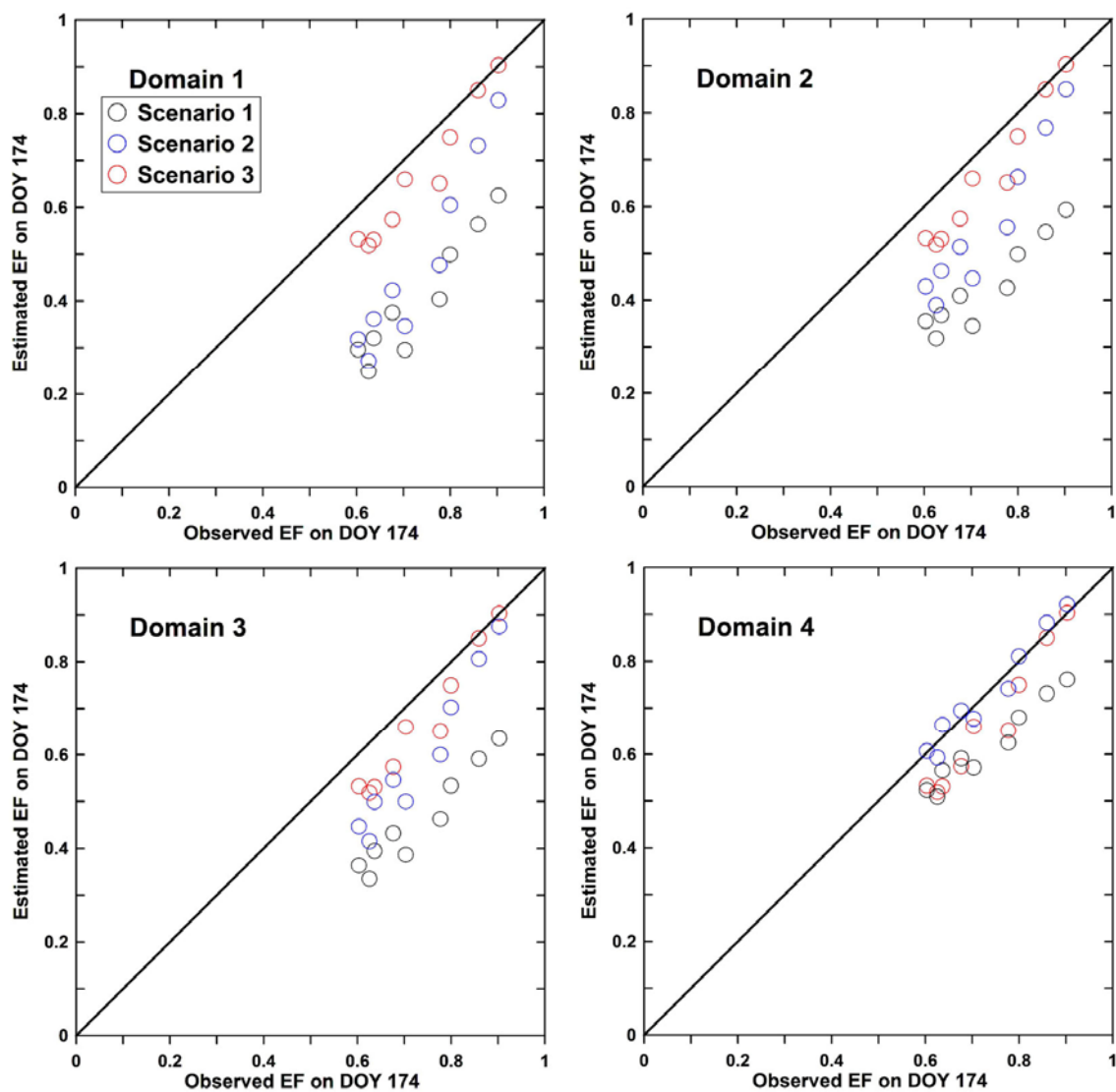


Figure 7.5 Comparison of EF estimates from triangle models and corresponding flux tower-based measurements for four domains on DOY 174 under three scenarios.

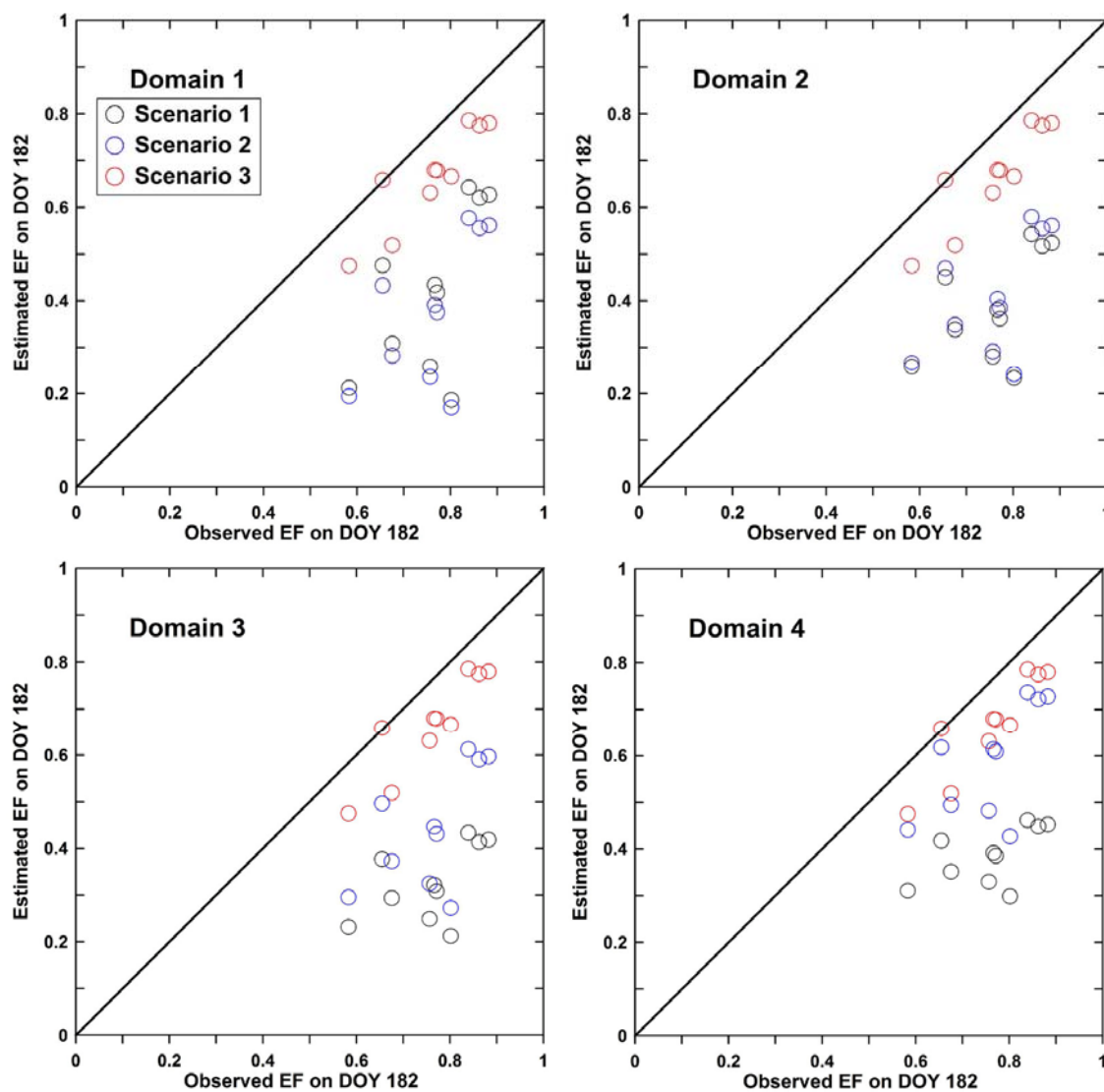


Figure 7.6 Comparison of EF estimates from triangle models and corresponding flux tower-based measurements for four domains on DOY 182 under three scenarios.

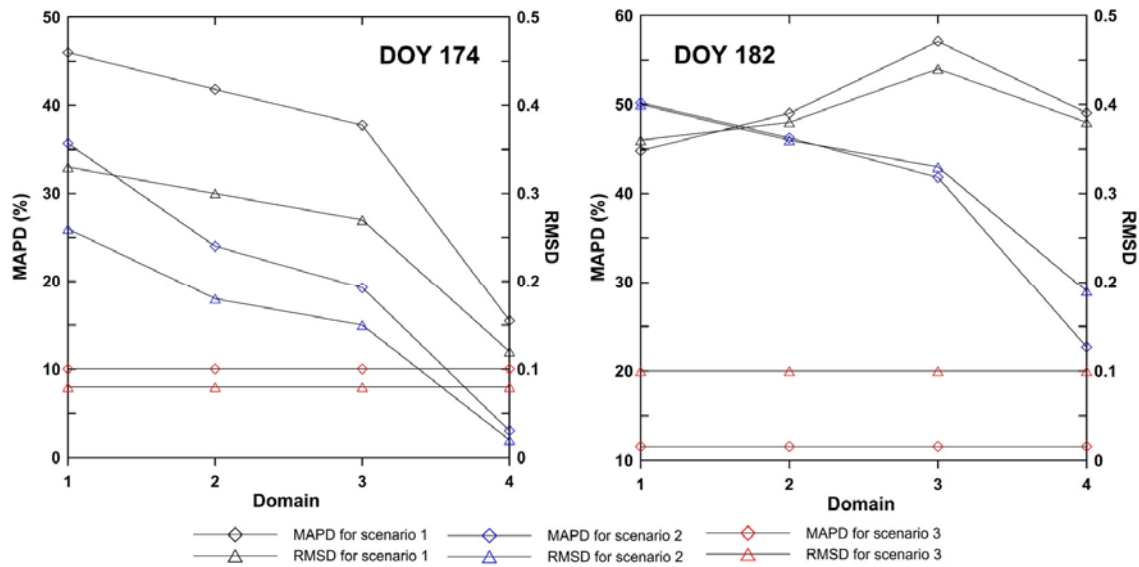


Figure 7.7 Variations in the mean absolute percentage difference (MAPD) and the root mean square deviation (RMSD) between the EF estimates from triangle models under three scenarios and the measurements with domain for DOY 174 and 182, respectively.

Table 7.2 Differences between the Landsat TM/ETM⁺-based EF estimates and the measurements, e.g., Root Mean Square Difference (RMSD), Mean Absolute Percentage Difference (MAPD), and Bias within four study domains at the SMACEX site on DOY 174 and 182 under three scenarios of limiting edges

Domain	Difference	DOY 174			DOY 182		
		Scenario 1	Scenario 2	Scenario 3	Scenario 1	Scenario 2	Scenario 3
1	RMSD	0.33	0.26	0.08	0.36	0.40	0.10
	MAPD	45.98	35.69	10.03	44.81	50.19	11.55
	Bias	-0.33	-0.25	-0.07	-0.34	-0.38	-0.09
2	RMSD	0.30	0.18		0.38	0.36	
	MAPD	41.81	24.02	—	49.02	46.26	—
	Bias	-0.30	-0.17		-0.37	-0.35	
3	RMSD	0.27	0.15		0.44	0.33	
	MAPD	37.76	19.26	—	57.08	41.83	—
	Bias	-0.27	-0.13		-0.43	-0.32	
4	RMSD	0.12	0.02		0.38	0.19	
	MAPD	15.50	3.04	—	49.07	22.68	—
	Bias	-0.11	0.00		-0.37	-0.17	

It is important to note that in general scenario 2 results in relatively higher accuracy than does scenario 1. In addition, with enlarging domains from 1-4, the discrepancies between the EF estimates and the measurements decrease consistently (see DOY 174 in Fig. 7). The shift of limiting edges with differing domains can explain these trends. First, for domain 1, EF was significantly underestimated with the triangle model and the observed limiting edges, which could be ascribed to a significant downward shift of the observed warm edge compared with the real physical limit, therefore resulting in the underestimated EF in terms of the monotonicity of Eq. (7.3). As the domain is enlarged, the observed warm edge tends to move upward (EF tends to increase) and the observed cold edge tends to move downward (EF tends to decrease) due to a broader range of surface wetness conditions, with the magnitude of variation in the warm edge being larger than that of the cold edge. Therefore, the underestimation of EF from the observed limiting edges within domain 1 is mitigated to varying degrees as the domain is enlarged under both scenarios 1 and 2. In particular, scenario 2 leads to a more efficient improvement in these discrepancies due to the use of a fixed cold edge for domain 1.

For scenario 3, the theoretically determined limiting edges within domain 1 result in an MAPD of 10.03% and 11.5% and an RMSD of 0.08 and 0.10 on DOY 174 and 182, respectively. This demonstrates that the proposed method of deriving theoretical limits for domain 1 can essentially represent the real physical limits for domain 1, greatly improving the accuracy of EF estimates from the triangle model in combination with the observed limiting edges in terms of MAPD on the order of 30%~50% and RMSD on the order of 0.2~0.4. In particular, on DOY 182, the theoretical limiting edges resulted in the

highest accuracy in the four comparative domains than did the observed limiting edges. The retrieval accuracy of EF on DOY 182 under scenarios 1 and 2 did not result in a marked improvement as the domain was enlarged, suggesting an MAPD on the order of 40~60% and 20~50% for the two scenarios, respectively. This might be introduced by a significantly higher real warm edge compared with the observed ones. Even domain 4, which is most likely to generate the highest observed warm edge, does not produce a reasonable warm edge and then EF estimates.

It is particularly important to note that even though emplacement of the triangle model within domain 4 on DOY 174 under scenario 2 showed greater accuracy than scenario 3, it is not the general case in practical applications since absolutely clear satellite imageries are not often available. More importantly, the user cannot precisely determine on which domain scale the real physical limits exist and can be approximated by the observed limits. This corresponds to the case of DOY 182 that even though the entire imagery were used to deduce the real limiting edges, the EF estimates were still unacceptable.

7.3.3. Summary of domain scale effects of triangle models

It is concluded that triangle models would fail to generate EF with reasonable accuracy due to the absence of a broad range of soil wetness conditions. This situation would be exacerbated if the real limiting edges are beyond the range of soil wetness reflected by a scene of satellite imagery or a portion of imagery useable. Emplacement of triangle models within varying domains could result in varying observed limiting

edges and consequently EF estimates. In general, the observed warm edge tends to move upward as the domain is enlarged, and the cold edge tends to move in the opposite direction. The movement in the observed limiting edges can be ascribed to a broader range of soil wetness conditions as the domain is enlarged. To that end, deviations of the EF estimates at the smallest domain scale could be exacerbated or alleviated with an enlarged domain, depending on the magnitude of displacement of the observed edges relative to the real physical limits. The use of the triangle models raises a significant scale question associated with the domain of a study site being considered or the size of imagery being used. The use of theoretical boundary conditions of the f_c - T_{rad} space at a given study site with generally uniform meteorological fields can be a promising way to address the domain dependence intrinsic in triangle models.

7.4. Resolution scale effects

The performance of triangle models is largely dependent on their limiting edges of the NDVI- T_{rad} space. The limiting edges are traditionally determined by the observed envelopes derived from the NDVI- T_{rad} space or by the newly proposed method of deducing theoretical limits for a given study site. In addition to the domain where the triangle models are applied, varying spatial resolutions of satellite imagery would also result in differing T_{rad} retrievals, observed limiting edges, and then EF/LE estimates. Here, DOY 182 permitted acquisition of one scene of clear Landsat ETM⁺ imagery and one scene of clear Terra-MODIS T_{rad} covering the entire scene of the Landsat ETM⁺ imagery for almost the same overpass (Landsat ETM⁺: 10:42 a.m.; MODIS 11:00 a.m.).

This provides a unique opportunity to synthetically investigate differences in the observed limiting edges and the EF estimates due to differing spatial resolutions of satellite imagery.

7.4.1. MODIS-based contextual relationship

We derived limiting edges for domains 1-4 from the scatterplots of NDVI- T_{rad} from MODIS imagery. The MODIS-based scatterplots (Fig. 7.8) were formed by MOD11_L2 1 km-resolution LST products (including both LST and quality control images) and MOD13A2 1 km-resolution NDVI products (including both NDVI and quality control images). It is apparent that the MODIS-based scatterplots and their warm edges differ significantly from that from the Landsat ETM⁺ imagery for any of the study domains (with reference to Fig. 7.4). In general, the MODIS-based warm edges show gentler slopes and smaller intercepts than those derived from the Landsat ETM⁺ imagery and the theoretical warm edge (see Fig. 7.8 and Table 7.3). This is likely due to the disparate capacity of the two sensors in discriminating variations in T_{rad} and soil wetness conditions. The 1-km resolution of thermal infrared bands of the MODIS sensor is not able to discriminate variations in T_{rad} and soil moisture conditions at field scales (e.g., <500 m), resulting in reductions in the range of T_{rad} and the generally downward displacement of the observed warm limits compared with that derived from the Landsat ETM⁺ imagery for each domain. As such, moderate or low spatial resolution sensors would not be able to capture the complete picture of the contextual relationship between NDVI and T_{rad} , and the corresponding EF for a given study site. On the other hand, as

the domain is enlarged, the warm edges tend to move upward due to the inclusion of a broader range of soil wetness. Therefore, the deviation of observed warm edges from the real physical one is mitigated to a certain degree.

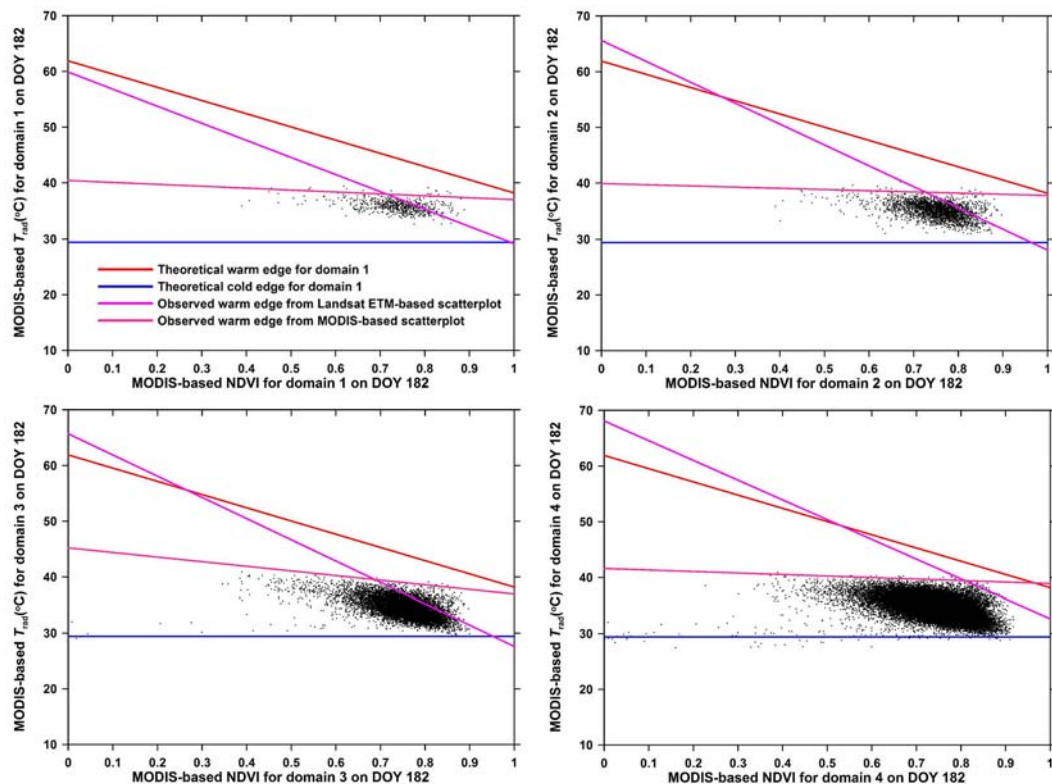


Figure 7.8 Scatterplots of 16-day composite NDVI (MOD13A2 on DOY 177) and T_{rad} (MOD11_L2 on DOY 182) for four domains with relevant observed and theoretically derived limiting edges.

Table 7.3 Regression coefficients of observed limiting edges derived from Landsat ETM⁺ imagery and MODIS-based T_{rad} and NDVI products for four domains around the SMACEX site on two study days in 2002

Domain	Warm edge				Cold edge			
	slope		intercept		slope		intercept	
	Landsat ETM	MODIS	Landsat ETM	MODIS	Landsat ETM	MODIS	Landsat ETM	MODIS
1	-30.71	-3.44	59.9	40.4	-1.80	-6.68	31.5	39.7
2	-38.09	-2.15	65.7	39.9	-0.42	-6.76	29.2	37.5
3	-37.53	-8.27	65.6	45.2	3.35	-1.79	23.7	32.6
4	-35.45	-2.71	68.1	41.6	1.35	-0.41	21.6	29.4

7.4.2. MODIS-based EF estimates

Estimated EF from the triangle model in conjunction with the MODIS-based warm edge for each domain and the cold edge of T_m was compared with the corresponding flux tower measurements. It is noted that towers 151, 152, and 162 are located within the same pixel of the MODIS-based EF estimate. In this case, the EF estimate was compared with the averaged EF measurements within the pixel. There is, however, a scale issue of site representativeness to sensor pixel scale involved in this kind of comparison (McCabe and Wood, 2006). The source areas/footprint of flux towers are generally smaller than the pixel resolution of the MODIS-based EF estimates. This would introduce uncertainties in comparison and validation. Evaluation of the MODIS-based EF estimates still remains a big challenge in the operational ET estimation community. Given these limitations, the validation performed here would not be perfect. However, it

might also provide valuable information about error propagation and the performance of the triangle model.

Results (Fig. 7.9) indicate that the MODIS-based EF estimates from the triangle model in combination with the observed warm edges are degraded compared with that from the Landsat ETM⁺ imagery, showing a bias on the order of -0.4~-0.5, an MAPD on the order of 50~70%, and an RMSD on the order of 0.4~0.5 for the four domains. The EF was significantly underestimated. These differences are substantially larger than that from the Landsat ETM⁺ data. Nonetheless, the triangle model with the theoretical warm edge results in an MAPD of 25.53% and an RMSD of 0.22, which are the smallest in the results from all observed warm edges within the four domains. This demonstrates that the use of the theoretical limiting edges would provide an opportunity to constrain in part errors arising from the deviation of the observed limiting edges from the realistic ones due to the use of moderate and low spatial resolution satellite sensors.

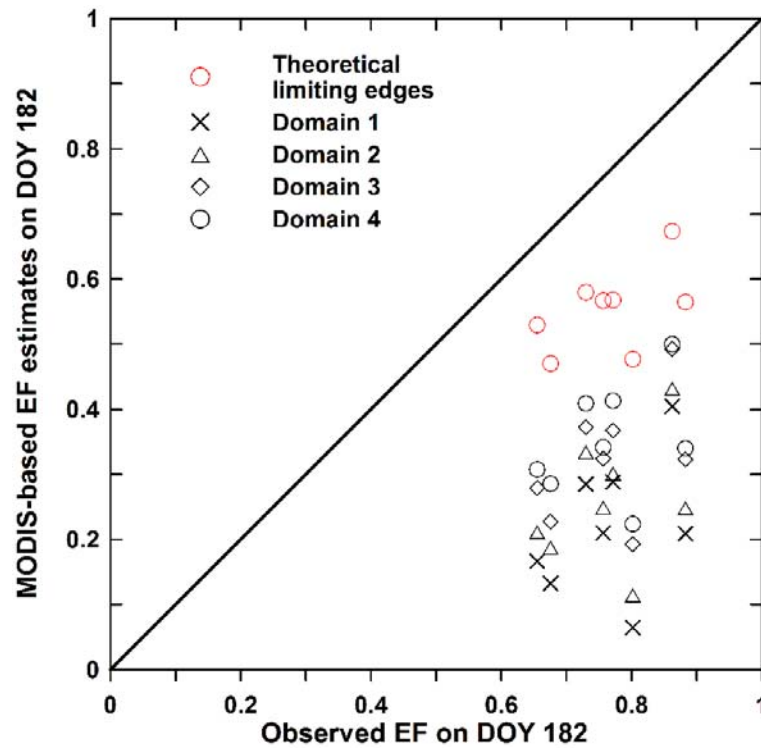


Figure 7.9 MODIS-based EF estimates and corresponding EF measurements for four domains on DOY 182, red circles represent EF estimates from the theoretical warm edge and the cold edge of average air temperature of domain 1 (T_m), and black symbols represent EF estimates from the observed warm edge and the cold edge formed by T_m .

Fig. 7.10 and Table 7.4 show variations in MAPD and RMSD between the MODIS-based EF estimates and the corresponding measurements with domain. Results suggest that as the domain is enlarged, MAPD and RMSD consistently decrease. However, these differences are still considerably larger than those of the Landsat ETM⁺-based estimates for each domain. The mitigation of deviation with enlarging domains is a result of a rising warm edge of the MODIS-based NDVI- T_{rad} space as shown in Fig. 7.8. On the other hand, even though applying the triangle model to a relatively large domain seems to result in ameliorated outputs observed at a handful of flux towers, the intrinsic assumption of similar radiation energy for the same NDVI/ f_c

class in the triangle models would not be satisfied. This would result in distorted EF and LE distributions across the entire scene.

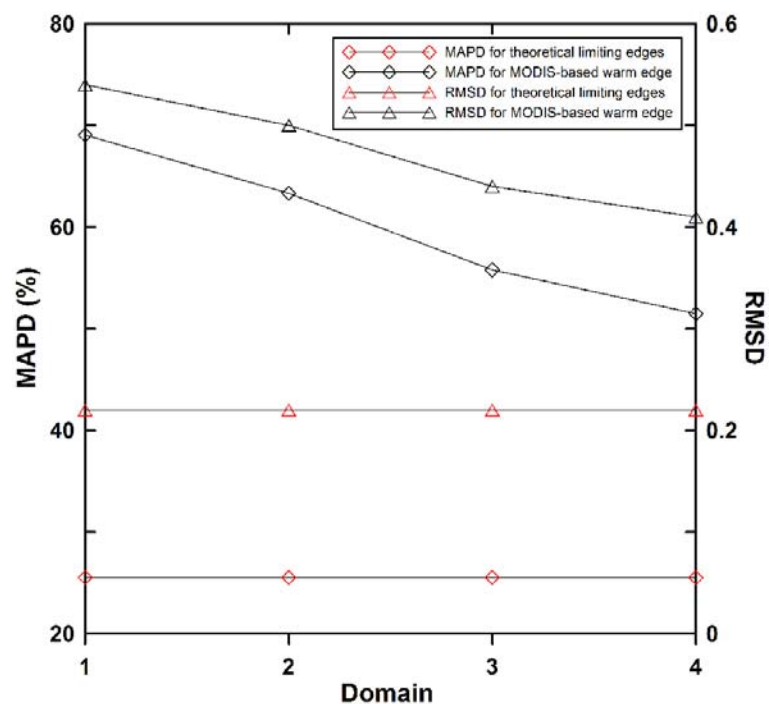


Figure 7.10 Variations in MAPD and RMSD between the MODIS-based EF estimates and the corresponding measurements with domain on DOY 182.

Table 7.4 Differences between the MODIS-based EF estimates and the measurements, e.g., RMSD, MAPD, and bias within four study domains at the SMACEX site on 182 under three scenarios of limiting edges

Domain	Difference	DOY 182		
		Scenario 1	Scenario 2	Scenario 3
1	RMSD	0.28	0.54	0.22
	MAPD	29.78	69.06	25.53
	Bias	-0.12	-0.53	-0.20
2	RMSD	0.36	0.50	—
	MAPD	43.20	63.32	
	Bias	-0.33	-0.48	
3	RMSD	0.36	0.44	—
	MAPD	45.00	55.8	
	Bias	-0.35	-0.43	
4	RMSD	0.42	0.41	—
	MAPD	52.70	51.48	
	Bias	-0.40	-0.40	

7.4.3. Coincident good EF estimates from triangle models

As illustrated in Sections 7.3, 7.4.1, and 7.4.2, triangle models suffer significantly from domain scale effects and resolution scale effects due to the dependence of their limiting edges on the domain being considered or the resolution of imagery being used. However, published studies associated with triangle models seem to report promising EF/LE results at a handful tower sites. We suggest that there is a possibility that can result in coincident good EF estimates from the triangle models. Fig. 7.11 shows the MODIS-based scatterplot of NDVI- T_{rad} for domain 1 with the observed warm and cold edges. We simulated EF with the triangle model in combination with both observed limiting edges. Estimated EF from this model set up resulted in an MAPD of 27.49% and an RMSD of 0.22, which appears to be better than the results from the use of the theoretical cold edge for domain 1 (T_m) and the observed warm edge (MAPD of 69.06% and RMSD of 0.54). This is primarily because even though the observed warm edge is

significantly underestimated, the observed cold edge is significantly overestimated compared with the theoretical cold edge. The underestimation of EF due to the downward shift of the warm edge and the overestimation of EF due to the upward shift of the cold edge seem to offset each other, thereby resulting in seemingly promising results at a handful of flux towers in some cases.

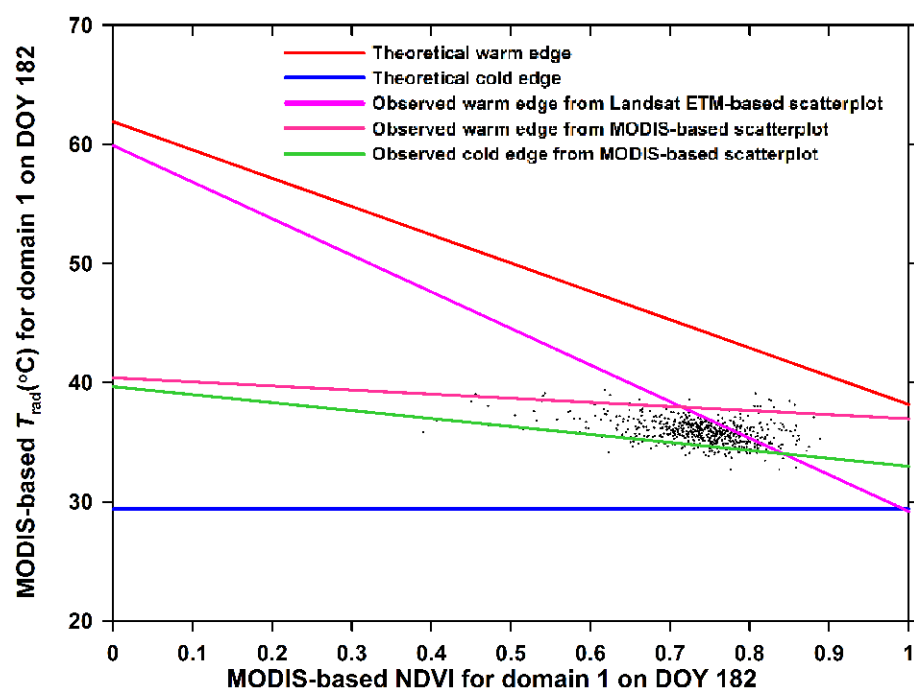


Figure 7.11 MODIS-based scatterplot of NDVI- T_{rad} for domain 1 with observed and theoretically derived limiting edges on DOY 182.

It is particularly important to note that the promising results at a handful of flux towers do not necessarily mean generally reasonable EF/LE retrievals throughout a scene. In extreme cases, pixels on the observed warm and cold edges are mistakenly

taken as hydrologic limits (i.e., for the warm edge with the largest water stress and for the cold edge $EF=1$); and EF for pixels in the vicinity of the two pseudo observed limiting edges are overestimated (near cold edge) or underestimated (near the warm edge). Only pixels located around the middle portion of the T_{rad} distribution would show reasonable results as that from the theoretical limiting edges.

If flux towers are not representatively distributed over a study site (e.g., across a range of soil wetness and in particular including extreme T_{rad} surfaces) or primarily concentrate on the middle portion of the T_{rad} distribution, i.e., the moderate soil moisture conditions, the resulting EF estimates would also be able to show reasonable accuracy. Fig. 7.12 gives the MODIS-based T_{rad} distribution for domain 1 and remotely sensed T_{rad} values at flux towers, showing that these T_{rad} values are essentially concentrated on the middle portion of the T_{rad} distribution. This means that EF estimated from the observed limiting edges at these flux towers was probably coincidentally reasonable.

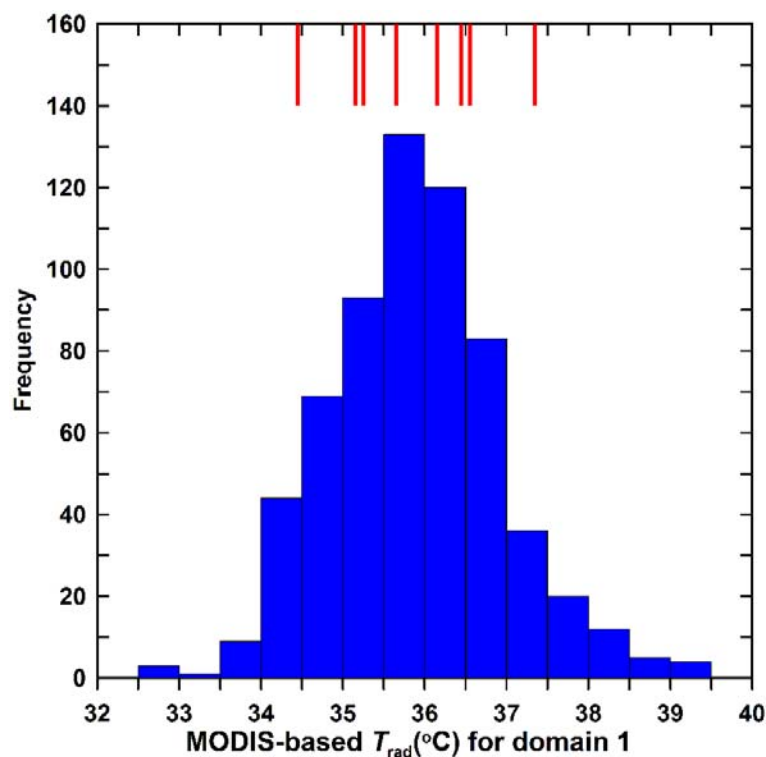


Figure 7.12 MODIS-based T_{rad} distribution (blue bars with a bin size of 0.5 °C) for domain 1 and remotely sensed T_{rad} values at flux towers (red bars) on DOY 182.

This is the reason why validation against a number of flux towers representatively distributed over a range of land covers and soil moisture conditions plays a critical role in the evaluation of remote sensing-based ET modeling results and further applications. However, validation of remote sensing-based EF and ET estimates over large heterogeneous areas still remains a big challenge for the operational ET estimation community due to expensive instruments and other factors. Our simulations and analyses have unraveled one possibility of the coincidentally promising results produced at a handful of flux towers in the use of the triangle models. This further underscores the relevance of validation of remote sensing-based ET.

7.4.4. Summary of resolution scale effects

Different sensors onboard a variety of satellite platforms bear varying capacity to discriminate the land surface, therefore resulting in different spatial resolutions of imageries, in particular for the thermal infrared bands. For a given study site, the use of imageries of different spatial resolutions can result in largely different scatterplots of $\text{NDVI}-T_{\text{rad}}$ and consequently different observed limiting edges. This would probably result in different magnitudes and distributions of EF and ET estimates. In general, the use of moderate or low spatial resolution satellite sensors would lose more information on variations in T_{rad} and in particular hydrologic extremes compared with the high resolution imagery. To that end, the triangle models suffer somewhat from the resolution scale effects. The use of theoretical boundaries of the trapezoid framework could alleviate the resolution scale effects to a certain degree. On the other hand, coincident good results from triangle models in combination with both observed warm and cold edges would take place for pixels with moderate T_{rad} values across the entire scene, where flux towers are located.

7.5. Conclusions

Amongst a series of satellite-based ET models, the triangle models are unique in interpreting the contextual relationship between NDVI/f_c and T_{rad} to deduce EF and LE/ET. However, published studies often show consistent underestimation or overestimation of EF/ET from the triangle models. In addition, the triangle models are rarely combined with high spatial resolution imageries (e.g., Landsat TM/ETM⁺) to

estimate EF/ET. Furthermore, for some algorithms, their outputs and performance can be dependent on the domain of a study site being considered and the resolution of satellite imagery being used.

Motivated by interpreting the consistent underestimation or overestimation of EF/ET by triangle models from a standpoint of model physics and scale effects and testing out the utility of triangle models in combination with high spatial resolution imageries, we performed a comprehensive analysis of the domain and resolution dependencies of triangle models by applying them to areas with progressively growing domains and to Landsat ETM⁺ and MODIS imageries, respectively, at the SMACEX site in central Iowa, U.S., in 2002. In addition, the trapezoid framework developed in Chapter IV was used to restrain the domain and resolution dependencies of the triangle models. The major findings are as follows:

(1) With growing domains, the observed warm edge tends to move upward (extreme high T_{rad} values increase) and the observed cold edge tends to move downward (extreme low T_{rad} values decrease). The triangle models can be domain-dependent.

(2) Discrepancies in EF estimates from triangle models for a given study site can be alleviated by selecting a larger domain, showing a broader range of soil wetness conditions. This effect is more prominent under the condition of taking average air temperature for the study site as the cold edge of the NDVI- T_{rad} space. The discrepancies between the EF estimates from triangle models and the corresponding measurements for a small domain can be alleviated to a certain degree as the domain is enlarged.

(3) The use of moderate or low spatial resolution satellite imageries could fail to

discriminate extreme soil wetness conditions and consequently to detect EF for a given study site. The triangle models can be resolution-dependent. The use of high spatial resolution sensors may alleviate the resolution scale effect to a certain degree.

(4) The realistic boundaries of the NDVI- T_{rad} space constitute neither a triangle, nor a rectangle, but a trapezoid. Given a study site with a relatively small domain, the triangle models can still be applicable by incorporating realistic physical limits.

(5) The derived physical limits can restrain the domain and resolution dependencies of triangle models to a certain degree, making the triangle models applicable to small areas.

(6) The use of observed warm and cold edges may coincidentally result in good EF estimates for pixels with moderate T_{rad} values across the scene due to an underestimation of the warm edge, tending to underestimate EF, and an overestimation of the cold edge, tending to overestimate EF. The two effects offset each other. Distorted EF estimates may occur over areas close to the observed edges.

CHAPTER VIII

CONCLUSIONS, LIMITATIONS AND RECOMMENDATIONS FOR FUTURE RESEARCH

8.1. Conclusions

Satellite remote sensing has provided an unprecedented opportunity to capture surface properties and information on heat and water transfer at the interface between the land surface and the lower atmosphere. A range of models which primarily incorporate remotely sensed land surface temperature (LST)/radiative temperature (T_{rad}) and Vegetation Index (VI) have been developed over the past three decades, with the aim to provide spatially consistent and temporally continuous ET estimates. There are, however, large grey areas in these modeling schemes and techniques. The dissertation research presented in Chapters II-VII primarily focuses on improving the spatial and temporal representation and retrieval accuracy of ET from satellite imagery and modeling. In general, the overall objective is achieved through two aspects: improving the key component in the energy balance equation and improving the derivation of boundary conditions of latent heat flux (LE)/ET involved in satellite-based models.

Aiming at improving the key variable in determining daily ET estimation, daily net radiation, in Chapter II, a model depicting the geometric relationship between the incident radiation and the sloping land surface was adopted to compute available shortwave radiation for sloping land surfaces throughout a day. In addition, four observations of MODIS-based LST products were tentatively used to estimate daily net

longwave radiation. Improvements in the two components of daily net radiation have shown to effectively improve the overall representation of daily net radiation for ET estimation at large heterogeneous areas on clear sky days. In resulting daily net radiation maps, differences in daily net radiation retrievals for different slopes, azimuths, and dates are explicitly shown, which restore the realistic heterogeneity in surface radiative energy status and consequently improves ET estimation at a daily timescale.

Satellite-based ET models have been constrained to work under cloud-free days, which significantly limit application of satellite-based ET estimates to a variety of disciplines and areas. Chapter III provides a new integrated technique of a continuous monitoring capability of ET by combining a satellite-based ET model with a large-scale feedback model (GG). Conventional temporal extrapolation/interpolation techniques based on evaporative fraction or crop coefficient estimates on cloud-free days do not seem to conserve the temporal characteristics of the complementary relationship (CR) between the potential/pan ET and the terrestrial actual ET. The proposed technique can provide spatially distributed and temporal consistent ET estimates by a few scenes of usable satellite imageries and routinely observed weather data due to the incorporation of strengths of the two methodologies. More importantly, the ET time series from the proposed approach can be indicative of CR at the Baiyangdian watershed in North China where CR has been shown valid. This attribute lends credence to the integration approach. Water budget calculations at an annual scale performed in the watershed suggested that the ET time series from the proposed technique has the highest accuracy compared with evaporative fraction and crop coefficient methods.

Chapter IV gives a new Two-source Trapezoid Model for ET (TTME) based on deriving theoretical boundaries of EF and the concept of soil surface moisture availability isopleths. Unlike other one-source models which require determination of boundary conditions of EF/LE by the operator (e.g., extreme pixels in SEBAL and warm and cold edges in triangle models), the TTME algorithm utilizes and derives theoretical boundary conditions, which has shown to greatly reduce subjectivity involved in these models. In addition, T_{rad} is decomposed into temperature components for soil and vegetation (T_c and T_s) based on the isopleths of soil surface moisture availability superimposed into the trapezoid space. Vegetation transpiration and soil surface evaporation can subsequently parameterize without computing networks of surface, canopy, and aerodynamic resistances as Two-source Energy Balance (TSEB). TTME was applied to the SMACEX site in central Iowa, U.S., on three Landsat TM/ETM⁺ imagery acquisition days in 2007. Results indicate that TTME shows a comparable accuracy of RMSD within 10% for EF and LE with TSEB but requires fewer data. Neither the one-source models applied to the same study site showed a higher accuracy of EF/LE than TTME and TSEB nor can they discriminate vegetation transpiration from soil surface evaporation.

Most spatial variability models (e.g., SEBAL, METRIC, and triangle models) are constrained by boundary conditions of EF/ET to infer EF/ET pixels with moderate T_{rad} and f_c states. Unfortunately, these boundary conditions should have to be visually identified/directly derived from satellite imageries. Different sizes and spatial resolutions of satellite imageries being used can result in varying boundary conditions, which is

even exacerbated by the subjectivity of the operator. Motivated by investigating the resolution and domain dependences of two widely used one-source models, SEBAL and the triangle model, and making attempt to address these scale dependencies, systematic analyses of the dependences of SEBAL and triangle models on input, domain size, and spatial resolution are presented in Chapters V and VII, respectively. Results show that these models are both domain and resolution dependent. SEBAL is most sensitive to temperatures of two extreme pixels and the available energy for the hot extreme. The two extremes show a similar influence on the magnitude and distribution of LE and ET retrievals, i.e., with increasing the temperature of the hot/cold extreme, the LE estimates would be increased and *vice versa*.

Chapter VI develops a modified SEBAL model (M-SEBAL), which does not involve visually selected extreme pixels by the operator and assumes that coefficients of the linear relationship between the temperature difference and T_{rad} in the H algorithm of SEBAL vary with f_c but remain invariant within the same f_c . Results suggest that the M-SEBAL model is capable of reproducing EF and LE with an MAPD of 6.3% and 8.9%, respectively, at the SMACEX site, and significantly reducing the subjectivity in selection of extremes.

In Chapter VII, the introduction of the trapezoid framework developed in Chapter IV has shown to be able to effectively restrain uncertainties/errors of LE/EF retrievals from triangle models when applied to the SMACEX site. The domain and resolution dependencies involved can be alleviated to a certain extent.

Overall, the spatial representation and accuracy of ET retrievals from satellite

remote sensing have been improved due to improvements in the key variable, daily net radiation, and the derivation of boundary conditions (extreme pixels/edges) of spatial variability models (i.e., SEBAL and triangle models). In addition, their domain and spatial resolution dependencies have been constrained to varying degrees. The proposed TTME has the potential to reproduce soil surface evaporation and vegetation transpiration with reasonable accuracy using fewer data than TSEB. The ET time series modeling system, consisting of TTME, a new algorithm of computing daily net radiation, and the GG model, seems to be capable of reproducing ET time series with reasonable temporal and spatial distribution on a daily timescale.

8.2. Limitation of research

Validation plays a critically fundamental role in model development. In particular, validating satellite-based flux estimates at pixel scales ranging $10^2 \sim 10^3$ m poses a big challenge in the development of satellite-based ET models. LE and ET measurements at pixel scales ranging between $10^2 \sim 10^3$ from eddy covariance techniques seem to be controversial. The model outputs of H and LE can be interpreted by flux tower measurements after forcing closure by the Bowen ratio method or the energy balance method. There are a $\sim 20 \text{ W m}^{-2}$ difference in LE measurements between the two closure methods. Other ground-based measurement techniques also involve uncertainties, e.g., a large aperture scintillometer (LAS) tends to underestimate H . The difficulty of validating LE retrievals over heterogeneous landscapes and large river basins would be further aggravated. To that end, uncertainties in the “ground truth” of surface fluxes should be

taken into account when performing model validation and comparison.

Only after going through comprehensive validation under a range of climatic, environmental, meteorological, and surface wetness circumstances can a model have the potential to be used and popularized. Given the availability of ground-based surface flux measurements, the new algorithm of daily net radiation and the integration method to produce ET time series were validated at a watershed having an area of 312,500 km² comprising plains and mountains in relatively equal proportions in the semi-humid climatic zone in North China. The modeling scheme of daily net longwave radiation can only be effective on cloud-free days. The daily net shortwave radiation estimates under rugged terrain conditions from the proposed algorithm warrants further validation based on ground radiation measurements. Second, the annual ET estimates from the integration technique appear reasonable, and the temporal distribution of the ET time series exhibited complementary relationship at watershed scales. However, the daily ET estimates at pixel scales from the proposed integration method under cloudy days will be further validated.

The newly developed TTME model, and the framework to restrain the domain and resolution dependencies of SEBAL and the triangle model, were validated in a small watershed (~100 km²) at the SMACEX site (670 km²) dominated by agricultural crops (soybean and corn) in a humid climatic zone on three Landsat TM/ETM⁺ acquisition days during the period from mid-June through early July in 2002. This set-up provides generally high f_c and large ET conditions. The robustness in satellite-based ET models would be manifested under dry and low f_c conditions. As illustrated in Section 6.3.4, f_c

values at 12 flux towers were generally larger than 0.5, which virtually provided a model set-up of relatively high f_c . Section 4.5.3 has illustrated the limitations of the proposed model arising from three important assumptions: linear combination of component temperatures, the use of areal averaged T_a to be the cold edge of the lower boundary condition of the model, and generally homogenous meteorological conditions. The applicability of TTME under the dry environments and arid/semi-arid climatic conditions will be further investigated. The data set of the Southern Great Plains in the U.S. and the Heihe River basin in northwestern China would be acquired for validating the TTME algorithm over large areas and the arid environments.

8.3. Recommendations of future research

With the experience and insight gained from the studies, the following perspectives are recommended for future research:

- (1) Data assimilation may offer a potential way to combine the complementary information from measurements and models of the Earth system into an optimal estimate of the geophysical field of interest. In doing so, data assimilation systems interpolate and extrapolate remote sensing observations and provide complete estimates at the scales required by the application-both in time and spatial dimensions (Reichle, 2008). Data assimilation techniques would also provide an opportunity to more effectively incorporate remotely sensed ET estimates into hydrologic modeling and make other hydrologic processes and states have more

reasonable magnitude and representation.

- (2) Downscaling of ET estimates from coarser spatial resolution images to finer ones will be further investigated so as to provide more useful ET estimates at field scales by operational satellite data, e.g., MODIS, NOAA, and GOES. The core issue of downscaling of satellite-based ET estimates lies in the downscaling of coarser LST retrievals. Information on subpixel variations in land cover, VI, and terrain would be useful for downscaling coarser LST retrievals.

REFERENCES

- Agam, N., Kustas, W.P., Anderson, M.C., Norman, J.M., Colaizzi, P.D. et al., 2010. Application of the Priestley-Taylor approach in a two-source surface energy balance model. *Journal of Hydrometeorology*, 11(1): 185-198.
- Ahmad, M.D., Biggs, T., Turrall, H. and Scott, C.A., 2006. Application of SEBAL approach and MODIS time-series to map vegetation water use patterns in the data scarce Krishna river basin of India. *Water Science and Technology*, 53(10): 83-90.
- Ahmed, B.M., Tanakamaru, H. and Tada, A., 2010. Application of remote sensing for estimating crop water requirements, yield and water productivity of wheat in the Gezira Scheme. *International Journal of Remote Sensing*, 31(16): 4281-4294.
- Allen, R.G., 2000. Using the FAO-56 dual crop coefficient method over an irrigated region as part of an evapotranspiration intercomparison study. *Journal of Hydrology*, 229(1-2): 27-41.
- Allen, R.G., Pereira, L.S., Raes, D. and Smith, M., 1998. Crop evapotranspiration-guidelines for computing crop water requirements. FAO irrigation and drainage paper 56. United Nations Food and Agriculture Organization, Rome.
- Allen, R.G., Tasumi, M. and Trezza, R., 2007. Satellite-based energy balance for mapping evapotranspiration with internalized calibration (METRIC) - Model. *Journal of Irrigation and Drainage Engineering-ASCE*, 133(4): 380-394.

- Allen, R.G., Trezza, R. and Tasumi, M., 2006. Analytical integrated functions for daily solar radiation on slopes. *Agricultural and Forest Meteorology*, 139(1-2): 55-73.
- Anderson, M.C., Norman, J.M., Kustas, W.P., Li, F., Prueger, J.H. et al., 2005. Effects of vegetation clumping on two-source model estimates of surface energy fluxes from an agricultural landscape during SMACEX. *Journal of Hydrometeorology*, 6(6): 892-909.
- Anderson, M.C., Norman, J.M., Mecikalski, J.R., Otkin, J.A. and Kustas, W.P., 2007a. A climatological study of evapotranspiration and moisture stress across the continental United States based on thermal remote sensing: 1. Model formulation. *Journal of Geophysical Research-Atmospheres*, 112(D10): D10117.
- Anderson, M.C., Norman, J.M., Mecikalski, J.R., Otkin, J.A. and Kustas, W.P., 2007b. A climatological study of evapotranspiration and moisture stress across the continental United States based on thermal remote sensing: 2. Surface moisture climatology. *Journal of Geophysical Research-Atmospheres*, 112: D10117.
- Armstrong, R.N., Pomeroy, J.W. and Martz, L.W., 2008. Evaluation of three evaporation estimation methods in a Canadian prairie landscape. *Hydrological Processes*, 22(15): 2801-2815.
- Arnold, J.G., Allen, P.M. and Bernhardt, G., 1993. A comprehensive surface-groundwater flow model. *Journal of Hydrology*, 142(1-4): 47-69.
- Baldocchi, D., Falge, E., Gu, L.H., Olson, R., Hollinger, D. et al., 2001. FLUXNET: a new tool to study the temporal and spatial variability of ecosystem-scale carbon dioxide, water vapor, and energy flux densities. *Bulletin of the American*

- Meteorological Society, 82(11): 2415-2434.
- Bashir, M.A., Tanakamaru, H. and Tada, A., 2009. Spatial and temporal analysis of evapotranspiration using satellite remote sensing data: a case study in the Gezira Scheme, Sudan. *Journal of Environmental Informatics*, 13(2): 86-92.
- Bastiaanssen, W., Thoreson, B., Clark, B. and Davids, G., 2010. Discussion of "Application of SEBAL Model for Mapping Evapotranspiration and Estimating Surface Energy Fluxes in South-Central Nebraska" by Ramesh K. Singh, Ayse Irmak, Suat Irmak, and Derrel L. Martin. *Journal of Irrigation and Drainage Engineering-ASCE*, 136(4): 282-283.
- Bastiaanssen, W.G.M., 1995. Regionalization of surface flux densities and moisture indicators in composite terrain: a remote sensing approach under clear skies in Mediterranean climates. Publisher, Wageningen, The Netherlands.
- Bastiaanssen, W.G.M., 2000. SEBAL-based sensible and latent heat fluxes in the irrigated Gediz Basin, Turkey. *Journal of Hydrology*, 229(1-2): 87-100.
- Bastiaanssen, W.G.M., Ahmad, M.U.D. and Chemin, Y., 2002. Satellite surveillance of evaporative depletion across the Indus Basin. *Water Resources Research*, 38(12): 1273.
- Bastiaanssen, W.G.M. and Chandrapala, L., 2003. Water balance variability across Sri Lanka for assessing agricultural and environmental water use. *Agricultural Water Management*, 58(2): 171-192.
- Bastiaanssen, W.G.M., Menenti, M., Feddes, R.A. and Holtslag, A.A.M., 1998a. A remote sensing surface energy balance algorithm for land (SEBAL) - 1.

- Formulation. *Journal of Hydrology*, 213(1-4): 198-212.
- Bastiaanssen, W.G.M., Noordman, E.J.M., Pelgrum, H., Davids, G., Thoreson, B.P. et al., 2005. SEBAL model with remotely sensed data to improve water-resources management under actual field conditions. *Journal of Irrigation and Drainage Engineering-ASCE*, 131(1): 85-93.
- Bastiaanssen, W.G.M., Pelgrum, H., Wang, J., Ma, Y., Moreno, J.F. et al., 1998b. A remote sensing surface energy balance algorithm for land (SEBAL) - 2. Validation. *Journal of Hydrology*, 213(1-4): 213-229.
- Batra, N., Islam, S., Venturini, V., Bisht, G. and Jiang, J., 2006. Estimation and comparison of evapotranspiration from MODIS and AVHRR sensors for clear sky days over the Southern Great Plains. *Remote Sensing of Environment*, 103(1): 1-15.
- Betts, A.K., Chen, F., Mitchell, K.E. and Janjic, Z.I., 1997. Assessment of the land surface and boundary layer models in two operational versions of the NCEP Eta Model using FIFE data. *Monthly Weather Review*, 125(11): 2896-2916.
- Beven, K.J. and Fisher, J., 1996. Remote sensing and scaling in hydrology. *Scaling up in hydrology using remote sensing*. John Wiley & Sons., Chichester, UK.
- Biftu, G.F. and Gan, T.Y., 2000. Assessment of evapotranspiration models applied to a watershed of Canadian Prairies with mixed land-uses. *Hydrological Processes*, 14(7): 1305-1325.
- Bisht, G., Venturini, V., Islam, S. and Jiang, L., 2005. Estimation of the net radiation using MODIS (Moderate Resolution Imaging Spectroradiometer) data for clear

- sky days. *Remote Sensing of Environment*, 97(1): 52-67.
- Bois, B., Pieri, P., Van Leeuwen, C., Wald, L., Huard, F. et al., 2008. Using remotely sensed solar radiation data for reference evapotranspiration estimation at a daily time step. *Agricultural and Forest Meteorology*, 148(4): 619-630.
- Bouchet, R.J., 1963. Evapotranspiration réelle et potentielle, signification climatique, 66. Int. Assoc. Sci. Hydrol., Gentbrugge, Belgium, General Assembly Berkeley.
- Brotzge, J.A. and Crawford, K.C., 2003. Examination of the surface energy budget: a comparison of eddy correlation and Bowen ratio measurement systems. *Journal of Hydrometeorology*, 4(2): 160-178.
- Brunner, P., Li, H.T., Kinzelbach, W., Li, W.P. and Dong, X.G., 2008. Extracting phreatic evaporation from remotely sensed maps of evapotranspiration. *Water Resources Research*, 44(8): W08428.
- Brutsaert, W., 1975. Derivable formula for longwave radiation from clear skies. *Water Resources Research*, 11(5): 742-744.
- Brutsaert, W., 1982. Evaporation into the atmosphere: theory, history, and applications. D. Reidel, Boston.
- Brutsaert, W., 2005. Hydrology: an introduction. Cambridge University Press, New York.
- Brutsaert, W. and Sugita, M., 1992. Application of self-preservation in the diurnal evolution of the surface-energy budget to determine daily evaporation. *Journal of Geophysical Research-Atmospheres*, 97(D17): 18377-18382.
- Carlson, T., 2007. An overview of the "triangle method" for estimating surface

- evapotranspiration and soil moisture from satellite imagery. *Sensors*, 7(8): 1612-1629.
- Carlson, T.N., Capehart, W.J. and Gillies, R.R., 1995a. A new look at the simplified method for remote-sensing of daily evapotranspiration. *Remote Sensing of Environment*, 54(2): 161-167.
- Carlson, T.N., Gillies, R.R. and Perry, E.M., 1994. A method to make use of thermal infrared temperature and NDVI measurements to infer surface soil water content and fractional vegetation cover. *Remote Sensing Reviews*, 9: 161-173.
- Carlson, T.N., Gillies, R.R. and Schmugge, T.J., 1995b. An interpretation of methodologies for indirect measurement of soil-water content. *Agricultural and Forest Meteorology*, 77(3-4): 191-205.
- Carlson, T.N. and Ripley, D.A., 1997. On the relation between NDVI, fractional vegetation cover, and leaf area index. *Remote Sensing of Environment*, 62(3): 241-252.
- Chander, G., Markham, B.L. and Helder, D.L., 2009. Summary of current radiometric calibration coefficients for Landsat MSS, TM, ETM+, and EO-1 ALI sensors. *Remote Sensing of Environment*, 113(5): 893-903.
- Chen, Y.M., Guo, G.S. and Wang, G.X., 1995. Main crop water requirement and irrigation in China. China Waterpower Press, Beijing.
- Choi, M., Kustas, W.P., Anderson, M.C., Allen, R.G., Li, F.Q. et al., 2009. An intercomparison of three remote sensing-based surface energy balance algorithms over a corn and soybean production region (Iowa, US) during SMACEX.

- Agricultural and Forest Meteorology, 149(12): 2082-2097.
- Choudhury, B.J., 1997. Global pattern of potential evaporation calculated from the Penman-Monteith equation using satellite and assimilated data. *Remote Sensing of Environment*, 61(1): 64-81.
- Compaore, H., Hendrickx, J.M.H., Hong, S.H., Friesen, J., van de Giesen, N.C. et al., 2008. Evaporation mapping at two scales using optical imagery in the white Volta basin, upper east Ghana. *Physics and Chemistry of the Earth*, 33(1-2): 127-140.
- Courault, D., Jacob, F., Benoit, V., Weiss, M., Marloie, O. et al., 2009. Influence of agricultural practices on micrometeorological spatial variations at local and regional scales. *International Journal of Remote Sensing*, 30(5): 1183-1205.
- Crago, R. and Crowley, R., 2005. Complementary relationships for near-instantaneous evaporation. *Journal of Hydrology*, 300(1-4): 199-211.
- Crago, R.D., 1996. Conservation and variability of the evaporative fraction during the daytime. *Journal of Hydrology*, 180(1-4): 173-194.
- Crow, W.T., Kustas, W.P. and Prueger, J.H., 2008. Monitoring root-zone soil moisture through the assimilation of a thermal remote sensing-based soil moisture proxy into a water balance model. *Remote Sensing of Environment*, 112(4): 1268-1281.
- Droogers, P. and Bastiaanssen, W., 2002. Irrigation performance using hydrological and remote sensing modeling. *Journal of Irrigation and Drainage Engineering-ASCE*, 128(1): 11-18.
- Engman, E.T., 1996. Remote sensing applications to hydrology: Future impact.

- Hydrological Sciences Journal-Journal Des Sciences Hydrologiques, 41(4): 637-647.
- Farah, H.O., 2000. Estimation of regional evaporation under all sky conditions with satellite and routine weather data. Ph.D Thesis, Wageningen University, Netherlands, 200 pp.
- Farah, H.O., Bastiaanssen, W.G.M. and Feddes, R.A., 2004. Evaluation of the temporal variability of the evaporative fraction in a tropical watershed. *International Journal of Applied Earth Observation and Geoinformation*, 5: 129-140.
- Flerchinger, G.N., Hanson, C.L. and Wight, J.R., 1996. Modeling evapotranspiration and surface energy budgets across a watershed. *Water Resources Research*, 32(8): 2539-2548.
- Folhes, M.T., Renno, C.D. and Soares, J.V., 2009. Remote sensing for irrigation water management in the semi-arid Northeast of Brazil. *Agricultural Water Management*, 96(10): 1398-1408.
- Forman, B.A. and Margulis, S.A., 2009. High-resolution satellite-based cloud-coupled estimates of total downwelling surface radiation for hydrologic modeling applications. *Hydrology and Earth System Sciences*, 13(7): 969-986.
- Fortin, J.G., Anctil, F., Parent, L.E. and Bolinder, M.A., 2008. Comparison of empirical daily surface incoming solar radiation models. *Agricultural and Forest Meteorology*, 148(8-9): 1332-1340.
- French, A.N., Jacob, F., Anderson, M.C., Kustas, W.P., Timmermans, W. et al., 2005a. Corrigendum to "Surface energy fluxes with the Advanced Spaceborne Thermal

- Emission and Reflection radiometer (ASTER) at the Iowa 2002 SMACEX site (USA) (vol 99, pg 55, 2005)". *Remote Sensing of Environment*, 99(4): 471-471.
- French, A.N., Jacob, F., Anderson, M.C., Kustas, W.P., Timmermans, W. et al., 2005b. Surface energy fluxes with the Advanced Spaceborne Thermal Emission and Reflection radiometer (ASTER) at the Iowa 2002 SMACEX site (USA). *Remote Sensing of Environment*, 99(1-2): 55-65.
- Fu, B.P., 1983. *Upland Climatology*. Science Press, Beijing.
- Gao, B.C. and Kaufman, Y.J., 2003. Water vapor retrievals using moderate resolution Imaging spectroradiometer (MODIS) near-infrared channels. *Journal of Geophysical Research-Atmospheres*, 108(D13): 4389.
- Gao, Y.C. and Long, D., 2008. Intercomparison of remote sensing-based models for estimation of evapotranspiration and accuracy assessment based on SWAT. *Hydrological Processes*, 22(25): 4850-4869.
- Gao, Y.C., Long, D. and Li, Z.L., 2008. Estimation of daily actual evapotranspiration from remotely sensed data under complex terrain over the upper Chao river basin in North China. *International Journal of Remote Sensing*, 29(11): 3295-3315.
- Garrison, J.D. and Adler, G.P., 1990. Estimation of precipitable water over the united-states for application to the division of solar-radiation into its direct and diffuse components. *Solar Energy*, 44(4): 225-241.
- Gates, D.M., 1980. *Biophysical Ecology*. Springer-Verlag, New York.
- Gebremichael, M., Wang, J.M. and Sammis, T.W., 2010. Dependence of remote sensing evapotranspiration algorithm on spatial resolution. *Atmospheric Research*, 96(4):

489-495.

- Gentine, P., Entekhabi, D., Chehbouni, A., Boulet, G. and Duchemin, B., 2007. Analysis of evaporative fraction diurnal behaviour. *Agricultural and Forest Meteorology*, 143(1-2): 13-29.
- Gillies, R.R. and Carlson, T.N., 1995. Thermal remote-sensing of surface soil-water content with partial vegetation cover for incorporation into climate-models. *Journal of Applied Meteorology*, 34(4): 745-756.
- Gillies, R.R., Carlson, T.N., Cui, J., Kustas, W.P. and Humes, K.S., 1997. A verification of the 'triangle' method for obtaining surface soil water content and energy fluxes from remote measurements of the Normalized Difference Vegetation Index (NDVI) and surface radiant temperature. *International Journal of Remote Sensing*, 18(15): 3145-3166.
- Gonzalez-Dugo, M.P., Neale, C.M.U., Mateos, L., Kustas, W.P., Prueger, J.H. et al., 2009. A comparison of operational remote sensing-based models for estimating crop evapotranspiration. *Agricultural and Forest Meteorology*, 149(11): 1843-1853.
- Goward, S.N., Xue, Y.K. and Czajkowski, K.P., 2002. Evaluating land surface moisture conditions from the remotely sensed temperature/vegetation index measurements: An exploration with the simplified simple biosphere model. *Remote Sensing of Environment*, 79(2-3): 225-242.
- Granger, R.J., 1989. A complementary relationship approach for evaporation from nonsaturated surfaces. *Journal of Hydrology*, 111(1-4): 31-38.

- Granger, R.J., 1996. Summer energy balance at Wolf Creek Research Basin, Yukon, Hydro-Ecology Workshop on the Arctic Environmental Strategy-Action of Water, Milburn D(ed.), Canadian Geophysical Union: Banff, Alberta.
- Granger, R.J., 1998. Partitioning of energy during the snow-free season at the Wolf Creek Research Basin, J.W. Pomeroy and R.J. Granger (Eds.), Proceedings of a Workshop held in Whitehorse, Saskatoon, pp. 33-43.
- Granger, R.J. and Gray, D.M., 1989. Evaporation from natural nonsaturated surfaces. *Journal of Hydrology*, 111(1-4): 21-29.
- Hobbins, M.T., Ramirez, J.A. and Brown, T.C., 2004. Trends in pan evaporation and actual evapotranspiration across the conterminous US: Paradoxical or complementary? *Geophysical Research Letters*, 31(13): L13503.
- Hong, S.H., Hendrickx, J.M.H. and Borchers, B., 2009. Up-scaling of SEBAL derived evapotranspiration maps from Landsat (30 m) to MODIS (250 m) scale. *Journal of Hydrology*, 370(1-4): 122-138.
- Hurtado, E. and Sobrino, J.A., 2001. Daily net radiation estimated from air temperature and NOAA-AVHRR data: a case study for the Iberian Peninsula. *International Journal of Remote Sensing*, 22(8): 1521-1533.
- Immerzeel, W.W. and Droogers, P., 2008. Calibration of a distributed hydrological model based on satellite evapotranspiration. *Journal of Hydrology*, 349(3-4): 411-424.
- Immerzeel, W.W., Gaur, A. and Zwart, S.J., 2008. Integrating remote sensing and a process-based hydrological model to evaluate water use and productivity in a south Indian catchment. *Agricultural Water Management*, 95(1): 11-24.

- Irmak, S., Irmak, A., Jones, J.W., Howell, T.A., Jacobs, J.M. et al., 2003. Predicting daily net radiation using minimum climatological data. *Journal of Irrigation and Drainage Engineering-ASCE*, 129(4): 256-269.
- Jacobs, J.M., Myers, D.A., Anderson, M.C. and Diak, G.R., 2000. GOES surface insolation to estimate wetlands evapotranspiration. *Journal of Hydrology*, 266(1-2): 53-65.
- Jegade, O.O., 1997. Daily averages of net radiation measured at Osu, Nigeria in 1995. *International Journal of Climatology*, 17(12): 1357-1367.
- Jiang, L. and Islam, S., 1999. A methodology for estimation of surface evapotranspiration over large areas using remote sensing observations. *Geophysical Research Letters*, 26(17): 2773-2776.
- Jiang, L. and Islam, S., 2001. Estimation of surface evaporation map over southern Great Plains using remote sensing data. *Water Resources Research*, 37(2): 329-340.
- Jiang, L. and Islam, S., 2003. An intercomparison of regional latent heat flux estimation using remote sensing data. *International Journal of Remote Sensing*, 24(11): 2221-2236.
- Jiang, L., Islam, S., Guo, W., Jutla, A.S., Senarath, S.U.S. et al., 2009. A satellite-based Daily Actual Evapotranspiration estimation algorithm over South Florida. *Global and Planetary Change*, 67(1-2): 62-77.
- Jimenez-Munoz, J.C. and Sobrino, J.A., 2003. A generalized single-channel method for retrieving land surface temperature from remote sensing data. *Journal of Geophysical Research-Atmospheres*, 108(D22): 4688.

- Kahler, D.M. and Brutsaert, W., 2006. Complementary relationship between daily evaporation in the environment and pan evaporation. *Water Resources Research*, 42(5): W05413.
- Kalma, J.D., McVicar, T.R. and McCabe, M.F., 2008. Estimating land surface evaporation: A review of methods using remotely sensed surface temperature data. *Surveys in Geophysics*, 29(4-5): 421-469.
- Karatas, B.S., Akkuzu, E., Unal, H.B., Asik, S. and Avci, M., 2009. Using satellite remote sensing to assess irrigation performance in Water User Associations in the Lower Gediz Basin, Turkey. *Agricultural Water Management*, 96(6): 982-990.
- Kempf, S.K. and Tyler, S.W., 2006. Spatial characterization of land surface energy fluxes and uncertainty estimation at the Salar de Atacama, Northern Chile. *Advances in Water Resources*, 29(2): 336-354.
- Kim, J.Y. and Hogue, T.S., 2008. Evaluation of a MODIS-based potential evapotranspiration product at the point scale. *Journal of Hydrometeorology*, 9(3): 444-460.
- Kleissl, J., Hong, S.H. and Hendrickx, J.M.H., 2009. NEW MEXICO SCINTILLOMETER NETWORK Supporting Remote Sensing and Hydrologic and Meteorological Models. *Bulletin of the American Meteorological Society*, 90(2): 207-218.
- Kondo, J., 1994. *Meteorology of Water Environment*. Asakura-shoten, Tokyo.
- Kongo, V.M. and Jewitt, G.P.W., 2006. Preliminary investigation of catchment hydrology in response to agricultural water use innovations: A case study of the Potshini

- catchment - South Africa. *Physics and Chemistry of the Earth*, 31(15-16): 976-987.
- Krajewski, W.F., Anderson, M.C., Eichinger, W.E., Entekhabi, D., Hornbuckle, B.K. et al., 2006. A remote sensing observatory for hydrologic sciences: A genesis for scaling to continental hydrology. *Water Resources Research*, 42(7): W07301.
- Kustas, W. and Anderson, M., 2009. Advances in thermal infrared remote sensing for land surface modeling. *Agricultural and Forest Meteorology*, 149(12): 2071-2081.
- Kustas, W.P., Anderson, M.C., Norman, J.M. and Li, F.Q., 2007. Utility of radiometric-aerodynamic temperature relations for heat flux estimation. *Boundary-Layer Meteorology*, 122(1): 167-187.
- Kustas, W.P., Hatfield, J.L. and Prueger, J.H., 2005. The soil moisture-atmosphere coupling experiment (SMACEX): Background, hydrometeorological conditions, and preliminary findings. *Journal of Hydrometeorology*, 6(6): 791-804.
- Kustas, W.P., Li, F., Jackson, T.J., Prueger, J.H., MacPherson, J.I. et al., 2004. Effects of remote sensing pixel resolution on modeled energy flux variability of croplands in Iowa. *Remote Sensing of Environment*, 92(4): 535-547.
- Kustas, W.P. and Norman, J.M., 1996. Use of remote sensing for evapotranspiration monitoring over land surfaces. *Hydrological Sciences Journal-Journal Des Sciences Hydrologiques*, 41(4): 495-516.
- Kustas, W.P. and Norman, J.M., 1999. Evaluation of soil and vegetation heat flux predictions using a simple two-source model with radiometric temperatures for

- partial canopy cover. *Agricultural and Forest Meteorology*, 94(1): 13-29.
- Kustas, W.P., Perry, E.M., Doraiswamy, P.C. and Moran, M.S., 1994a. Using satellite remote-sensing to extrapolate evapotranspiration estimates in time and space over a semiarid rangeland basin. *Remote Sensing of Environment*, 49(3): 275-286.
- Kustas, W.P., Pinker, R.T., Schmugge, T.J. and Humes, K.S., 1994b. Daytime net-radiation estimated for a semi-arid rangeland basin from remotely-sensed data. *Agricultural and Forest Meteorology*, 71(3-4): 337-357.
- Lagouarde, J.P. and Brunet, Y., 1993. A Simple-Model for Estimating the Daily Upward Longwave Surface Radiation Flux from NOAA-AVHRR Data. *International Journal of Remote Sensing*, 14(5): 907-925.
- Lambin, E.F. and Ehrlich, D., 1996. The surface temperature-vegetation index space for land cover and land-cover change analysis. *International Journal of Remote Sensing*, 17(3): 463-487.
- Li, F.Q., Jackson, T.J., Kustas, W.P., Schmugge, T.J., French, A.N. et al., 2004. Deriving land surface temperature from Landsat 5 and 7 during SMEX02/SMACEX. *Remote Sensing of Environment*, 92(4): 521-534.
- Li, F.Q., Kustas, W.P., Anderson, M.C., Prueger, J.H. and Scott, R.L., 2008a. Effect of remote sensing spatial resolution on interpreting tower-based flux observations. *Remote Sensing of Environment*, 112(2): 337-349.
- Li, F.Q., Kustas, W.P., Prueger, J.H., Neale, C.M.U. and Jackson, T.J., 2005. Utility of remote sensing-based two-source energy balance model under low- and

- high-vegetation cover conditions. *Journal of Hydrometeorology*, 6(6): 878-891.
- Li, H.J., Zheng, L., Lei, Y.P., Li, C.Q., Liu, Z.J. et al., 2008b. Estimation of water consumption and crop water productivity of winter wheat in North China Plain using remote sensing technology. *Agricultural Water Management*, 95(11): 1271-1278.
- Li, S.B. and Zhao, W.Z., 2010. Satellite-based actual evapotranspiration estimation in the middle reach of the Heihe River Basin using the SEBAL method. *Hydrological Processes*, 24(23): 3337-3344.
- Liang, S.L., 2004. Quantitative remote sensing of land surfaces. John Wiley & Sons, Hoboken, New Jersey.
- Liu, B.Y.H. and Jordan, R.C., 1960. The Interrelationship and Characteristic Distribution of Direct, Diffuse and Total Solar Radiation. *Solar Energy*, 4(3): 1-19.
- Liu, S.M., Sun, R., Sun, Z.P., Li, X.O. and Liu, C.M., 2006. Evaluation of three complementary relationship approaches for evapotranspiration over the Yellow River basin. *Hydrological Processes*, 20(11): 2347-2361.
- Lucht, W., Schaaf, C.B. and Strahler, A.H., 2000. An algorithm for the retrieval of albedo from space using semiempirical BRDF models. *IEEE Transactions on Geoscience and Remote Sensing*, 38(2): 977-998.
- Mahmood, R. and Hubbard, K.G., 2002. Effect of time of temperature observation and estimation of daily solar radiation for the northern Great Plains, USA. *Agronomy Journal*, 94(4): 723-733.
- Marx, A., Kunstmann, H., Schuttemeyer, D. and Moene, A.F., 2008. Uncertainty analysis

- for satellite derived sensible heat fluxes and scintillometer measurements over Savannah environment and comparison to mesoscale meteorological simulation results. *Agricultural and Forest Meteorology*, 148(4): 656-667.
- McCabe, M.F. and Wood, E.F., 2006. Scale influences on the remote estimation of evapotranspiration using multiple satellite sensors. *Remote Sensing of Environment*, 105(4): 271-285.
- Melesse, A.M. and Nangia, V., 2005. Estimation of spatially distributed surface energy fluxes using remotely-sensed data for agricultural fields. *Hydrological Processes*, 19(14): 2653-2670.
- Mira, M., Valor, E., Boluda, R., Caselles, V. and Coll, C., 2007. Influence of soil water content on the thermal infrared emissivity of bare soils: Implication for land surface temperature determination. *Journal of Geophysical Research-Earth Surface*, 112(F4): F04003.
- Mohamed, Y.A., Bastiaanssen, W.G.M. and Savenije, H.H.G., 2004. Spatial variability of evaporation and moisture storage in the swamps of the upper Nile studied by remote sensing techniques. *Journal of Hydrology*, 289(1-4): 145-164.
- Mohamed, Y.A., Savenije, H.H.G., Bastiaanssen, W.G.M. and van den Hurk, B.J.J.M., 2006. New lessons on the Sudd hydrology learned from remote sensing and climate modeling. *Hydrology and Earth System Sciences*, 10(4): 507-518.
- Monteith, J.L., 1965. Evaporation and environment, *Symposia of the Society for Experimental Biology (SAUS)*, pp. 205-224.
- Moran, M.S., Clarke, T.R., Inoue, Y. and Vidal, A., 1994. Estimating crop water-deficit

using the relation between surface-air temperature and spectral vegetation index. *Remote Sensing of Environment*, 49(3): 246-263.

Morse, A., Tasumi, M., Allen, R.G. and Kramber, W.J., 2000. Final Report. Application of the SEBAL methodology for estimating consumptive use of water and streamflow depletion in the Bear River Basin of Idaho through remote sensing, Idaho Department of Water Resources and University of Idaho.

Morton, F.I., 1983. Operational estimates of areal evapotranspiration and their significance to the science and practice of hydrology. *Journal of Hydrology*, 66: 1-76.

Nemani, R., Pierce, L., Running, S. and Goward, S., 1993. Developing satellite-derived estimates of surface moisture status. *Journal of Applied Meteorology*, 32(3): 548-557.

Nemani, R.R. and Running, S.W., 1989. Estimation of Regional Surface-Resistance to Evapotranspiration from Ndvi and Thermal-Ir Avhrr Data. *Journal of Applied Meteorology*, 28(4): 276-284.

Nishida, K., Nemani, R.R., Running, S.W. and Glassy, J.M., 2003. An operational remote sensing algorithm of land surface evaporation. *Journal of Geophysical Research-Atmospheres*, 108(D9): 4270.

Norman, J.M., Anderson, M.C. and Kustas, W.P., 2006. Are single-source, remote sensing surface flux models too simple? In: G. D'Urso, M.A.O. Jochum and J. Moreno (Editors), *Proceedings of the international conference on earth observation for vegetation monitoring and water management*. American Institute

of Physics, pp. 170-177.

Norman, J.M., Anderson, M.C., Kustas, W.P., French, A.N., Mecikalski, J. et al., 2003.

Remote sensing of surface energy fluxes at 10(1)-m pixel resolutions. *Water Resources Research*, 39(8): WR001775.

Norman, J.M., Kustas, W.P. and Humes, K.S., 1995. A two-source approach for estimating soil and vegetation energy fluxes in observations of directional radiometric surface-temperature. *Agricultural and Forest Meteorology*, 77(3-4): 263-293.

Oberg, J.W. and Melesse, A.M., 2006. Evapotranspiration dynamics at an ecohydrological restoration site: An energy balance and remote sensing approach. *Journal of the American Water Resources Association*, 42(3): 565-582.

Owen, T.W., Carlson, T.N. and Gillies, R.R., 1998. An assessment of satellite remotely-sensed land cover parameters in quantitatively describing the climatic effect of urbanization. *International Journal of Remote Sensing*, 19(9): 1663-1681.

Paulson, C.A., 1970. The mathematical representation of wind speed and temperature profiles in the unstable atmospheric surface layer. *Journal of Applied Meteorology*, 9(6): 857-861.

Pelgrum, H. and Bastiaanssen, W.G.M., 1996. An intercomparison of techniques to determine the area-averaged latent heat flux from individual in situ observations: A remote sensing approach using the European Field Experiment in a Desertification-Threatened Area data. *Water Resources Research*, 32(9):

2775-2786.

Penman, H.L., 1948. Natural evaporation from open water, bare soil and grass.

Proceedings of the Royal Society of London Series a-Mathematical and Physical Sciences, 193(1032): 120-145.

Petropoulos, G., Carlson, T.N., Wooster, M.J. and Islam, S., 2009. A review of T-s/VI remote sensing based methods for the retrieval of land surface energy fluxes and soil surface moisture. *Progress in Physical Geography*, 33(2): 224-250.

Price, J.C., 1990. Using spatial context in satellite data to infer regional scale evapotranspiration. *IEEE Transactions on Geoscience and Remote Sensing*, 28(5): 940-948.

Priestley, C.H.B. and Taylor, R.J., 1972. Assessment of surface heat-flux and evaporation using large-scale parameters. *Monthly Weather Review*, 100(2): 81-92.

Prueger, J.H., Hatfield, J.L., Kustas, W.P., Hipps, L.E., MacPherson, J.I. et al., 2005. Tower and aircraft eddy covariance measurements of water vapor, energy, and carbon dioxide fluxes during SMACEX. *Journal of Hydrometeorology*, 6(6): 954-960.

Qiu, X.F., Zeng, Y., Miao, Q.L. and Yu, Q., 2004. Estimation of annual actual evapotranspiration from nonsaturated land surfaces with conventional meteorological data. *Science in China Series D-Earth Sciences*, 47(3): 239-246.

Ramos, J.G., Cratchley, C.R., Kay, J.A., Casterad, M.A., Martinez-Cob, A. et al., 2009. Evaluation of satellite evapotranspiration estimates using ground-meteorological data available for the Flumen District into the Ebro Valley of NE Spain.

- Agricultural Water Management, 96(4): 638-652.
- Refsgaard, J.C., 1997. Parameterisation, calibration and validation of distributed hydrological models. *Journal of Hydrology*, 198(1-4): 69-97.
- Reichle, R.H., 2008. Data assimilation methods in the Earth sciences. *Advances in Water Resources*, 31(11): 1411-1418.
- Roerink, G.J., Bastiaanssen, W.G.M., Chambouleyron, J. and Menenti, M., 1997. Relating Crop Water Consumption to Irrigation Water Supply by Remote Sensing. *Water Resources Management*, 11(6): 445-465.
- Rubio, E., Caselles, V., Coll, C., Valour, E. and Sospedra, F., 2003. Thermal-infrared emissivities of natural surfaces: improvements on the experimental set-up and new measurements. *International Journal of Remote Sensing*, 24(24): 5379-5390.
- Samani, Z., Bawazir, A.S., Bleiweiss, M., Skaggs, R. and Tran, V.D., 2007. Estimating daily net radiation over vegetation canopy through remote sensing and climatic data. *Journal of Irrigation and Drainage Engineering-ASCE*, 133(4): 291-297.
- Sanchez, J.M., Kustas, W.P., Caselles, V. and Anderson, M.C., 2008. Modelling surface energy fluxes over maize using a two-source patch model and radiometric soil and canopy temperature observations. *Remote Sensing of Environment*, 112(3): 1130-1143.
- Sandholt, I., Rasmussen, K. and Andersen, J., 2002. A simple interpretation of the surface temperature/vegetation index space for assessment of surface moisture status. *Remote Sensing of Environment*, 79(2-3): 213-224.
- Schuermans, J.M., Troch, P.A., Veldhuizen, A.A., Bastiaanssen, W.G.M. and Bierkens,

- M.F.P., 2003. Assimilation of remotely sensed latent heat flux in a distributed hydrological model. *Advances in Water Resources*, 26(2): 151-159.
- Shuttleworth, W.J., Gurney, R.J., Hsu, A.Y. and Ormsby, J.R., 1989. FIFE: the variation in energy the variation in energy partition at surface flux sites, *Proceedings of the IAHS Third Int. IAHS publ, Assembly, Baltimore, MD*, pp. 67-74.
- Singh, R.K., Irmak, A., Irmak, S. and Martin, D.L., 2008. Application of SEBAL model for mapping evapotranspiration and estimating surface energy fluxes in south-central Nebraska. *Journal of Irrigation and Drainage Engineering-ASCE*, 134(3): 273-285.
- Sobrino, J.A., Caselles, V. and Becker, F., 1990. Significance of the remotely sensed thermal infrared measurements obtained over a citrus orchard. *ISPRS Journal of Photogrammetry and Remote Sensing*, 44(6): 343-354.
- Sobrino, J.A. and Raissouni, N., 2000. Toward remote sensing methods for land cover dynamic monitoring: application to Morocco. *International Journal of Remote Sensing*, 21(2): 353-366.
- Stisen, S., Sandholt, I., Norgaard, A., Fensholt, R. and Jensen, K.H., 2008. Combining the triangle method with thermal inertia to estimate regional evapotranspiration - Applied to MSG-SEVIRI data in the Senegal River basin. *Remote Sensing of Environment*, 112(3): 1242-1255.
- Su, H., Wood, E.F., McCabe, M.F. and Su, Z., 2007. Evaluation of remotely sensed evapotranspiration over the CEOP EOP-1 reference sites. *Journal of the Meteorological Society of Japan*, 85A: 439-459.

- Su, H.B., McCabe, M.F., Wood, E.F., Su, Z. and Prueger, J.H., 2005. Modeling evapotranspiration during SMACEX: Comparing two approaches for local- and regional-scale prediction. *Journal of Hydrometeorology*, 6(6): 910-922.
- Su, Z., 2002. The Surface Energy Balance System (SEBS) for estimation of turbulent heat fluxes. *Hydrology and Earth System Sciences*, 6(1): 85-99.
- Tang, R.L., Li, Z.L. and Tang, B.H., 2010. An application of the T-s-VI triangle method with enhanced edges determination for evapotranspiration estimation from MODIS data in and semi-arid regions: Implementation and validation. *Remote Sensing of Environment*, 114(3): 540-551.
- Tasumi, M., Allen, R.G. and Trezza, R., 2008. At-surface reflectance and albedo from satellite for operational calculation of land surface energy balance. *Journal of Hydrologic Engineering*, 13(2): 51-63.
- Teixeira, A.H.D.C., Bastiaanssen, W.G.M., Ahmad, M.D. and Bos, M.G., 2009a. Reviewing SEBAL input parameters for assessing evapotranspiration and water productivity for the Low-Middle Sao Francisco River basin, Brazil Part A: Calibration and validation. *Agricultural and Forest Meteorology*, 149(3-4): 462-476.
- Teixeira, A.H.D.C., Bastiaanssen, W.G.M., Ahmad, M.D. and Bos, M.G., 2009b. Reviewing SEBAL input parameters for assessing evapotranspiration and water productivity for the Low-Middle Sao Francisco River basin, Brazil Part B: Application to the regional scale. *Agricultural and Forest Meteorology*, 149(3-4): 477-490.

- Thornton, P.E., Hasenauer, H. and White, M.A., 2000. Simultaneous estimation of daily solar radiation and humidity from observed temperature and precipitation: an application over complex terrain in Austria. *Agricultural and Forest Meteorology*, 104(4): 255-271.
- Thornton, P.E. and Running, S.W., 1999. An improved algorithm for estimating incident daily solar radiation from measurements of temperature, humidity, and precipitation. *Agricultural and Forest Meteorology*, 93(4): 211-228.
- Timmermans, W.J., Kustas, W.P., Anderson, M.C. and French, A.N., 2007. An intercomparison of the Surface Energy Balance Algorithm for Land (SEBAL) and the Two-Source Energy Balance (TSEB) modeling schemes. *Remote Sensing of Environment*, 108(4): 369-384.
- Twine, T.E., Kustas, W.P., Norman, J.M., Cook, D.R., Houser, P.R. et al., 2000. Correcting eddy-covariance flux underestimates over a grassland. *Agricultural and Forest Meteorology*, 103(3): 279-300.
- Venturini, V., Bisht, G., Islam, S. and Jiang, L., 2004. Comparison of evaporative fractions estimated from AVHRR and MODIS sensors over South Florida. *Remote Sensing of Environment*, 93(1-2): 77-86.
- Voroshmarty, C.J., Federer, C.A. and Schloss, A.L., 1998. Evaporation functions compared on US watersheds: Possible implications for global-scale water balance and terrestrial ecosystem modeling. *Journal of Hydrology*, 207(3-4): 147-169.
- Wan, Z.M. and Dozier, J., 1996. A generalized split-window algorithm for retrieving

- land-surface temperature from space. *IEEE Transactions on Geoscience and Remote Sensing*, 34(4): 892-905.
- Wan, Z.M. and Li, Z.L., 1997. A physics-based algorithm for retrieving land-surface emissivity and temperature from EOS/MODIS data. *IEEE Transactions on Geoscience and Remote Sensing*, 35(4): 980-996.
- Wang, J., Sammis, T.W., Gutschick, V.P., Gebremichael, M. and Miller, D.R., 2009. Sensitivity Analysis of the Surface Energy Balance Algorithm for Land (SEBAL). *Transactions of the Asabe*, 52(3): 801-811.
- Wang, K.C., Li, Z.Q. and Cribb, M., 2006. Estimation of evaporative fraction from a combination of day and night land surface temperatures and NDVI: A new method to determine the Priestley-Taylor parameter. *Remote Sensing of Environment*, 102(3-4): 293-305.
- Webb, E.K., 1970. Profile relationships: The log-linear range, and extension to strong stability. *Quarterly Journal of the Royal Meteorological Society*, 96(407): 67-90.
- Winsemius, H.C., Savenije, H.H.G. and Bastiaanssen, W.G.M., 2008. Constraining model parameters on remotely sensed evaporation: justification for distribution in ungauged basins? *Hydrology and Earth System Sciences*, 12(6): 1403-1413.
- Wu, C.D., Cheng, C.C., Lo, H.C. and Chen, Y.K., 2010. Application of SEBAL and Markov models for future stream flow simulation through remote sensing. *Water Resources Management*, 24(14): 3773-3797.
- Wu, W., Hall, C.A.S., Scatena, F.N. and Quackenbush, L.J., 2006. Spatial modeling of evapotranspiration in the Luquillo experimental forest of Puerto Rico using

- remotely-sensed data. *Journal of Hydrology*, 328(3-4): 733-752.
- Xu, C.Y. and Singh, V.P., 2005. Evaluation of three complementary relationship evapotranspiration models by water balance approach to estimate actual regional evapotranspiration in different climatic regions. *Journal of Hydrology*, 308(1-4): 105-121.
- Xu, Z.X. and Li, J.Y., 2003. Estimating basin evapotranspiration using distributed hydrologic model. *Journal of Hydrologic Engineering*, 8(2): 74-80.
- Yang, D.W., Sun, F.B., Liu, Z.T., Cong, Z.T. and Lei, Z.D., 2006. Interpreting the complementary relationship in non-humid environments based on the Budyko and Penman hypotheses. *Geophysical Research Letters*, 33(18): L18402.
- Yao, W., Han, M. and Xu, S.G., 2010. Estimating the regional evapotranspiration in Zhalong wetland with the Two-Source Energy Balance (TSEB) model and Landsat7/ETM+ images. *Ecological Informatics*, 5(5): 348-358.
- Yin, Y.H., Wu, S.H., Zheng, D. and Yang, Q.Y., 2008. Radiation calibration of FAO56 Penman-Monteith model to estimate reference crop evapotranspiration in China. *Agricultural Water Management*, 95(1): 77-84.
- Yu, J., Zhang, Y. and Liu, C., 2009. Validity of the Bouchet's complementary relationship at 102 observatories across China. *Science in China Series D-Earth Sciences*, 52(5): 708-713.
- Yunusa, I.A.M., Walker, R.R. and Lu, P., 2004. Evapotranspiration components from energy balance, sapflow and microlysimetry techniques for an irrigated vineyard in inland Australia. *Agricultural and Forest Meteorology*, 127(1-2): 93-107.

- Zhang, R.H., 2009. Quantitative thermal infrared remote sensing and its ground experimental basis. Science Press, Beijing.
- Zhang, R.H., Sun, X.M., Wang, W.M., Xu, J.P., Zhu, Z.L. et al., 2005. An operational two-layer remote sensing model to estimate surface flux in regional scale: Physical background. Science in China Series D-Earth Sciences, 48: 225-244.
- Zwart, S.J. and Bastiaanssen, W.G.M., 2007. SEBAL for detecting spatial variation of water productivity and scope for improvement in eight irrigated wheat systems. Agricultural Water Management, 89(3): 287-296.
- Zwart, S.J., Bastiaanssen, W.G.M., de Fraiture, C. and Molden, D.J., 2010. WATPRO: A remote sensing based model for mapping water productivity of wheat. Agricultural Water Management, 97(10): 1628-1636.

VITA

Name: Di Long

Address: Scoates Hall 321, BAEN, Texas A&M University, College Station,
TX 77843-2117

Email: gucas2005@hotmail.com

Education: B.S., Hydraulic and Hydropower Engineering, Tsinghua University,
China, 2005
M.S., Physical Geography, Institute of Geographic Sciences and
Natural Resources Research, Chinese Academy of Sciences, 2008
Ph.D., Biological and Agricultural Engineering, Texas A&M
University, 2011